TEL AVIV UNIVERSITY

THE IBY AND ALADAR FLEISCHMAN FACULTY OF ENGINEERING

The Zandman-Slaner School of Graduate Studies

MIXED MODE FRACTURE BEHAVIOR OF A MULTI-DIRECTIONAL PLAIN WEAVE COMPOSITE - AN INTERFACE DELAMINATION BETWEEN A 0°/90° AND A +45°/-45° WEAVE

By

Orly Dolev

THESIS SUBMITTED TO THE SENATE OF TEL-AVIV UNIVERSITY

in partial fulfillment of the requirements for the degree of

"DOCTOR OF PHILOSOPHY"

December 2020

ISBN: 9788831482172

THE IBY AND ALADAR FLEISCHMAN FACULTY OF ENGINEERING
The Zandman-Slaner School of Graduate Studies

MIXED MODE FRACTURE BEHAVIOR OF A MULTI-DIRECTIONAL PLAIN WEAVE COMPOSITE - AN INTERFACE DELAMINATION BETWEEN A 0°/90° AND A +45°/-45° WEAVE

By

Orly Dolev

THESIS SUBMITTED TO THE SENATE OF TEL-AVIV UNIVERSITY
in partial fulfillment of the requirements for the degree of
"DOCTOR OF PHILOSOPHY"

Under The Supervision of Prof. Leslie Banks-Sills
December 2020

THE IBY AND ALADAR FLEISCHMAN FACULTY OF ENGINEERING
The Zandman-Slaner School of Graduate Studies

This work was carried out under the supervision of

Research Supervisor: Prof. Leslie Banks-Sills

To my beloved family

Acknowledgement

I would like to express my sincere gratitude and acknowledgement to my supervisor, Professor Leslie Banks-Sills, for her direction, support and advice throughout all stages of this work. I greatly appreciate her enormous contribution of time, her uncompromising quest for excellence and the knowledge I have gained from her in the field of fracture mechanic.

I would like to gratefully thank Dr. Victor Forman for his assistance, support and advice in the experimental part of this investigation. His enormous technical knowledge, along with his permanent willingness to help, contributed a lot to the current investigation. I would like to gratefully thank Rami Eliasy for his assistance in the numerical part of this investigation, and his words of encouragement. Thank you for being a great friend.

I would like to thank my friends and colleagues at IAI for their help, for productive discussions and words of encouragement.

I would like to thank all of my colleagues/friends at the fracture mechanics laboratory for the discussions and cooperations that have contributed substantially to this work.

I owe a special gratitude to my beloved family, Moshe, Ofir, Eyal and Adi, for continuous and unconditional support during the last six years. There is no doubt that without their loving and understanding I would not been able to complete this work.

Abstract

Currently, the advantages of composite materials, such as high strength and toughness to weight ratios, corrosion and fatigue resistance, make these materials very attractive and desirable to work with, especially in the aerostructure industry. However, composite material structures are sensitive to the presence of damage such as delamination, which is one of the most typical failure modes in laminate composites. A delamination may be induced during the manufacturing process or may be caused by inadvertent impact damage after manufacturing. The main problem is that most of composite structural damage is difficult to detect or follow. The lack of accurate and reliable fracture toughness, fatigue and damage tolerance properties, which enable the evaluation of damage growth within a composite structure, results in an over-designed structure due to the high safety margin regulations. In order to better understand the mixed mode I/II fracture (initiation and propagation) behavior of a carbon/epoxy multi-directional (MD) woven composite containing an interlaminar delamination between two plain woven plies, with tows in the $0°/90°$ and $+45°/-45°$-directions, a comprehensive investigation has been performed, involving analytical, numerical and experimental work.

The first term of the asymptotic expansion for the stress and displacement fields in the neighborhood of the investigated delamination front have been developed analytically by employing the formalisms of Lekhnitskii (1950) and Stroh (1958). The in-plane stress and displacement fields were related to the complex in-plane stress intensity factor $K = K_1 + iK_2$; the out-of-plane stress and displacement fields were related to the real out-of-plane stress intensity factor K_{III}. These expressions are further used in two separate methods, displacement extrapolation (DE) and the conservative M-integral, for calculation of the stress intensity factors.

All test specimens are analysed by means of the finite element method (FEM) and the M-integral and/or the DE method to determine the stress intensity factors; these are used to obtain the critical interface energy release rate and two phase angles (mode mixities). The software written for the M-integral and the DE method, as well as the first term of the asymptotic displacement field, are verified and both methods are validated by performing numerical analyses on three benchmark problems. Excellent agreement was found by

comparison of the calculated (M-integral and DE) and exact values of the stress intensity factors (analytic solution). In addition, solution convergence and path independence were examined and fulfilled.

Mixed-mode fracture toughness tests are carried out on an MD laminate making use of the Brazilian disk (BD) specimen, containing a delamination, at various loading angles in order to obtain a wide range of mode mixities. Employing the experimentally and numerically obtained results at fracture, a two and three-dimensional failure criterion are generated. A statistical analysis with a 10% probability of unexpected failure and a 95% confidence is performed, in order to account for scatter in the results. These failure criteria may be used for safer design purposes for the investigated interface.

Fracture toughness tests for delamination initiation and propagation under quasi-static loading are carried out making use of three beam-type specimens: double cantilever beam (DCB), calibrated end-loaded split (C-ELS) and mixed mode end-loaded split (MMELS). The deformation modes considered are nearly mode I, nearly mode II and one in-plane mixed mode ratio, respectively. Based upon the experimentally and numerically obtained results, a fracture toughness resistance $\mathcal{G}_{iR}$-curve is generated, for each kind of beam-type specimen. In addition, the critical values of the interface energy release rate for initiation $\mathcal{G}_{ic}$ and steady-state propagation $\mathcal{G}_{iss}$ are determined.

Quantification of the critical energy release rate $\mathcal{G}_{ic}$ values obtained for delamination initiation in all tested specimens, as a function of the in-plane mode mixity, is presented. Use of an empirical failure criterion proposed by Benzeggagh and Kenane (1996) for the beam-type specimens is made. For both specimen configurations (BD and beam-type), it is found that as $\hat{\psi} \to 0$, the value of $\mathcal{G}_{ic}$ decreases. However, the value of $\mathcal{G}_{ic}$ for $\hat{\psi} = 0$ is found to be sensitive to the thickness of the test specimen. Thus, it would appear that for nearly mode I deformation, the thickness of the structural element in question should govern the specimen thickness.

Contents

List of Symbols

Lower Case Latin letters

a	delamination length for an edge delamination, half crack/delamination length for a central crack/delamination in Section 4.5: parameter in the z-variate model
$2a$	BD specimen delamination length
$2a_c$	BD specimen critical delamination length
$2a_c^{(re)}$	remaining critical delamination length in a BD specimen with an arrest hole
Δa	change in crack length
a_c	delamination length at fracture
a_0	an initial artificial (PTFE film) delamination length for beam-type specimen
a_p	a natural pre-delamination length for beam-type specimen
a_f	final delamination length for tested beam-type specimen
$a_n^{(m)}$ $(m = f,\ b;\ n = 0,\ f)$	initial/final delamination length a measured on the front/back side of a beam-type specimen
$\overline{a}_n$ $(n = 0,\ p,\ f)$	beam-type average delamination length corresponding to n
a_i	arbitrary complex constants
$\mathbf{a}$	eigenvector of Stroh formalism
a_α $(\alpha = 1, \cdots, 6)$	eigenvectors of Stroh formalism
b	beam-type specimen width in Section 4.5: parameter in the z-variate model
b_j $(j = 1, \cdots, 5)$	beam-type specimen width at measurement location j
$\overline{b}$	average specimen width
b_i	complex constants related to a_i

$\mathbf{b}$	eigenvector of Stroh formalism related to $\mathbf{a}$
b_α $(\alpha = 1, \cdots, 6)$	eigenvectors of Stroh formalism related to a_α
c	lever length of the MMB test apparatus
c_g	lever length to the center of gravity
c_{hole}	offset distance between the delamination and the center of the arrest hole in a BD specimen
${}_k c_s^*$ $(s = 1, 2)$	elements in the asymptotic displacement and stress fields
d	loading machine actuator displacement
d_{hole}	diameter of arrest hole in BD specimen
$d_{hole}^{(eff)}$	effective diameter of arrest hole in BD specimen
$\mathbf{d}$	arbitrary complex vector
$\mathbf{d}$, $\mathbf{d}_m$ $(m = 1, 2)$	arbitrary vectors corresponding to stress singularity δ_m, related to oscillatory part of solution
$\mathbf{d}^*$, $\mathbf{d}_3$	arbitrary vector corresponding to stress singularity δ_3, related to regular square-root singularity part of solution
d_m $(m = 2, 3)$	unknown constant within $\mathbf{d}_m$, related to the oscillatory part and the regular square-root singularity part of the solution, respectively
$f_m(a/w)$ $(m = I, II)$	normalized geometric factors
$f(z)$	arbitrary function
$f(z_\alpha^{(k)})$ $(\alpha = * = 1, 2, 3)$	arbitrary functions in the Stroh formalism for material k
$f_\alpha(z_\alpha)$ $(\alpha = 1, 2, 3)$	arbitrary functions in the Stroh formalism
$\langle f(z_*) \rangle$	diagonal matrix of functions of $z_\alpha = z_*$
$\mathbf{g}_k$ $(k = 1, 2)$	arbitrary complex vector of material k
g	fitting parameter in eq. (5.4)
h	half-thickness of test specimen
$2h$	beam-type specimen thickness
$\overline{2h}$	average specimen height
h_i $(i = Up,\ Low)$	height of each laminate segment
h_m $(m = t,\ b)$	height of upper $(m = t)$ / lower $(m = b)$ aluminum partial disk of a BD specimen
h_{mj} $(m = T,\ B;\ j = 1, \cdots, 5)$	height of upper $(m = T)$ / lower $(m = B)$ sub-laminate or arm of a beam-type specimen at measurement location j
$2h_j$ $(j = 1, \cdots, 5)$	beam-type specimen thickness at measurement location j
$\overline{h}_m$ $(m = T,\ B)$	average value of h_{mj} $(m = T,\ B)$

$h_{mj}^{(sc)}$ $(m = T,\ B;\ j = 1, \cdots, 5)$	scaled value of h_{mj} $(m = T,\ B)$
$\overline{h}_{m}^{(sc)}$ $(m = T,\ B)$	average value of $h_{mj}^{(sc)}$
k	parameter in compliance calibration equation
k_j $(j = 1, 2, 3)$	normalization factors in Stroh formalism
$k_j^{(k)}$ $(j = 1, 2, 3)$	normalization factors in Stroh formalism for material k
$\ell_1^{(N)}(x_3)$	a parabolic normalized virtual crack extension along the crack front within element N in the x_1-direction
l	beam-type specimen length
$l_j(p)$ $(j = 2, 3, 4)$	polynomials in p of degree j
m	exponent in the Benzeggagh and Kenane (1996) failure criterion
${}_km_s$ $(s = 1, 2)$	elements in the asymptotic displacement and stress fields
n	number of experimental data points located below the statistical failure criterion
n_i $(i = 1, 2, 3)$	components of the normal vector
${}_kn_{st}$; ${}_kn_{st}^*$ $(s = 1, 2, 3;\ t = 1, 2)$	elements in the asymptotic displacement and stress fields
p	complex constant
p_α $(\alpha = * = 1, 2, 3)$	eigenvalues obtained by Lekhnitskii and Stroh formalisms
$p_\alpha^{(k)} = p_*^{(k)}$ $(k = 1, 2)$	eigenvalues $p_\alpha = p_*$ for material k
$\mathbf{q}_k$ $(k = 1, 2)$	arbitrary 3×1 constant vector for material k
$\tilde{\mathbf{q}}_k$ $(k = 1, 2)$	arbitrary 3×1 constant vector for material k
q_α	arbitrary complex constants
$\tilde{q}_\alpha$	arbitrary complex constants
q_1	normalized virtual crack extension function
q_{1i}	values of the function q_1 at element nodal points in Freed and Banks-Sills (2005)
r	radius in polar coordinate system; distance from crack front on a ray orthogonal to the crack front
r_c	estimated small scale interpenetration length Rice (1988)
s	in Section 4.5: standard deviation
s_{ij}	components of the compliance matrix
$\mathbf{s}^{(k)}$ $(k = 1, 2)$	compliance matrix of material k
$s_{\alpha\beta}^{(k)}$	components of the compliance matrix $\mathbf{s}^{(k)}$
s'_{ij}	components of the reduced compliance matrix
$\mathbf{s}'^{(k)}$ $(k = 1, 2)$	reduced compliance matrix of material k

$s'^{(k)}_{\alpha\beta}$	components of the reduced compliance matrix $\mathbf{s}'^{(k)}$
t	specimen thickness
$\mathbf{u}$	vector form of the displacement field
$\mathbf{u}^{(k)}$ $(k = 1, 2)$	displacement vector for material k
u_i $(i = 1, 2, 3)$, or u, v, w	components of displacement field
$\mathbf{u}^{(k)}_{os}$ $(k = 1, 2)$	oscillatory singular part of $\mathbf{u}^{(k)}$
$\mathbf{u}^{(k)}_{s}$ $(k = 1, 2)$	regular square-root singular part of $\mathbf{u}^{(k)}$
$u^{(k)}_{\alpha}$ $(\alpha = 1, 2)$	in-plane displacement components for material k
$u^{(k)}_{3}$	out-of-plane displacement components for material k
${}_k u^{(1)}_i$ $(i = 1, 2, 3)$	components of displacement field of the problem sought for material k
${}_k u^{(2\alpha)}_i$ $(i = 1, 2, 3;\ \alpha = a, b, c)$	components of displacement field of the auxiliary solution for material k
Δu_i $(i = 1, 2, 3)$	the "jump" in the crack face displacement in the i-direction
$\Delta\mathbf{u}_{os}$	oscillatory singularity crack face displacement "jump" vector
$\Delta\mathbf{u}_{s}$	regular square-root singularity crack face displacement "jump" vector
$\Delta u_{i os}$ $(i = 1, 2, 3)$	components of oscillatory singularity crack face displacement "jump" vector $\Delta\mathbf{u}_{os}$ in the i-direction
$\Delta u_{i s}$ $(i = 1, 2, 3)$	components of regular square-root singularity crack face displacement "jump" vector $\Delta\mathbf{u}_{s}$ in the i-direction
w	height of significant zone in the Arcan test specimen
x_i $(i = 1, 2, 3)$, or x, y, z	axes in cartesian coordinate system
z	complex variable in Section 4.5: standard variate
z_α	complex variable related to p_α
$z^{(k)}_\alpha = z^{(k)}_* \ (k = 1, 2)$	complex variable related to $p_\alpha = p_*$ of material k
z_γ	confidence level z-variate following the standard normal distribution
z_P	probability level z-variate following the standard normal distribution

Upper Case Latin letters

$\mathbf{A}$	complex 3×3 matrix composed of the Stroh eigenvectors
$\mathbf{A}_k$ $(k = 1, 2)$	complex 3×3 matrix composed of the Stroh eigenvectors for material k
A_1	integration area
B	thickness of BD specimen
$\mathbf{B}$	complex 3×3 matrix composed of the Stroh eigenvectors
$\mathbf{B}_k$ $(k = 1, 2)$	complex 3×3 matrix composed of the Stroh eigenvectors for material k
${}_kB_s$ $(s = 1, 2, 3)$	elements in the asymptotic displacement and stress fields
$\mathbf{C}$	stiffness matrix
C	compliance of beam-type specimen (d/P)
C_0	parameter in compliance calibration equation, a fitting parameter in eq. (5.4)
C_{ijmn}	stiffness tensor
$C_{\alpha\beta}$	stiffness tensor under contracted notation
C_1, C_2 C_3	in Sections 5.1.2 and 5.3.2: values of fitting parameters in a second order polynomial curve fit between $\mathcal{G}_i^{FEA}$ and corresponding a
D	total length of the delaminated interface in a BD specimen
$\mathbf{D}$	3×3 matrix related to $\mathbf{L}_k$
D_{ij}	components of the matrix $\mathbf{D}$
$\widetilde{D}$	constant related to the first two diagonal members of matrix $\mathbf{D}$
DE	displacement extrapolation method
E	Young's modulus or flexural modulus
E_{ii} $(i = 1, 2, 3)$	Young's moduli in the x_i-direction, no summation implied
$\overline{E}_k$	effective Young's modulus of material k in the bimaterial interface
E_{1f}	flexural modulus
EI	equivalent bending stiffness
$(EI)_i$ $(i = Up,\ Low)$	bending stiffness of each laminate segment
$F(z)$	arbitrary function of z
G_{ij} $(i, j = 1, 2, 3)$	shear moduli
$\mathcal{G}$	energy release rate

$\mathcal{G}_m$ $(m = I, II, III)$	energy release rate corresponding to deformation mode m
$\mathcal{G}_R$	interlaminar fracture resistance
$\mathcal{G}_{mR}$ $(m = I, II, i)$	interlaminar fracture resistance corresponding to m
$\mathcal{G}_c$	critical strain energy release rate
$\mathcal{G}_i$	interface energy release rate
$\mathcal{G}_{ic}$	critical interface energy release rate
$\mathcal{G}_{1c}$	mode-1 critical energy release rate
$\mathcal{G}_{Ic}$	mode I delamination initiation
$\mathcal{G}_{IIc}$	mode II delamination initiation
$\mathcal{G}_{ss}$	steady-state energy release rate
$\overline{\mathcal{G}}_{1c}$	average of mode-1 critical energy release rate
$\mathcal{G}_{i-2D}$	interface energy release rate related to the in-plane stress intensity factors
$\mathcal{G}_i^{FEA}$	interface energy release rate obtained by means of FEA
$\mathcal{G}_i^{FEA}(x_3/b, a)$	$\mathcal{G}_i^{FEA}$ as a function of the normalized delamination front coordinate x_3/b and delamination length a
$\mathcal{G}_I^{FEA}(a)$	average mode I energy release rate obtained by means of FEA
$\mathcal{G}_i^{FEA}(a)$	average interface energy release rate for nearly one ratio of mixed mode I/II deformation obtained by means of FEA
$\mathcal{G}_i^{Test}$	interface energy release rate related to experimental data
H_1, H_2	interface parameters
H_m $(m = T,\ B)$	height of upper $(m = T)$ / lower $(m = B)$ sub-laminate of a composite strip within a BD specimen
I	intercept of new segment in the BD specimens fracture criterion
I^*	reduced value of I
$\mathbf{I}$	the identity matrix
I_{zz}	second moment of area
I_m $(m = Up,\ Low)$	second moment of area of each laminate segment
$\Im$	imaginary part of a complex expression
J	J-integral
K	complex stress intensity factor, in Section 4.5: a statistical real factor
$\hat{K}$	in-plane stress intensity factor with regular units

$\tilde{K}$	non-dimensional in-plane complex stress intensity factor
$\widetilde{K}_m^{(f)}\ (a/R)\ (m=1,2)$	mechanical normalized stress intensity factors
$\widetilde{K}_m^{(r)}\ (a/R)\ (m=1,2)$	residual thermal normalized stress intensity factors
$K^{(f)}$	critical mechanical complex stress intensity factor
$K^{(r)}$	critical thermal complex stress intensity factor
$K^{(T)}$	total critical complex stress intensity factor
$K_m\ (m=1,2,3,I,II,III)$	stress intensity factors
$\hat{K}_m\ (m=1,2)$	normalized in-plane stress intensity factors
$K_{mc}\ (m=I,II,III)$	fracture toughness, corresponding to mode m
$K_m^*\ (m=1,2)$	local in-plane stress intensity factors
K_{III}^*	local out-of-plane stress intensity factor
$K_m^{(1)}\ (m=1,2,III)$	stress intensity factors of the problem sought
$K_m^{(2\alpha)}\ (m=1,2,III;\ \alpha=a,b,c)$	stress intensity factors of the auxiliary solution
$K_m^{(j)}\ (m=1,2,III;\ j=\mathrm{ch},\mathrm{ref})$	stress intensity factors of examined (checked, $j=\mathrm{ch}$) / base-line (reference, $j=\mathrm{ref}$) value
$\hat{K}_2^\sharp$	maximum value of $\hat{K}_2$ for which $\hat{K}_1$ is nearly constant
$\hat{K}_{mc}\ (m=1,2)$	critical normalized in-plane stress intensity factors
$\hat{K}_m^{(j)}\ (m=1,2;\ j=N,P)$	normalized in-plane stress intensity factors for negativ ($j=N$)/ positive ($j=P$) loading angles
$\hat{K}_m^{\prime(j)}\ (m=1,2;\ j=N,P)$	normalized in-plane stress intensity factors for negativ ($j=N$)/ positive ($j=P$) loading angles in auxiliary rotated coordinate system
$\hat{K}_m^{(j)*}\ (m=1,2;\ j=N,P)$	reduced value of $\hat{K}_m^{(j)}$ obtained by means of statistical analysis
$\hat{K}_m^{\prime(j)*}\ (m=1,2;\ j=N,P)$	value of $\hat{K}^{(j)*}$ in a rotated auxiliary coordinate system
$K_j^{FEA}\ (j=1,2,III)$	stress intensity factors related to FEA results, corresponding to mode j
$K_j^{Test}\ (j=1,2,III)$	stress intensity factors related to experimental data, corresponding to mode j
L	in Section 1.2: an arbitrary length parameter in Section 1.3: beam-type specimen half-span
$\mathbf{L}_k\ (k=1,2)$	one of the three real Barnett-Lothe tensors for material k
$L_j\ (j=2,3,4)$	differential operators of order j, functions of the reduced elastic compliance coefficients
L_f	beam-type specimen free length

L_0	an initial beam-type specimen free length, with specimen delamination length a_0
L_p	beam-type specimen free length in test with a natural pre-delamination
L_N	length of element N along the crack front
$\hat{L}$	arbitrary length parameter
M, $M^{(1,2\alpha)}$ $(\alpha = a, b, c)$	M-integral
M, M_m $(m = I, II)$	total bending moment, bending moment corresponding to pure mode m
M_m $(m = Up,\ Low)$	bending moment corresponding to sublaminate segment
$M_N^{(1,2\alpha)}$ $(\alpha = a, b, c)$	average value of M-integral within element N
${}_kM_{st}$ $(s = 1, 2;\ t = 1, \cdots, 4)$	elements in the asymptotic displacement and stress fields
${}_kM_{st}^*$ $(s = 1, 2;\ t = 1, 2)$	elements in the asymptotic displacement and stress fields
N	in Section 4.5: number of data points/samples in the z-variate model
N_i	shape functions of a twenty noded isoparametric, brick element in parent domain
${}_kN_{st}$; ${}_kN_{st}^*$; ${}_k\widetilde{N}_{st}$ $(s = 1, 2;\ t = 1, 2)$	elements in the asymptotic displacement and stress fields
P	applied load
	in Section 4.5: level of probability in the z-variate model
P_c	critical fracture load
P_g	weight of the lever and attached apparatus of the MMB specimen
P_i	initial propagation load seen visually in images of DCB specimen
P^{FEA}	load applied in FEA
P^{Test}	load applied in experiment
P_{NL}	applied load at test for which a deviation from the linear load-displacement curve observed
P_{vis}	applied load at test for which a visual delamination initiation obtained
$P_{5\%/\max}$	applied load at test for which a 5% increase obtained in the compliance (load-displacement) or maximum load value
$\mathbf{Q}$	3×3 matrix composed of components of the stiffness matrix

Q_{im}	components of the matrix $\mathbf{Q}$
${}_kQ_s$; ${}_kQ_{s+2}$ $(s = 1, 2)$	elements in the asymptotic displacement and stress fields
$\mathbf{R}$	3×3 matrix composed of components of the stiffness matrix
R_{im}	components of the matrix $\mathbf{R}$
R	radius of BD spscimen
R^2	coefficient of determination
$2R$	BD specimen total diameter
R_m $(m = L,\ R)$	horizontal distance between LHS/RHS delamination tip to its closest composite strip edge
$R_m^{(sc)}$ $(m = L,\ R)$	scaled parameter of R_m
$R_L^{(lig)}$	interfacial remaining ligament in a BD specimen with an arrest hole
$R_L^{(lig,sc)}$	scaled parameter of $R_L^{(lig)}$
$\Re$	real part of a complex expression
RH_j $(j = initial,\ final)$	initial/final relative humidity
S	slope of new segment in the BD specimens fracture criterion
S^*	reduced value of S
$\mathbf{S}_k$ $(k = 1, 2)$	one of the three real Barnett-Lothe tensors for material k
$\breve{\mathbf{S}}$	3×3 matrix related to $\mathbf{D}$ and $\mathbf{W}$
$\mathbf{T}$	3×3 matrix composed of components of the stiffness matrix
T_{im}	components of the matrix $\mathbf{T}$
ΔU	difference between the external work and the strain energy
ΔU_j $(j = \text{mode I},\ \text{mode II})$	change of the elastic potential energy corresponding to pure mode j
${}_kU_\alpha^{(1)}(\theta)$, ${}_kU_\alpha^{(2)}(\theta)$ $(k = 1, 2)$	in-plane displacement functions for material k
${}_kU_3^{(III)}(\theta)$ $(k = 1, 2)$	out-of-plane displacement function for material k
V_k $(k = 1, 2)$	integration volume in material k
V_f	fiber volume fraction
${}_kW^{(1,2\alpha)}$ $(k = 1, 2)$	interaction or mutual strain energy in material k
$\mathbf{W}$	3×3 matrix related to $\mathbf{L}_k$ and $\mathbf{S}_k$
W_{ij}	components of $\mathbf{W}$
X_i $(i = 1, 2, 3)$	axes in cartesian coordinate system

ΔX_i $(i = 1, 2, 3)$	segment along X_i-axis in cartesian coordinate system

Lower Case Greek letters

α	in Section 1.3: loading angle of the Arcan fixture
α_{ii} $(i = 1, 2, 3)$	thermal expansion coefficients in the x_i-direction no summation implied
β	in Section 2.1: related to ε in Section 4.5: slope of the oblique line in Fig. 4.11b
β_α $(\alpha = 1, 2, 3)$	real constants related to imaginary part of p_α
$\beta_\alpha^{(k)}$ $(\alpha = s = 1, 2, 3)$	real constants related to imaginary part of $p_\alpha^{(k)}$ for material k
$\beta_s^{*(k)}$ $(s = 1, 2)$	elements in the asymptotic displacement and stress fields
$\beta^{(j)}$ $(j = N, P)$	slope of the oblique line obtained for negativ $(j = N)$/ positive $(j = P)$ loading angles
β_{Dun}	one of the two Dundurs' parameters (Dundurs, 1969)
γ	in Section 4.5: level of confidence in the z-variate model
δ	stress singularity
δ_m $(m = 1, 2, 3)$	stress singularities obtained from eq. (2.44)
δ_{ij}	Kronecker delta
ε	oscillatory parameter, with positive sign
ε_{ij}	components of the strain tensor
${}_k\varepsilon_{ij}^{(1)}$	strain components of the problem sought
${}_k\varepsilon_{ij}^{(2\alpha)}$ $(\alpha = a, b, c)$	strain components of the auxiliary solution
ε_α	strain components under contracted notation
ϵ	isotropic bimaterial oscillatory parameter
$\zeta_*^{(k)}$ $(k = 1, 2)$	parameter depends on the eigenvalues of material k and angle θ
η_α $(\alpha = 1, 2, 4)$	auxiliary function in Lekhnitskii formalism
θ	angle in polar coordinate system; angle of a ray perpendicular to the crack front in respect to the crack plane
$\theta^{(j)}$ $(j = N, P)$	angle of rotation between two coordinate systems, experimental data and auxiliary, for negativ $(j = N)$/ positive $(j = P)$ loading angles

ϑ	temperature
ϑ_j $(j = initial,\ final)$	initial/final room temperature
λ_α $(\alpha = 1, 2, 3)$	auxiliary function in Lekhnitskii formalism
μ	shear modulus
ν	Poisson's ratio
ν_{ij} $(i, j = 1, 2, 3)$	Poisson's ratios
ξ_α $(\alpha = 1, 2, 4)$	auxiliary function in Lekhnitskii formalism
σ	applied remote stress
$\sigma_{\alpha\beta}^{(k)}$	bimaterial interface in-plane stress components for material k under contracted notation
$\sigma_{\alpha 3}^{(k)}$	bimaterial interface out-of-plane stress components for material k under contracted notation
σ_α	stress components under contracted notation
σ_{ij}	components of the stress tensor
${}_k\sigma_{ij}^{(1)}$	stress components of the problem sought
${}_k\sigma_{ij}^{(2\alpha)}$ $(\alpha = a, b, c)$	stress components of the auxiliary solution
$\sigma^{(r)}$	residual thermal stress
ϕ	phase angle or mode mixity of the ACP specimen Charalambous et al. (2015a)
$\boldsymbol{\phi}$	stress function vector
$\boldsymbol{\phi}^{(k)}$ $(k = 1, 2)$	stress function vector of material k
$\phi_j^{(k)}$ $(j = 1, 2, 3)$	complement of the stress function vector of material k
$\boldsymbol{\phi}_{os}^{(k)}$ $(k = 1, 2)$	oscillatory singular part of $\boldsymbol{\phi}^{(k)}$
$\boldsymbol{\phi}_{s}^{(k)}$ $(k = 1, 2)$	regular square-root singular part of $\boldsymbol{\phi}^{(k)}$
φ_i $(i = 1, 2, 3)$	components of Airy stress function
${}_k\varphi_s$ $(s = 1, 2, 3)$	elements in the asymptotic displacement and stress fields
χ	ratio of the number of cut plies to total number of plies or one of the two Airy potential functions
ψ	equivalent bending stiffnesses ratio between upper and lower sublaminates or one of the two Airy potential functions
$\hat{\psi}$	in-plane phase angle
$\hat{\psi}^{(j)}$ $(j = N, P)$	in-plane phase angle for negativ $(j = N)$/ positive $(j = P)$ loading angles
$\hat{\psi}^{(j)*}$ $(j = N, P)$	reduced value of $\hat{\psi}^{(j)}$ obtained after statistical analysis

	was performed
$\hat{\psi}^{(j)\sharp}$ $(j = N, P)$	in-plane phase angle, $\hat{K}_2^{(j)\sharp}$ dependent, for negativ $(j = N)$/ positive $(j = P)$ loading angles
$\hat{\psi}^{(j)\sharp *}$ $(j = N, P)$	in-plane phase angle, $\hat{K}_2^{(j)\sharp *}$ and $\hat{K}_1^{(j)*}$ dependent, for negativ $(j = N)$/ positive $(j = P)$ loading angles
ω	BD specimen loading angle or arbitrary constant associated with torsion about the x_3-axis

Upper Case Greek letters

Δ_{clamp}	clamp correction parameter in eq. (5.12)
$\lvert\Delta_n\rvert$ $(n = 0,\ f)$	initial/final absolute difference between delamination length a on both sides of a beam-type specimen, front and back
${}_k\Sigma_{\alpha\beta}^{(1)}$, ${}_k\Sigma_{\alpha\beta}^{(2)}$	bimaterial interface in-plane stress functions for material k under contracted notation
${}_k\Sigma_{\alpha 3}^{(III)}$	bimaterial interface out-of-plane stress functions for material k under contracted notation
${}_k\Sigma_{\alpha\beta}^{(1)}(\theta)$, ${}_k\Sigma_{\alpha\beta}^{(2)}(\theta)$ $(k = 1, 2)$	in-plane stress functions for material k
${}_k\Sigma_{3\beta}^{III}(\theta)$ $(k = 1, 2)$	out-of-plane stress functions for material k

Abbreviation

ACP	asymmetric cut-ply
ADCB	asymmetric double cantilever beam
APC	artificial pre-crack
ASTM	American Society for Testing and Materials
BD	Brazilian disk
B-K	Benzeggagh and Kenane (1996)
C-ELS	calibrated end-loaded split
CFRP	carbon fiber reinforced polymer
CLS	cracked-lap-shear
CV	coefficient of variation
DCB	double cantilever beam

DE	displacement extrapolation
DIC	digital image correlation
DoC	degree of cure
ECM	experimental compliance method
ESIS	European Structural Integrity Society
ENF	end notch flexure
4ENF	four-point bending, end notch flexure
ELS	end loaded split
FE	finite element
FEA	finite element analysis
FEM	finite element method
FPB	four-point bend
FRM	fiber reinforced materials
FRMM	fixed-ratio mixed-mode
FRP	fiber reinforced polymeric
HFGMC	High Fidelity Generalized Method of Cells
ISO	International Organization for Standardization
JIS	Japanese Industrial Standard
LHS	left hand side
LVDT	linearly variable displacement transducer
MD	multidirectional
MMB	mixed mode bending
MMF	mixed mode flexure
MMELS	mixed mode end-loaded split
NASA	the National Aeronautics and Space Administration
NDT	non-destructive test
PC	pre-crack
PTFE	polytetrafluoroethylene
PTU	programable timing unit
RFI	resin film infusion
RH	relative humidity
RHS	right hand side
RTM	resin transfer molding
SEM	scanning electron microscopy
SLB	single leg bending

SSY	small scale yielding
STD	standard deviation
UD	unidirectional

List of Figures

List of Tables

Chapter 1

Introduction

The establishment of failure criteria for both static and fatigue loads for composite structures is of great interest to many manufacturers in various industries, such as biomedical, sport, automotive and aircraft industries. The knowledge of failure criteria prior to manufacturing will contribute to a low cost product with the best performance available. Hence, industrialists would like to have a full-field method or technique which provides the stress and displacement fields at every critical location within structures. While designing a composite structure, first its material system should be determined. This stage is crucial, since once a material system has been chosen it affects stages from initial design to the final product. The fact that much effort is being made in order to achieve innovations in the field of composite materials leads sometimes to confusing outcomes as a result of its complexity. These innovations may be related to the chemistry involved in developing a new material system and its constituent equations or may be related to a new analysis modeling tool or algorithm to predict the material behavior under certain conditions. Thus, a better understanding of the material structure and its behavior is the first step in establishing failure criteria.

The well known advantages of composite materials, such as high strength and toughness to weight ratios, corrosion and fatigue resistance, and a variety of manufacturing processes permitting a one-step final structural configuration with all necessary structural elements integrally attached, make these materials very attractive and desirable to work with (see Schwartz, 2002; and Garg et al. 2001). However, composite material structures are sensitive to the presence of damage such as delamination, which may sometimes lead to sudden catastrophes such as aircraft or space shuttle crashes, ending with loss of human lives. Damage may be induced during the manufacturing process as a result of improper molding tool usage, application of insufficient pressure on the preformed structure, absence of resin, application of a lower or much higher temperature than the resin glass

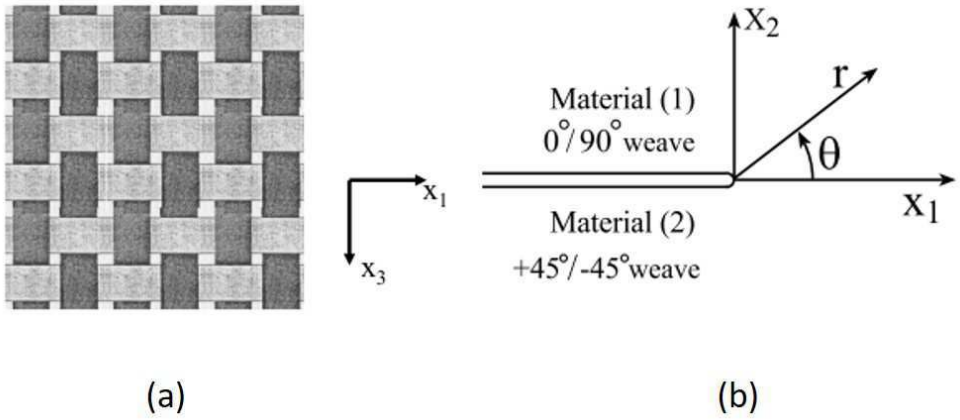

Figure 1.1: (a) Typical balanced plain weave configuration. (b) Delamination orientation.

temperature during the curing stage, etc. or may be caused by inadvertent impact damage after manufacturing. The main problem is that most of composite structural damage is barely visible to the human eye and is difficult to detect or follow. The lack of accurate and reliable fracture toughness, fatigue and damage tolerance properties, which enable the evaluation of damage growth within a composite structure, results in an over-designed structure due to the high safety margin regulations.

In this study, one of the most typical failure modes is investigated: the delamination between two adjacent plies in a composite structure. The delamination is assumed to be along the interface between a $0°/90°$ and a $+45°/-45°$ balanced plain weave, and may represent a common design detail within a composite structure used in the civil aircraft industry. An illustration of a typical balanced plain weave configuration and the delamination with its orientation are shown in Figs. 1.1a and 1.1b, respectively.

A brief introduction to the field of polymer-fiber composites is given in Section 1.1, where a description of some of the difficulties raised by the composite structure manufacturing process are given, as well. The stress and displacement fields near the tip of an interface crack, which is located between two linear elastic isotopic materials, are described in Section 1.2. A literature review of mixed mode fracture toughness measurements is given in Section 1.3, where examples of various bimaterial interface delaminations within a multidirectional composite laminate are also described. The aims of this study are described in Section 1.4.

1.1 Composite material

A reinforced polymeric material is a composite material usually constructed from high toughness fibers embedded in a low toughness polymeric matrix. The material properties of the fiber and matrix, as well as their bonding connections, which exist between the outer surface of the fiber and the matrix, determine the load carrying capacity of the composite material. The composite material properties may be tailored to sustain the predicted loads applied to the entire composite structure. The pre-tailored composite material properties may be obtained by selecting the desired material for both fibers and matrix, the volume fraction (the fiber to composite ratio) and the fiber orientation at each location within the composite structure, and by determining the preferred manufacturing process. The reinforcing fibers may be made of carbon, polyamide, boron, glass etc., whereas the polymeric matrix may be either a thermoplastic or thermosetting resin. The huge progress within the field of reinforced polymeric materials depends upon historical events, which the most significant one would be the energy crisis, which occurred in the early 1970s.

Two major American national programs led by the National Aeronautics and Space Administration (NASA), the Aircraft Energy Efficiency (ACEE) program begun in the mid-1970s followed by the Advanced Composites Technology (ACT) program (Dow and Dexter, 1997) begun in the mid-1980s, aimed to achieve an effective reduction of fuel consumption in commercial and military transport aircraft. Both expensive and ambitious programs were embarked upon as a result of the oil embargo imposed by OPEC members between the years 1973 and 1975. The embargo led to a dramatic increase in the price of petroleum-based fuels, interpreted as a threat by the U.S. government (Bowles, 2010). The fundamental ACEE program focused mainly on research and development made in the fields of advanced propulsion systems (Ciepluch et al., 1987), advanced metallic alloys and composite materials (Sakata and Ostrom, 1978; Blankenship and Teichman, 1982) and advanced aerodynamics (Bartlett, 1981), all considered as significant parameters affecting the energy consumption of aircraft. The main purpose of the ACEE program was to achieve energy saving by reducing the total drag on and weight of the aircraft structure. After the ACEE period was ended, it was concluded that the current composites may not be applicable in robust primary structures, since their manufacturing process was overpriced compare to metal primary structures. Furthermore, despite the developments made in the mechanical properties of composites, it was found that the conventional laminated structures, made of two-dimensional ply stackups, had poor damage tolerance capabilities. Hence, such composite structures would not be able to withstand the severe flight service loads with minimal damage.

The ACT program was prompt to solve two main obstacles regarding composite primary

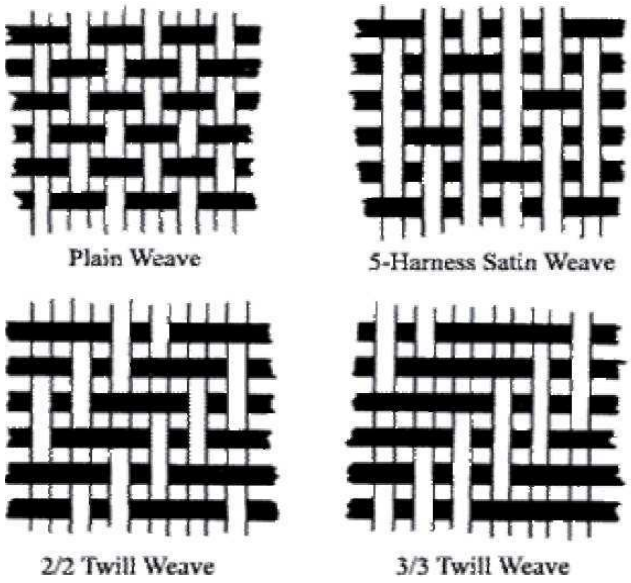

Figure 1.2: Several two-dimensional woven fabric configurations.

structures: expensive manufacturing and low damage tolerance. By adopting the textile industry automated manufacturing methods, dry preformed structures were produced with internal through-the-thickness reinforcements (Poe et al., 1999), such as braided and stitched tows. Indeed, the dry preformed structure technology enforced the development of adequate processes, which enabled optimal resin infiltration while supporting the pre-cured composite structure, all to ensure the manufacture of a net-shape fully cured part. The resin transfer molding (RTM) and the resin film infusion (RFI) tooling concepts and processes, as well as the developments of new epoxy resins, were investigated, monitored, analytically and numerically modeled and experimentally validated. The new methodology, which included simplification of material architecture, material manufacture process modeling and experimental tests for obtaining macroscopic mechanical properties and design allowables, was recognized by the federal authorities and set the foundations to the contemporary standards.

The complicated textile architecture was simplified by assuming it may be treated as a homogeneous anisotropic media, characterized by its effective mechanical properties, as if it had an orthotropic or tetragonal material configuration. The effective properties were mathematically derived as a combination of the mechanical properties of the composite constituents, and describe relatively well the overall composite structure elastic behavior (see Shankar and Marrey, 1997). The calculated effective moduli were determined by performing analytical or numerical modeling and were verified by experimental tests. A detailed review of models for predicting the effective mechanical properties of textile composites is presented in Tan et al. (1997).

Though the mechanical properties of a composite material depend upon its architecture, they are also governed by its manufacturing process. The mechanical properties are highly affected by changes in temperature and heating rate during cure and cool-down stages (see Weideman et al., 1992; Golestanian and El-Gizawy, 1997), which determine the obtained chemical and thermal shrinkage and the composite degree of cure (DoC). Since residual stresses are inevitable, intensive investigations in order to minimize them have been made (see White and Hahn, 1992; Golestanian and El-Gizawy, 2001), and currently being made, including improvements in process modeling (see Carlone et al., 2014), intermediate temperature monitoring and measurement equipment and techniques (see de Oliveira et al., 2008).

Two-dimensional woven fabrics are still the most commonly used form in composite structure manufacturing (Khan, 2009) because of their well known advantages, such as good in-plane properties, good drapability (determined by a combination of several factors, such as stiffness, flexural rigidity, weight, thickness etc.), highly automated and relatively inexpensive preform fabrication process and their good ability to cover large areas (Poe et al., 1999). Several two-dimensional woven fabric configurations, such as plain, satin and twill weaves, are presented in Fig. 1.2. It should be noted, as well, that unidirectional lamina continue to be used in industry in applications, such as floor beams (for the Boeing company commercial aircrafts 777 and 787), where high axial strength and good in-plane properties are required.

1.2 Stress and displacement fields in the neighborhood of an interface crack tip

According to Williams (1959), in the neighborhood of an interface crack tip located between two different elastic isotropic materials, the stress and displacement fields behave as

$$\sigma \propto \frac{1}{\sqrt{r}} \left\{ \begin{array}{c} \sin(\epsilon \ln r) \\ \cos(\epsilon \ln r) \end{array} \right\}, \tag{1.1}$$

$$u \propto \sqrt{r} \left\{ \begin{array}{c} \sin(\epsilon \ln r) \\ \cos(\epsilon \ln r) \end{array} \right\}. \tag{1.2}$$

The distance from the crack tip is denoted by r, as shown in Fig. 1.1b, and ϵ is the isotropic bimaterial oscillatory parameter, which depends upon the mechanical properties

of both materials. Explicitly, ϵ may be written by means of β_{Dun}, which is one of the two Dundurs' parameters (Dundurs, 1969), as

$$\epsilon = \frac{1}{2\pi} \ln \left(\frac{1 + \beta_{Dun}}{1 - \beta_{Dun}} \right), \tag{1.3}$$

where

$$\beta_{Dun} = \frac{\mu_2(1 - 2\nu_1) - \mu_1(1 - 2\nu_2)}{2[\mu_2(1 - \nu_1) + \mu_1(1 - \nu_2)]}. \tag{1.4}$$

The shear moduli are denoted by μ_k, ν_k are the Poisson's ratios and $k = 1, 2$ represents the upper and lower materials, respectively.

In the case of a bimaterial interface crack, the in-plane stress components in the vicinity of the crack tip may be written as

$$\sigma_{\alpha\beta}^{(k)} = \frac{1}{\sqrt{2\pi r}} \left[\Re \left(K r^{i\epsilon} \right)_k \Sigma_{\alpha\beta}^{(1)}(\theta, \epsilon) + \Im \left(K r^{i\epsilon} \right)_k \Sigma_{\alpha\beta}^{(2)}(\theta, \epsilon) \right], \tag{1.5}$$

where r and θ are polar coordinates, similar to those shown in Fig. 1.1b, $\alpha, \beta = 1, 2$, $i = \sqrt{-1}$ and $k = 1, 2$ represents the upper and lower materials, respectively. The in-plane stress functions ${}_k\Sigma_{\alpha\beta}^{(1)}$ and ${}_k\Sigma_{\alpha\beta}^{(2)}$ are given in polar coordinates by Rice et al. (1990) and in Cartesian coordinates by Deng (1993). The in-plane complex stress intensity factor K is defined by

$$K = K_1 + iK_2, \tag{1.6}$$

where K_1 and K_2 are not associated with a single deformation mode. Furthermore, if the applied stress is given in units of $\mathrm{N/m^2}$, the obtained units of K are $\mathrm{N \times m^{-(3/2+i\epsilon)}}$. Conversion from one system of units to another will lead to a different ratio between the real and imaginary parts of K. In order to resolve the complex units, K may be written as

$$\hat{K} = K L^{i\epsilon}, \tag{1.7}$$

where L is an arbitrary length parameter. The choice of L depends upon use of the stress intensity factor and will be discussed later. It may be noted that

$$\left| L^{i\epsilon} \right| = 1, \tag{1.8}$$

so that

$$|K| = |\hat{K}|. \tag{1.9}$$

The in-plane complex stress intensity factor in eq. (1.6) may be presented in a non-dimensional form as

$$\tilde{K} = \frac{K L^{i\epsilon}}{\sigma \sqrt{\pi L}}, \tag{1.10}$$

where σ is the applied remote stress. The non-dimensional in-plane complex stress intensity factor may be written as

$$\tilde{K} = |\tilde{K}| e^{i\hat{\psi}}, \tag{1.11}$$

so that the phase angle or mode mixity are found to be

$$\hat{\psi} = \arctan\left[\frac{\Im\left(KL^{i\epsilon}\right)}{\Re\left(KL^{i\epsilon}\right)}\right] = \arctan\left[\frac{\sigma_{12}}{\sigma_{22}}\right]\Bigg|_{\theta=0,r=L}. \tag{1.12}$$

In the case of a three-dimensional problem, where the stress and displacement fields vary along the crack front, the local in-plane stress components remain the same as given in eq. (1.5), and the local out-of-plane stress components may be written as

$$\sigma_{\alpha 3}^{(k)} = \frac{K_{III}}{\sqrt{2\pi r}}\ {}_k\Sigma_{\alpha 3}^{(III)}(\theta). \tag{1.13}$$

The out-of-plane stress intensity factor is denoted by K_{III}, which is solely associated with the tearing deformation mode, ${}_k\Sigma_{\alpha 3}^{(III)}(\theta)$ is the out-of-plane stress function of material k with $\alpha = 1, 2$ and may be found in Deng (1993); all other variables are defined as for eq. (1.5). A ratio exists between the out-of-plane and the in-plane deformations denoted by a second phase angle ϕ, which is defined as

$$\phi = \arctan\left[\sqrt{\frac{H_1}{H_2}}\frac{K_{III}}{\sqrt{K_1^2 + K_2^2}}\right] = \arctan\left[\sqrt{\frac{H_1}{H_2}}\frac{\sigma_{32}}{\sqrt{\sigma_{22}^2 + \sigma_{12}^2}}\right]\Bigg|_{\theta=0,r=L}. \tag{1.14}$$

The parameters H_1 and H_2 depend upon the mechanical properties of both materials above and below the interface, and may be written as

$$\begin{aligned} \frac{1}{H_1} &= \frac{1}{\cosh^2 \pi\epsilon}\left(\frac{1}{\overline{\overline{E}}_1} + \frac{1}{\overline{\overline{E}}_2}\right), \\ \frac{1}{H_2} &= \frac{1}{4}\left(\frac{1}{\mu_1} + \frac{1}{\mu_2}\right), \end{aligned} \tag{1.15}$$

where

$$\frac{1}{\overline{\overline{E}}_k} = \begin{cases} \dfrac{1-\nu_k^2}{E_k} & \text{plane strain} \\ \dfrac{1}{E_k} & \text{generalized plane stress.} \end{cases} \tag{1.16}$$

The Young's moduli are denoted by E_k and $k = 1, 2$ represents the upper and lower materials, respectively.

At every position along the crack front, the local interface energy release rate $\mathcal{G}_i$ is related to the local stress intensity factors by

$$\mathcal{G}_i = \frac{1}{H_1}\left(K_1^2 + K_2^2\right) + \frac{1}{H_2}K_{III}^2, \tag{1.17}$$

where the subscript i represents interface.

The predicted oscillatory behavior of the stress and displacement fields in the vicinity of the interface crack tip (see eqs. (1.1) and (1.2)), implying crack face interpenetration,

has delayed the development of this research field. In order to resolve this problem, several models were proposed. Two models made use of three parallel layers of different homogeneous materials, in which the stress singularity was $1/\sqrt{r}$ (Atkinson, 1977). The layers were assumed to be perfectly bonded at their interfaces, and the crack was assumed to be parallel to both interfaces. In the first model, the crack was located within the mid-layer, meaning it was a crack within a homogeneous media. In the second model, the crack was located along the interface, between the upper and middle layers. Furthermore, it was assumed that the mechanical properties of the mid-layer varied through the mid-layer height, from the upper layer mechanical properties to the lower layer mechanical properties. Hence, continuity of mechanical properties at the interfaces existed. In that work, an expression for the energy release rate $\mathcal{G}$ as a function of the model thickness was presented for each model. For both models it was found that for a mid-layer height much smaller than the height of both outer layers, the expression obtained for $\mathcal{G}$ was equal to that of a crack within a homogenous material; the error was order of the ratio of the heights of the outer layers.

Another model consisted of a contact zone, in which the interface crack faces were assumed to be in frictionless contact in a region adjacent to the crack tip (Comninou, 1977, 1978; and Comninou and Schmueser, 1979). In those studies, which dealt with a finite interface crack of length $2a$ within an infinite bimaterial body subjected to tensile (Comninou, 1977), shear (Comninou, 1978) and combined remote stresses (Comninou and Schmueser, 1979), the region in the vicinity of both crack tips was divided into three distinguishable zones: the zone ahead of the crack tip where continuity of tractions and displacements exists along the interface; the zone behind the crack tip where crack faces were open and free of traction; and in between, the contact zone where crack face interpenetration was prohibited and its length s was derived as part of the solution, while linear elastic fracture mechanics was assumed. In those investigations, it was found that the first term of the asymptotic solution depended upon K_{II} and β_{Dun} in eq. (1.4). Numerical results for several values of β_{Dun} were presented, as well. Under tensile loading conditions (Comninou, 1977) the normalized length of the contact zone s/a varied between $O(10^{-4})$ to $O(10^{-7})$ depending on β_{Dun}. Under pure shear loading conditions (Comninou, 1978) for $\beta_{Dun} = 0.5$, $s/a = 1/3$ adjacent to one crack tip, whereas at the other tip it was $O(10^{-7})$. It should be noted that for smaller values of β_{Dun}, the obtained normalized length of the contact zone decreases at both crack tips.

The work presented by Rice (1988) renewed interest for further investigations. In that work, it was determined that the oscillatory parameter ϵ in eq. (1.3) may not be neglected, although it is very small. An estimate of the small scale interpenetration length r_c, measured from the crack tip to the farthest location where crack face interpenetration is predicted, was presented. If this length is sufficiently small and included within a

small scale yielding (SSY) zone, linear elastic fracture mechanics may be employed for predicting the behavior of the stress and displacement fields in the neighborhood of the crack tip. Hence, both fields may be described by means of the complex stress intensity factor K.

In a K dominant regime, an interface fracture criterion may be described by means of the interface energy release rate and two phase angles or by means of the three stress intensity factors. An example of a three-dimensional energy based criterion is presented in Banks-Sills et al. (2006), where the critical interface energy release rate $\mathcal{G}_{ic}$ was derived as

$$\mathcal{G}_{ic} = \overline{\mathcal{G}}_{1c} \left(1 + \tan^2 \hat{\psi}\right) \left(1 + \tan^2 \phi\right). \tag{1.18}$$

The mode-1 critical energy release rate, denoted by $\mathcal{G}_{1c}$, is given by

$$\mathcal{G}_{1c} = \frac{\left[\Re(KL^{i\epsilon})\right]^2}{H_1}, \tag{1.19}$$

where H_1 is given in eq. (1.15) for two isotropic materials and the phase angles $\hat{\psi}$ and ϕ are defined in eqs. (1.12) and (1.14), respectively. In carrying out a test, L is chosen to center the fracture data in the $\mathcal{G}_{ic}$, $\hat{\psi}$ and ϕ space. For each data point, the value of $\mathcal{G}_{1c}$ is computed. The average value $\overline{\mathcal{G}}_{1c}$ in eq. (1.19) is calculated from all obtained values of $\mathcal{G}_{1c}$ of all data points.

1.3 Mixed mode fracture toughness testing of laminates

Interlaminar fracture toughness describes the resistance to delamination of a composite laminate structure by means of a critical strain energy release rate $\mathcal{G}_c$. The delamination toughness properties are commonly measured via test methods that have received recognition by at least one of the federal authorities across the world. These serve as standard methods, since their technical procedures and obtained results were found to be relatively accurate and repeatable, even though a complex process of measured data reduction was involved. There are several organizations handling composite structure standardization test methods (O'Brien, 1998), such as the International Organization for Standardization (ISO), the American Society for Testing and Materials (ASTM) and the European Structural Integrity Society (ESIS), dominated by industry, academia and government fracture mechanics experts. Hence, standards may be associated with one or more organizations.

The interlaminar fracture toughness of unidirectional composites is related to the fracture deformation modes, which are presented in Fig. 1.3. Mode I is shown in Fig. 1.3a, where the crack faces open perpendicular to crack propagation plane. Mode II is shown in

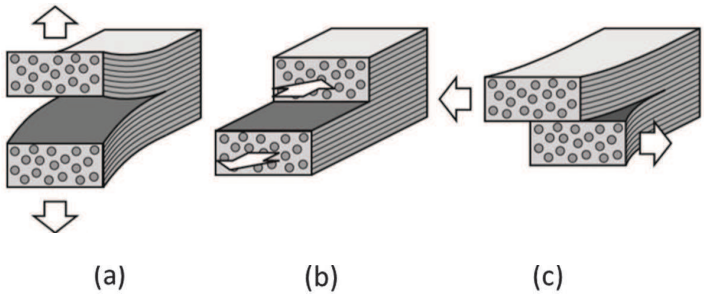

Figure 1.3: Fracture deformation modes: (a) mode I - opening, (b) mode II - sliding, (c) mode III - tearing (see Balzani et al., 2012).

Fig. 1.3b, in which the crack faces slide perpendicular to the crack front. In Fig. 1.3c, mode III is presented, where the crack faces move parallel to crack front known as the tearing mode.

Great effort has been and still is being made in order to determine experimentally the delamination toughness of composite structures under pure or mixed fracture deformation modes (see O'Brien, 1998; Brunner et al., 2008). Although many test techniques and specimens have been examined during the last fifteen years, only a few test methods were approved to serve as standards. Furthermore, although the composite structure architecture, its constituents and applied in-service loads are complicated in most cases, the standards are limited to unidirectionally carbon or glass fiber-reinforced polymer matrix specimens, which are subjected to quasi-static loading conditions. In the three mode I test methods, ASTM Standard D 5528-13 (2014), ISO 15024 (2011), and the Japanese Industrial Standard (JIS) K 7086 published in 1993 (Hojo et al., 1995), the double cantilever beam (DCB) test configuration is employed. The test specimen consists of an even number of unidirectional plies oriented in the same direction, in which all fibers are aligned parallel to the specimen length. A non-adhesive thin film, which is recommended to be less than 13 μm thick, is placed at the specimen midplane and serves as an initial delamination. The specimen is loaded normal to its thickness through piano hinges or load blocks, which are attached to the specimen at its delaminated upper and lower ends. Using displacement control, stable delamination propagation is obtained. While conducting a DCB test, the instantaneous applied load and load-point displacement are recorded in order to provide a load-displacement curve. During the test, the delamination length is determined visually via a traveling optical microscope. Once the specimen compliance has been calibrated, the mode I interlaminar fracture toughness of the composite material being investigated may be determined.

It should be noted, that while testing multidirectional laminates, the obtained delamination resistance values may represent only delamination initiation properties (see ISO 15024:2001(E) Sec. B.1; O'Brien, 1998; Brunner et al., 2008). In such cases, delamination growth may involve phenomena such as crack branching and/or deviations from the initial central plane containing the non-adhesive film insert. It may be mentioned that the delamination initiation value $\mathcal{G}_{Ic}$ determined via the ASTM D 5528-13 (2014) and ISO 15024 (2011) standards is based upon an artificial initial delamination. It was found to be almost the same as that obtained for pre-cracked specimens (see Davies et al., 1998, p. 354). Although the effect of the artificial delamination is considered negligible, the initiation value $\mathcal{G}_{Ic}$ is based upon a pre-cracked specimen.

There are currently three international standards available for mode II testing. In two of them, the end notch flexure (ENF) specimen is employed; whereas in the third standard, the calibrated end-loaded split (C-ELS) specimen is used. In the ASTM standard D 7905 (2014), which was developed by Subcommittee D30.06 on Interlaminar Properties (Davidson, 2014), and in the JIS K 7086 established in March 1993 (Tanaka et al., 1995), in which the mode I test method via a DCB specimen is also included, the three-point bending ENF test configuration is employed. The ENF specimen is identical to the DCB specimen, although their test fixtures, constraints and applied loads differ. On the ENF specimen mid-span, a vertical load is applied to produce a sliding shear displacement between the upper and lower delamination faces. Generally unstable delamination growth is obtained for short delamination lengths, so that only initiation values may be determined. A ratio of delamination length a to specimen half-span L greater than 0.7 will result in stable delamination propagation (Davies et al., 1998). On the other hand, stable growth may be obtained by means of machine feedback control of the current relative shear displacement, which is measured between the delaminated ends of the upper and lower delamination faces (see O'Brien, 1998; Brunner et al., 2008). In this way, both delamination initiation and growth resistance properties may be determined. As with the DCB specimen, under stabilized delamination growth conditions, the instantaneous applied load and load-point displacement are recorded in order to provide a load-displacement curve. During the test, the delamination length is determined visually via a traveling optical microscope. Once the specimen compliance has been calibrated, the mode II interlaminar fracture toughness of the composite material being investigated may be determined.

Since the delamination growth via an ENF test is usually unstable, several other test configurations have been examined (4ENF - four-point bending, end notch flexure, ELS - end loaded split, etc.) in order to characterize mode II fracture behavior (Brunner et al., 2008). The great advantage of those configurations is that stable delamination propagation may be obtained for a normalized delamination length $a/L < 0.7$. However, the influence of other test parameters require evaluation. It was found that the ENF

test configuration was less sensitive to roller diameter, specimen shortening, friction and fixture compliance, despite the complicated procedure and special equipment needed in the case of ratios $a/L < 0.7$, to assure stable delamination propagation.

The C-ELS test configuration is suggested in the ISO 15114 (2014) standard. The C-ELS test specimen also consists of an even number of unidirectional plies, in which fibers are aligned parallel to the specimen length. A non-adhesive thin film, which is recommended to be between 10 μm and 13 μm thick, is placed at the specimen midplane and serves as an initial delamination. The specimen is loaded normal to its thickness through a load block, which is attached to the specimen at its lower delaminated end. Its other end is constrained by means of a clamping fixture, so that free horizontal sliding is allowed but rotation and vertical movement are prohibited. While carrying out a C-ELS test, the experimental data recording procedure is done similarly to that of an ENF test. Once the specimen compliance has been calibrated and a clamping correction evaluated, the mode II interlaminar fracture toughness of the composite material being investigated may be determined.

It may be pointed out that in order to determine the delamination initiation value $\mathcal{G}_{IIc}$, it is recommended by the ISO 15114 (2014) standard to use a pre-cracked specimen, in which the specimen containing an artificial delamination is loaded until its delamination is slightly extended (see Davies et al., 1998). If a mode II unstable delamination propagation occurs while performing the pre-cracking procedure, a mode I pre-cracking procedure may be employed. The values obtained after specimen pre-cracking were found to be lower than those obtained for a specimen containing only the non-adhesive thin film. Furthermore, mode I pre-cracking may lead to lower mode II initiation values (see Davies et al., 1998, p. 354).

There is currently one international standard for the mixed mode I/II test method, which has been widely used for failure criteria acquisition (see Mollón et al., 2010). In the ASTM standard D 6671-13 (2014), the mixed mode bending (MMB) test configuration is employed. The MMB test specimen is similar to the DCB specimen (see ASTM D 6671-13, 2014). Furthermore, the testing system is a simple superposition of the DCB (pure mode I) and the ENF (pure mode II) tests, so that every combination of mode mixity may be obtained (Reeder and Crews, 1990). The test specimen within the MMB test apparatus, is shown in Fig. 1.4. Several significant MMB test parameters, which are defined in the ASTM standard D 6671-13 (2014), are also presented in Fig. 1.4. The weight of the lever and attached apparatus are denoted by P_g, P is the applied load, c_g is the lever length to the center of gravity, a is the delamination length, h is the half-thickness of the test specimen, L is the half-span length of the specimen and c is the lever length of the MMB test apparatus. The specimen is loaded via the test apparatus, which is subjected to a single vertical load P (point E in Fig. 1.4). The use

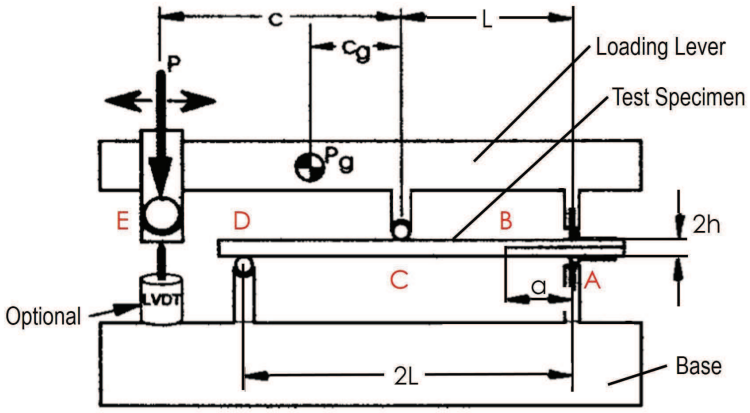

Figure 1.4: MMB test configuration (see ASTM standard D 6671-13, 2014).

of a linearly variable displacement transducer (LVDT) as an external device indicating the instantaneous load-point displacement is optional according to the ASTM standard D 6671-13 (2014). When an external displacement gage or transducer is employed, the laminate bending modulus and the calculated delamination resistance are independent of the loading system compliance (see ASTM D 6671-13, 2014).

The load P at point E causes a normal load at the piano hinges or load blocks (point A in Fig. 1.4), combined with a vertical load acting on the upper surface of the specimen at point C in Fig. 1.4. Thus, both delamination face opening and sliding may be obtained. The mixed mode ratio applied to the MMB specimen is determined by the position of the vertical load introduced by the loading lever. The applied load P acting on the loading lever and its reaction forces, which are derived from satisfying force and moment equations of equilibrium on the loading lever, are presented in Fig. 1.5a. The consequent resultant forces applied to the MMB specimen and their reaction forces are shown in Fig. 1.5b. These forces may be thought of as a simple superposition of the mode I (DCB) and mode II (ENF) specimens, presented in Figs. 1.5c and 1.5d, respectively. The variety of mixed mode ratios is easily achieved by changing the lever length c of the test apparatus.

As with the DCB specimen, under stabilized delamination growth conditions, the instantaneous applied load and load-point displacement (point E in Fig. 1.4) are recorded in order to provide a load-displacement curve. During the test, the delamination length is determined visually via a traveling optical microscope. Once the specimen compliance has been calibrated, the mixed mode interlaminar fracture toughness of the composite material being investigated may be determined for the examined mixed mode ratio. It should be mentioned that elevation of the mode II deformation component in the MMB test results in unstable delamination growth (see Brunner et al., 2008).

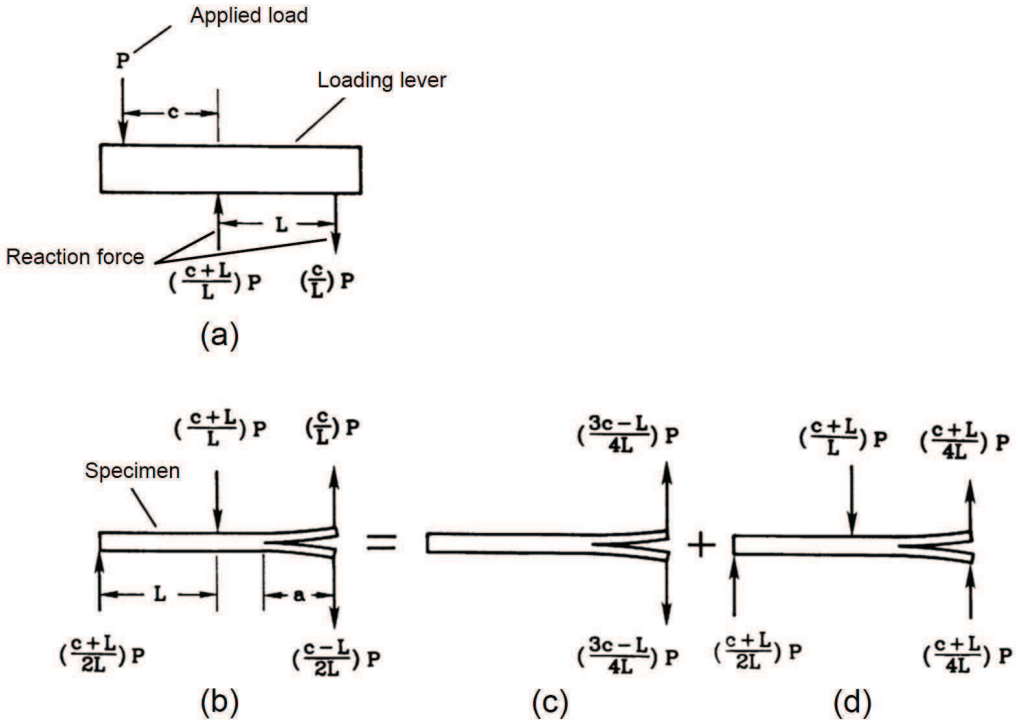

Figure 1.5: Loads applied to (a) loading lever, and (b) MMB specimen. The MMB specimen may be described by superposition of the (c) DCB, and (d) ENF specimens (see Crews and Reeder, 1988).

Peng et al. (2012) employed the DCB and the MMB test methods for measuring the fatigue delamination growth of multidirectional (MD) CFRP laminate composites, made of T700/Qy811 (carbon/bismaleimide) prepregs, at different mixed mode ratios $\mathcal{G}_{II}/\mathcal{G}$ of 0, 0.25, 0.5 and 0.75. The ply stacking sequence of $(+45°/-45°/0°_6)_s//(-45°/+45°/0°_6)_s$ was used for the MD laminate composite plate, in which a $+45°//-45°$ delamination was artificially induced. The layup was designed to avoid coupling between bending and twisting deformation, as well as to achieve the same flexural modulus in all specimen laminate segments (upper sublaminate, lower sublaminate and intact laminate). One hundred and eighty millimeter long specimens with a width b of 25 mm and a nominal thickness $2h$ of 4.16 mm were machined to their final dimensions from an MD laminate composite plate. The test specimen design allowed installation of a modified Brandt (1998) hinge at the upper and lower sublaminate ends of the specimen. Each sublaminate end of the specimen was confined within the fastener box of the modified hinge with tightened screws. It should be noted that a Brandt (1998) hinge type was employed to reduce eccentricity effects caused by an attached load block or piano hinge, which may be significant for a specimen with a short delamination. Its "load application point" is vertically positioned next to the curvature line of the upper sublaminate end. Use of the Brandt hinge saves

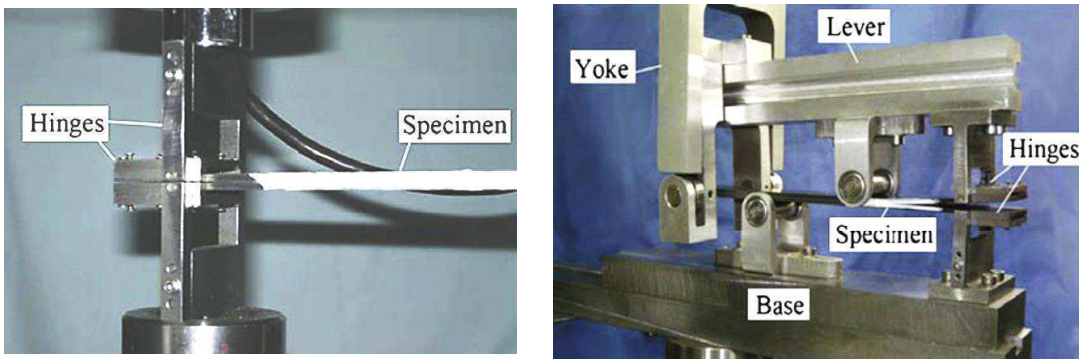

Figure 1.6: Illustration of testing configurations employed by Peng et al. (2012): (a) DCB and (b) MMB.

time as compared to a piano hinge or load blocks. The DCB and MMB test configurations, which were employed by Peng et al. (2012), are illustrated in Figs. 1.6a and 1.6b, respectively. Also, the modified Brandt (1998) hinge used for applying the load to the upper and lower sublaminate ends of the specimens may be seen in Figs. 1.6a and 1.6b.

In Peng et al. (2012), both quasi-static and fatigue tests were carried out. Some details about those quasi-static tests are given in Table 1.1. Based upon the quasi-static test results, it was found that both initiation and propagation values of the fracture toughness increased with mode mixity. For each mode mixity, a $\mathcal{G}_R$-curve was plotted from quasi-static experimental data. A linear fit was made to each of the mode mixity plots. It was found that within the normalized delamination length range of $1.4 < a/b < 2.0$, the behavior of the investigated interface may be characterized by a linear relationship between the mixed mode fracture toughness and the delamination length.

The mixed-mode end-loaded split (MMELS) test method, which is also may be called the fixed-ratio mixed-mode (FRMM) test method (Kinloch et al., 1993; Blanco et al., 2004;

Table 1.1: Some details about specimen testing that were performed by Peng et al. (2012).

test type	DCB test set-up	MMB test set-up
static	displacement rate of 0.5 mm/min N/A	displacement rate of 0.1 mm/min at certain intervals the applied displacement was held for 10 min until delamination propagation stopped and an equilibrium position was reached, so that a single lower $\mathcal{G}_c$ value was measured

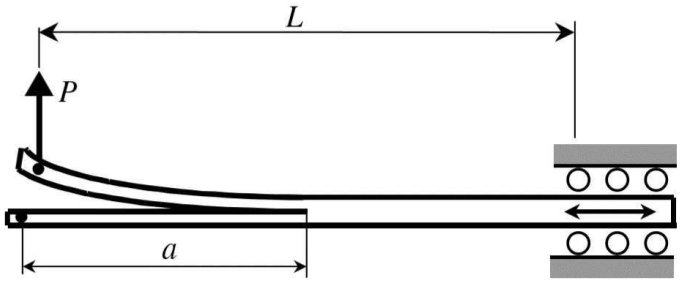

Figure 1.7: Fixed-ratio mixed-mode (FRMM) test configuration (see Kinloch et al., 1993).

Szekrényes and Uj, 2004), where its beam-type specimen loading configuration is shown schematically in Fig. 1.7, was employed by ESIS and was explored in several round robin tests, in which suggested test methods and procedures are usually examined prior to their approval as standard test methods. The great advantage of the MMELS test method is that its UD laminate composite beam type specimen and test fixture are identical to those of the C-ELS test method, so that delamination resistance properties may be determined for both pure mode II and a specific ratio of mode mixity.

Szekrényes and Uj (2004) employed the single leg bending (SLB) and the mixed-mode end-loaded split (MMELS) test methods for measuring the mixed mode interlaminar fracture toughness of UD glass/polyester laminate composites. The MMELS and the SLB test configurations are illustrated in Figs. 1.7 and 1.8, respectively. Twenty millimeter wide beam-type specimens with a nominal thickness of 6 mm were machined to their final dimensions from a UD laminate composite plate, which contained 14 UD plies. An artificial initial delamination thickness was set to 40 μm, which was introduced by means of a nylon insert placed at the laminate midplane. It should be pointed out that the thickness of the non-adhesive thin film is recommended to be between 10 μm and 13 μm according to standardized guidelines in ISO 15114 (2014). In both test set-ups, the SLB and the MMELS, which differ in the applied load direction, load application position and

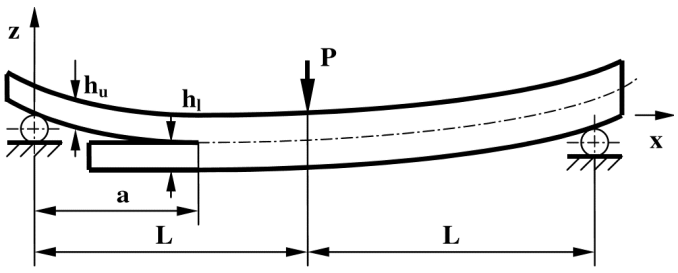

Figure 1.8: Mixed-mode single-leg bending (SLB) test configuration (see Szekrényes and Uj, 2004).

specimen constraints, the mode mixity was set to $\mathcal{G}_I/\mathcal{G}_{II} = 4/3$. Delamination initiation values were obtained by means of FEM analyses and experimental tests. A set of analytical expressions was developed for characterizing the beam-type behavior of both specimen configurations for a "symmetric" specimen (with upper and lower arms being the same thickness). To this end, use of linear beam theory and the Winkler elastic foundation model. With the latter, the specimen is assumed to be constructed from two linear beams which are connected by linear springs along the zone where the specimen is intact.

In this investigation, delamination initiation values were obtained from the SLB and the MMELS quasi-static tests, which were performed in displacement control. In both test configurations, linear load-displacement curves were obtained until fracture occurred. For each test configuration, the characteristic compliance C versus delamination length a curve was established by means of the compliance calibration method, in which specimen compliance may be written as

$$C = C_0 + ka^3. \tag{1.20}$$

The parameters C_0 and k are the coefficients of the line, which was obtained by applying a least square fit to the test results. It may be pointed out that the compliance of the MMELS test configuration was found to be larger than that of the SLB test configuration. This is as a result of the relatively large displacement (deflection) of the MMELS test specimens. Nevertheless, the dependence of the delamination initiation values upon delamination length was found to be similar with a mode mixity of 4/3. Also, it may be noted that the curve obtained between the mixed mode energy release rate $\mathcal{G}_c$ at fracture and the delamination length a from the SLB specimen was found to be in good agrement with the curve predicted by the beam model developed by Szekrényes and Uj (2004). As for the MMELS test method, despite higher mixed mode delamination initiation values (obtained test results), a similar trend was found to exist between the experimental data mixed mode energy release rate $\mathcal{G}_c$ at fracture and the corresponding beam model mixed mode energy release rate predictions. Since in both test configurations, similar experimental data based values for steady-state mixed mode energy release rate ($\mathcal{G}_{I/IIss}$) were obtained for delamination lengths longer than 60 mm, it may be concluded that the beam model proposed by Szekrényes and Uj (2004) is insufficient for cases of large specimen arm deflection.

In the work carried out by Albertsen et al. (1995), the fracture toughness for different deformation modes was examined, as well as the influence of the fiber surface treatment upon the fracture toughness values at initiation and propagation. Albertsen et al. (1995) employed the mixed-mode flexure (MMF) and the cracked-lap-shear (CLS) test methods for measuring the mixed mode interlaminar fracture toughness of UD carbon/epoxy laminate composites. The MMF and the CLS test configurations are illustrated in Figs. 1.9a and 1.9b, respectively. The MMF configuration is similar to the ENF test configuration,

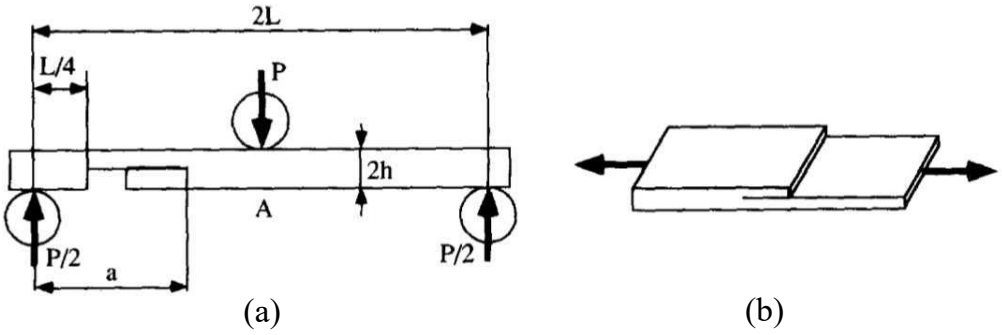

Figure 1.9: (a) Mixed-mode flexure (MMF) test configuration, and (b) cracked-lap-shear (CLS) test configuration (see Albertsen et al., 1995).

which is used for measuring the mode II fracture toughness. Since the lower arm of the specimen was cut as illustrated in Fig. 1.9a, and the delamination tip was aligned midway, between the loading roller and the left outer support, the load applied to the specimen was transferred only to the specimen upper arm resulting in a dominant mode I deformation. In this way, a ratio of $\mathcal{G}_I/\mathcal{G}_{II} = 1.33$ was obtained between the modes I and II energy release rates. The CLS test configuration, which is similar to a unidirectional tensile test configuration, employs a specimen with a stepped thickness in which a delamination is introduced through the specimen as illustrated in Fig. 1.9b. The obtained mixed-mode ratio depends upon the specimen thicknesses on each side of the transition region. Since in Albertsen et al. (1995) one side of the CLS specimen was two times thicker than the other, a ratio of $\mathcal{G}_I/\mathcal{G}_{II} = 0.25$ was obtained, indicating the dominance of mode II deformation. It may be noted that several data points for delamination resistance were obtained for each of the CLS test specimens. However, large scatter in the measurements was found, especially for increasing delamination length. Hence, characterization of fracture behavior for propagation was unavailable.

The Arcan specimen and test fixture, which were first introduced by Arcan et al. (1978) and are shown in Fig. 1.10, produce a uniform two-dimensional stress state within the examined significant section AB, located along the narrowest region of the test specimen between its two notches. It was prompted to serve as a simple test method to measure and determine the shear moduli of fiber reinforced materials (FRM). By changing the loading angle α, which is presented in Fig. 1.10a and varies within the range of $-45° \leq \alpha \leq 45°$, various two-dimensional stress states (from pure shear when $\alpha = 0°$ up to any arbitrary combination of normal principal stresses) may be achieved. In that work, experimentally obtained shear moduli for aluminum and FRM specimens were presented. While each specimen was loaded, strain measurements were performed by means of both strain gages and photoelastic methods, to assess the existence of a uniform two-dimensional stress

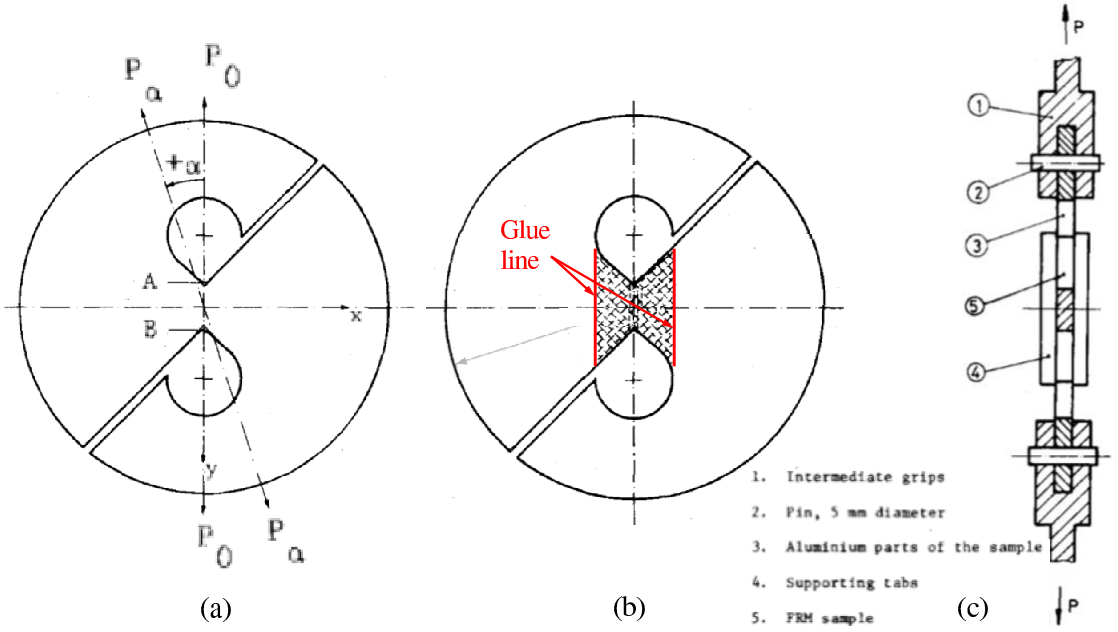

Figure 1.10: (a) Arcan circular test fixture and specimen with the significant section AB. (b) Arcan test specimen within the fixture. (c) Load setup of the Arcan fixture with an FRM specimen (see Arcan et al., 1978).

state within the significant section AB. The shear moduli measured while employing the Arcan test specimen were relatively close to values obtained by means of other common, but relatively complicated, test methods, such as the thin cylinder pure shear test. It should be noted that in the case of an FRM specimen, the central part of the original aluminum sample was cut out and an FRM specimen was glued to the aluminum grips. Four supporting tabs along the glue lines were also attached (see Figs. 1.10b and 1.10c), to ensure proper load transfer between the loaded grips and the FRM specimen.

Hung and Liechti (1997) employed the Arcan specimen and test fixture to determine the shear moduli of a unidirectional AS4/PEEK laminated plate. Prior to conducting tests, a preliminary optimization analysis was performed by means of finite element method to obtain the radii of the specimen notches at points A and B in Fig. 1.10a. A uniform strain field within the section was found for a notch radius of 2.38 mm. Specimens with different fiber orientation were produced from the same plate. While each specimen was tested, the distribution of strains within the significant zone AB was obtained by correlating the in-plane displacements, which were measured via Moiré interferometry, with the instantaneous applied load while $\alpha = 0°$. Also, the shear strain was measured by a strain-gage mounted within section AB at its mid-height. Deviations from uniformity along section AB were found near the tip of the notches in cases where the specimen fibers were oriented perpendicular to the notch-to-notch line (see Fig. 1.10a), implying further

optimization of the notch radius should have been performed. It may be noted that in several tests, non-linear effects were observed and were caused by the adhesion/clamping constraints existing between the specimen and the grips.

In order to resolve some of the problems which arose, as described in the work of Hung and Liechti (1997), several modifications were proposed. In the investigation performed by Yen et al. (1988), the adhesive requirements were excluded and a smooth load transfer was established. A 3.2 mm deep trapezoidal cutout was machined in each half of the stainless-steel fixture, so that a specimen up to 6.4 mm thick could be confined within the modified Arcan fixture. Each of the butterfly specimen sides was fastened to its grip by a line of 3 bolts.

In the study performed by El-Hajjar and Haj-Ali (2004), the adhesive requirements were also excluded. The modified Arcan fixture was assembled from four similar parts, where the front pair were aligned parallel to the rear pair. Each side of the butterfly specimen was confined between its two part grip and was fastened to its grip by two lines of 3 sleeve bolts. Hence, a two lines double shear lap-joint mechanism prevented eccentricity effects in each specimen side and a smooth load transfer was obtained. In that configuration, the load was applied to the four part fixture by clevis pins, to minimize out-of-plane forces and moments, while the range of test specimen thicknesses was extended. Specimens of 12.2 mm thick, which were machined from a pultruded fiber reinforced polymeric (FRP) plate made of E-glass/polyester, were examined in order to measure the non-linear stress-strain shear response. Shear moduli at axial and transverse roving orientations, as well as the material strength envelope, which was experimentally obtained by employing several biaxial loading conditions, were presented. While each specimen was tested, the sum of the in-plane normal stresses (first stress invariant) or strains throughout the specimen surface was measured by means of an infrared thermographic stress analysis technique. Also, the values of the shear and normal strains were calculated from the readings of a strain-gage rosette, which was mounted within section AB at its mid-height.

Heydari et al. (2011) have employed both experimental and numerical methods to determine the mixed mode fracture toughness of a laminate woven carbon-polyester composite. Ten millimeter thick, laminate specimens containing a pre through-the-thickness edge-delamination were machined to their final butterfly shape from a $350\times50\times26$ mm^3 laminate composite plate. The composite plate was hand layered with 130 carbon-polyester woven plies, each 0.2 mm thick, all oriented in the same direction. Hence, a stress singularity of $1/\sqrt{r}$ was obtained in the vicinity of the delamination tip. The initial delamination length a was set to 15 mm and it was located between layers 65 and 66. Also, the direction of the delamination coincided with the $0^\circ-$ direction of the weave. For each specimen, the height of section AB (see Fig. 1.10), denoted as w, was set to 30 mm. Thus, an initial delamination length ratio $a/w = 0.5$ was obtained. Prior to testing, a typical butterfly

shaped specimen was assembled by gluing each side of the inner composite specimen to its outer aluminum frame, in which a suitable inner cutout was already machined. The butterfly shaped assembly was fastened to the modified Arcan test fixture in a way similar to that described in Yen et al. (1988). The initial delamination was located along section AB. Tests were carried out under several loading conditions, in which the loading angle (see Fig. 1.10) α was changed to obtain different fracture mode mixities (from pure opening mode $\alpha = 90°$ up to pure shearing mode $\alpha = 0°$). Thus, for each mixed mode ratio, the critical fracture load P_c was obtained from the load-displacement curve in a test. The critical stress intensity factors for each mode mixity were calculated from

$$\begin{aligned} K_{Ic} &= \frac{P_c\sqrt{\pi a_c}}{wt} f_I\left(\frac{a_c}{w}\right) \\ K_{IIc} &= \frac{P_c\sqrt{\pi a_c}}{wt} f_{II}\left(\frac{a_c}{w}\right), \end{aligned} \tag{1.21}$$

where t represents specimen thickness and a_c represents the delamination length at fracture. The normalized geometric factors $f_I\left(\frac{a}{w}\right)$ and $f_{II}\left(\frac{a}{w}\right)$ refer to K_I and K_{II}, respectively. Their fourth order polynomial expressions were determined by means of finite element analyses of both the modified Arcan test fixture and the investigated specimen for each loading angle. It was found that for the interlaminar fracture toughness of the investigated material $K_{IIc} > K_{Ic}$. Also, it was observed that the shear mode fracture became dominant for loading angle values α less than 15°.

In an investigation performed by Taher et al. (2012), a new modified Arcan fixture was proposed to determine the mechanical properties of polymer foam materials. By changing the configuration of the rigs, compressive loads along with shear loads may be applied to a test specimen.

The Brazilian disk (BD) test method enables determination of delamination or crack initiation properties of a specimen containing an artificial delamination or pre-crack under various mixed mode ratios. In Fig. 1.11, an example of two investigated BD test specimens used to determine the fracture toughness of a bimaterial interface crack, is shown. It may be pointed out, that only one specimen and test fixture are required to attain all mode mixities. The specimen is loaded directly by an applied load P, through a stiff loading frame. Hence, no additional adhesives and/or fasteners are required. Furthermore, the values obtained by this method are independent of specimen and test machine compliances. A test specimen may be rotated within the loading frame by a loading angle ω, which may vary within the range of $-15° \leq \omega \leq 15°$ to avoid contact and friction effects.

Atkinson et al. (1982) investigated the BD test specimen, which was made from a homogeneous elastic isotropic material, to determine its fracture properties under mixed

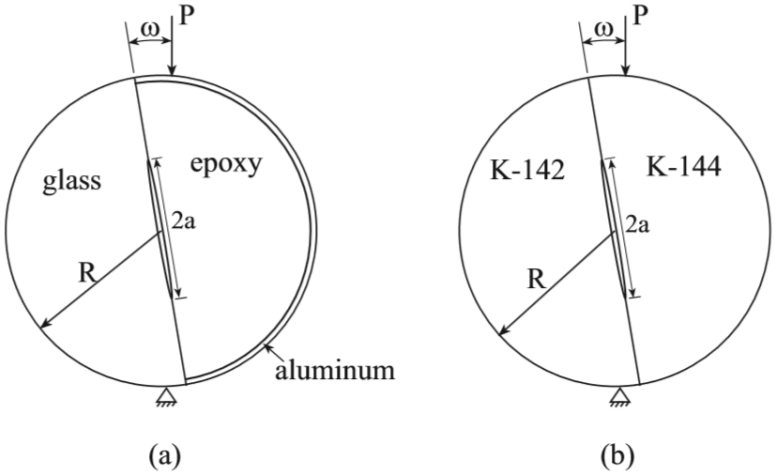

Figure 1.11: Brazilian disk specimen with an interface crack between two isotropic homogeneous materials: (a) glass/epoxy pair investigated by Banks-Sills et al. (1999), (b) two ceramic clays - K-142/K-144 pair investigated by Banks-Sills et al. (2000) (see Banks-Sills, 2015).

mode loading conditions. In that study, explicit expressions for the stress intensity factors at the crack tips were developed for different crack lengths and loading angles. Those expressions were verified experimentally for mode I and mode II. It was found that the crack tended to close when the value of the loading angle reached 20°, which meant a fracture deformation of pure mode II at the crack tip was obtained. Explicit expressions to account for contact and/or friction phenomena near the crack tips were developed and presented, as well.

In the work of Banks-Sills et al. (1999) and Banks-Sills et al. (2000), methodologies for measuring the two-dimensional composite bimaterial interface fracture properties via a BD test specimen were developed. In both investigations, the interface crack was between two isotropic homogeneous materials and a plane-strain stress state was assumed. Hence, out-of-plane deformations were excluded ($K_{III} = 0$). Both mechanical and thermal loadings were characterized, separately, by two-dimensional FE analyses. Some characteristic parameters of those investigations, where the nominal specimen radius was set to $R = 20$ mm, are shown in Table 1.2.

In both studies, mechanical FE analyses were performed for several loading conditions, in which the loading angle ω (see Fig. 1.11) was changed to obtain different fracture mode mixities. For each crack tip, fourth order polynomial expressions of the mechanical normalized stress intensity factors, $\widetilde{K}_1^{(f)}(a/R)$ and $\widetilde{K}_2^{(f)}(a/R)$, were determined by means of the mechanical M-integral, which was first introduced by Chen and Shield (1977) for cracks within an isotropic media and was extended for interface cracks between two

Table 1.2: Some characteristic parameters of bimaterial interface crack investigations performed via a BD specimen (see Banks-Sills, 2015).

bimaterial interface	oscillatory param. ϵ	loading angle ω	half crack length to specimen radius a/R	specimen thickness t (mm)	arbitrary length param. L (μm)
glass/epoxy Banks-Sills et al. (1999)	-0.0881	$-10^\circ \le \omega \le 13^\circ$	$0.45 \le \frac{a}{R} \le 0.57$	$7.79 \le t \le 7.92$	100
ceramic clays K-142/K-144 Banks-Sills et al. (2000)	-0.00563	$-15^\circ \le \omega \le 15^\circ$	$0.27 \le \frac{a}{R} \le 0.32$	$9.23 \le t \le 10.71$	600
AS4/3502 UD $0^\circ/90^\circ$ Banks-Sills et al. (2005)	-0.03627	$-10^\circ \le \omega \le 10^\circ$	$0.36 \le \frac{a}{R} \le 0.43$	$7.82 \le t \le 8.20$	100
AS4/3502 UD $+45^\circ/-45^\circ$ Banks-Sills et al. (2006)	0.000615	$2^\circ \le \omega \le 13^\circ$	$\frac{a}{R} \sim 0.38$	$7.94 \le t \le 8.17$	200

isotropic materials as a line integral by Wang and Yau (1981). Fourth order polynomial expressions of the residual thermal normalized stress intensity factors, $\widetilde{K}_1^{(r)}(a/R)$ and $\widetilde{K}_2^{(r)}(a/R)$, which are related to the change in specimen temperature (between room temperature during a test and the curing temperature during specimen manufacture), were determined by means of the weight function method and FE analysis. It should be noted, that the obtained normalized expressions depended upon the BD specimen geometry and its constituent material properties. Furthermore, the effect of contact between the crack faces was examined by means of a FE analysis; negligible contact near the crack tip was found for the tip at which propagation occurred. Hence, frictional effects were not accounted for.

Tests were carried out for different values of ω, so that both the critical fracture load P_c and the half crack length a_c were obtained. The critical mechanical and thermal complex stress intensity factors for each test were calculated from

$$\begin{aligned} K^{(f)} &= \frac{P_c\sqrt{\pi a_c}}{2\pi R t {a_c}^{i\epsilon}}\widetilde{K}^{(f)}\left(\frac{a_c}{R}\right), \\ K^{(r)} &= \frac{\sigma^{(r)}\sqrt{\pi a_c}}{{a_c}^{i\epsilon}}\widetilde{K}^{(r)}\left(\frac{a_c}{R}\right), \end{aligned} \tag{1.22}$$

where $\sigma^{(r)}$ represents the residual thermal stress caused by the mismatch in the mechanical and thermal properties between the two materials. For each mixed mode ratio, the total complex stress intensity factors $K^{(T)}$ were obtained by superposing the mechanically and thermally calculated stress intensity factors, meaning

$$K^{(T)} = K^{(f)} + K^{(r)}. \tag{1.23}$$

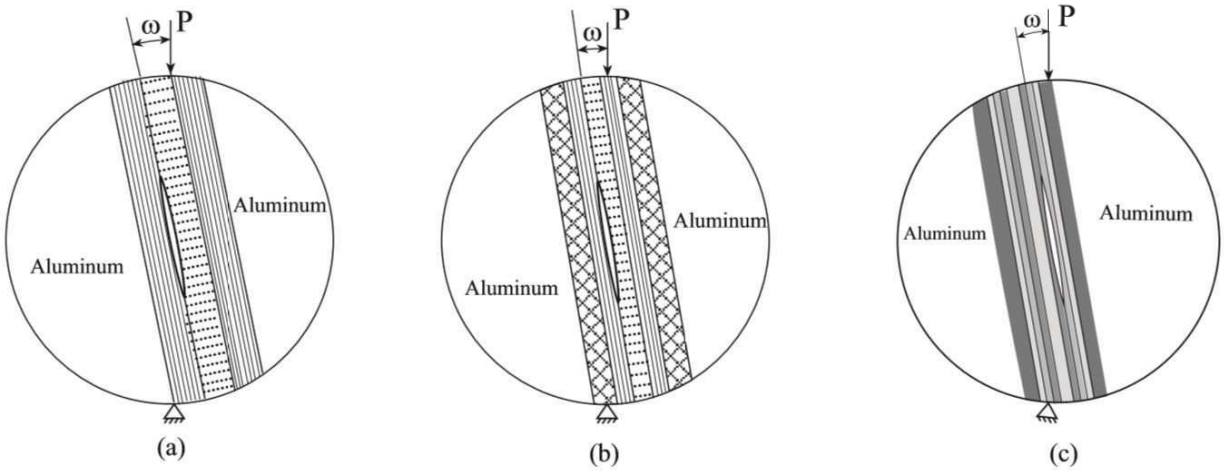

Figure 1.12: Brazilian disk specimen with an interface delamination between two different fiber orientated transversely isotropic composite layers: (a) $0°/90°$ pair investigated by Banks-Sills et al. (2005) (laminate lay-up $[0°/90°/0°]$), (b) $0°/90°$ pair investigated by Banks-Sills et al. (2005) (laminate lay-up $[\pm 45°/0°/90°/0°/\pm 45°]$), (c) $+45°/-45°$ pair investigated by Banks-Sills et al. (2006) (laminate lay-up $[\pm 45°/[0°/+45°/-45°/0°]_S/\pm 45°]$).

In both investigations, the critical interface fracture properties were determined and presented by means of the critical interface energy release rate $\mathcal{G}_{ic}$ and the phase angle $\hat{\psi}$, which are given in eqs. (1.17) and (1.12), respectively. Recall that it was assumed that $K_{III} = \phi = 0$. The value of the arbitrary length parameter L in eq. (1.7) used to center the computed critical interface energy release rate data in each investigation is also shown in Table 1.2. It may be pointed out that those values were chosen to be within the $K-$dominant region of each investigated bimaterial interface crack and to obtain the best curve fit.

Following Banks-Sills et al. (1999) and Banks-Sills et al. (2000), Banks-Sills et al. (2005) developed a methodology for measuring the two-dimensional laminate composite interface delamination properties via a BD test specimen. In that study, an interface delamination was located between two transversely isotropic unidirectional composite plies fabricated from AS4/3502 (graphite/epoxy). The upper ply contained reinforcing fibers oriented in the $0°-$ direction; whereas, the lower ply contained fibers oriented in the $90°-$ direction. The composite laminate $0°-$ direction coincided with the X_1- axis; the coordinate system is shown in Fig 1.1b. Homogenization of ply material properties according to its constituents was performed, so that each laminate fiber direction ($0°$ or $90°$) was treated as a homogeneous anisotropic media with its corresponding effective material properties. Plane-strain conditions were assumed, so that out-of-plane deformation was excluded, i.e,

$K_{III} = 0$. Prior to testing, the first terms of the asymptotic stress and displacement fields were developed by Banks-Sills and Boniface (2000). Those expressions were used as the auxiliary displacement field in the M-integral. Use of the FE method and the M-integral allowed extraction of the complex stress intensity factors for this interface.

Two BD specimen configurations, which are shown in Figs. 1.12a and 1.12b, were considered in Banks-Sills et al. (2005). The $90°-$ direction ply in both configurations contained intralaminar cracks, caused by the mismatch in the mechanical and thermal properties between two adjacent plies (between the inner $90°-$ direction ply and the two outer $0°-$ direction plies) during the cool-down stage. The pattern of intralaminar cracks was found to be unique within each specimen, even for specimens of the same configuration. Hence, FE models were prepared for each specimen in order to correctly calculate the complex stress intensity factors. Some characteristic parameters of that investigation, where the nominal specimen radius was set to $R = 20$ mm, are also shown in Table 1.2.

Tests were carried out for different values of ω (see Figs. 1.12a and 1.12b), so that both the critical fracture load P_c and the delamination length $2a_c$ were obtained. The critical mechanical complex stress intensity factor $K^{(f)}$ of each specimen was calculated by means of the FE method and a mechanical M-integral. The residual thermal complex stress intensity factor $K^{(r)}$ of each specimen was calculated by means of the FE method and a conservative thermal M-integral, which was extended for thermal loads by Banks-Sills and Dolev (2004). For each mixed mode ratio, the total complex stress intensity factor was obtained by superposing the mechanically and thermally calculated stress intensity factors, as defined in eq. (1.23). A fracture criterion for the investigated interface delamination was determined using the critical interface energy release rate $\mathcal{G}_{ic}$ and the phase angle $\hat{\psi}$, which are given in eqs. (1.17) and (1.12), respectively; (recall $K_{III} = \phi = 0$). The value of the arbitrary length parameter L used to center the computed critical interface energy release rate data is also shown in Table 1.2.

In the work of Banks-Sills et al. (2006), a methodology for measuring the three-dimensional laminate composite interface delamination properties via a BD test specimen was developed. The investigated interface delamination was located between two unidirectional composite plies fabricated from AS4/3502 (graphite/epoxy). The upper ply contained reinforcing fibers oriented in the $+45°-$ direction; whereas, the lower ply contained fibers oriented in the $-45°-$ direction. Both laminate fiber directions were with respect to the X_1- axis in the $X_2 = 0$ plane; the coordinate system is shown in Fig 1.1b. Homogenization of ply material properties according to its constituents was performed, so that effective material properties of a ply were determined according to its fiber direction coordinate system. The first terms of the asymptotic stress and displacement fields were developed based on the assumption of plane deformation as prescribed by the Stroh (1958) formalism (see Appendix B). In the FE analyses, fine subdivisions along the specimen

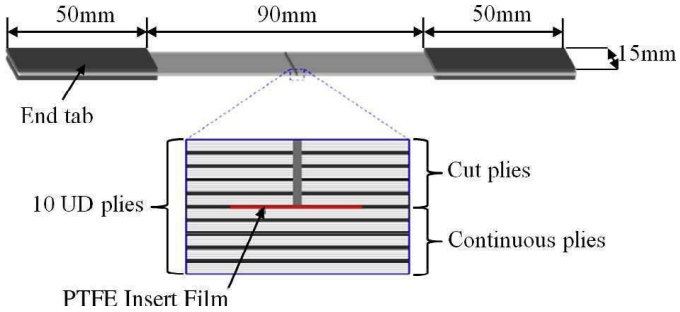

Figure 1.13: Schematic view of the asymmetric cut-ply (ACP) specimen (see Charalambous et al., 2015a).

thickness (X_3- axis) were assumed, so that within each volumetric segment $(X_1, X_2, \Delta X_3)$ the assumption of plane deformation was fulfilled. The expressions for the displacement field were used as the auxiliary solution in the M-integrals. The M-integral was extended for three-dimensional problems for both mechanical (see Freed and Banks-Sills, 2005) and thermal loads (see Banks-Sills et al., 2006). Use of the FE method and a three-dimensional M-integral allowed extraction of the complex stress intensity factors for the investigated interface. The BD specimen configuration, which is shown in Fig. 1.12c, was considered in Banks-Sills et al. (2006). Some characteristic parameters of that investigation, where the nominal specimen radius was set to $R = 20$ mm, are also shown in Table 1.2.

Tests were carried out for different values of ω (see Figs. 1.12c), so that both the critical fracture load P_c and the delamination length $2a_c$ were obtained. The mechanical complex stress intensity factor $K^{(f)}$ of each specimen was calculated by means of the FE method and a three-dimensional mechanical M-integral. The residual thermal complex stress intensity factor $K^{(r)}$ of the specimens was calculated by means of the FE method and a thermal three-dimensional M-integral, for a given temperature change. For each mixed mode ratio, the total complex stress intensity factors was obtained by superposing the mechanically and thermally calculated stress intensity factors, as defined in eq. (1.23). Values of the critical interface energy release rate $\mathcal{G}_{ic}$ and both phase angles $\hat{\psi}$ and ϕ, which are given in eqs. (1.17), (1.12) and (1.14), respectively, were determined leading to a failure surface. The value of the arbitrary length parameter L in eq. (1.7) used to center the computed critical interface energy release rate data in that investigation is also shown in Table 1.2.

Charalambous et al. (2015a) employed the asymmetric cut-ply (ACP) specimen and an adjusted four-point bend (FPB) test fixture for measuring the mixed mode interlaminar fracture toughness and fatigue delamination growth rate of a UD CFRP composite, which was made of IM7/8552 (carbon/epoxy). This method is based upon the Santa-Barbara specimen and the FPB test configuration presented in the work of Charalambides et

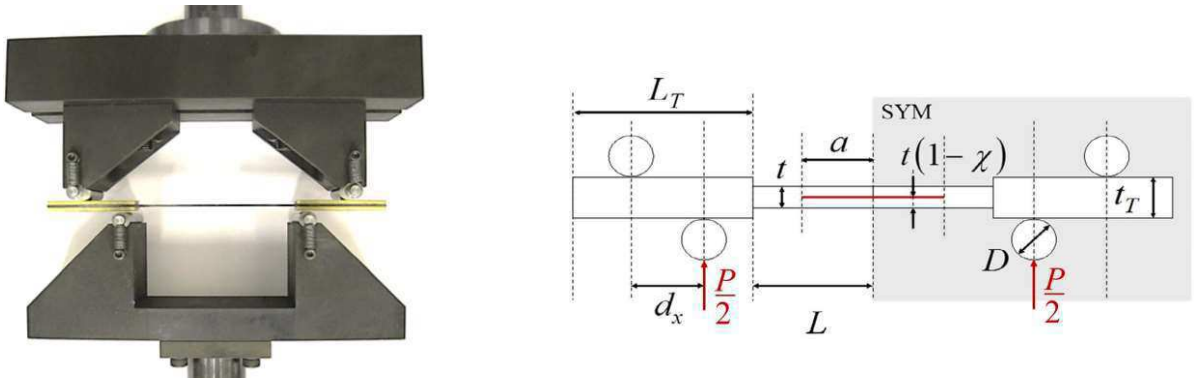

(a) (b)

Figure 1.14: ACP specimen testing: (a) adjusted FPB test fixture and test specimen; (b) loading configuration (see Charalambous et al., 2015a).

al. (1989), in which it was demonstrated that a steady-state energy release rate $\mathcal{G}_{ss}$ is obtained when an interface crack is positioned within the constant moment region. It should be noted that the steady-state energy release rate $\mathcal{G}_{ss}$ is the value of the energy release rate $\mathcal{G}$ which is independent of crack length. In addition, since the obtained values were found to be independent of specimen and testing machine compliances, unlike other test methods such as the MMB test method mentioned earlier, reduction procedures of experimental data are simplified. Furthermore, when $\mathcal{G}$ reaches $\mathcal{G}_{ss}$, the delamination length has no influence on $\mathcal{G}$. Thus, the continuous detection of delamination tip (or delamination propagation) via optical means becomes irrelevant, so that such a test may be performed under extreme environmental conditions. However, each mode mixity will involve manufacture of another composite plate.

The investigated ACP specimen is shown schematically in Fig. 1.13. It was prepared by gluing 2.45 mm thick aluminum end-tabs on the upper and lower surfaces of the composite strip ends. The specimen in its loading fixture is presented in Fig. 1.14a; a schematic loading configuration, in which the overall applied load P is symmetrically applied on specimen end-tabs, is shown in Fig. 1.14b. The symbols in Fig. 1.14b are defined in Table 1.3. During the test, the ACP specimen tabbed ends are loaded normal to their thickness through the rigid rollers of the adjusted FPB test fixture (see Fig. 1.14a).

The applied force Q, which is given by

$$Q = \frac{P}{2\cos\beta}, \tag{1.24}$$

as well as the frictional forces which maintain specimen stability during test performance, and the formed moment arms, denoted by t_T and d_e, where

$$d_e = (D + t_T)\tan\beta - d_x/\cos\beta, \tag{1.25}$$

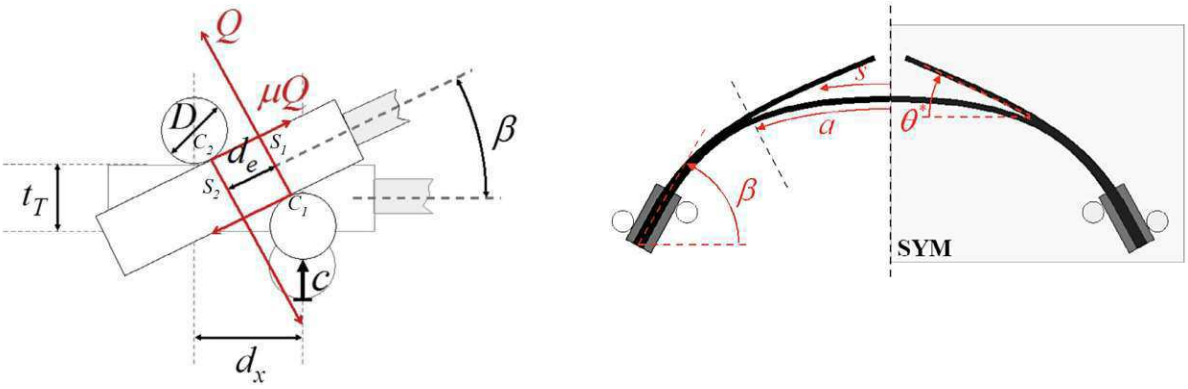

(a) (b)

Figure 1.15: Loaded ACP specimen: (a) large end-tab rotation β, applied contact forces Q, μQ, and moment arms t_T, d_e; (b) deformed configuration of the loaded ACP specimen (see Charalambous et al., 2015a).

are shown in Fig. 1.15a, in which one tabbed end of the ACP specimen is presented. Both, ACP specimen and FPB test fixture, are symmetric, so that the obtained specimen deformation, which is presented in Fig. 1.15b, is symmetric too. Additional symbols in Fig. 1.15 are given in Table 1.3.

Fifteen millimeter wide strips were machined from a 300×300×1.25 mm^3 UD CFRP composite plate, which was fabricated from two sublaminates. Each sublaminate was hand layered with 5 continuous carbon-epoxy UD plies, each 0.125 mm thick, all oriented in the same direction. Both sublaminates were laid down and vacuum de-bulked, separately. The second sublaminate was cut in half by a sharp blade, perpendicular to the fiber direction. A non-adhesive thin film (12.7 μm thick) was placed over the first sublaminate, so that an initial delamination 20 mm long was formed while the second sublaminate was placed on the top of them; mid-surfaces of sublaminates and film were co-linearly aligned; the delamination front was perpendicular to the fiber direction. The pre-cured plate was then vacuum de-bulked. A caul plate was used above the composite plate while it was autoclave-cured to avoid residual thermal stresses. Prior to testing, each of the ACP specimens was loaded in tension using displacement control until the first load drop was observed in order to fracture the resin joint, that was formed during the cure process, along the cut-plies; verification of a valid initial delamination front was performed by means of C-scan inspections.

The loaded ACP specimen delamination deformation modes may be described as a combination of delamination face opening and sliding modes, in a way similar to the one used in the case of the MMB specimen (see Crews and Reeder, 1988). It should be noted that the interlaminar delamination toughness mode partitioning is based upon the global

Table 1.3: Some characteristic parameters of the ACP specimen (see Charalambous et al., 2015a).

label	description
B	specimen width
t	thickness of specimen gauge section
$2L$	length of specimen gauge section
$2a$	delamination length
χ	number of cut plies to total number of UD plies ratio, $0< \chi <1$
t_T	total thickness of specimen tabbed area
L_T	length of specimen tabbed area
D	rollers diameter at end tabs
d_x	distance between roller centers at tabbed area, $d_x > D + t_T$
P	testing machine overall load applied to the rollers, measured by testing machine load cell
Q	normal force transferred to specimen end-tabs by the rollers
β	rigid rotation of specimen end-tabs, $\beta = [0; \frac{\pi}{2})$
μ	Coulomb coefficient of friction
μQ	frictional tangential forces between rollers and end-tabs
d_e	distance between rollers' normal forces at tabbed area
M	overall bending moment acting on specimen gauge section
c	testing machine cross-head displacement
s	specimen's curvilinear abscissa
θ^*	rotation angle at delamination tip
C_1, C_2	coordinates of the roller/tab contact points with respect to the center of the support (lower) roller
S_1, S_2	coordinates of the intersection points between the lines normal to each roller at the contact point and the mid-through-thickness plane of the end-tabs

(loading) method, in which the obtained energy release rate depends upon specimen load application configuration rather than delamination tip local deformation (see Kinloch et al., 1993). Furthermore, based upon the case study investigated within the recent work of Conroy et al. (2015), use of the global partitioning approach was suggested for cases where carbon/epoxy material systems are investigated. Although only laminate composite material specimens made of UD reinforced fibers oriented perpendicular to delamination front were investigated by Conroy et al. (2015), some insights presented in that work might be applicable for specimens made of MD laminates. Thus, it may be assumed that for beam-like specimens the global and the local solutions of the mixed mode partitioning approach the same value as the bending stiffnesses of specimen sublaminates approach each other.

The ACP specimen delamination mode partition is illustrated in Fig. 1.16. Determination of the loading mode mixity presented in the study of Charalambous et al. (2015a) is suited to laminate and sublaminates of the same flexural modulus. The energy release rate expressions may be extended for the general case where the flexural modulus of laminate and sublaminates is not the same.

Referring to Williams (1988) and Charalambous et al. (2015a), the ACP specimen may be treated as an Euler-Bernoulli beam. Next to the delamination tip, the change of the

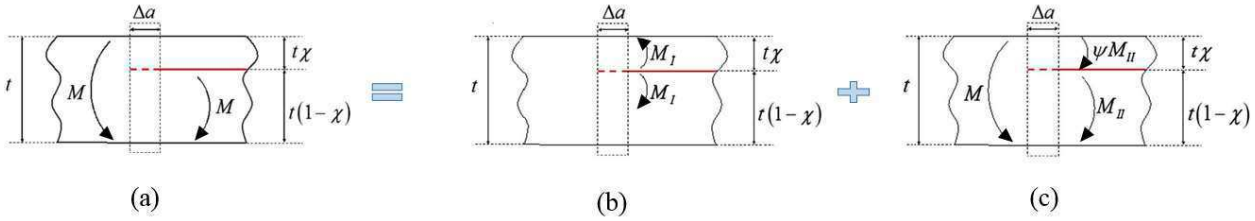

Figure 1.16: Delamination applied load mode partitioning for the ACP specimen: (a) mixed mode, (b) mode I, and (c) mode II (see Charalambous et al., 2015a).

elastic potential energy ΔU is equal to the difference between the external work performed by the applied moment and the strain energy (see Williams, 1988). Hence, this change caused by an incremental delamination extension Δa may be obtained to be

$$\Delta U = \frac{M^2}{2(EI)_{Tot}} \left[\frac{(EI)_{Tot}}{(EI)_{Low}} - 1 \right] \Delta a, \tag{1.26}$$

where the bending stiffness of the intact composite laminate and the lower sublaminate are denoted by $(EI)_{Tot}$ and $(EI)_{Low}$, respectively, and the overall bending moment is denoted by M. It should be noted that the second term in eq. (1.26) represents the external work of the applied bending moment; since no moment is applied on the upper sublaminate, the change in the strain energy is related only to the lower sublaminate (see Fig. 1.16a).

The expression EI refers to the equivalent bending stiffness, which depends upon the flexural modulus and the second moment of area I_{zz} of all plies within the laminate segment being analyzed. A schematic view of the equivalent cross-section of sublaminate i for $i = Up,\ Low$ is shown in Fig. 1.17, in which a local coordinate system is located at the equivalent cross-section centroid; B and h_i represent the width and the height of sublaminate i, respectively. Since all laminate segments have the same flexural modulus

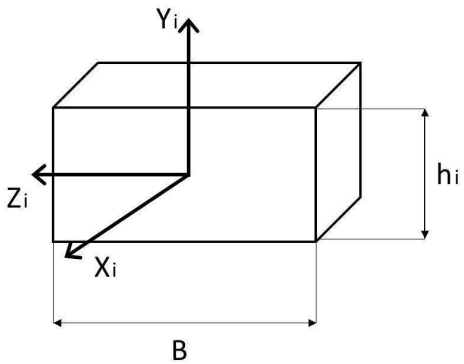

Figure 1.17: Schematic view of the ACP specimen sublaminate equivalent cross-section.

E, the bending stiffness of each laminate segment is explicitly given as

$$\begin{aligned}
(EI)_{Up}\big|_{identical\ plies\ lay-up} &= E \cdot I_{Up} = E \cdot \frac{B\chi^3 t^3}{12}, \\
(EI)_{Low}\big|_{identical\ plies\ lay-up} &= E \cdot I_{Low} = E \cdot \frac{B(1-\chi)^3 t^3}{12}, \\
(EI)_{Tot}\big|_{identical\ plies\ lay-up} &= E \cdot I_{Tot} = E \cdot \frac{Bt^3}{12},
\end{aligned} \tag{1.27}$$

where χ is the ratio of the number of cut plies to total number of plies and t refers to the total thickness of the intact composite segment (see Fig. 1.16a). Thus, from eq. (1.26), the expression for the total energy release rate may be written as

$$\begin{aligned}
\mathcal{G} &= \lim_{\Delta a \to 0} \frac{1}{B} \frac{\Delta U}{\Delta a}; \\
\mathcal{G} &= \frac{M^2}{2BEI_{Tot}} \left[\frac{I_{Tot}}{I_{Low}} - 1 \right].
\end{aligned} \tag{1.28}$$

Referring to Fig. 1.16b, pure mode I is obtained when M_I is applied to both sublaminates in opposite directions; whereas, pure mode II in Fig. 1.16c is obtained when the curvature of both sublaminates is the same. An identical sublaminate curvature in the vicinity of the delamination tip may be written as

$$\frac{\psi M_{II}}{(EI)_{Up}} = \frac{M_{II}}{(EI)_{Low}}, \tag{1.29}$$

so that the ratio of the upper sublaminate equivalent bending stiffness to the lower sublaminate equivalent bending stiffness (see Fig. 1.16c), denoted by ψ, may be written as

$$\psi = \frac{(EI)_{Up}}{(EI)_{Low}}. \tag{1.30}$$

In eq. (1.30), $(EI)_{Up}$ is the equivalent bending stiffness of the upper sublaminate. Accounting for laminate segments of the same flexural modulus E (substituting eqs. $(1.27)_1$ and $(1.27)_2$ into eq. (1.30)), leads to

$$\psi = \frac{\chi^3}{(1-\chi)^3}. \tag{1.31}$$

Using Fig. 1.16, the moment equilibrium of the upper sublaminate and the lower sublaminate, which are given by

$$\begin{aligned}
\text{Upper sublaminate: } 0\big|_{\text{Fig. 1.16a}} &= -M_I\big|_{\text{Fig. 1.16b}} + \psi M_{II}\big|_{\text{Fig. 1.16c}} \\
\text{Lower sublaminate: } M\big|_{\text{Fig. 1.16a}} &= M_I\big|_{\text{Fig. 1.16b}} + M_{II}\big|_{\text{Fig. 1.16c}}
\end{aligned} \tag{1.32}$$

respectively, must be fulfilled. Also, the moment equilibrium in Figs. 1.16b (mode I) and 1.16c (mode II), which are given by

$$\begin{aligned} 0\big|_{\text{Fig. 1.16b}} &= -M_I\big|_{\text{Fig. 1.16b}} + M_I\big|_{\text{Fig. 1.16b}} \\ M\big|_{\text{Fig. 1.16c}} &= \psi M_{II}\big|_{\text{Fig. 1.16c}} + M_{II}\big|_{\text{Fig. 1.16c}} \end{aligned} \tag{1.33}$$

respectively, must be fulfilled too. Thus, from eq. $(1.33)_2$,

$$M_{II} = \frac{M}{(1+\psi)}, \tag{1.34}$$

and from eqs. $(1.32)_2$ and (1.34),

$$M_I = \frac{\psi M}{(1+\psi)}. \tag{1.35}$$

Referring to Williams (1988), the change of the elastic potential energy ΔU_j for j = mode I, mode II, which is associated with each delamination deformation mode, may be written as

$$\Delta U_j = \frac{1}{2(EI)_{Tot}} \left[\frac{M_{Low\,j}^2 (EI)_{Tot}}{(EI)_{Low}} + \frac{M_{Up_j}^2 (EI)_{Tot}}{(EI)_{Up}} - \left(M_{Low\,j} + M_{Up_j}\right)^2 \right] \Delta a, \tag{1.36}$$

where the total change of the elastic potential energy is given by $\Delta U = \Delta U_{\text{mode I}} + \Delta U_{\text{mode II}}$, as presented in eq. (1.26). One may obtain eq. (1.26) with the aid of eqs. (1.30), (1.34) and (1.35). Substitution of the proper laminate segment bending moments for each delamination deformation mode, which are presented in eq. (1.32), into eq. (1.36), results in

$$\begin{aligned} \Delta U_{\text{mode I}} &= \frac{1}{2(EI)_{Tot}} \left[\frac{M_I^2 (EI)_{Tot}}{(EI)_{Low}} + \frac{M_I^2 (EI)_{Tot}}{(EI)_{Up}} \right] \Delta a, \\ \Delta U_{\text{mode II}} &= \frac{1}{2(EI)_{Tot}} \left[\frac{M_{II}^2 (EI)_{Tot}}{(EI)_{Low}} + \frac{\psi^2 M_{II}^2 (EI)_{Tot}}{(EI)_{Up}} - \left(M_{II} + \psi M_{II}\right)^2 \right] \Delta a. \end{aligned} \tag{1.37}$$

Referring to Williams (1988) and Charalambous et al. (2015a), the specimen composite strip lay-up consists of plies of identical properties (same thickness, material properties and orientation). Substituting eqs. (1.37) into eq. $(1.28)_1$, the components of the total energy release rate associated with each delamination deformation mode may be written as

$$\begin{aligned} \mathcal{G}_I &= \frac{{M_I}^2}{2BEI_{Tot}} \left[\frac{I_{Tot}}{I_{Low}} + \frac{I_{Tot}}{I_{Up}} \right], \\ \mathcal{G}_{II} &= \frac{(1+\psi)^2 {M_{II}}^2}{2BEI_{Tot}} \left[\frac{I_{Tot}}{(1+\psi)^2 I_{Low}} + \frac{\psi^2 I_{Tot}}{(1+\psi)^2 I_{Up}} - 1 \right]. \end{aligned} \tag{1.38}$$

The components of the energy release rate associated with each delamination deformation mode written as a function of the overall applied bending moment M may be obtained by substituting the appropriate deformation mode moment expression given in eqs. (1.34) and (1.35) into eq. (1.38), as well as use of eqs. $(1.27)_1$, $(1.27)_3$ and (1.31), results in

$$\begin{aligned} \mathcal{G}_I &= \frac{\psi^2 M^2}{2BEI_{Tot}\chi^3(1+\psi)}, \\ \mathcal{G}_{II} &= \frac{M^2}{2BEI_{Tot}}\left[\frac{\psi}{\chi^3(1+\psi)} - 1\right]. \end{aligned} \tag{1.39}$$

In eqs. (1.39), the bending stiffness of the composite intact strip segment is denoted by EI_{Tot}. The expression for the overall bending moment M, which is based upon a kinematic analysis of the ACP specimen including large end-tab rotations performed by Charalambous et al. (2015a), as well as other expressions may be found in Charalambous et al. (2015a).

It should be recalled, that the total energy release rate is given by

$$\mathcal{G} = \mathcal{G}_I + \mathcal{G}_{II}. \tag{1.40}$$

Using the expression for $\mathcal{G}_{II}$ in eq. $(1.39)_2$ and substituting eqs. $(1.39)_1$ and $(1.39)_2$ into eq. (1.40), the mode mixity of the ACP specimen may be expressed solely by means of χ, as presented in the work of Charalambous et al. (2015a), in which

$$\phi\big|_{identical\ plies\ lay-up} = \frac{\mathcal{G}_{II}}{\mathcal{G}} = \frac{3(1-\chi)^4}{(1-3\chi+3\chi^2)(3-3\chi+\chi^2)}. \tag{1.41}$$

In Charalambous et al. (2015a), in which the mixed mode ratio was set to 0.43, quasi-static tests were carried out with precracked specimens, as well as specimens which were not precracked. All UD CFRP laminate composite specimens were made of IM7/8552 (carbon/epoxy). For both delamination types, an elastic response was observed in the curve of the overall bending moment M per specimen width versus the applied testing machine cross-head displacement until the delamination initiation point. The maximum overall bending moment was measured. The results were verified by means of FE analyses, in which the delamination tip behavior was characterized by a coupled, linear softening-like cohesive zone model. The numerical results were verified from experiments found in the literature by means of the MMB test method. Excellent agreement was found between the MMB values (Allegri et al., 2013) for the same material and the ACP obtained delamination initiation values. It should be pointed out, that the obtained FEA results supported the analytical expressions developed for the predicted large rotation occurring at the rigid end-tabs of the specimen.

Charalambous et al. (2015b) employed the ACP specimen and the FPB test fixture for measuring the mixed mode interlaminar fracture toughness and fatigue delamination growth rate of a UD CFRP composite. Again, the material studied was composed of IM7/8552 (carbon/epoxy). Several temperatures, which represent the operating temperatures of composite structures in aeronautical applications were used; these included -50 °C, 20 °C, 50 °C and 80 °C. As in Charalambous et al. (2015a), the mixed mode ratio was set to 0.43. The obtained experimental data was based upon tests carried out on specimens which were not precracked.

In Charalambous et al. (2015b), the quasi-static tests were carried out in displacement control with a constant cross-head displacement rate of 1 mm/min and an upper bound for the applied cross-head displacement of 10 mm; both specimen and test fixture were housed in an environmental chamber. For all examined temperatures, an elastic response was observed in the curve of the overall bending moment per specimen width versus the applied testing machine cross-head displacement until the delamination initiation point. As before, the maximum overall bending moment was measured. Also, the fracture surfaces of all quasi-static test specimens were analysed by means of scanning electron microscopy (SEM). The specimens which were tested in the temperature range of -50 °C to 50 °C showed a similar elastic response, as well as similar delamination initiation value. Furthermore, their fracture surfaces were found to be similar, according to the SEM analyses. This implies that within the temperature range of -50 °C to 50 °C, the rise in matrix ductility was "balanced" by the accompanied fiber-matrix interfacial strength reduction. At 80 °C, higher delamination initiation values were obtained as a result of a significant rise in matrix ductility, which was indicated by the presence of matrix plastic deformation (evident by shear cusps in the SEM examinations) on the fracture surface. Nevertheless, SEM analyses of fracture surfaces of the quasi-static test specimens for all temperatures examined showed that a significant amount of matrix material was still attached to the fibers. Thus, it was concluded that the dominant failure mechanism was a cohesive failure of the matrix.

1.4 Aims of this study

In this study, one of the most typical failure modes is investigated: the delamination between two adjacent plies in a composite structure. The delamination is assumed to be along the interface between a $0°/90°$ and a $+45°/-45°$ balanced plain weave, and may represent a common design detail within a composite structure used in the civil aircraft industry. The woven multidirectional composite is fabricated from a prepreg containing carbon fibers in an epoxy matrix (G0814/913). An illustration of a typical balanced

plain weave and the delamination with its orientation are shown in Figs. 1.1a and 1.1b, respectively.

The main goals of this study are: (1) determination of the stress intensity factors and the energy release rate and phase angles for an interlaminar delamination in the investigated MD laminate composite material, which may be subjected to mixed mode loading conditions (mechanical and/or thermal residual stresses), by employing analytical and numerical methods; (2) measurement of the three-dimensional laminate composite interface delamination properties (fracture toughness) via the Brazilian disk specimen, in which a range of mode mixities is applied to the same specimen configuration; (3) development of a delamination initiation failure criterion (fracture under static load); (4) measurement of the interlaminar fracture toughness: delamination initiation and propagation under quasi-static loading by means of the DCB, C-ELS and the MMELS specimens, in which the specimen is subjected to nearly pure mode I, nearly pure mode II and mixed mode I/II deformations, respectively; and (5) comparison of the fracture toughness results which are obtained by means of the BD specimens to those obtained by means of the beam-type specimens. By achieving these goals, design allowables for delamination initiation and propagation fracture toughness will be determined to meet both regulation demands and manufacturer needs (reliable low cost and easy to maintain composite structures).

Chapter 2

First Term of The Asymptotic Solution for an Interface Delamination

Failure criteria for an interface delamination are usually based on the critical interface energy release rate, $\mathcal{G}_{ic}$ and phase angles, $\hat{\psi}$ and ϕ or on the stress intensity factors, K_1, K_2 and K_{III} as described in Section 1.2. In order to define a failure criterion, the first term of the asymptotic stress and displacement fields must be determined in the neighborhood of a delamination front. The development of these fields is very similar to the work carried out by Ting (1996), Banks-Sills and Boniface (2000), Freed and Banks-Sills (2005) and Rogel and Banks-Sills (2010). In his book, Ting (1996) describes the formalisms of Lekhnitskii (1950) and Stroh (1958). Both formalisms, independently, may be used to develop the stress function and displacement fields within an anisotropic elastic material, under the assumption that the three-dimensional fields depend solely on the two in-plane coordinates, say x_1 and x_2, of the media. The Lekhnitskii (1950) formalism is based on the stress expressions of an anisotropic elastic material, whereas the Stroh (1958) formalism is based on the displacement expressions of an anisotropic elastic material. Both formalisms of Lekhnitskii (1950) and Stroh (1958) are briefly summarized in Appendices A and B, respectively. A combination of those two formalisms leads to a closed form solution for the asymptotic stress and displacement fields. Barnett and Kirchner (1997) showed the equivalence between the Lekhnitskii (1950) sextic equation and the Stroh (1958) sextic equation.

2.1 Description of the plain-weave composite material properties

In order to develop the asymptotic stress and displacement fields in the vicinity of the delamination front explicitly, it is necessary to first define the mechanical and thermal properties of the materials. Hence, they are presented in this section. Furthermore, all of the relevant explicit expressions of the matrices involved in the development of the asymptotic solution for an interface delamination between two tetragonal anisotropic elastic materials are presented, as well. As noted in Section 1.2, in this investigation the bimaterial interface is between a $0°/90°$ and a $+45°/-45°$ balanced plain weave (see Fig. 1.1b).

Stroh eigenvectors $\mathbf{A}_k$ and $\mathbf{B}_k$ (see Appendix B) depend upon the elastic compliance components $s^{(k)}_{\alpha\beta}$ of each material (for $\alpha, \beta = 1, \cdots, 6$) where $k = 1, 2$ represent the upper and lower materials, respectively (see the definition of contracted notation in Appendix A). Using the coordinate system shown in Fig. 1.1b and applying the symmetry which exists in the case of a tetragonal anisotropic elastic material, one may obtain their general form as

$$\mathbf{s}^{(k)} = \begin{bmatrix} s^{(k)}_{11} & s^{(k)}_{12} & s^{(k)}_{13} & 0 & 0 & 0 \\ & s^{(k)}_{22} & s^{(k)}_{12} & 0 & 0 & 0 \\ & & s^{(k)}_{11} & 0 & 0 & 0 \\ & & & s^{(k)}_{44} & 0 & 0 \\ & & \text{sym} & & s^{(k)}_{55} & 0 \\ & & & & & s^{(k)}_{44} \end{bmatrix}. \tag{2.1}$$

The components of $\mathbf{s}^{(1)}$ for the upper material are given by

$$\begin{aligned} s^{(1)}_{11} &= \frac{1}{E_{11}} \\ s^{(1)}_{12} &= -\frac{\nu_{12}}{E_{11}} \\ s^{(1)}_{13} &= -\frac{\nu_{13}}{E_{11}} \\ s^{(1)}_{22} &= \frac{1}{E_{22}} \\ s^{(1)}_{44} &= \frac{1}{G_{23}} \\ s^{(1)}_{55} &= \frac{1}{G_{13}} \end{aligned} \tag{2.2}$$

where E_{ii} are the Young's moduli in the x_i-direction (for $i = 1, 2, 3$), no summation implied. The Poisson's ratios are given by ν_{ij} and G_{ij} are the shear moduli (for $i, j =$

$1, 2, 3$). The relation between the Young's moduli and the Poisson's ratios is given by

$$\frac{\nu_{ij}}{E_{ii}} = \frac{\nu_{ji}}{E_{jj}}, \tag{2.3}$$

no summation implied. Both upper and lower materials are made of the same woven composite; hence, the compliance matrix of the lower material may be obtained by rotating $\mathbf{s}^{(1)}$ by 45° about the x_2-axis. The expressions for the lower material $\mathbf{s}^{(2)}$ are found as (see Fig. 1.1b)

$$\begin{aligned}
s_{11}^{(2)} &= \frac{1-\nu_{13}}{2E_{11}} + \frac{1}{4G_{13}} \\
s_{12}^{(2)} &= -\frac{\nu_{12}}{E_{11}} \\
s_{13}^{(2)} &= \frac{1-\nu_{13}}{2E_{11}} - \frac{1}{4G_{13}} \\
s_{22}^{(2)} &= \frac{1}{E_{22}} \\
s_{44}^{(2)} &= \frac{1}{G_{23}} \\
s_{55}^{(2)} &= \frac{2(1+\nu_{13})}{E_{11}}.
\end{aligned} \tag{2.4}$$

A detailed explanation about the transformation of both stiffness and compliance matrices may be found in Ting (1996, pp. 53-56).

The Stroh eigenvectors may be expressed by means of the reduced compliance matrix components, $s'^{(k)}_{\alpha\beta}$, which are given in eq. (A-8). Based on this relation, the reduced compliance matrix of the upper and lower materials may be written as

$$\mathbf{s}'^{(k)} = \begin{bmatrix}
s'^{(k)}_{11} & s'^{(k)}_{12} & 0 & 0 & 0 \\
 & s'^{(k)}_{22} & 0 & 0 & 0 \\
 & & s'^{(k)}_{66} & 0 & 0 \\
 & \text{sym} & & s'^{(k)}_{44} & 0 \\
 & & & & s'^{(k)}_{55}
\end{bmatrix}. \tag{2.5}$$

For the upper material, the components of $\mathbf{s}'^{(1)}$ are given by

$$\begin{aligned} s_{11}'^{(1)} &= \frac{1}{E_{11}}(1-\nu_{13}^2) \\ s_{12}'^{(1)} &= -\frac{\nu_{12}}{E_{11}}(1+\nu_{13}) \\ s_{22}'^{(1)} &= \frac{E_{11}-E_{22}\nu_{12}^2}{E_{11}E_{22}} \\ s_{66}'^{(1)} &= s_{44}'^{(1)} = \frac{1}{G_{23}} \\ s_{55}'^{(1)} &= \frac{1}{G_{13}}\ ; \end{aligned} \tag{2.6}$$

whereas for the lower material, the components of $\mathbf{s}'^{(2)}$ are given by

$$\begin{aligned} s_{11}'^{(2)} &= \frac{2(1-\nu_{13})}{E_{11}+2G_{13}(1-\nu_{13})} \\ s_{12}'^{(2)} &= -\frac{2\nu_{12}}{E_{11}+2G_{13}(1-\nu_{13})} \\ s_{22}'^{(2)} &= \frac{1}{E_{22}} - \frac{4G_{13}\nu_{12}^2}{E_{11}[E_{11}+2G_{13}(1-\nu_{13})]} \\ s_{66}'^{(2)} &= s_{44}'^{(2)} = \frac{1}{G_{23}} \\ s_{55}'^{(2)} &= \frac{2(1+\nu_{13})}{E_{11}}. \end{aligned} \tag{2.7}$$

Some of the material properties of the $0°/90°$ plain weave are based on tests performed following acceptable standard methods in Israel Aerospace Industries (IAI) laboratories. A complete set of the needed material properties was obtained via the High Fidelity Generalized Method of Cells (HFGMC), described in detail in Aboudi (2004). This method allows homogenization of the material properties of the constituents within one ply or within a stackup of several different plies. Applying this method results in all the effective material properties needed to characterize a complex structure. The material properties of the plain woven plies with yarn in the $0°/90°$-directions and the $+45°/-45°$-directions are given in Banks-Sills et al. (2013) and Ishbir (2014) and are presented in Tables 2.1 and 2.2, where α_{ii} are the thermal expansion coefficients in the x_i-direction (for $i = 1, 2, 3$), no summation implied. By using these mechanical properties, the components of both compliance matrices $s_{\alpha\beta}'^{(k)}$ may be calculated. Thus, their values are presented in Table 2.3. It should be noted that the properties of the ply with yarn in the $+45°/-45°$-directions

Table 2.1: Mechanical properties of the $0°/90°$ plain weave ($V_f = 0.51$).

layer type	$E_{11} = E_{33}$ (GPa)	E_{22} (GPa)	G_{13} (GPa)	$G_{23} = G_{12}$ (GPa)	ν_{13}	$\nu_{23} = \nu_{21}$
$0°/90°$	57.3	7.6	3.9	2.5	0.039	0.066
$+45°/-45°$	13.5	7.6	27.6	2.5	0.774	0.066

were obtained by rotating the properties of the $0°/90°$ ply about the x_2-axis (shown in Fig. 1.1) by $45°$.

Substitution of the reduced compliance components $s'^{(k)}_{\alpha\beta}$, given in eq. (2.5), into the sextic equation of Lekhnitskii (1950), shown in eq. (A-14), leads to

$$l_2(p)l_4(p) = 0. \tag{2.8}$$

The solution of eq. (2.8) results in expressions for the eigenvalues $p^{(k)}_\alpha$ of both materials given as

$$\begin{aligned} p^{(k)}_{1,2} &= \sqrt{\frac{-\left(2s'^{(k)}_{12} + s'^{(k)}_{66}\right) \pm \sqrt{\left(2s'^{(k)}_{12} + s'^{(k)}_{66}\right)^2 - 4s'^{(k)}_{11}s'^{(k)}_{22}}}{2s'^{(k)}_{11}}} \\ p^{(k)}_3 &= \sqrt{-\frac{s'^{(k)}_{44}}{s'^{(k)}_{55}}}. \end{aligned} \tag{2.9}$$

In this particular case, substitution of the components of both reduced compliance matrices, shown in Table 2.3, reveals that $p^{(k)}_1$ and $p^{(k)}_2$ are fully imaginary, resulting in

$$\begin{aligned} p^{(k)}_1 &= i\beta^{(k)}_1 \\ p^{(k)}_2 &= i\beta^{(k)}_2 \\ p^{(k)}_3 &= i\beta^{(k)}_3, \end{aligned} \tag{2.10}$$

Table 2.2: Coefficients of thermal expansion of the $0°/90°$ plain weave ($V_f = 0.51$).

layer type	$\alpha_{11} = \alpha_{33}$ ($\times 10^{-6}/°$C)	α_{22} ($\times 10^{-6}/°$C)
$0°/90°$	2.9	52.1

Table 2.3: Values of the reduced compliance matrix components for upper and lower materials.

layer type weave orientation	$s_{11}^{\prime(k)}$ (1/TPa)	$s_{12}^{\prime(k)}$ (1/TPa)	$s_{22}^{\prime(k)}$ (1/TPa)	$s_{66}^{\prime(k)} = s_{44}^{\prime(k)}$ (1/TPa)	$s_{55}^{\prime(k)}$ (1/TPa)
$k = 1$, $0°/90°$	17.42	-9.06	127.72	400.0	259.74
$k = 2$, $+45°/-45°$	29.71	-15.46	131.04	400.0	36.25

where

$$\beta_{1,2}^{(k)} = \sqrt{\frac{\left(2s_{12}^{\prime(k)} + s_{66}^{\prime(k)}\right) \mp \sqrt{\left(2s_{12}^{\prime(k)} + s_{66}^{\prime(k)}\right)^2 - 4s_{11}^{\prime(k)} s_{22}^{\prime(k)}}}{2s_{11}^{\prime(k)}}}$$

$$\beta_3^{(k)} = \sqrt{\frac{s_{44}^{\prime(k)}}{s_{55}^{\prime(k)}}}. \tag{2.11}$$

It may be noted that the term in the inner square-root is positive.

By substituting the retrieved eigenvalues $p_\alpha^{(k)}$ and the reduced compliance components $s_{\alpha\beta}^{\prime(k)}$ into the expressions of the Stroh eigenvectors, given in eqs. (B-16) and (B-17), one obtains explicitly the forms for the matrices $\mathbf{A}_k$, $\mathbf{B}_k$ and $\mathbf{B}_k^{-1}$ as

$$\mathbf{A}_k = \begin{bmatrix} k_1^{(k)}\left(s_{12}^{\prime(k)} - s_{11}^{\prime(k)}{\beta_1^{(k)}}^2\right) & k_2^{(k)}\left(s_{12}^{\prime(k)} - s_{11}^{\prime(k)}{\beta_2^{(k)}}^2\right) & 0 \\ -i\dfrac{k_1^{(k)}}{\beta_1^{(k)}}\left(s_{22}^{\prime(k)} - s_{12}^{\prime(k)}{\beta_1^{(k)}}^2\right) & -i\dfrac{k_2^{(k)}}{\beta_2^{(k)}}\left(s_{22}^{\prime(k)} - s_{12}^{\prime(k)}{\beta_2^{(k)}}^2\right) & 0 \\ 0 & 0 & i\dfrac{k_3^{(k)}}{\beta_3^{(k)}}s_{44}^{\prime(k)} \end{bmatrix}, \tag{2.12}$$

$$\mathbf{B}_k = \begin{bmatrix} -ik_1^{(k)}\beta_1^{(k)} & -ik_2^{(k)}\beta_2^{(k)} & 0 \\ k_1^{(k)} & k_2^{(k)} & 0 \\ 0 & 0 & -k_3^{(k)} \end{bmatrix}, \tag{2.13}$$

$$\mathbf{B}_k^{-1} = \frac{1}{\beta_2^{(k)} - \beta_1^{(k)}} \begin{bmatrix} -\dfrac{i}{k_1^{(k)}} & \dfrac{\beta_2^{(k)}}{k_1^{(k)}} & 0 \\ \dfrac{i}{k_2^{(k)}} & -\dfrac{\beta_1^{(k)}}{k_2^{(k)}} & 0 \\ 0 & 0 & -\dfrac{\left(\beta_2^{(k)} - \beta_1^{(k)}\right)}{k_3^{(k)}} \end{bmatrix}. \tag{2.14}$$

The result of the matrix multiplication $\mathbf{A}_k\mathbf{B}_k^{-1}$ which is required in developing the asymptotic displacement and stress fields in the vicinity of the delamination front is given explicitly by

$$\mathbf{A}_k\mathbf{B}_k^{-1} = \begin{bmatrix} -is_{11}^{\prime(k)}\left(\beta_1^{(k)}+\beta_2^{(k)}\right) & s_{12}^{\prime(k)}+\sqrt{s_{11}^{\prime(k)}s_{22}^{\prime(k)}} & 0 \\ -\left(s_{12}^{\prime(k)}+\sqrt{s_{11}^{\prime(k)}s_{22}^{\prime(k)}}\right) & -i\sqrt{s_{11}^{\prime(k)}s_{22}^{\prime(k)}}\left(\beta_1^{(k)}+\beta_2^{(k)}\right) & 0 \\ 0 & 0 & -i\sqrt{s_{44}^{\prime(k)}s_{55}^{\prime(k)}} \end{bmatrix}. \tag{2.15}$$

The expression for $\mathbf{A}_k\mathbf{B}_k^{-1}$, shown in eq. (2.15), are related to two of the three real Barnett-Lothe tensors, $\mathbf{S}_k$ and $\mathbf{L}_k$, as

$$\mathbf{A}_k\mathbf{B}_k^{-1} = -\mathbf{S}_k\mathbf{L}_k^{-1} - i\mathbf{L}_k^{-1}, \tag{2.16}$$

where no summation is implied. Since $\mathbf{S}_k$ and $\mathbf{L}_k$ are real, it is possible to write

$$\mathbf{S}_k\mathbf{L}_k^{-1} = \begin{bmatrix} 0 & -\left(s_{12}^{\prime(k)}+\sqrt{s_{11}^{\prime(k)}s_{22}^{\prime(k)}}\right) & 0 \\ s_{12}^{\prime(k)}+\sqrt{s_{11}^{\prime(k)}s_{22}^{\prime(k)}} & 0 & 0 \\ 0 & 0 & 0 \end{bmatrix}, \tag{2.17}$$

and

$$\mathbf{L}_k^{-1} = \begin{bmatrix} s_{11}^{\prime(k)}\left(\beta_1^{(k)}+\beta_2^{(k)}\right) & 0 & 0 \\ 0 & \sqrt{s_{11}^{\prime(k)}s_{22}^{\prime(k)}}\left(\beta_1^{(k)}+\beta_2^{(k)}\right) & 0 \\ 0 & 0 & \sqrt{s_{44}^{\prime(k)}s_{55}^{\prime(k)}} \end{bmatrix}. \tag{2.18}$$

There are three other important matrices, $\mathbf{D}$, $\mathbf{W}$ and $\breve{\mathbf{S}}$, which are also required in developing the asymptotic displacement and stress fields. They are given by

$$\begin{aligned} \mathbf{D} &= \mathbf{L}_1^{-1} + \mathbf{L}_2^{-1}, \\ \mathbf{W} &= \mathbf{S}_1\mathbf{L}_1^{-1} - \mathbf{S}_2\mathbf{L}_2^{-1}, \\ \breve{\mathbf{S}} &= \mathbf{D}^{-1}\mathbf{W}. \end{aligned} \tag{2.19}$$

Thus, from eqs. $(2.19)_1$ and $(2.19)_2$

$$\mathbf{D} = \begin{bmatrix} \sum_{k=1}^{2} s_{11}^{\prime(k)}\left(\beta_1^{(k)}+\beta_2^{(k)}\right) & 0 & 0 \\ 0 & \sum_{k=1}^{2}\sqrt{s_{11}^{\prime(k)}s_{22}^{\prime(k)}}\left(\beta_1^{(k)}+\beta_2^{(k)}\right) & 0 \\ 0 & 0 & \sum_{k=1}^{2}\sqrt{s_{44}^{\prime(k)}s_{55}^{\prime(k)}} \end{bmatrix}, \tag{2.20}$$

and

$$\mathbf{W} = \begin{bmatrix} 0 & \sum_{k=1}^{2}(-1)^{k}\left(s_{12}^{\prime(k)} + \sqrt{s_{11}^{\prime(k)}s_{22}^{\prime(k)}}\right) & 0 \\ \sum_{k=1}^{2}(-1)^{k+1}\left(s_{12}^{\prime(k)} + \sqrt{s_{11}^{\prime(k)}s_{22}^{\prime(k)}}\right) & 0 & 0 \\ 0 & 0 & 0 \end{bmatrix}, \quad (2.21)$$

where

$$\mathbf{D}^{-1} = \begin{bmatrix} \dfrac{1}{\sum_{k=1}^{2} s_{11}^{\prime(k)}\left(\beta_1^{(k)} + \beta_2^{(k)}\right)} & 0 & 0 \\ 0 & \dfrac{1}{\sum_{k=1}^{2}\sqrt{s_{11}^{\prime(k)}s_{22}^{\prime(k)}}\left(\beta_1^{(k)} + \beta_2^{(k)}\right)} & 0 \\ 0 & 0 & \dfrac{1}{\sum_{k=1}^{2}\sqrt{s_{44}^{\prime(k)}s_{55}^{\prime(k)}}} \end{bmatrix}. \quad (2.22)$$

The matrix $\breve{\mathbf{S}}$ is defined in eq. $(2.19)_3$, so that

$$\breve{\mathbf{S}} = \begin{bmatrix} 0 & \breve{S}_{12} & 0 \\ \breve{S}_{21} & 0 & 0 \\ 0 & 0 & 0 \end{bmatrix}, \quad (2.23)$$

where its non-zero components are given explicitly by

$$\begin{aligned} \breve{S}_{12} &= \frac{\sum_{k=1}^{2}(-1)^{k}\left(s_{12}^{\prime(k)} + \sqrt{s_{11}^{\prime(k)}s_{22}^{\prime(k)}}\right)}{\sum_{k=1}^{2} s_{11}^{\prime(k)}\left(\beta_1^{(k)} + \beta_2^{(k)}\right)}, \\ \breve{S}_{21} &= \frac{\sum_{k=1}^{2}(-1)^{k+1}\left(s_{12}^{\prime(k)} + \sqrt{s_{11}^{\prime(k)}s_{22}^{\prime(k)}}\right)}{\sum_{k=1}^{2}\sqrt{s_{11}^{\prime(k)}s_{22}^{\prime(k)}}\left(\beta_1^{(k)} + \beta_2^{(k)}\right)}. \end{aligned} \quad (2.24)$$

2.2 The first term of the asymptotic solution of the interface delamination

In this section, the first term of the asymptotic solution of both stress and displacement fields is developed for the interface delamination between two tetragonal anisotropic elastic materials as shown in Fig. 1.1b. The development is based upon the anisotropic bimaterial interface crack representation of Ting (1996, pp. 341-345). The general forms of the displacement vector $\mathbf{u}^{(k)}$ and stress function vector $\boldsymbol{\phi}^{(k)}$ for a bimaterial interface delamination, as presented by Ting (1996, p. 341) and following the Stroh formalism (see Appendix B eq. (B-13) to eq. (B-15)), are considered. The arbitrary functions $f(z_\alpha^{(k)})$ in the Stroh formalism (see Appendix B eq. (B-15)) were defined by Ting (1996) as

$$f(z_\alpha^{(k)}) = z_\alpha^{(k)\delta+1} = z_*^{(k)\delta+1} \qquad \text{for } \alpha = * = 1,2,3 \tag{2.25}$$

for an interface crack. Then, the displacement vector $\mathbf{u}^{(k)}$ and stress function vector $\boldsymbol{\phi}^{(k)}$ may be written as

$$\mathbf{u}^{(k)} = \mathbf{A}_k \langle z_*^{(k)\delta+1} \rangle \mathbf{q}_k + \overline{\mathbf{A}}_k \langle \overline{z}_*^{(k)\delta+1} \rangle \tilde{\mathbf{q}}_k \tag{2.26}$$

and

$$\boldsymbol{\phi}^{(k)} = \mathbf{B}_k \langle z_*^{(k)\delta+1} \rangle \mathbf{q}_k + \overline{\mathbf{B}}_k \langle \overline{z}_*^{(k)\delta+1} \rangle \tilde{\mathbf{q}}_k, \tag{2.27}$$

where $k = 1, 2$ represent the upper and lower anisotropic elastic materials, respectively. The 3×3 matrices, $\mathbf{A}_k$ and $\mathbf{B}_k$, are the Stroh eigenvectors as described in Appendix B (see eqs. (B-16) and (B-17)). Both $\mathbf{q}_k$ and $\tilde{\mathbf{q}}_k$ are arbitrary 3×1 constant vectors determined, eventually, by satisfying the boundary conditions of traction free crack faces and traction continuity along the interface. The overbar in eqs. (2.26) and (2.27) represents the complex conjugate of the quantity, the angle brackets denote a diagonal matrix and $z_*^{(k)} = r\zeta_*^{(k)}$ where

$$\zeta_*^{(k)}(\theta) = \cos(\theta) + p_*^{(k)} \sin(\theta). \tag{2.28}$$

The polar coordinate system (r, θ) at the delamination front is shown in Fig. 1.1b. The parameters $p_*^{(k)}$ are the complex eigenvalues of each material which depend solely on its mechanical properties, as may be seen from eqs. (2.10) and (2.11). They satisfy the sextic equation for $p_*^{(k)}$, which is given in eqs. (A-14) and (B-8) following the Lekhnitskii (1950) and the Stroh (1958) formalisms, respectively. The complex constant δ is the eigenvalue of the crack problem; its lowest real part gives the stress singularity. Its imaginary part may differ for every material pair of the interface.

For each material the stress function $\boldsymbol{\phi}^{(k)}$ is related to the stress field components by

$$\sigma_{j1}^{(k)} = -\phi_{j,2}^{(k)}, \qquad \sigma_{j2}^{(k)} = \phi_{j,1}^{(k)}. \tag{2.29}$$

The traction free crack face ($\theta = \pm\pi$) boundary conditions may be written as

$$\sigma_{j2}{}^{(1)}\Big|_{\theta=+\pi} = \sigma_{j2}{}^{(2)}\Big|_{\theta=-\pi} = 0, \tag{2.30}$$

where $\sigma_{j2}^{(k)}$ are the stress tensor components of material k. Referring to eq. $(2.29)_2$ along the crack faces, one may write that

$$\phi_{j,1}^{(k)}\Big|_{\theta=\pm\pi} = 0. \tag{2.31}$$

Integration of eq. (2.31) by x_1 along the crack faces results in

$$\phi_{j}^{(k)}\Big|_{\theta=\pm\pi} = \text{constant}. \tag{2.32}$$

Without loss of solution generality, along the crack faces the stress function vector may be defined as

$$\boldsymbol{\phi}^{(k)}\Big|_{\theta=\pm\pi} = 0. \tag{2.33}$$

In order to satisfy eq. (2.33), substitution of $\theta = \pm\pi$ in eq. (2.27) will determine the form of the arbitrary 3×1 constant vectors $\mathbf{q}_k$ and $\tilde{\mathbf{q}}_k$, which appear in eqs. (2.26) and (2.27), and are given by

$$\mathbf{q}_k = (-1)^k \frac{i}{2}\mathbf{B}_k^{-1} e^{(-1)^k i\pi\delta}\mathbf{g}_k, \qquad \tilde{\mathbf{q}}_k = (-1)^{k+1}\frac{i}{2}\overline{\mathbf{B}}_k^{-1} e^{(-1)^{k+1} i\pi\delta}\mathbf{g}_k. \tag{2.34}$$

The arbitrary complex vector $\mathbf{g}_k$ is determined by satisfying the continuity of traction along the interface. Under the assumption that the bimaterial interface is perfectly bonded, both displacements and tractions are continuous along the interface where $\theta = 0$ for every value of r. Traction continuity along the interface may be written as

$$\sigma_{j2}{}^{(1)}\Big|_{\theta=0} = \sigma_{j2}{}^{(2)}\Big|_{\theta=0}. \tag{2.35}$$

Referring to eq. $(2.29)_2$, along the interface and similar to eq. (2.33)

$$\phi_{j}^{(1)}\Big|_{\theta=0} = \phi_{j}^{(2)}\Big|_{\theta=0}. \tag{2.36}$$

This equivalence leads to the relationship which exists between the arbitrary complex vector $\mathbf{g}_k$ of both materials, meaning

$$\mathbf{g}_1 = \mathbf{g}_2 = \mathbf{d}. \tag{2.37}$$

Hence, the expressions for the displacement and stress function fields become

$$\mathbf{u}^{(k)} = \frac{i}{2}\left\{(-1)^k e^{(-1)^k i\pi\delta}\mathbf{A}_k\langle z_*^{(k)\delta+1}\rangle\mathbf{B}_k^{-1} + (-1)^{k+1}e^{(-1)^{k+1}i\pi\delta}\overline{\mathbf{A}}_k\langle \overline{z}_*^{(k)\delta+1}\rangle\overline{\mathbf{B}}_k^{-1}\right\}\mathbf{d} \tag{2.38}$$

and

$$\boldsymbol{\phi}^{(k)} = \frac{i}{2}\left\{(-1)^k e^{(-1)^k i\pi\delta}\mathbf{B}_k\langle z_*^{(k)\delta+1}\rangle\mathbf{B}_k^{-1} + (-1)^{k+1}e^{(-1)^{k+1}i\pi\delta}\overline{\mathbf{B}}_k\langle\overline{z}_*^{(k)\delta+1}\rangle\overline{\mathbf{B}}_k^{-1}\right\}\mathbf{d}, \quad (2.39)$$

respectively.

Next, in order to determine the stress singularities δ, displacement continuity along the interface is satisfied. Continuity of the displacement vector along the interface may be written as

$$\mathbf{u}^{(1)}\Big|_{\theta=0} = \mathbf{u}^{(2)}\Big|_{\theta=0}. \quad (2.40)$$

Substitution of $\theta = 0$ within the expression of the displacement field of each material, given in eq. (2.38), leads to

$$\left\{\breve{\mathbf{S}} - \cot\delta\pi\mathbf{I}\right\}\mathbf{d} = 0, \quad (2.41)$$

where $\mathbf{I}$ is the identity matrix and the matrix $\breve{\mathbf{S}}$ is defined in eq. $(2.19)_3$.

The values of δ may be obtained from the complex eigenvalues $\cot\delta\pi$, which are derived by setting

$$|\breve{\mathbf{S}} - \cot\delta\pi\mathbf{I}| = 0 \quad (2.42)$$

for every nontrivial solution of $\mathbf{d}$. While solving eq. (2.42), one will obtain the three eigenvalues $\cot\delta\pi$ which posses the form of

$$\cot\delta\pi = \mp i\beta, 0, \quad (2.43)$$

where

$$0 \leq \beta = \left\{-\frac{1}{2}\mathrm{tr}\left(\breve{\mathbf{S}}^2\right)\right\}^{1/2} < 1. \quad (2.44)$$

The value of β was chosen to be positive without loss of generality and tr represents the trace of the matrix. Extraction of the stress singularities δ_m for $m = 1, 2, 3$, reveals that

$$\delta_1 = -\frac{1}{2} + i\varepsilon, \qquad \delta_2 = -\frac{1}{2} - i\varepsilon, \qquad \delta_3 = -\frac{1}{2}, \quad (2.45)$$

where the oscillatory parameter ε is given by

$$\varepsilon = \frac{1}{2\pi}\ln\left(\frac{1+\beta}{1-\beta}\right). \quad (2.46)$$

The values of the eigenvectors $\mathbf{d}_m$ for $m = 1, 2, 3$ are obtained by substitution of the corresponding stress singularity δ_m into eq. (2.41), resulting in

$$\mathbf{d}_1 = \mathbf{d}, \qquad \mathbf{d}_2 = \overline{\mathbf{d}}, \qquad \mathbf{d}_3 = \mathbf{d}^*, \quad (2.47)$$

where

$$\mathbf{d} = \left\{ \begin{array}{c} i\sqrt{\dfrac{D_{22}}{D_{11}}} \\ 1 \\ 0 \end{array} \right\} d_2, \qquad \mathbf{d}^* = \left\{ \begin{array}{c} 0 \\ 0 \\ 1 \end{array} \right\} d_3. \tag{2.48}$$

The unknown constants d_2 and d_3 are complex and real, respectively. Both will be obtained by their relationship to the stress intensity factors $K = K_1 + iK_2$ and K_{III}. The components D_{jj} for $j = 1, 2$ (no summation) are given explicitly in eq. (2.20).

Based upon the expressions of the stress singularities given in eq. (2.45) and their corresponding eigenvectors shown in eq. (2.47), it is clear that the displacement vector $\mathbf{u}^{(k)}$ and the stress function vector $\boldsymbol{\phi}^{(k)}$ are actually a superposition of the solutions obtained above, meaning that each vector is constructed from an oscillatory singular part (os) and a regular square-root singular part (s), namely

$$\begin{aligned} \mathbf{u}^{(k)} &= \mathbf{u}^{(k)}_{os} + \mathbf{u}^{(k)}_{s}, \\ \boldsymbol{\phi}^{(k)} &= \boldsymbol{\phi}^{(k)}_{os} + \boldsymbol{\phi}^{(k)}_{s}. \end{aligned} \tag{2.49}$$

The oscillatory part is obtained by superposing the two oscillatory solutions for δ_1, $\mathbf{d}$ and δ_2, $\overline{\mathbf{d}}$. Nevertheless, despite the oscillatory singularity, the results for both vectors, the displacement and the stress function, are real quantities.

For the displacement vector and the stress function vector, respectively, expressions are given by

$$\begin{aligned} \mathbf{u}^{(k)}_{os} &= \Re\left\{ e^{(-1)^{k+1}\pi\varepsilon}\mathbf{A}_k \langle z_*^{(k)\left(\frac{1}{2}+i\varepsilon\right)} \rangle \mathbf{B}_k^{-1}\mathbf{d} + e^{(-1)^{k}\pi\varepsilon}\mathbf{A}_k \langle z_*^{(k)\left(\frac{1}{2}-i\varepsilon\right)} \rangle \mathbf{B}_k^{-1}\overline{\mathbf{d}} \right\} \\ \boldsymbol{\phi}^{(k)}_{os} &= \Re\left\{ e^{(-1)^{k+1}\pi\varepsilon}\mathbf{B}_k \langle z_*^{(k)\left(\frac{1}{2}+i\varepsilon\right)} \rangle \mathbf{B}_k^{-1}\mathbf{d} + e^{(-1)^{k}\pi\varepsilon}\mathbf{B}_k \langle z_*^{(k)\left(\frac{1}{2}-i\varepsilon\right)} \rangle \mathbf{B}_k^{-1}\overline{\mathbf{d}} \right\}. \end{aligned} \tag{2.50}$$

For the regular square-root singularity, the displacement vector and the stress function vector, may be found as

$$\begin{aligned} \mathbf{u}^{(k)}_{s} &= \Re\left\{ \mathbf{A}_k \langle z_*^{(k)\left(\frac{1}{2}\right)} \rangle \mathbf{B}_k^{-1} \right\} \mathbf{d}^* \\ \boldsymbol{\phi}^{(k)}_{s} &= \Re\left\{ \mathbf{B}_k \langle z_*^{(k)\left(\frac{1}{2}\right)} \rangle \mathbf{B}_k^{-1} \right\} \mathbf{d}^*. \end{aligned} \tag{2.51}$$

In order to achieve the explicit first terms of the asymptotic solution, the values of the unknown constant d_2 and d_3, shown in eq. (2.48), must be determined. As described previously, it is assumed that the bimaterial interface is perfectly bonded so that both displacement and traction are continuous along the interface where $\theta = 0$ for every value

of r (the interface is shown in Fig. 1.1b). The traction continuity condition along the interface ($x_2 = x_3 = 0$) is given in eq. (2.35). Referring to eq. $(2.29)_2$, where the relation between stresses and the stress function components are defined, differentiating $\boldsymbol{\phi}^{(k)}$ once by x_1 and then substituting $\theta = 0$ in the resultant will provide the following oscillatory singular and regular square-root singular expressions, respectively

$$\boldsymbol{\phi}^{(k)}_{os,1}\Big|_{\theta=0} = \frac{\cosh \pi\varepsilon}{\sqrt{r}}\, \Re\left\{(1+2i\varepsilon)r^{i\varepsilon}\mathbf{d}\right\} \tag{2.52}$$

and

$$\boldsymbol{\phi}^{(k)}_{s,1}\Big|_{\theta=0} = \frac{1}{2\sqrt{r}}\, \mathbf{d}^{*}. \tag{2.53}$$

Substitution of the terms of $\mathbf{d}$ and $\mathbf{d}^{*}$, given in eq. (2.48), leads to the expressions of $\sigma^{(k)}_{j2}$, where each stress component is constructed from an oscillatory singular part and a regular square-root singular part, resulting in

$$\left\{\begin{array}{c}\sigma_{12}\\ \sigma_{22}\\ \sigma_{32}\end{array}\right\}\Bigg|_{\theta=0} = \left\{\begin{array}{c}\sigma_{12_{os}}\\ \sigma_{22_{os}}\\ \sigma_{32_{os}}\end{array}\right\}\Bigg|_{\theta=0} + \left\{\begin{array}{c}\sigma_{12_{s}}\\ \sigma_{22_{s}}\\ \sigma_{32_{s}}\end{array}\right\}\Bigg|_{\theta=0}. \tag{2.54}$$

The oscillatory singular part is given by

$$\left\{\begin{array}{c}\sigma_{12_{os}}\\ \sigma_{22_{os}}\\ \sigma_{32_{os}}\end{array}\right\}\Bigg|_{\theta=0} = \frac{\cosh \pi\varepsilon}{\sqrt{r}} \left\{\begin{array}{c} -\sqrt{\dfrac{D_{22}}{D_{11}}}\,\Im\left[(1+2i\varepsilon)r^{i\varepsilon}d_2\right] \\ \Re\left[(1+2i\varepsilon)r^{i\varepsilon}d_2\right] \\ 0 \end{array}\right\}, \tag{2.55}$$

whereas, the regular square-root singular part is given by

$$\left\{\begin{array}{c}\sigma_{12_{s}}\\ \sigma_{22_{s}}\\ \sigma_{32_{s}}\end{array}\right\}\Bigg|_{\theta=0} = \frac{d_3}{2\sqrt{r}} \left\{\begin{array}{c} 0 \\ 0 \\ 1 \end{array}\right\}. \tag{2.56}$$

The expression for the in-plane stress components for an elastic anisotropic bimaterial interface crack may be represented similarly to that of an isotropic bimaterial interface crack, shown in eq. (1.5). In the case of an elastic anisotropic bimaterial interface crack, the expression for the in-plane stress components may be written as

$$\sigma^{(k)}_{\alpha\beta} = \frac{1}{\sqrt{2\pi r}}\left[\Re\left(Kr^{i\varepsilon}\right)_k \Sigma^{(1)}_{\alpha\beta}(\theta) + \Im\left(Kr^{i\varepsilon}\right)_k \Sigma^{(2)}_{\alpha\beta}(\theta)\right]; \tag{2.57}$$

the out-of-plane components are

$$\sigma_{3\beta}^{(k)} = \frac{1}{\sqrt{2\pi r}} \left(K_{III}\right)_k \Sigma_{3\beta}^{III}(\theta), \tag{2.58}$$

where $\alpha, \beta = 1, 2$. The in-plane complex stress intensity factor K is defined in eq. (1.6) and K_{III} is the out-of-plane real mode III stress intensity factor. The stress functions ${}_k\Sigma_{\alpha\beta}^{(1)}(\theta)$, ${}_k\Sigma_{\alpha\beta}^{(2)}(\theta)$ and ${}_k\Sigma_{3\beta}^{III}(\theta)$ depend upon the mechanical properties of the materials on both sides of the interface and will be given explicitly in the sequel.

Since eqs. (2.57) and (2.58) describe the stress field in the vicinity of the delamination front where $r \to 0$ for every value of θ, by setting $\theta = 0$ it will be possible to describe the stress components along the interface. By setting $r \to 0$ in eq. (2.54), the same expressions for the stress components should be obtained. This equivalence enables determination of the vectors $\mathbf{d}$ and $\mathbf{d}^*$ in terms of the stress intensity factors.

The in-plane complex stress intensity factor K is related only to the oscillatory singular stress components by

$$K \equiv \lim_{r\to 0} \frac{\sqrt{2\pi r}}{r^{i\varepsilon}} \left(\sigma_{22} - i\sqrt{\frac{D_{11}}{D_{22}}}\sigma_{12} \right) \Bigg|_{\theta=0}, \tag{2.59}$$

resulting in

$$d_2 = \frac{K}{\sqrt{2\pi}(1+2i\varepsilon)\cosh \pi\varepsilon}. \tag{2.60}$$

The out-of-plane real stress intensity factor K_{III} is related only to the regular square-root singular stress component by

$$K_{III} \equiv \lim_{r\to 0} \sqrt{2\pi r}\sigma_{32} \Bigg|_{\theta=0}, \tag{2.61}$$

resulting in

$$d_3 = \sqrt{\frac{2}{\pi}} K_{III}. \tag{2.62}$$

Hence, by substituting the expressions obtained for d_2 and d_3 given in eqs. (2.60) and (2.62), respectively, into eq. (2.48) results in

$$\mathbf{d} = \left\{ \begin{array}{c} i\sqrt{\dfrac{D_{22}}{D_{11}}} \\ 1 \\ 0 \end{array} \right\} \frac{K}{\sqrt{2\pi}(1+2i\varepsilon)\cosh \pi\varepsilon}, \qquad \mathbf{d}^* = \left\{ \begin{array}{c} 0 \\ 0 \\ 1 \end{array} \right\} \sqrt{\frac{2}{\pi}} K_{III}. \tag{2.63}$$

The representation of the displacement components and the stress components by means of the stress intensity factors at this stage is now possible. The in-plane displacement components may be written as

$$u_\alpha^{(k)} = \sqrt{\frac{r}{2\pi}} \left[\Re\left(Kr^{i\varepsilon}\right) \ {}_kU_\alpha^{(1)}(\theta) + \Im\left(Kr^{i\varepsilon}\right) \ {}_kU_\alpha^{(2)}(\theta) \right]; \tag{2.64}$$

whereas, the out-of-plane displacement component is given by

$$u_3^{(k)} = \sqrt{\frac{r}{2\pi}} K_{III}\ {}_kU_3^{(III)}(\theta). \tag{2.65}$$

The parameter $\alpha = 1, 2$ and $k = 1, 2$ designates the upper and lower materials, respectively. The displacement functions ${}_kU_\alpha^{(1)}(\theta)$, ${}_kU_\alpha^{(2)}(\theta)$ and ${}_kU_3^{(III)}(\theta)$ depend on the angle θ as shown in Fig. 1.1b and on the mechanical properties of the materials on both sides of the interface. The in-plane displacement functions of both materials are given by

$$\begin{aligned}
{}_kU_1^{(1)} &= {}_kc_1^* \sum_{s=1}^{2}\sum_{t=1}^{2} (-1)^{s+t}\ {}_k\widetilde{N}_{st}\ {}_kQ_s \left({}_kN_{st}^*\,\widetilde{D} + \beta_s^{*(k)}\right) \\
{}_kU_1^{(2)} &= {}_kc_1^* \sum_{s=1}^{2}\sum_{t=1}^{2} (-1)^{s}\ {}_k\widetilde{N}_{st}\ {}_kQ_s \left({}_kn_{st}^*\,\widetilde{D} + {}_kM_{st}^*\,\beta_s^{*(k)}\right) \\
{}_kU_2^{(1)} &= {}_kc_1^* \sum_{s=1}^{2}\sum_{t=1}^{2} (-1)^{s}\ {}_k\widetilde{N}_{st}\ {}_kQ_{s+2} \left[\beta_s{}^{(k)}\right]^{-1} \left({}_kM_{st}^*\,\widetilde{D} + {}_kn_{st}^*\,\beta_s{}^{*(k)}\right) \\
{}_kU_2^{(2)} &= -{}_kc_1^* \sum_{s=1}^{2}\sum_{t=1}^{2} (-1)^{s+t}\ {}_k\widetilde{N}_{st}\ {}_kQ_{s+2} \left[\beta_s{}^{(k)}\right]^{-1} \left(\widetilde{D} + {}_kN_{st}^*\,\beta_s^{*(k)}\right)
\end{aligned} \tag{2.66}$$

where $\widetilde{D}$ is given by means of two diagonal members of the matrix $\mathbf{D}$ as

$$\widetilde{D} = \sqrt{\frac{D_{22}}{D_{11}}}. \tag{2.67}$$

The auxiliary functions within eqs. (2.66) for $s = 1, 2, 3$ are defined as

$$\begin{aligned}
{}_kB_s = \cos^2\theta + [\beta_s^{(k)}]^2 \sin^2\theta, \qquad {}_k\varphi_s = \arg\left(\cos\theta + i\,\beta_s^{(k)} \sin\theta\right), \\
{}_kn_{s1} = \cos\frac{{}_k\varphi_s}{2}, \qquad {}_kn_{s2} = \sin\frac{{}_k\varphi_s}{2},
\end{aligned} \tag{2.68}$$

whereas, for $s, t = 1, 2$ they are given by

$$\begin{aligned}
{}_kc_s^* &= \frac{2\left[\frac{1}{2}(1+4\varepsilon^2)\right]^{s-1}}{(\beta_1^{(k)} - \beta_2^{(k)})(1+4\varepsilon^2)\cosh\pi\varepsilon}, & {}_km_s &= \frac{\varepsilon}{2}\ln\,{}_kB_s, \\
{}_kQ_s &= -s_{12}^{\prime(k)} + \left[\beta_s^{(k)}\right]^2 s_{11}^{\prime(k)}, & {}_kQ_{s+2} &= s_{22}^{\prime(k)} - \left[\beta_s^{(k)}\right]^2 s_{12}^{\prime(k)}, \\
{}_kN_{s1} &= \cosh\left[\varepsilon(\pi + (-1)^k\,{}_k\varphi_s)\right], & {}_kN_{s2} &= \sinh\left[\varepsilon(\pi + (-1)^k\,{}_k\varphi_s)\right], \\
{}_kM_{s1} &= {}_kM_{s3} + 2\varepsilon\,{}_kM_{s4}, & {}_kM_{s2} &= {}_kM_{s4} - 2\varepsilon\,{}_kM_{s3}, \qquad {}_kM_{s3} = \cos\,{}_km_s, \\
{}_kM_{s4} &= \sin\,{}_km_s, & {}_kM_{st}^* &= {}_kM_{s1}\,{}_kM_{s2}\,{}_kM_{st}^{-2}, \qquad \beta_s^{*(k)} = \beta_1^{(k)}\,\beta_2^{(k)}\,\beta_s^{(k)^{-1}} \\
{}_kN_{st}^* &= {}_kN_{s1}\,{}_kN_{s2}\,{}_kN_{st}^{-2}, & {}_kn_{st}^* &= {}_kn_{s1}\,{}_kn_{s2}\,{}_kn_{st}^{-2}, \quad {}_k\widetilde{N}_{st} = {}_kn_{st}\,{}_kN_{st}\,{}_kM_{st}\,{}_kB_s^{\frac{1}{4}},
\end{aligned} \tag{2.69}$$

The out-of-plane displacement function ${}_kU_3^{III}$ is given by

$$\begin{aligned}
{}_kU_3^{III} &= 2s_{44}^{\prime(k)} \left[\beta_3^{(k)}\right]^{-1}\ {}_kB_3^{\frac{1}{4}}\ {}_kn_{32} \\
&= 2\sqrt{s_{44}^{\prime(k)} s_{55}^{\prime(k)}}\ {}_kB_3^{\frac{1}{4}}\ {}_kn_{32}.
\end{aligned} \tag{2.70}$$

The first term of the asymptotic solution for the stress components is given in eqs. (2.57) and (2.58). The in-plane stress functions ${}_k\Sigma^{(1)}_{\alpha\beta}(\theta)$ and ${}_k\Sigma^{(2)}_{\alpha\beta}(\theta)$ may be written as

$$\begin{aligned}
{}_k\Sigma^{(1)}_{11} &= -\,{}_kc^*_2 \sum_{s=1}^{2}\sum_{t=1}^{2} (-1)^s\, {}_k\widetilde{N}_{st}\, {}_kB_s^{-\frac{1}{2}} \left[\beta_s^{(k)}\right]^2 \left({}_kN^*_{st}\, \widetilde{D} + \beta_s^{*(k)} \right) \\
{}_k\Sigma^{(2)}_{11} &= {}_kc^*_2 \sum_{s=1}^{2}\sum_{t=1}^{2} (-1)^{s+t}\, {}_k\widetilde{N}_{st}\, {}_kB_s^{-\frac{1}{2}} \left[\beta_s^{(k)}\right]^2 \left({}_kn^*_{st}\, \widetilde{D} - {}_kM^*_{st}\, \beta_s^{*(k)} \right) \\
{}_k\Sigma^{(1)}_{12} &= -\,{}_kc^*_2 \sum_{s=1}^{2}\sum_{t=1}^{2} (-1)^{s+t}\, {}_k\widetilde{N}_{st}\, {}_kB_s^{-\frac{1}{2}} \beta_s^{(k)} \left({}_kM^*_{st}\, \widetilde{D} - {}_kn^*_{st}\, \beta_s^{*(k)} \right) \\
{}_k\Sigma^{(2)}_{12} &= {}_kc^*_2 \sum_{s=1}^{2}\sum_{t=1}^{2} (-1)^{s}\, {}_k\widetilde{N}_{st}\, {}_kB_s^{-\frac{1}{2}} \beta_s^{(k)} \left(\widetilde{D} + {}_kN^*_{st}\, \beta_s^{*(k)} \right) \\
{}_k\Sigma^{(1)}_{22} &= {}_kc^*_2 \sum_{s=1}^{2}\sum_{t=1}^{2} (-1)^{s}\, {}_k\widetilde{N}_{st}\, {}_kB_s^{-\frac{1}{2}} \left({}_kN^*_{st}\, \widetilde{D} + \beta_s^{*(k)} \right) \\
{}_k\Sigma^{(2)}_{22} &= -\,{}_kc^*_2 \sum_{s=1}^{2}\sum_{t=1}^{2} (-1)^{s+t}\, {}_k\widetilde{N}_{st}\, {}_kB_s^{-\frac{1}{2}} \left({}_kn^*_{st}\, \widetilde{D} - {}_kM^*_{st}\, \beta_s^{*(k)} \right)
\end{aligned} \tag{2.71}$$

where all functions are defined in eqs. (2.67) to (2.69).

Again, the out-of-plane stress functions are much simpler and given by

$$\begin{aligned}
{}_k\Sigma^{III}_{31} &= -\beta_3^{(k)}\, {}_kB_3^{-\frac{1}{4}}\, {}_kn_{32} \\
&= -\sqrt{\frac{s'^{(k)}_{44}}{s'^{(k)}_{55}}}\, {}_kB_3^{-\frac{1}{4}}\, {}_kn_{32}, \\
{}_k\Sigma^{III}_{32} &= {}_kB_3^{-\frac{1}{4}}\, {}_kn_{31}.
\end{aligned} \tag{2.72}$$

It may be noted that in Banks-Sills et al. (2013), where the same interface is considered, the expressions for the stress functions, denoted by ${}_k\Sigma^{(1)}_{\alpha\beta}(\theta)$, ${}_k\Sigma^{(2)}_{\alpha\beta}(\theta)$ and ${}_k\Sigma^{III}_{3\beta}(\theta)$ in eqs. (2.57) and (2.58), as well as for the displacement functions, denoted by ${}_kU^{(1)}_{\alpha}(\theta)$, ${}_kU^{(2)}_{\alpha}(\theta)$ and ${}_kU^{(III)}_{3}(\theta)$ in eqs. (2.64) and (2.65), are also presented within the Appendices of that study. To use them, further algebra is required. Here, those stress and displacement functions, as well as other expressions, which were also required in developing the asymptotic displacement and stress fields, are given explicitly in a much simpler form.

The first term of the asymptotic displacement field given in eqs. (2.64) and (2.65) is used in the M-integral and displacement extrapolation methods which are presented in Chapter 3.

Chapter 3

Methods of Calculating Stress Intensity Factors

There are several methods to obtain all stress intensity factors separately, meaning calculating the contribution of each factor K_1, K_2 and K_{III} to the overall stress. Once the first terms of the asymptotic stress and displacement fields in the vicinity of a delamination front were determined for a specific interface, the extraction of each stress intensity factor is possible. In this chapter two methods for extracting the stress intensity factors are presented. The straightforward method is based upon displacement extrapolation and is being presented in Section 3.1. The second method is being presented in Section 3.2. It is based on conservative integrals and therefore it is more complicate and accurate. In general, both methods are applicable for every interface delamination. In this research the following expressions are valid only for the particular case of an interface delamination between two tetragonal anisotropic elastic materials where the interface is constructed of $0°/90°$ and a $+45°/-45°$ balanced plain weaves as shown in Fig. 1.1b.

3.1 Displacement extrapolation

While using the same coordinate system at the crack tip, as shown in Fig. 1.1b, the relative displacement of the crack faces or the "jump" in the crack face displacements within the neighborhood of a delamination front may be given by

$$\Delta u_i \equiv u_i^{(1)}(r, \theta = \pi) - u_i^{(2)}(r, \theta = -\pi). \tag{3.1}$$

Here the superscripts (1) and (2) represent the upper and lower materials, respectively, and u_i is the displacement in the x_i direction for $i = 1, 2, 3$.

Substitution of $\theta = \pi$ and $\theta = -\pi$ for the upper and lower materials, respectively, in the oscillatory singularity displacement expressions given in eq. $(2.50)_1$ will result in the following reduced expressions

$$\begin{aligned} \mathbf{u}_{os}^{(1)}\Big|_{\theta=\pi} &= 2\sqrt{r}\,\mathbf{L}_1^{-1}\Re\left\{r^{i\varepsilon}\mathbf{d}\right\}, \\ \mathbf{u}_{os}^{(2)}\Big|_{\theta=-\pi} &= -2\sqrt{r}\,\mathbf{L}_2^{-1}\Re\left\{r^{i\varepsilon}\mathbf{d}\right\}, \end{aligned} \tag{3.2}$$

where $\mathbf{L}_k^{-1}$ is defined as

$$\mathbf{L}_k^{-1} = \Im\left\{-\mathbf{A}_k\mathbf{B}_k^{-1}\right\}, \tag{3.3}$$

and explicitly presented in eq. (2.18).

Substitution of $\theta = \pi$ and $\theta = -\pi$ for the upper and lower materials, respectively, in the regular square-root singularity displacement expressions given in eq. $(2.51)_1$ will result, again, in reduced expressions given by

$$\begin{aligned} \mathbf{u}_{s}^{(1)}\Big|_{\theta=\pi} &= \sqrt{r}\,\mathbf{L}_1^{-1}\mathbf{d}^*, \\ \mathbf{u}_{s}^{(2)}\Big|_{\theta=-\pi} &= -\sqrt{r}\,\mathbf{L}_2^{-1}\mathbf{d}^*. \end{aligned} \tag{3.4}$$

Following eq. (3.1) the oscillatory singularity crack face displacement "jump" vector is given by

$$\Delta\mathbf{u}_{os} = 2\sqrt{r}\,\mathbf{D}\Re\left\{r^{i\varepsilon}\mathbf{d}\right\}, \tag{3.5}$$

whereas the regular square root singularity crack face displacement "jump" vector is given by

$$\Delta\mathbf{u}_{s} = \sqrt{r}\,\mathbf{D}\mathbf{d}^*. \tag{3.6}$$

Substitution of $\mathbf{D}$ and $\mathbf{d}$ as given in eq. $(2.19)_2$ and eq. $(2.63)_1$, respectively, into eq. (3.5) will lead to the following representation of the oscillatory singularity crack face displacement "jump" vector

$$\left\{\begin{array}{c} \Delta u_{1os} \\ \Delta u_{2os} \\ \Delta u_{3os} \end{array}\right\} = \sqrt{\frac{2r}{\pi}}\frac{D_{22}}{\cosh\pi\varepsilon}\left\{\begin{array}{c} -\sqrt{\dfrac{D_{11}}{D_{22}}}\Im\left[\dfrac{Kr^{i\varepsilon}}{(1+2i\varepsilon)}\right] \\ \Re\left[\dfrac{Kr^{i\varepsilon}}{(1+2i\varepsilon)}\right] \\ 0 \end{array}\right\}. \tag{3.7}$$

The following representation of the regular square root singularity crack face displacement "jump" vector is obtained by substituting $\mathbf{D}$ and $\mathbf{d}^*$ as given in eq. $(2.19)_2$ and eq. $(2.63)_2$, respectively, into eq. (3.6)

$$\left\{ \begin{array}{c} \Delta u_{1s} \\ \Delta u_{2s} \\ \Delta u_{3s} \end{array} \right\} = \sqrt{\frac{2r}{\pi}} D_{33} K_{III} \left\{ \begin{array}{c} 0 \\ 0 \\ 1 \end{array} \right\}. \tag{3.8}$$

At this stage, one may extract the local stress intensity factors K_1^*, K_2^* and K_{III}^* from their relations with the values of the crack faces displacement jumps. Generally, these values may obtained via finite element model analyses or digital imaging of test specimens. The local in-plane complex stress intensity factor components K_1^* and K_2^* are related to the in-plane displacement jumps by

$$\left\{ \begin{array}{c} K_1^*(r) \\ K_2^*(r) \end{array} \right\} = \sqrt{\frac{\pi}{2r}} \frac{\cosh \pi\varepsilon}{D_{22}} \left[\begin{array}{cc} \sqrt{\frac{D_{22}}{D_{11}}} \Im \left[r^{-i\varepsilon}(1+2i\varepsilon) \right] & \Re \left[r^{-i\varepsilon}(1+2i\varepsilon) \right] \\ -\sqrt{\frac{D_{22}}{D_{11}}} \Re \left[r^{-i\varepsilon}(1+2i\varepsilon) \right] & \Im \left[r^{-i\varepsilon}(1+2i\varepsilon) \right] \end{array} \right] \left\{ \begin{array}{c} \Delta u_1(r)_{os} \\ \Delta u_2(r)_{os} \end{array} \right\} \tag{3.9}$$

whereas the local out-of-plane stress intensity factor component K_{III}^* is related to the out-of-plane displacement jump by

$$K_{III}^*(r) = \sqrt{\frac{\pi}{2r}} \frac{\Delta u_3(r)_s}{D_{33}}. \tag{3.10}$$

3.2 M-integral

As mentioned in Section 1.3, the conservative mechanical M-integral was first introduced by Chen and Shield (1977) for cracks within a linear elastic, homogeneous and isotropic medium and was extended for interface cracks between two linear elastic, homogeneous and isotropic materials as a line integral by Wang and Yau (1981). Since the M-integral method was found to produce accurate results for the stress intensity factors, it was implemented by others and was further extended to account for different cases of interest. It was extended for bimaterial interface cracks in two dimensions under thermal loads by Banks-Sills and Dolev (2004). It was further extended for three-dimensional problems for both mechanical (see Freed and Banks-Sills, 2005) and thermal residual stresses (see Banks-Sills et al., 2006). The moving least-square method was employed by Nagai et al. (2007) to calculate stress intensity factors in three-dimensional interface crack problems by means of the M-integral. Following the moving least-square, each term of the M-integral is approximated by solely employing the nodal point displacements obtained via FEM in the location where integration is performed. This work was extended by Nagai

Table 3.1: Stress intensity factors for the three-dimensional auxiliary solutions.

solution	K_1	K_2	K_{III}
$2a$	1	0	0
$2b$	0	1	0
$2c$	0	0	1

et al. (2012) for three-dimensional problems involving thermal residual stresses and was further extended by Nagai et al. (2013) for three-dimensional problems, in which the FE mesh is modeled with tetrahedral elements.

The discussion below follows the presentation in Banks-Sills et al. (2013), for the investigated interface between two tetragonal anisotropic elastic materials subjected to a mechanical applied load. For completeness, it is presented once again here. The three-dimensional M-integral is given by

$$M_N^{(1,2\alpha)} = \frac{1}{A_1}\sum_{k=1}^{2}\int_{V_k}\left\{ {}_k\sigma_{ij}^{(1)}\frac{\partial_k u_i^{(2\alpha)}}{\partial x_1} + {}_k\sigma_{ij}^{(2\alpha)}\frac{\partial_k u_i^{(1)}}{\partial x_1} - {}_kW^{(1,2\alpha)}\delta_{1j}\right\}\frac{\partial q_1}{\partial x_j}\,dV, \qquad (3.11)$$

where $k = 1, 2$ represents the upper and lower materials, respectively. The superscript (1) represents the solution being sought while the superscript (2α) for $\alpha = a, b, c$ represents the auxiliary solutions, which consist of three independent (separate) components, each component with its particular stress intensity factor, as detailed in Table 3.1. These stress intensity factors are in turn substituted into the auxiliary solutions which come from the first term of the asymptotic solution, as presented in Section 2.2. The volume V_k of finite elements, where the integration is performed, is one element thick along the model thickness and δ_{ij} is the Kronecker delta. The subscript N denotes the element along the delamination or crack front, as shown in Fig. 3.1, in which the crack front is along the x_3-axis. The area A_1 is given by

$$A_1 = \int_0^{L_N} \ell_1^{(N)}(x_3)dx_3\ , \qquad (3.12)$$

where L_N is the length of the element and $\ell_1^{(N)}(x_3)$ is a parabolic virtual crack extension, also illustrated in Fig. 3.1. It should be noted that the value of $M_N^{(1,2\alpha)}$ is an average value of $M^{(1,2\alpha)}$ along the delamination front of element N.

In eq. (3.11), the mutual strain energy density ${}_kW^{(1,2\alpha)}$ of the two solutions in the upper and lower materials is given by

$${}_kW^{(1,2\alpha)} = {}_k\sigma_{ij}^{(1)}\ {}_k\varepsilon_{ij}^{(2\alpha)} = {}_k\sigma_{ij}^{(2\alpha)}\ {}_k\varepsilon_{ij}^{(1)}\ , \qquad (3.13)$$

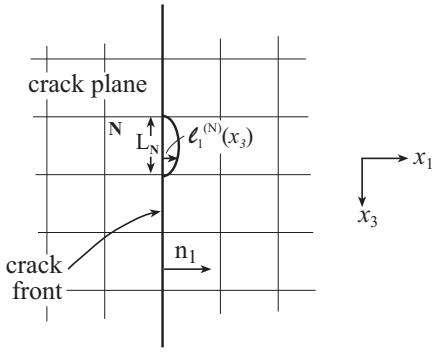

Figure 3.1: Illustration of a finite element mesh along a delamination/crack front and a virtual crack extension $\ell_1^{(N)}(x_3)$.

whereas the function q_1 is a normalized virtual crack extension given by

$$q_1 \;=\; \sum_{i=1}^{20} N_i(\xi,\eta,\zeta)\, q_{1i} \;. \tag{3.14}$$

In eq. (3.14), $N_i(\xi,\eta,\zeta)$ are the shape functions of a twenty noded isoparametric, brick element and q_{1i} is a vector which determines the virtual displacement of the element nodal points, as detailed in Freed and Banks-Sills (2005). The expression in eq. (3.11) is also applicable for two general anisotropic materials.

The interaction energy may also be expressed by means of the stress intensity factors of both solutions (1) and (2α). From eq. (1.17), it may be shown that

$$M_N^{(1,2\alpha)} = \frac{2}{H_1}\left(K_1^{(1)}K_1^{(2\alpha)} + K_2^{(1)}K_2^{(2\alpha)}\right) + \frac{2}{H_2}\,K_{III}^{(1)}K_{III}^{(2\alpha)} \;, \tag{3.15}$$

where

$$\frac{1}{H_1} = \frac{D_{22}}{4\cosh\pi\varepsilon} \;, \qquad \frac{1}{H_2} = \frac{D_{33}}{4} \;. \tag{3.16}$$

The oscillatory parameter ε is defined in eq. (2.46), whereas D_{22} and D_{33} are two diagonal members of the matrix $\mathbf{D}$ given in eq. (2.20).

Substitution of the auxiliary solutions (2α) according to Table 3.1 into eqs. (3.11) and (3.15) results in the following separate expressions for the stress intensity factors of the desired solution (1)

$$K_1^{(1)} \;=\; \frac{H_1}{2A_1}\sum_{k=1}^{2}\int_{V_k}\left[{}_k\sigma_{ij}^{(1)}\,\frac{\partial_k u_i^{(2a)}}{\partial x_1} \;+\; {}_k\sigma_{ij}^{(2a)}\,\frac{\partial_k u_i^{(1)}}{\partial x_1} \;-\; {}_kW^{(1,2a)}\delta_{1j}\right]\frac{\partial q_1}{\partial x_j}\,dV \;, \tag{3.17}$$

$$K_2^{(1)} \;=\; \frac{H_1}{2A_1}\sum_{k=1}^{2}\int_{V_k}\left[{}_k\sigma_{ij}^{(1)}\,\frac{\partial_k u_i^{(2b)}}{\partial x_1} \;+\; {}_k\sigma_{ij}^{(2b)}\,\frac{\partial_k u_i^{(1)}}{\partial x_1} \;-\; {}_kW^{(1,2b)}\delta_{1j}\right]\frac{\partial q_1}{\partial x_j}\,dV \tag{3.18}$$

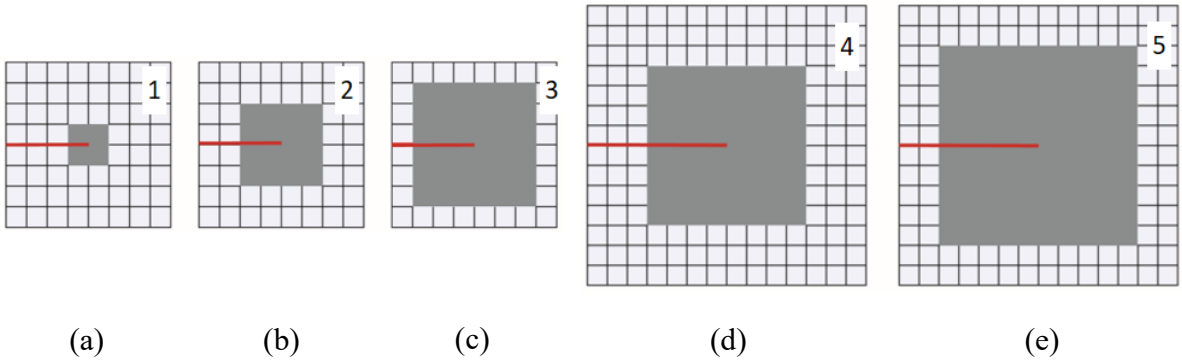

Figure 3.2: Two-dimensional cross-sections of integration domains; each domain is one element thick along the delamination/crack front.

and

$$K_{III}^{(1)} = \frac{H_2}{2A_1} \sum_{k=1}^{2} \int_{V_k} \left[{}_k\sigma_{ij}^{(1)} \frac{\partial_k u_i^{(2c)}}{\partial x_1} + {}_k\sigma_{ij}^{(2c)} \frac{\partial_k u_i^{(1)}}{\partial x_1} - {}_kW^{(1,2c)} \delta_{1j} \right] \frac{\partial q_1}{\partial x_j} \, dV \, . \tag{3.19}$$

Software was written to carry out the calculation of these integrals. Use of the FE method to determine the displacement field of the solution being sought (1) and the M-integral allow extraction of the stress intensity factors for the investigated interface. An illustration of five representative V_k volumes (domains), where the integration is performed, is presented in Fig. 3.2. A square-root singularity is imposed upon elements with nodal points that intersect the delamination front, by means of a quarter-point distance definition for nodes that are adjacent to the delamination front.

It may be pointed out that thermal residual stresses or strains generally occur during the manufacturing process of a laminate composite plate (mostly at the curing stage). Here, the small residual strains resulting from the mismatch between the carbon fiber and epoxy matrix are neglected. For the investigated MD balanced plain woven interface (0°/90° // +45°/-45°), there is no mismatch in the thermal properties between the laminate composite plies, so that the residual thermal strains are the same in each ply. Hence, the residual stresses of this laminate are minimal.

3.3 Benchmark problem

The developed methods for stress intensity factor extraction, DE in Section 3.1 and the three-dimensional conservative M-integral in Section 3.2, are validated in this section. To this end, three benchmark problems using the known asymptotic solutions in eqs. (2.64)

and (2.65) with the stress intensity factors in Table 3.1 were solved by performing numerical analyses. The FE model of a disk with an edge delamination was constructed in ADINA (Bathe, 2011), as presented in Fig. 3.3. The dimensions of the model are

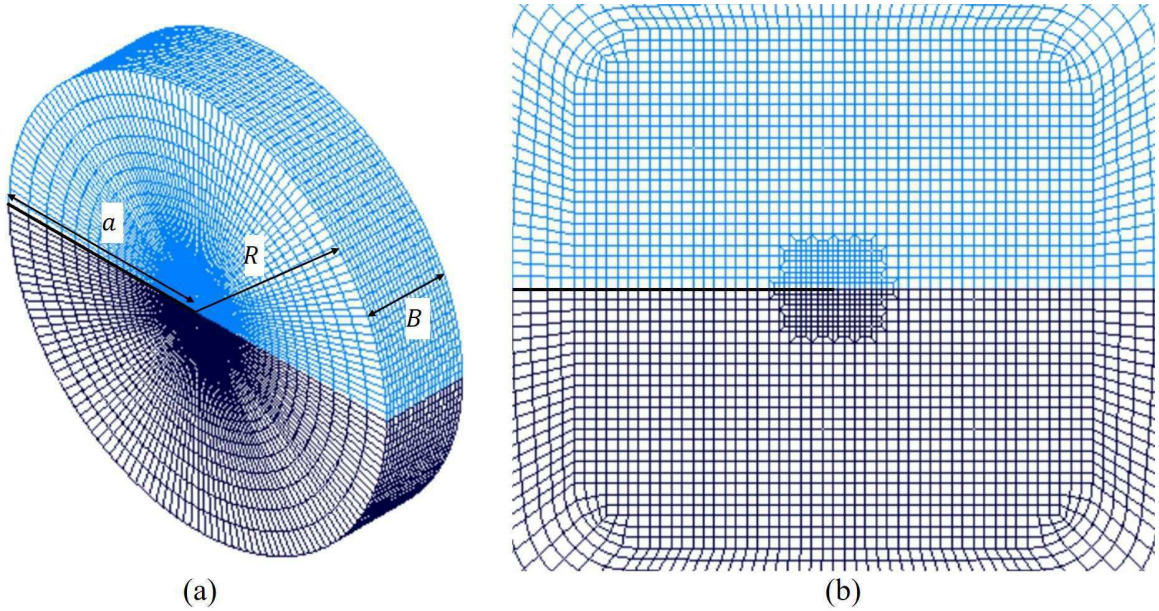

Figure 3.3: FE model used to analyze each of the benchmark problems containing 131,360 twenty noded isoparametric, brick elements and 947,821 nodal points. (a) Isometric-view of the mesh and (b) detailed front-view of the delamination tip region.

$R = 20$ m, $R/a = 1$, $B/a = 0.4$, where a is the delamination length, and R and B are the radius and thickness of the disk, respectively. The FE model contains 131,360 twenty noded isoparametric, brick elements and 947,821 nodal points. Use of quarter-point elements was made in elements with edges along the delamination front, in order to model the square-root singularity next to the delamination tip. It should be noted that the in-plane stresses have a square-root, oscillatory singularity. Hence, the oscillatory part of the singularity is not modeled. In addition, the dimensions of the elements in the vicinity of the delamination tip were set to $0.055 \times 0.055 \times 0.4$ m^3, so that an in-plane aspect ratio of 1×1 was obtained. A maximum in-plane aspect ratio of 1×4 was maintained throughout the model. The material properties used to model the upper material are presented in Table 2.1. The properties of the lower material were obtained by rotating the properties of the upper material about the x_2-axis (shown in Fig. 1.1) by 45°. Displacement boundary conditions were applied to the outer surfaces of the disk maintaining traction free conditions on the delamination faces. For each benchmark problem, the first term of the asymptotic displacement field in eqs. (2.64) and (2.65) were used with the corresponding stress intensity factors, as detailed in Table 3.1. Then, the FE model was analyzed to obtain a displacement field throughout the model.

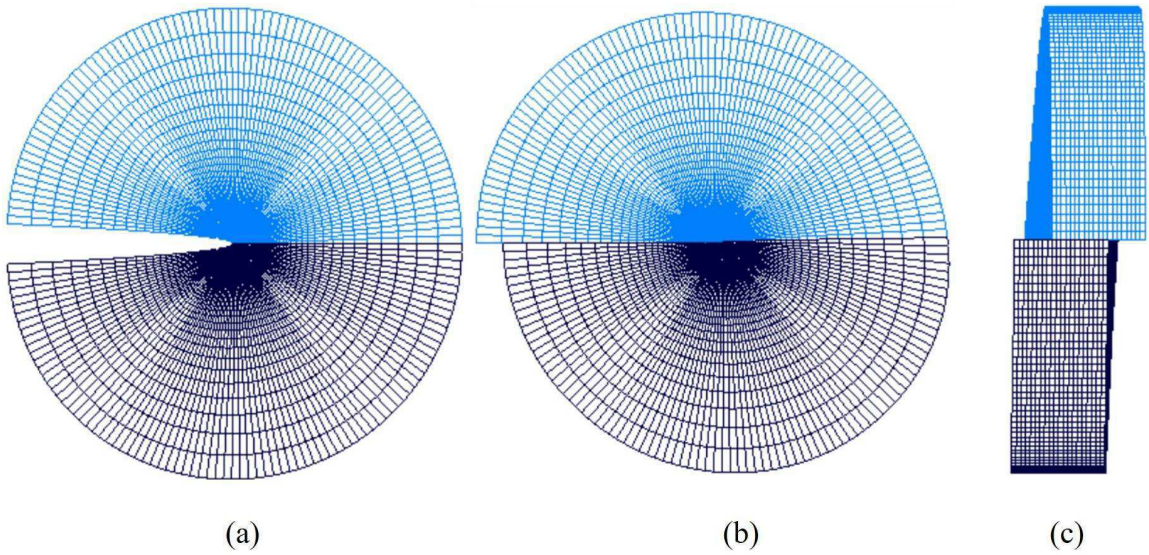

Figure 3.4: Deformed mesh of the three benchmark problems: (a) $K_1 = 1$, $K_2 = 0$, $K_{III} = 0$; (b) $K_1 = 0$, $K_2 = 1$, $K_{III} = 0$; (c) $K_1 = 0$, $K_2 = 0$, $K_{III} = 1$.

The deformed models of the three cases detailed in Table 3.1 are presented in Fig. 3.4. The obtained displacements were employed in the DE and the M-integral methods. In the DE method, the jump in the displacements of the nodes of the delamination faces (upper and lower, respectively), which were aligned to the same ray of nodes (emanating from the same location along the delamination front and orthogonal to it) across the model thickness, was used to evaluate the local stress intensity factors in eqs. (3.9) and (3.10). The value of each global stress intensity factor was determined by performing a best three point line fitting for adjacent points which are located in the vicinity of the delamination front. The three point line with a coefficient of determination R^2 closest to unity was used to determine the value of the global stress intensity factor. In calculating the M-integral, the elements surrounding the delamination front are employed. One slice of elements throughout the model thickness is applied to evaluate the $K_m^{(1)}$ $(m = 1, 2, III)$ values given in eqs. (3.17) to (3.19).

The obtained stress intensity factors for the three benchmark problems, which were calculated by means of DE and the M-integral in four domains, are presented in Figs. 3.5 through 3.7 as a function of the normalized coordinate x_3/B, which is located along the delamination front as shown in Fig. 3.1. As expected, it may be observed that for the first and second benchmark problems presented in Figs. 3.5 and 3.6, respectively, K_1 and K_2 are symmetric about the mid-surface $x_3/B = 0.5$ while K_{III} is anti-symmetric. As for the third benchmark problem presented in Fig. 3.7, it may be observed that K_{III} is symmetric about the mid-surface $x_3/B = 0.5$ while K_1 and K_2 are anti-symmetric. It should be noted that for the three benchmark problems, the DE evaluated stress intensity

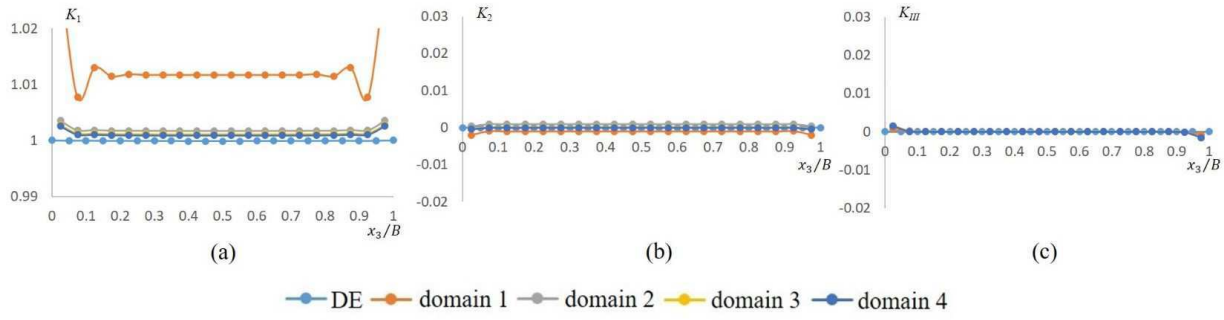

Figure 3.5: Results of the stress intensity factors for the first benchmark problem: $K_1 = 1$, $K_2 = 0$, $K_{III} = 0$; (a) K_1, (b) K_2 and (c) K_{III}.

factors were found to be more accurate than the stress intensity factors evaluated by the M-integral, especially at the outer surfaces of the FE model where $x_3/B \to 0, 1$. This typically occurs for benchmark problems. It will not be the case for actual problems.

Comparison of the calculated and exact stress intensity factor values (analytic solution) was quantified by means of a percent error, which is given by

$$\text{error}(\%) = \frac{K_m^{(1)} - K_m^{(e)}}{K_{\max}^{(e)}} \times 100 \tag{3.20}$$

where $K_m^{(1)}$, $m = 1, 2, III$, is the stress intensity factor calculated by means of the M-integral, $K_m^{(e)}$, $m = 1, 2, III$, is the analytic solution and $K_{\max}^{(e)}$ in the denominator is the maximum value of the analytic solution, which is unity.

For the first benchmark problem, the applied stress intensity factors are $K_1 = 1$, $K_2 = 0$ and $K_{III} = 0$. While neglecting edge effects in Fig. 3.5a, it may be seen that the value of K_1 obtained by integration performed in domain 1 (quarter-point elements next to the delamination front) is inaccurate (an error of 1% at the mid-surface) as a result of inaccurate representation of the fields. The values of K_1 obtained by integration performed in domains 3 and 4 almost converged to unity, with an error of 0.1% at the mid-surface and 0.3% at the outer surfaces of the model. The values obtained for K_2 and K_{III} in domains 3 and 4 are $O(10^{-4})$ to $O(10^{-7})$ except near the outer surfaces of the model. Tabulated results of the first benchmark problem are presented in Appendix D in Tables D.1 through D.3.

For the second benchmark problem, the applied stress intensity factors are $K_1 = 0$, $K_2 = 1$ and $K_{III} = 0$. While neglecting edge effects in Fig. 3.6b, it may be seen that the obtained results for K_2 from domain 1 are poor (an error of -21% at the mid-surface). In domain 2, the error decreased to -0.6% at the mid-surface of the model. The values of K_2 obtained by integration performed in domains 3 and 4 almost converged to unity, with an error

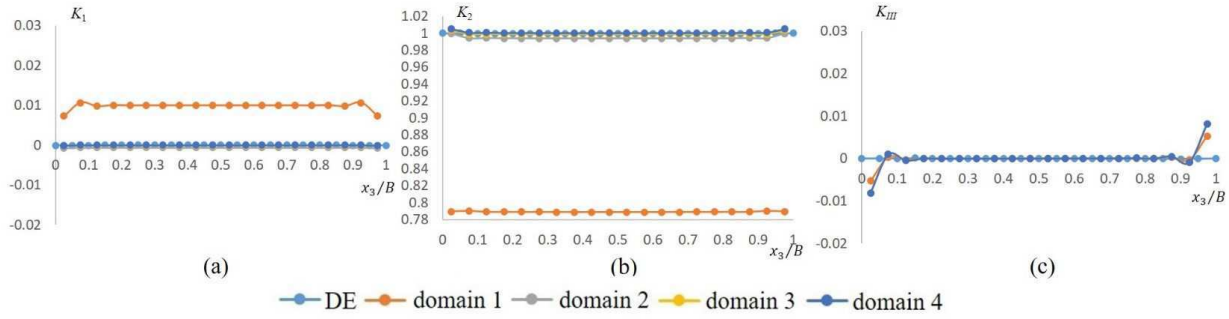

Figure 3.6: Results of the stress intensity factors for the second benchmark problem: $K_1 = 0$, $K_2 = 1$, $K_{III} = 0$; (a) K_1, (b) K_2 and (c) K_{III}.

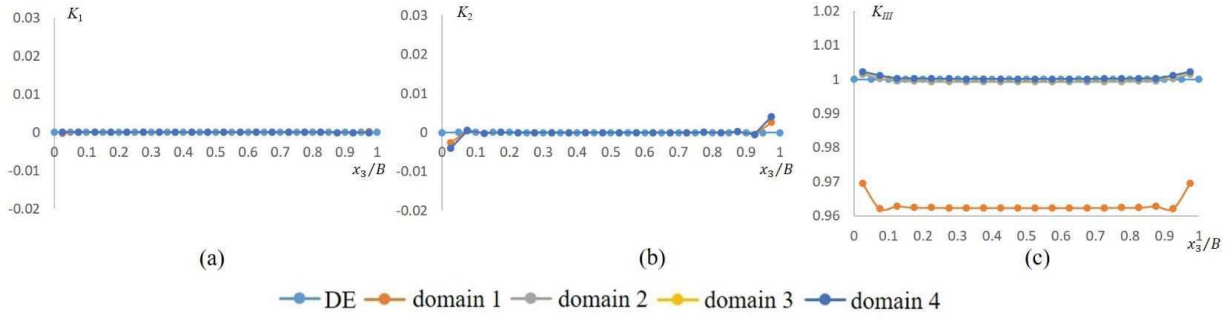

Figure 3.7: Results of the stress intensity factors for the third benchmark problem: $K_1 = 0$, $K_2 = 0$, $K_{III} = 1$; (a) K_1, (b) K_2 and (c) K_{III}.

of 0.03% at the mid-surface and 0.5% at the outer surfaces of the model, so that path independence as well as convergence to unity were validated. For K_1 and K_{III}, in domain 1 the maximum error was found to be approximately 1% and 0.5%, respectively. The values obtained for K_1 and K_{III} in domains 3 and 4 are $O(10^{-5})$ to $O(10^{-6})$ except near the outer surfaces of the model. Tabulated results of the second benchmark problem are presented in Appendix D in Tables D.4 through D.6.

In the third benchmark problem, K_{III} is the dominant stress intensity factor. While neglecting edge effects in Fig. 3.7c, it may be seen that the obtained results for K_{III} in domain 1 are inaccurate with an error of -3.8% at the mid-surface. In domain 2, the error decreased to -0.06% at the mid-surface of the model. The values of K_{III} obtained by integration performed in domains 3 and 4 almost converged to unity, with an error of 0.01% at the mid-surface and 0.2% at the outer surfaces of the model. For K_1 and K_2, in domain 1 the maximum error was found to be approximately 0.03% and 0.3%, respectively. Since both applied stress intensity factors are zero (see case 2*c* in Table 3.1),

the influence of the oscillatory singularity is mitigated. The values obtained for K_1 and K_2 in domains 3 and 4 are $O(10^{-5})$ to $O(10^{-7})$ except near the outer surfaces of the model. Tabulated results of the third benchmark problem are presented in Appendix D in Tables D.7 through D.9.

Excellent results were obtained by means of the DE and the M-integral methods (excluding the results obtained from domain 1). Also, for the M-integral, path independence as well as solution (single value) convergence were demonstrated. Hence, it may be concluded that the utilities (software) developed for both methods are valid and may be employed in this investigation.

Chapter 4

Mixed Mode Fracture Toughness

In this investigation, the BD specimen is used for measuring the mixed mode I/II interface fracture toughness $\mathcal{G}_{ic}$ for a delamination between two woven plain balanced plies. The upper ply has yarn in the $0°/90°$ directions and the lower ply has yarn in the $+45°/-45°$ directions. An illustration of a BD specimen, is presented in Fig. 4.1a. The layup of the BD, MD laminate composite strip is shown in Fig. 4.1b, in which the red and white layers represent the weave in the $0°/90°$ and $+45°/-45°$ directions, respectively. A compressive load P is applied to the BD specimen, through a stiff loading frame shown in Fig. 4.2a using an Instron loading machine (model number 8872, Bucks, UK). Test specimen dimensions were measured in the spirit of the ASTM E 399-12$^{\varepsilon 1}$ (2013) standard. The test procedure is based upon the protocol described in Section 4.1. In Section 4.2, some details about the chosen layup and the manufacturing process of the MD laminate composite plate (BD composite strip) are presented. A total of thirty tests were performed for several values of the loading angle ω shown in Fig. 4.1a to obtain a wide range of mode mixities. The measured dimensions of each specimen and test results were used while performing FE analyses. In Section 4.3, verification of FE mesh convergence, as well as, analysis and test results are presented. Finally, an energy based fracture criterion, which was established from the BD experimental data, is presented in Section 4.5.

4.1 Brazilian disk fracture test protocol

In this section the BD test protocol is presented. All BD specimens were put in a conditioning chamber (M.R.C. BTH80/-20, Holon, Israel), as recommended in ASTM Standard D5229/D5229M (2011), at $23 \pm 1°$ C and $50 \pm 3\%$ relative humidity (RH). Also, according to the ASTM Standard D5528-13 (2014), specimens should be tested at conditions of $23 \pm 3°$ C and $50 \pm 10\%$ RH. At the beginning of each test, the temperature and the RH

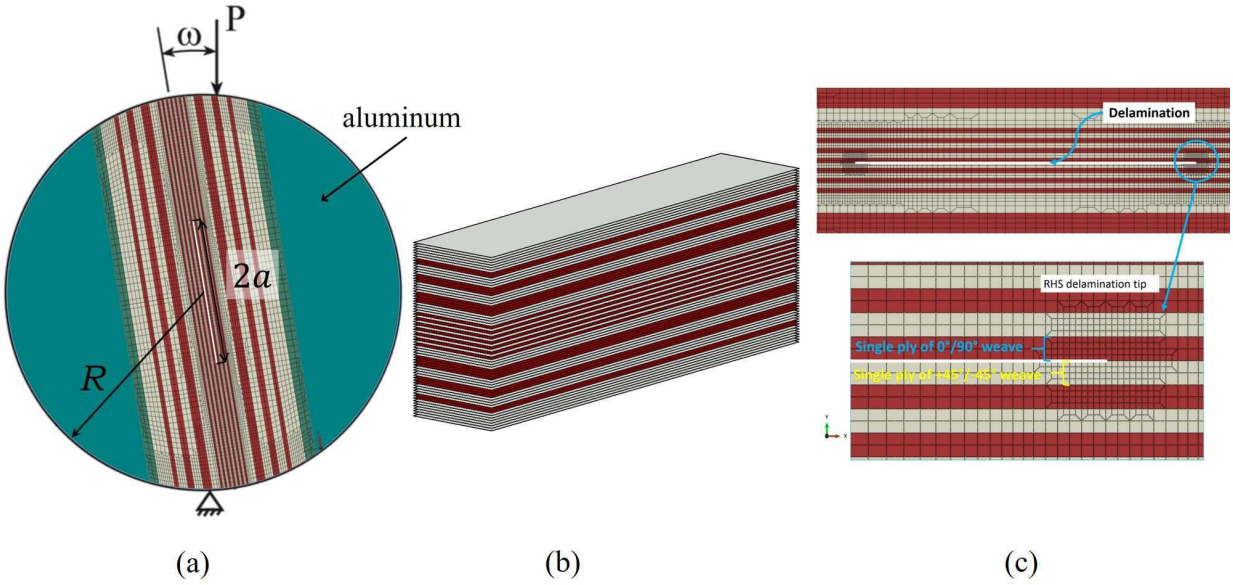

Figure 4.1: (a) Brazilian disk specimen containing a laminate composite strip with a delamination. (b) Laminate composite strip layup. (c) Delamination zone with mesh refinement about the upper delamination tip.

in the Instron work area are noted and their values are monitored continuously (every 5 min) throughout a test.

The Instron loading machine is employed with a load cell of maximum load 25 kN and a resolution of ±0.25% of the reading for a load greater than 250 N. The cross-head displacement of the Instron is increased quasi-statically at a rate of 0.5 mm/min until failure. The cross-head displacement and applied load are obtained by a computer which monitors the Instron machine. A LaVision system, consisting of computer software, a camera and a programable timing unit (PTU), is employed during the test. The LaVision monochrome CCD camera (model no. 1101396, Göttingen, Germany) has a Nikon Micro-Nikkor 105 mm f/2.8 lens, 5 MP Imager Pro SX and a resolution of 2456 × 2058 pixels. The DaVis (2015) computer software controls the LaVision camera, which is connected to the LaVision external PTU. Prior to testing, the camera is aligned using a level. Also, a specimen with millimetric paper attached to it is used to scale the images. During a test, images of the test specimen are taken at a rate of 5 Hz while the applied load is increased until fracture occurs and the test is stopped. The LaVision system enables synchronization between the load applied by the Instron machine and the images of the specimen acquired by the LaVision camera. In this way, the instantaneous applied load is displayed on the appropriate image of the test specimen.

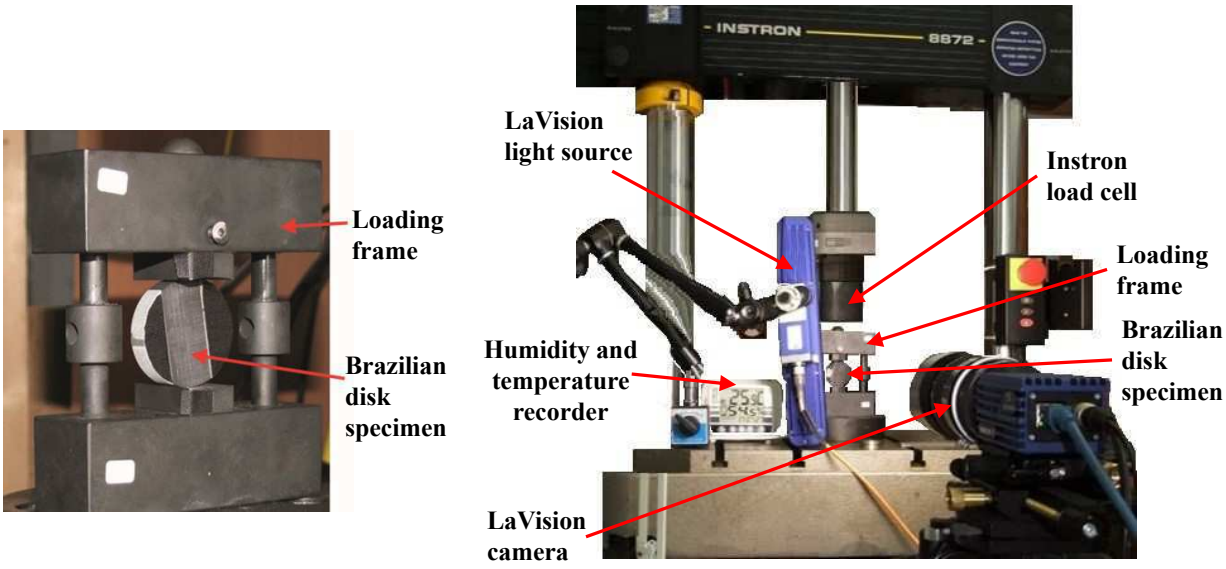

Figure 4.2: (a) Brazilian disk specimen inside a stiff metal loading frame. (b) Brazilian disk test setup.

Prior to carrying out a test, measurements of the geometric parameters of each BD specimen are made, as shown in Figs. 4.3a and 4.3b. The thickness of the BD composite strip B is measured with a digital micrometer, which has a resolution of 0.001 mm, at three locations ahead of each delamination tip, as marked with black stars in Fig. 4.3a. The diameter of the specimen $2R$ is measured four times, two measurements of the composite strip diameter and two measurements of the entire disk diameter (composed of the composite-strip and the two aluminum partial disks). The diameter measurements are made with an electronic digital caliper of resolution 0.01 mm. It should be noted that a small difference (about 0.1 mm) was found between the values of $2R$ measured from the composite strip and the entire disk, where $2R \sim 40$ mm. This difference is assumed to be negligible. The delamination length $2a$ and the horizontal distance between each delamination tip to its closest composite strip edge, shown in Fig. 4.3a and denoted by R_L and R_R, are measured with the optical mode of an Olympus Confocal Microscope (model number OLS4100; Tokyo, Japan), with a resolution of 0.16 $(\text{pixel}/\mu\text{m})^2$. The geometric parameters, $2a$, h_t and h_b (see Fig. 4.3a), are measured with an electronic digital caliper after a test is conducted when the specimen is in two parts. It should be noted that the delamination length $2a$ is actually the critical delamination length $2a_c$, which is measured three times along specimen thickness at $x_3 = B/4$, $B/2$ and $3B/4$. The critical delamination length $2a_c$ may be observed as the smooth zone of the fracture surface, which occurs from the 15 μm thick non-adhesive polytetrafluoroethylene (PTFE) film.

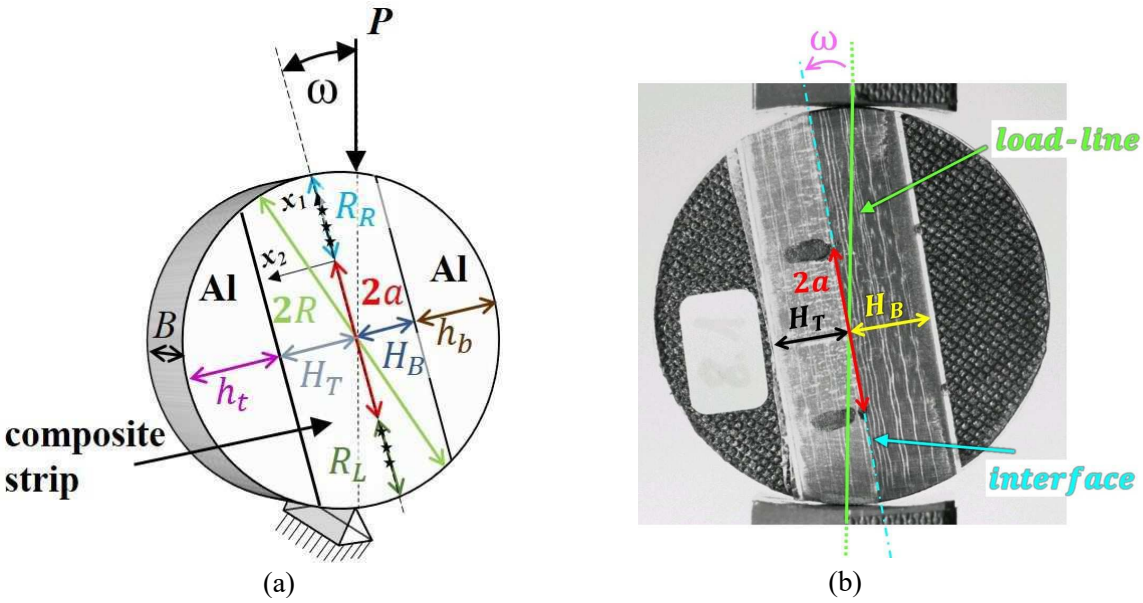

Figure 4.3: Brazilian disk specimen geometric parameters: (a) illustration of the BD specimen; (b) BD specimen inside a stiff metal loading frame before load is applied.

The height of the upper and lower sub-laminates H_T and H_B, respectively, are measured approximately at the delamination mid-point with an electronic digital caliper after a test is conducted when the specimen is in two parts. The total height of each part is measured approximately at the delamination mid-point with an electronic digital caliper, so that the height of each aluminum partial disk is obtained by subtracting the sub-laminate height from the total height of the appropriate part. The geometric parameters, R_L and R_R (see Fig. 4.3a), are measured from the end of the smooth zone of the fracture surface to its closest composite strip edge at specimen mid-thickness ($x_3 = B/2$) with an electronic digital caliper after a test is conducted when the specimen is in two parts. These dimensions, with some modifications as described below, were used in the FE model of each BD specimen.

The need of small adjustments of these measurements may be explained by considering Figs. 4.4a and 4.4b, in which the front and cross-sectional views of a typical BD specimen are schematically shown, respectively. It should be noted that the specimen was manufactured while only one side of its circular faces was aligned, as seen on the left side of Fig. 4.4b. The other side, as seen on the right side of Fig. 4.4b, had depth differences between the faces of the aluminum partial disks and the composite strip, which has a trapezoidal shaped cross-section. A typical difference of about 0.3 mm in the thickness of the upper and lower surfaces of the composite strip, which are glued to the aluminum partial disks, was detected. Thus, the specimen thickness B, which is measured along the investigated interface, averaged those differences and was used in the FE model of each

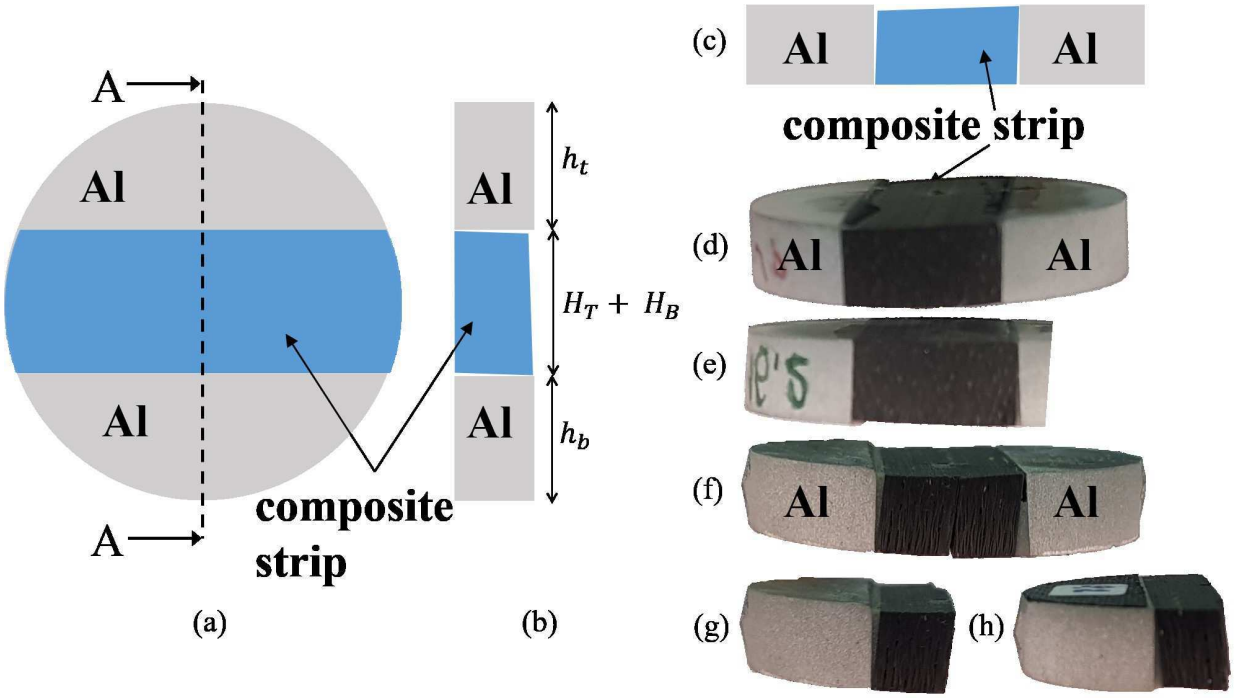

Figure 4.4: Views of a Brazilian disk specimen: (a) illustration of the front view and (b) the cross-section A-A view of a BD specimen; (c) same cross-sectional view rotated by 90°. Example of a complete BD specimen (**sp16.2**) pictured at (d) rear-to-front position, and (e) front-to-rear position. Example of a broken BD specimen (**sp5.2**) after it was tested (f) pictured at rear-to-front position; its upper broken part pictured at (g) rear-to-front position, and at (h) front-to-rear position.

BD specimen. The trapezoidal shape of the composite strip cross-section, as schematically presented in Fig. 4.4c and also emphasised with photographs of two representative specimens in Figs. 4.4d through 4.4h, is a result of the cutting procedure, in which a relatively thick rigid laminate composite-strip is cut via a water-jet machine, as described in the sequel. Also, it may be seen that the delamination faces are not parallel to the aluminum partial disks surfaces, which are glued to the composite strip upper and lower surfaces.

Since the total diameter is composed of h_t, H_T, H_B and h_b is more accurate (aluminum parts are not suspected to deform during specimen loading) the specimen diameter, denoted by $2R$, is taken as

$$2R = h_t + H_T + H_B + h_b. \tag{4.1}$$

The total length of the interface in which a delamination is introduced, denoted by D, is given by

$$D = R_R + R_L + 2a_c. \tag{4.2}$$

The parameters $2R$ and D, which are given respectively in eqs. (4.1) and (4.2), are used to scale both R_R and R_L, where their scaled values are further used in the FE model of each BD specimen. Scaling R_R and R_L helped to overcome the inaccuracies in measurements, which were encountered while using an electronic caliper to measure separately several segments along a given region, where the total length of that region should be equal to the sum of lengths from all segments. The scaled parameters are given as

$$\begin{aligned} R_L^{(sc)} &= \frac{2R(R_L + a_c)}{D} - a_c \\ R_R^{(sc)} &= \frac{2R(R_R + a_c)}{D} - a_c \end{aligned} \tag{4.3}$$

so that

$$2R = R_L^{(sc)} + 2a_c + R_R^{(sc)}. \tag{4.4}$$

The loading angle ω, as shown in Figs. 4.1a and 4.3, is measured from an image of the BD specimen located within the loading frame via the Vision Assistant (2005) software. Also, the location of the intersection between the specimen delamination and the load-line is examined to verify proper conditions of load distribution, achieved when the delamination center is located along the load-line, as shown in Fig. 4.3b. All geometric parameters, measured or scaled as described above, are used in the FE model of each BD specimen.

4.2 Materials

Prior to BD specimen manufacturing, different composite-strip layups were examined by means of FE analyses. The material properties used to model the plain woven plies with the yarn in the 0°/90°-directions are presented in Table 2.1. The properties of the ply with yarn in the +45°/-45°-directions were obtained by rotating the properties of the 0°/90° ply about the x_2-axis shown in Fig. 1.1b by 45° (Ting, 1996, pp.54-55), and are also presented in Table 2.1. A ply group or stack constructed from the same plain woven plies has the same material properties as a single ply with its total thickness the sum of thicknesses of each ply within the ply group. The layup contains 69 carbon/epoxy (G0814/913) prepreg plain woven plies in the following stacking sequence: $[(+45°/-45°)_7, (0°/90°)_2, (+45°/-45°)_4, (0°/90°)_3,\ [(+45°/-45°)_4, (0°/90°)_2]_s,$ $(0°/90°, +45°/-45°)_2, 0°/90°\ //\ +45°/-45°, (0°/90°, +45°/-45°)_3, 0°/90°,\ [(+45°/-45°)_4, (0°/90°)_2]_s, (0°/90°)_3, (+45°/-45°)_4, (0°/90°)_2, (+45°/-45°)_7]$, as shown in Fig. 4.1b. The gray stacks consist of +45°/-45° plain woven plies; the red stacks are 0°/90° plies.

Composite strips containing an artificial delamination, which were used in preparing the BD specimens, as shown in Fig. 4.1a, were cut via a water-jet machine from a composite

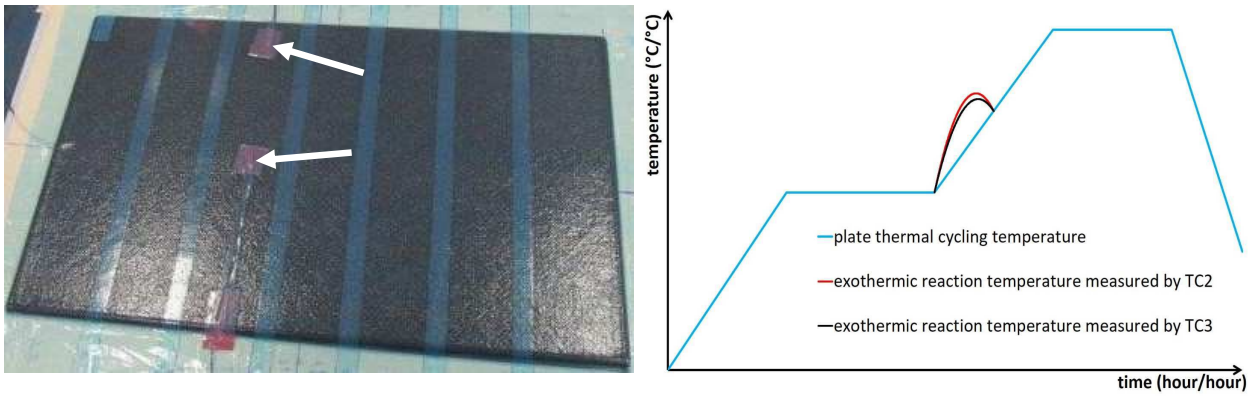

Figure 4.5: (a) Laminate composite plate during fabrication: PTFE films in blue and thermocouples marked with white arrows. (b) Autoclave thermal cycling of the laminate composite plate.

plate, which was fabricated and autoclave cured at IAI. The 300×500×15 mm^3 laminate composite plate was hand layered with 69 carbon/epoxy (G0814/913) prepreg plain woven plies, each ∼0.22 mm thick. Five thermo-couples were inserted during plate fabrication at different locations; hence, a uniform degree of cure was verified during the cure process. The initial delamination, which was set to 15 mm long, was introduced by means of a non-adhesive thin PTFE film. Only two thermocouples out of five, which were used to measure the temperature during the autoclave process, are shown in Fig. 4.5a, as well as the placement of the PTFE films. At those two thermocouples, the highest temperature was recorded during the autoclave process.

The normalized thermal cycling of the composite plate during the autoclave process is presented in Fig. 4.5b. It is normalized by means of the curing temperature of the G0814/913 carbon/epoxy prepreg and by means of the thermal cycling duration. Also shown in Fig. 4.5a are the thermocouples TC2, which is located in the center of the plate (both mid-thickness and mid-width), and TC3, which is located in the plate mid-thickness next to the plate edge. The increase in temperature is caused by the exothermic characteristic reaction of the epoxy matrix and seen in Fig. 4.5b as the red and black curves. Nevertheless, a uniform degree of cure was obtained within the composite plate, since the cure process temperature was higher than all former measured values.

A non-destructive test (NDT) was performed on the composite plate by means of the phased array inspection method. This was carried out in order to detect the PTFE films which serve as foreign objects. In this way, it was possible to cut composite strips to form the specimen shown in Fig. 4.1a.

Each composite strip was cut so that its thickness B was ∼8.1 mm; it also contained two non-adhesive PTFE films. The location of the PTFE films, which was marked on the upper surface of the composite plate while the NDT was performed, was copied to the orthogonal faces of the composite strip. Two aluminum rectangles, ∼8.1 mm thick, were glued (with 3M460 glue) above and beneath the composite strip after all faces (aluminum and composite) were cleaned with acetone. It should be noted that the glued aluminum-composite strip-aluminum assembly cross-section had a final shape as shown schematically in Fig. 4.4b, in which the trapezoidal shape of the composite strip is illustrated, so that depth differences and faces misalignments were obtained. After a glued aluminum-composite strip-aluminum assembly was prepared, two BD specimens were cut from it via a water-jet machine.

In each BD specimen, the delamination tips (PTFE ends) were detected and marked with the aid of a Carl Zeiss™ microscope (model Stemi 2000-C stereomicroscope, Göttingen, Germany). Prior to specimen testing, the location of the interface and the artificial delamination (PTFE) ends were marked with a non-structural transparent cello tape, which might be observed in Fig. 4.3b. Use of the transparent cello tape allowed easy placement of specimens within the loading frame, as well as fast adjustment of loading angle.

4.3 Test results

Thirty BD specimens were tested based on the methodology presented in Section 4.1. Twenty successful tests were carried out with the BD specimens subjected to different negative values of the loading angle ω (shown positively in Fig. 4.1a). The geometric parameters of these specimens are presented in Table 4.1. It should be noted that the low values of the standard deviations (STDs) demonstrate the repeatability in specimen fabrication, although the slit changes in the composite-strip cross-section width.

Ten successful tests were performed with BD specimens subjected to different positive values of ω. To this end, an arrest hole was cut by a water-jet machine at the lower delamination front, as shown in Fig. 4.6a, where the arrest hole in white is surrounded by a red circle and the artificial delamination is between the two dark points. It should be noted that without an arrest hole, the lower delamination front would propagate, repeating the results for negative loading angles. The average value of the diameter of the arrest hole was measured to be $d_{hole} = 1.76 \pm 0.02$ mm. Thus, it is considered to be constant in the FE analyses of all BD specimens. The center of the hole was not aligned with the investigated interface, nor did it coincide with the delamination tip as may be seen in Fig. 4.6b. Thus, the remaining critical delamination length, denoted by $2a_c^{(re)}$ in Fig. 4.6c

Table 4.1: Geometric parameters of the Brazilian disk specimens with $\omega < 0$.

specimen number	ω (°)	R_R (mm)	R_L (mm)	$2a_c$ (mm)	$R_R^{(sc)}$ (mm)	$R_L^{(sc)}$ (mm)	D (mm)	$2R$ (mm)	H_T (mm)	H_B (mm)	h_t (mm)	h_b (mm)	B (mm)
sp8.2	-2.06	12.92	12.03	15.60	12.75	11.86	40.55	40.21	7.72	8.19	12.04	12.26	8.16
sp9.1	-2.23	12.13	12.43	15.39	12.32	12.62	39.95	40.33	7.64	8.14	11.99	12.56	8.16
sp3.1	-2.23	12.05	12.42	16.00	12.15	12.53	40.47	40.68	7.40	8.26	12.40	12.62	8.24
sp1.1	-2.64	11.23	13.53	15.68	11.14	13.42	40.44	40.24	7.42	8.28	12.84	11.70	8.26
sp14.1	-2.73	13.80	11.85	15.67	13.19	11.30	41.32	40.16	7.38	8.12	12.42	12.24	8.20
sp7.2	-4.10	12.72	12.15	15.51	12.84	12.27	40.38	40.62	7.49	8.48	12.60	12.05	8.14
sp1.2	-4.94	12.44	12.18	15.40	12.59	12.33	40.02	40.32	7.52	8.29	12.59	11.92	8.25
sp12.1	-5.27	11.44	12.82	15.66	11.60	12.99	39.92	40.25	7.18	8.21	13.27	11.59	8.17
sp2.1	-5.86	13.29	11.56	15.48	13.22	11.50	40.33	40.20	7.17	8.33	12.53	12.17	8.21
sp11.2	-5.90	12.88	11.88	15.74	12.64	11.66	40.50	40.04	7.45	8.19	12.84	11.56	8.11
sp12.2	-9.21	11.83	13.21	15.17	11.84	13.22	40.21	40.23	7.38	7.83	13.08	11.94	8.15
sp13.2	-9.45	11.13	13.35	15.55	11.23	13.47	40.03	40.25	7.62	8.18	12.75	11.70	8.16
sp3.2	-9.67	11.45	13.24	15.35	11.53	13.33	40.04	40.21	7.52	8.23	12.47	11.99	8.24
sp8.1	-10.10	11.04	13.15	15.48	11.26	13.39	39.67	40.13	7.55	8.10	12.13	12.35	8.17
sp11.1	-10.11	13.05	11.95	15.39	13.08	11.97	40.39	40.44	7.18	7.97	13.28	12.01	8.16
sp4.2	-12.46	11.15	13.50	15.31	11.21	13.56	39.96	40.08	7.76	8.11	12.60	11.61	8.17
sp5.1	-12.94	11.63	13.57	15.19	11.53	13.45	40.39	40.17	7.86	8.01	11.50	12.80	8.17
sp2.2	-13.07	12.05	12.64	15.81	11.74	12.32	40.50	39.87	7.41	8.21	12.19	12.06	8.28
sp4.1	-13.20	11.27	13.83	15.24	11.15	13.70	40.34	40.09	7.39	8.24	12.78	11.68	8.11
sp6.2	-13.42	11.71	13.53	15.42	11.56	13.37	40.66	40.35	7.46	8.20	12.35	12.34	8.25
average		12.06	12.74	15.50	12.03	12.71	40.30	40.24	7.48	8.18	12.53	12.06	8.19
STD		0.82	0.71	0.21	0.74	0.77	0.35	0.19	0.19	0.14	0.44	0.36	0.05

and Table 4.2, and the interfacial remaining ligament at the bottom of the specimen, denoted by $R_L^{(lig)}$, were measured for each specimen. The remaining delamination length $2a_c^{(re)}$, is schematically shown in Fig. 4.6c and is measured three times along specimen thickness ($x_3 = B/4$, $B/2$ and $3B/4$) with an electronic digital caliper after a test is conducted when the specimen is in two parts. The interfacial remaining ligament $R_L^{(lig)}$, which is also presented in Fig. 4.6c, is measured with an electronic digital caliper at specimen mid-thickness ($x_3 = B/2$). In Table 4.2, all the geometric parameters which were measured are presented.

The effective diameter of the arrest hole along the delamination, $d_{hole}^{(eff)}$, shown in Figs. 4.6b and 4.6c, is evaluated from an image of the BD specimen located within the loading frame that was photographed prior to testing via the Vision Assistant (2005) software; those values of $d_{hole}^{(eff)}$ appear in Table 4.2 and are used in the FE model of each BD specimen. The offset distance, which is the distance between the delamination and the center of the arrest hole, is denoted by c_{hole} as shown in Fig. 4.6b. It is calculated for each specimen from

$$c_{hole} = \pm\frac{1}{2}\sqrt{d_{hole}^2 - d_{hole}^{(eff)^2}} \tag{4.5}$$

where its obtained values are presented in Table 4.3. In that table, parameters which were calculated are presented. Recall that d_{hole} is taken to be 1.76 mm. The positive and negative values of c_{hole} represent whether the center of the arrest hole is above or beneath

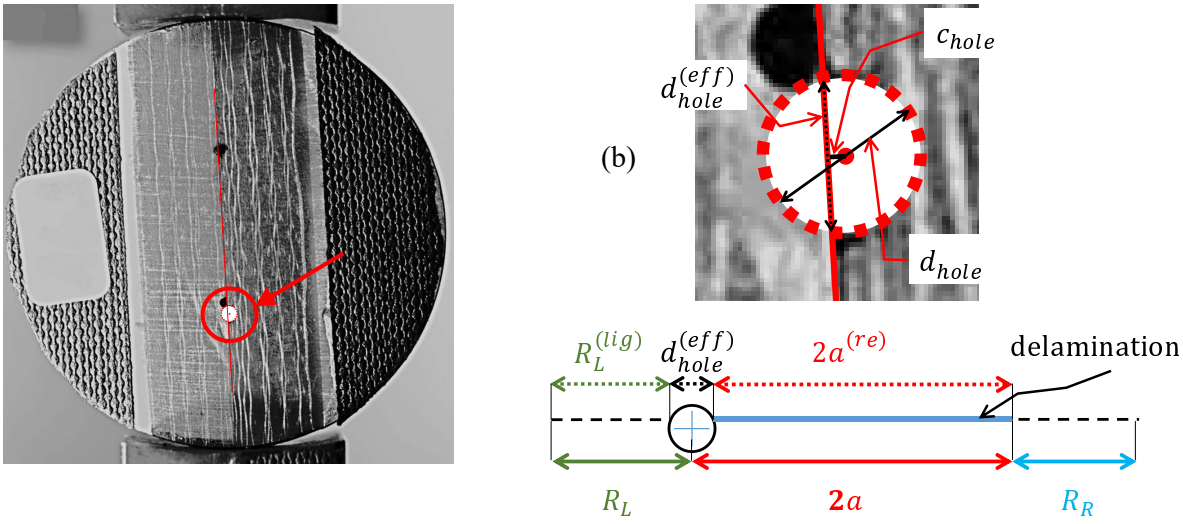

Figure 4.6: (a) BD specimen inside a stiff metal loading frame containing an arrest hole marked with a red circle and an arrow. (b) A detailed view of the arrest hole, where its center is shifted by c_{hole} from the delamination. (c) An illustration of the geometric parameters of a BD specimen containing an arrest hole.

the delamination, respectively. In this way, the location of the center of the arrest hole is accounted for in the FE analyses. The parameters R_R and R_L are scaled in a similar manner as given in eqs. (4.3) to obtain $R_R^{(sc)}$ and $R_L^{(sc)}$ with the appropriate value for $2a_c$ (see Fig. 4.6c) given as

$$2a_c = 2a_c^{(re)} + \frac{d_{hole}^{(eff)}}{2}. \tag{4.6}$$

It should be noted that prior to scaling R_L, it is first calculated as

$$R_L = R_L^{(lig)} + \frac{d_{hole}^{(eff)}}{2}. \tag{4.7}$$

After $R_L^{(sc)}$ is obtained from eq. $(4.3)_1$, the value of $R_L^{(lig,sc)}$ is extracted using eq. (4.7) with $R_L = R_L^{(sc)}$. The values of R_L, $R_L^{(sc)}$ and $R_L^{(lig,sc)}$ are presented in Table 4.3. Recall that the parameters $2R$ and D were calculated using eqs. (4.1) and (4.2), respectively, with $2a_c$ calculated from eq. (4.6) and R_L calculated from eq. (4.7). Additional geometric parameters of the tested BD specimens containing a delamination arrest hole are presented in Tables 4.2 and 4.3. Again, the STDs indicate repeatability in specimen fabrication.

The temperature ϑ and RH at the beginning of each test, as well as the applied loading angle and load at fracture P_c are summarized in Tables 4.4 and 4.5, where the data is for BD specimens which were subjected to negative and positive loading angles, respectively. For each test, the time between specimen removal from the conditioning chamber and

Table 4.2: Measured geometric parameters of the Brazilian disk specimens with a delamination arrest hole and loading angle $\omega > 0$.

specimen number	ω (°)	R_R (mm)	$R_L^{(lig)}$ (mm)	$2a_c^{(re)}$ (mm)	$d_{hole}^{(eff)}$ (mm)	H_T (mm)	H_B (mm)	h_t (mm)	h_b (mm)	B (mm)
sp10.1	1.72	12.07	11.90	14.74	1.51	7.47	8.37	12.52	11.95	8.08
sp14.2	2.50	13.32	11.54	14.09	1.50	7.56	8.28	11.90	12.28	8.16
sp10.2	2.69	12.14	11.94	14.48	1.76	7.38	8.36	12.37	12.05	8.17
sp16.1	2.74	12.20	11.63	13.84	1.76	7.63	8.44	12.12	12.13	8.14
sp15.1	4.03	11.84	11.57	14.40	1.76	7.86	8.10	11.94	12.08	8.18
sp9.2	4.30	11.70	12.45	14.70	1.50	7.64	8.14	12.05	12.41	8.05
sp15.2	4.67	10.82	12.11	15.39	1.76	7.48	8.27	13.40	11.49	8.15
sp7.1	5.35	11.57	13.20	13.89	1.50	7.56	8.35	12.31	11.87	8.17
sp6.1	9.89	12.57	10.32	15.37	1.50	7.64	8.33	12.30	12.17	8.18
sp5.2	10.43	13.20	11.01	14.28	1.50	7.70	8.15	11.36	12.93	8.15
average		12.14	11.77	14.52	1.61	7.59	8.28	12.23	12.14	8.14
STD		0.75	0.78	0.55	0.13	0.13	0.11	0.52	0.37	0.04

Table 4.3: Scaled and calculated geometric parameters of the Brazilian disk specimens with a delamination arrest hole and loading angle $\omega > 0$.

specimen number	$2R$ (mm)	D (mm)	$R_R^{(sc)}$ (mm)	$R_L^{(sc)}$ (mm)	$R_L^{(lig,sc)}$ (mm)	$2a_c$ (mm)	c_{hole} (mm)	R_L (mm)
sp10.1	40.31	40.21	12.11	12.70	11.95	15.49	-0.45	12.65
sp14.2	40.02	40.45	13.10	12.08	11.33	14.84	0.46	12.29
sp10.2	40.16	40.32	12.06	12.74	11.86	15.36	0.00	12.82
sp16.1	40.32	39.43	12.64	12.96	12.08	14.72	0.00	12.51
sp15.1	39.98	39.57	12.04	12.66	11.78	15.28	0.00	12.45
sp9.2	40.24	40.35	11.65	13.14	12.39	15.45	0.46	13.20
sp15.2	40.64	40.08	11.08	13.29	12.41	16.27	0.00	12.99
sp7.1	40.09	40.16	11.54	13.91	13.16	14.64	-0.46	13.95
sp6.1	40.44	39.76	12.92	11.40	10.65	16.12	0.46	11.07
sp5.2	40.14	39.99	13.28	11.83	11.08	15.03	0.46	11.76
average	40.23	40.03	12.24	12.67	11.87	15.32	0.09	12.57
STD	0.20	0.34	0.72	0.74	0.72	0.55	0.36	0.79

Table 4.4: Temperature, relative humidity, applied loading angle and load at fracture of the Brazilian disk specimens with $\omega < 0$.

specimen no.	ϑ (°C)	RH (%)	ω (°)	P_c (N)
sp8.2	23.6	40.7	-2.1	9336.8
sp9.1	22.6	41.3	-2.2	9497.6
sp3.1	23.5	41.8	-2.2	9710.3
sp1.1	22.8	41.1	-2.6	9963.1
sp14.1	23.3	41.5	-2.7	9750.5
sp7.2	28.6	25.5	-4.1	9888.1
sp1.2	28.4	25.1	-4.9	8298.4
sp12.1	25.4	52.9	-5.3	9630.1
sp2.1	23.0	52.9	-5.9	9782.1
sp11.2	28.8	24.0	-5.9	9452.7
sp12.2	23.0	51.3	-9.2	7866.5
sp13.2	22.4	41.5	-9.5	8158.7
sp3.2	25.6	51.8	-9.7	8147.3
sp8.1	23.7	49.6	-10.1	8204.3
sp11.1	22.2	39.4	-10.1	8111.9
sp4.2	22.7	39.6	-12.5	8039.7
sp5.1	23.2	41.8	-12.9	7758.5
sp2.2	23.1	42.9	-13.1	7616.1
sp4.1	22.6	40.6	-13.2	8043.1
sp6.2	22.6	40.0	-13.4	8165.9

Table 4.5: Temperature, relative humidity, applied loading angle and load at fracture of the Brazilian disk specimens with a delamination arrest hole and $\omega > 0$.

specimen no.	ϑ (°C)	RH (%)	ω (°)	P_c (N)
sp10.1	23.4	54.8	1.7	7783.9
sp14.2	23.4	54.2	2.5	7969.8
sp10.2	23.4	55.2	2.7	7295.7
sp16.1	23.6	50.6	2.7	7614.5
sp15.1	23.5	55.8	4.0	8153.5
sp9.2	23.6	50.1	4.3	8034.9
sp15.2	23.7	54.6	4.7	8430.9
sp7.1	23.6	50.3	5.4	8690.5
sp6.1	23.6	51.7	9.9	7441.5
sp5.2	23.7	52.6	10.4	8331.3

the end of the test was less than one hour. In Table 4.4, it may be observed that the load at fracture is generally higher for small absolute values of the loading angles. It should be noted that for specimen **sp1.2**, a low value of the fracture load was obtained as compared to other specimens for similar loading angles. Although pores were detected (via the Zeiss microscope) in specimen **sp1.2**, it was tested in order to quantify the effect of porosity upon fracture toughness. Recall that the ASTM Standard D5528-13 (2014) requires that the test conditions are such that the test temperature be $23 \pm 3^{\circ}$ C and the RH be $50 \pm 10\%$. In Table 4.4, it may be observed that for specimens **sp7.2**, **sp1.2** and **sp11.2**, the test temperature was above the recommended value, whereas the RH was slightly below the recommended value. For specimens **sp11.1** and **sp4.2**, the RH was below the recommended value in the standard. For Table 4.5, testing conditions were maintained according to the ASTM Standard D5528-13 (2014) recommendations.

4.4 Finite element analyses

All BD specimens were analyzed by means of the FE method using the ADINA (Bathe, 2011) software, with the geometric parameters listed in Tables 4.1 and 4.2. An example of a three-dimensional FE model is presented in Fig. 4.7, where the FE model was used in analyzing specimen **sp11.2**, for which $\omega = -5.9^{\circ}$. The three-dimensional FE models

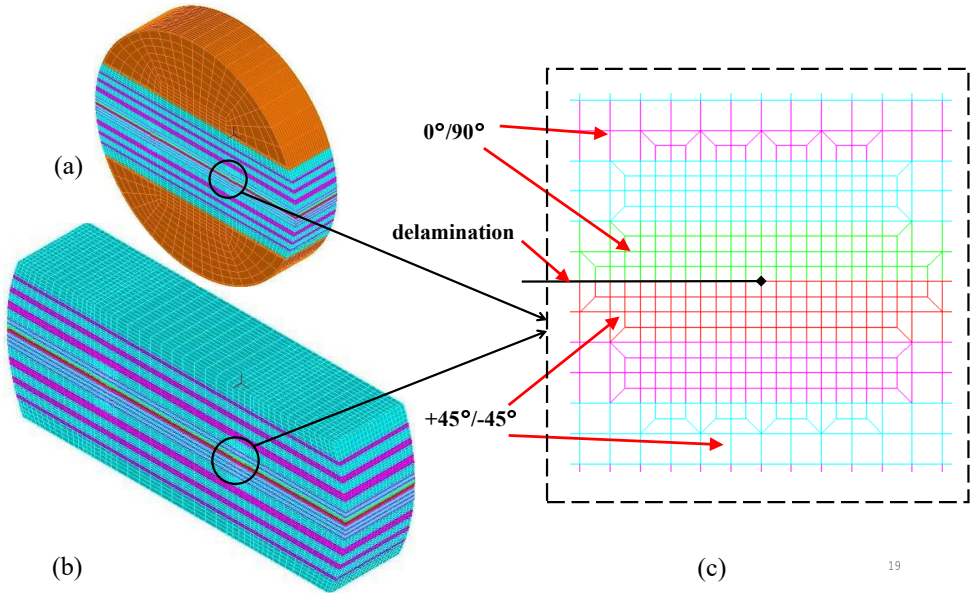

Figure 4.7: FE model used to analyze specimen **sp11.2** containing 117,760 twenty noded isoparametric, brick elements and 852,028 nodal points. (a) Isometric-view of the mesh, (b) isometric-view of the composite strip mesh and (c) detailed front-view of one delamination tip region.

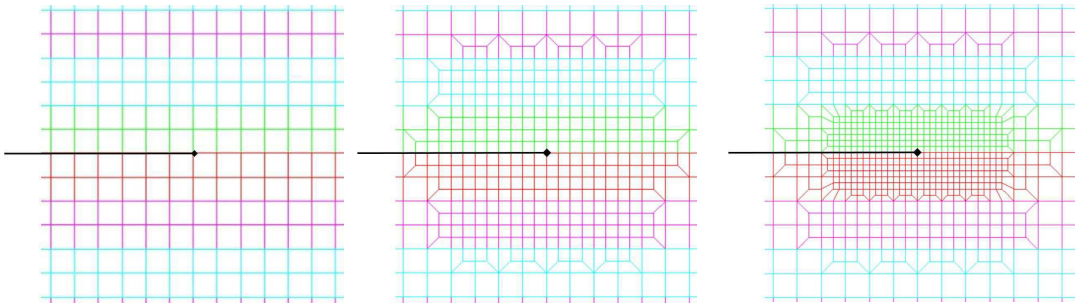

(a) (b) (c)

Figure 4.8: Detailed front-view of FE models of one delamination tip region of specimen **sp11.2** used in convergence study: (a) coarse mesh, (b) fine mesh and (c) finer mesh.

contained twenty noded isoparametric, brick elements. In order to model the square-root singularity along the delamination front, quarter-point elements were used. The oscillatory part of the singularity was not modeled. The material properties used to characterize the plain woven plies with the yarn in the 0°/90° and +45°/-45° directions are presented in Table 2.1. It may be noted that within the delamination region, a symmetric mesh was generated, so that the left delamination tip, also shown in Figs. 4.7a and 4.7b, is a mirror reflection of the right delamination tip, which is presented in detail in Fig. 4.7c.

4.4.1 Convergence study

To examine convergence, a coarse, fine and finer mesh were used with the geometric parameters of specimen **sp11.2** in Table 4.1. The in-plane dimensions of the elements in the vicinity of the delamination front were set to $1.1 \cdot 10^{-4} \times 1.1 \cdot 10^{-4}$ m^2, $5.5 \cdot 10^{-5} \times 5.5 \cdot 10^{-5}$ m^2 and $2.75 \cdot 10^{-5} \times 2.75 \cdot 10^{-5}$ m^2, as shown in Figs. 4.8a, 4.8b and 4.8c, respectively. In all meshes there were 20 elements along the delamination front, each $4.06 \cdot 10^{-4}$ m thick. It has been shown that quarter-point, crack tip elements for which the in-plane element geometry is square lead to the best results for homogenous materials (Banks -Sills and Bortman, 1984). A ply group consisting of several plies of the same plain woven material is assumed to serve as a single plain woven ply with the same material properties as described above, with a total thickness of all plies in the ply group. Mesh refinement was made in the regions where load or restraints were applied to obtain a better load distribution. A maximum in-plane element aspect ratio of 1×11.5 throughout the composite strip region was permitted away from regions of expected stress concentrations

Table 4.6: Characteristics of the three meshes which were used in the convergence study of the BD specimen.

mesh	no. of elements	no. of nodes	element in-plain size near delamination front (m^2)	no. of integration domains
coarse	107,040	774,636	$1.1 \cdot 10^{-4} \times 1.1 \cdot 10^{-4}$	2
fine	117,760	852,028	$5.5 \cdot 10^{-5} \times 5.5 \cdot 10^{-5}$	4
finer	130,560	944,416	$2.75 \cdot 10^{-5} \times 2.75 \cdot 10^{-5}$	5

(such as load application points, reactions, delamination front, etc.). Some characteristics of the FE meshes which were used in the convergence study are given in Table 4.6.

The stress intensity factors were calculated along the delamination front of each mesh by means of the three-dimensional M-integral, which was described in Section 3.2, and were verified by means of the DE method, which was presented in Section 3.1. The stress intensity factors obtained for the largest domain of each mesh as a function of the normalized delamination front coordinate (x_3/B) are shown in Fig. 4.9. Recall that the dimensions of the complex in-plane stress intensity factor components are $\mathrm{F}\times\mathrm{L}^{-(3/2+i\varepsilon)}$, where F and L represent force and length, respectively. The oscillatory parameter, ε, depends upon the mechanical properties of both materials on either side of the interface and for the investigated interface it is given in eq. (2.46). Both in-plane stress intensity factor components, K_1 and K_2, have units of $\mathrm{MPa}\sqrt{\mathrm{m}}\cdot\mathrm{m}^{-i\varepsilon}$ and are shown, respectively, in Figs. 4.9a and 4.9b. The dimensions of the out-of-plane stress intensity factor, K_{III}, are $\mathrm{F}\times\mathrm{L}^{-3/2}$ with units of $\mathrm{MPa}\sqrt{\mathrm{m}}$; it is presented in Fig. 4.9c.

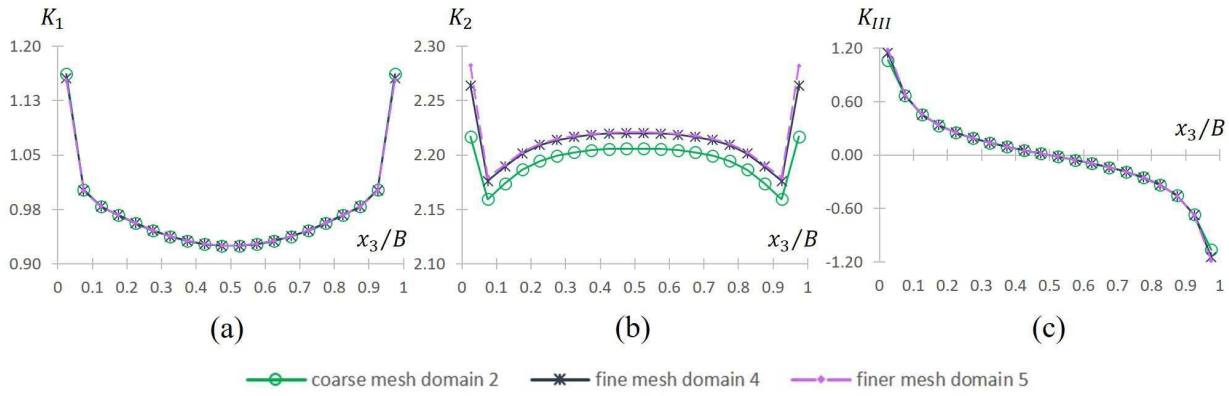

Figure 4.9: Stress intensity factors calculated along the delamination front by means of the three-dimensional M-integral for the largest domain of each FE mesh used to analyze specimen **sp11.2** (coarse, fine and finer meshes). (a) K_1 in $\mathrm{MPa}\sqrt{\mathrm{m}}\cdot\mathrm{m}^{-i\varepsilon}$, (b) K_2 in $\mathrm{MPa}\sqrt{\mathrm{m}}\cdot\mathrm{m}^{-i\varepsilon}$ and (c) K_{III} in $\mathrm{MPa}\sqrt{\mathrm{m}}$.

Table 4.7: Maximum percent difference (in absolute value) between the stress intensity factors calculated for the fifth integration domain (reference) and domains 2, 3 and 4 of the finer mesh shown in Fig. 4.8c.

percent difference								
domain 2			domain 3			domain 4		
K_1	K_2	K_{III}	K_1	K_2	K_{III}	K_1	K_2	K_{III}
0.051	0.719	0.241	0.019	0.221	0.059	0.008	0.045	0.012

The stress intensity factors obtained from the finer mesh and the M-integral served as reference values and were used for comparison. In order to quantify the change in the calculated stress intensity factors obtained for each mesh, a percent difference was defined, which is given by

$$\text{difference}(\%) = \frac{K_m^{(\text{ch})} - K_m^{(\text{ref})}}{K_m^{(\text{ref})}} \times 100 \tag{4.8}$$

were $m = 1, 2, III$. In eq. (4.8), the superscripts (ch) and (ref) represent the examined (checked) and base-line (reference) values, respectively. Demonstration of path independence for the finer mesh (shown in Fig. 4.8c) may be concluded from Table 4.7, in which the differences between the stress intensity factors obtained for the fifth (reference) and other domains of integration (see Fig. 3.2) are presented. It should be noted that the maximum percent difference shown in Table 4.7 occurred at different positions along the delamination front. When comparison is performed at the same location along the delamination front, the values obtained for the different integration domains appear to support path independence.

In addition to Fig. 4.9, solution convergence is examined in Table 4.8, in which the differences between the stress intensity factors obtained for pairs of meshes are presented. For each pair of meshes, the mesh which is more refined in the vicinity of the delamination front serves as the reference (ref) in eq. (4.8). It should be noted that the maximum percent difference shown in Table 4.8 occurred at different positions along the delamination

Table 4.8: Maximum percent difference (in absolute value) between the stress intensity factors for pairs of meshes, along the delamination front, calculated for the largest integration domain of each mesh.

percent difference						
meshes	coarse and fine			fine and finer		
range	K_1	K_2	K_{III}	K_1	K_2	K_{III}
$0.075 \leq x_3/B \leq 0.925$	0.077	0.774	0.644	0.028	0.158	0.278
$0.025 \leq x_3/B \leq 0.975$	0.506	2.076	7.180	0.242	0.799	3.240

front. It may be observed that convergence is obtained for both ranges of x_3/B. Results for $x_3/B = 0.025$ and 0.975, that is for the domain in the outermost elements, deteriorate as compared to the other domains. Recall that in the development of the first term of the asymptotic stress and displacement fields, conditions of plane deformation were assumed (Section 2.2). This assumption is common in cases of through cracks/delaminations, so that the singularity related to body/medium free surface is not represented. Therefore, the values calculated by means of the M-integral and the DE method at FE model outer faces are inaccurate. Since the absolute value of the maximum percent difference within the range of $0.075 \leq x_3/B \leq 0.925$ between the fine and the finer mesh is less than 0.3%, it may be concluded that the fine mesh (typical side view of one delamination tip region is shown in Fig. 4.8b) may be used in all FE models in this study.

4.4.2 Analysis of specimens

The results of the stress intensity factor components for specimen **sp11.2** are shown in Figs. 4.9a, 4.9b and 4.9c, in which K_1, K_2 and K_{III} are plotted, respectively, as a function of the normalized delamination front coordinate x_3/B. It may be observed that the in-plane stress intensity factor components are symmetric with respect to specimen mid-thickness ($x_3/B = 0.5$), whereas the out-of-plane stress intensity factor is anti-symmetric. This behavior of the stress intensity factors was observed in every analysis that was performed for each BD specimen FE model within the group of the thirty BD specimens that were tested. In order to resolve the complex units of the in-plane stress intensity factor components, K_1 and K_2 in eq. (1.6), an arbitrary length parameter $\hat{L}$ was used in a similar manner to L denoted in eq. (1.7), so that

$$\hat{K} = \hat{K}_1 + i\hat{K}_2 = K\hat{L}^{i\varepsilon}. \tag{4.9}$$

The general expressions for the two phase angles, $\hat{\psi}$ in eq. (1.12) and ϕ in eq. (1.14) with $L = \hat{L}$, remain the same. Also, the general expressions for the local interface energy release rate $\mathcal{G}_i$ in eq. (1.17), the critical interface energy release rate $\mathcal{G}_{ic}$ in eq. (1.18) and the mode 1 critical energy release rate $\mathcal{G}_{1c}$ in eq. (1.19), are used with $L = \hat{L}$ in the latter. For the particular case of a delamination between two tetragonal anisotropic elastic materials where the interface is between a $0°/90°$ and a $+45°/-45°$ balanced plain weave (see Fig. 1.1b), the oscillatory parameter ε is defined in eq. (2.46) and the parameters H_1 and H_2 are given in eqs. (3.16); their values are listed in Table 4.9.

It should be noted that in this investigation the mechanical properties of the plain woven ply with yarn in the $0°/90°$-directions presented in Table 2.1 were rounded; for the Young's moduli E_{ii} and the shear moduli G_{ij} (for $i, j = 1, 2, 3$, no summation implied) only the first significant digit after the decimal point was retained; whereas for Poisson's ratios ν_{ij},

Table 4.9: Values of some parameters for the particular case of a delamination between two tetragonal anisotropic elastic materials where the interface is between a $0°/90°$ and a $+45°/-45°$ balanced plain weave.

ε	H_1 (GPa)	H_2 (GPa)	D_{11} (1/GPa)	D_{22} (1/GPa)	D_{33} (1/GPa)	$W_{12}=-W_{21}$ (1/TPa)
0.00865	8.00	8.99	0.212	0.500	0.445	8.85

three digits after the decimal point were used for calculating the properties of each plain weave. In Banks-Sills et al. (2013) and Ishbir (2014) many more significant figures were used. Minor differences in the values of the interface delamination parameters, such as ε, H_1 and H_2, between the two studies are observed. Values of the members of the matrices $\mathbf{D}$ in eq. (2.20) and $\mathbf{W}$ in eq. (2.21) are also presented in Table 4.9.

The stress intensity factors were calculated by means of the three-dimensional M-integral for each slice of elements within domain 4 (one element thick through the model thickness, see Fig. 3.2d) along the delamination front of each specimen. Note that the delamination front and the FE model thickness were divided into 20 equal slices. The normalized in-plane stress intensity factors, $\hat{K}_1$ and $\hat{K}_2$, were calculated with a normalized length parameter of $\hat{L}=100$ μm. Based upon these results, the critical interface energy release rate $\mathcal{G}_{ic}$ using eq. (1.17), as well as the two phase angles, ψ and ϕ, were also calculated.

In Fig. 4.10, values of the critical interface energy release rate $\mathcal{G}_{ic}$ obtained for various BD specimens tested at different loading angles ω are plotted as a function of the normalized

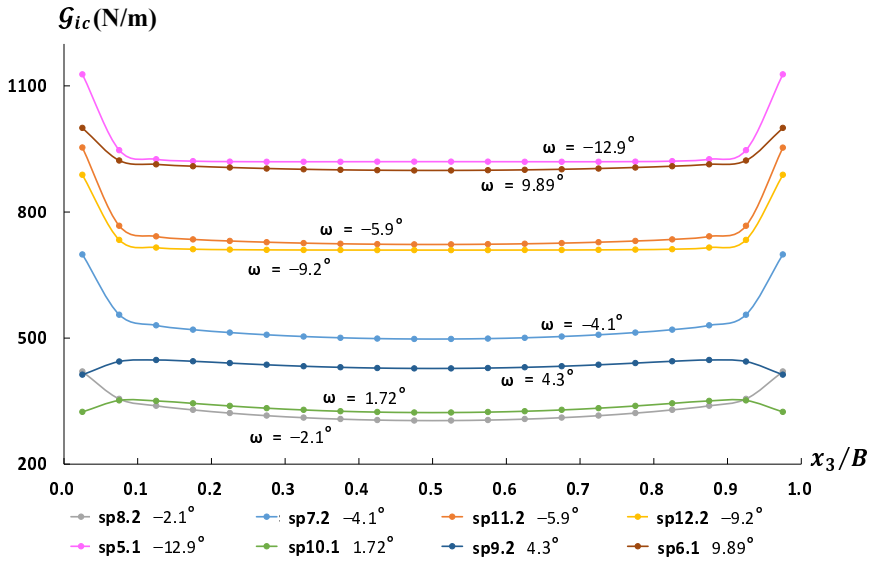

Figure 4.10: Critical interface energy release rate $\mathcal{G}_{ic}$ as a function of the normalized delamination front coordinate x_3/B within the range of $0 \leq x_3/B \leq 1$ for different loading angles ω.

delamination front coordinate x_3/B within the range of $0 \leq x_3/B \leq 1$. It may be observed that the values of $\mathcal{G}_{ic}$ through the thickness are nearly constant except at the outer surfaces of the specimen. This contrasts with the DCB specimen which exhibited parabolic behavior as presented in Fig. 13 of Banks-Sills et al. (2013). The results obtained for each BD specimen next to its mid-thickness, where $x_3/B = 0.475$, are presented in Table 4.10.

Since the in-plane stress intensity factors are symmetric with respect to specimen mid-thickness ($x_3/B = 0.5$), their values are approximately that of $x_3/B = 0.475$. The

Table 4.10: Results obtained for each BD specimen at $x_3/B = 0.475$. The loading angle is ω, and $\hat{K}_1$ and $\hat{K}_2$ are the in-plane normalized stress intensity factor components calculated with the length parameter $\hat{L} = 100$ μm. The out-of-plane stress intensity factor is K_{III}, $\mathcal{G}_{ic}$ is the critical interface energy release rate, and $\hat{\psi}$ and ϕ are the derived phase angles.

specimen number	ω (°)	$\hat{K}_1$ (MPa$\sqrt{\text{m}}$)	$\hat{K}_2$ (MPa$\sqrt{\text{m}}$)	K_{III} (MPa$\sqrt{\text{m}}$)	$\mathcal{G}_{ic}$ (N/m)	$\hat{\psi}$ (rad)	ϕ (rad)
sp8.2	-2.06	1.39	0.70	0.01	303.8	0.466	0.005
sp9.1	-2.23	1.39	0.74	0.01	310.8	0.489	0.006
sp3.1	-2.23	1.44	0.86	0.01	351.2	0.540	0.005
sp1.1	-2.64	1.43	1.27	0.01	456.6	0.728	0.005
sp14.1	-2.73	1.40	1.04	0.01	382.7	0.639	0.006
sp7.2	-4.10	1.33	1.48	0.01	497.7	0.839	0.006
sp1.2	-4.94	1.04	1.52	0.01	423.5	0.973	0.007
sp12.1	-5.27	1.12	2.12	0.02	719.1	1.087	0.006
sp2.1	-5.86	1.13	2.12	0.02	718.5	1.082	0.007
sp11.2	-5.90	1.10	2.14	0.02	722.8	1.096	0.007
sp12.2	-9.21	0.56	2.31	0.02	709.3	1.332	0.008
sp13.2	-9.45	0.58	2.49	0.02	816.1	1.341	0.008
sp3.2	-9.67	0.58	2.49	0.02	817.3	1.340	0.008
sp8.1	-10.10	0.54	2.64	0.02	910.1	1.368	0.008
sp11.1	-10.11	0.56	2.46	0.02	794.3	1.346	0.008
sp4.2	-12.46	0.25	2.73	0.02	942.1	1.480	0.009
sp5.1	-12.94	0.30	2.70	0.02	919.6	1.462	0.008
sp2.2	-13.07	0.25	2.70	0.02	918.6	1.478	0.009
sp4.1	-13.20	0.21	2.81	0.03	990.4	1.497	0.009
sp6.2	-13.42	0.23	2.85	0.03	1022.8	1.489	0.008
sp10.1	1.72	1.19	-1.08	-0.01	322.9	-0.738	-0.004
sp14.2	2.50	1.18	-0.65	0.00	225.8	-0.504	0.000
sp10.2	2.69	1.07	-1.01	0.00	271.4	-0.756	-0.003
sp16.1	2.74	1.08	-1.01	0.00	272.4	-0.752	-0.003
sp15.1	4.03	1.09	-1.67	-0.01	494.1	-0.993	-0.004
sp9.2	4.30	1.11	-1.48	-0.01	427.8	-0.925	-0.003
sp15.2	4.67	1.16	-1.96	-0.01	647.6	-1.035	-0.005
sp7.1	5.35	0.95	-2.48	-0.02	880.1	-1.204	-0.006
sp6.1	9.89	0.56	-2.62	-0.02	898.9	-1.361	-0.008
sp5.2	10.43	0.60	-2.83	-0.02	1048.3	-1.362	-0.008

same behavior occurs for the value of the in-plane mode mixity angle $\hat{\psi}$. The critical interface energy release rate $\mathcal{G}_{ic}$ calculated from eq. (1.17) is also symmetric with respect to specimen mid-thickness.

From Table 4.10 and Fig. 4.10, it may be observed that the critical interface energy release rate $\mathcal{G}_{ic}$ generally increases with $|\omega|$, as well as the absolute value of the in-plane mode mixity angle $|\hat{\psi}|$. It should be noted that the $\mathcal{G}_{ic}$ value of specimen **sp1.2** is exceptionally low. Perhaps this occurred because this specimen was found to have pores in it. Thus, its value was excluded from fracture criterion determination.

It may be noted that for specimens **sp5.2** and **sp6.1**, in which $\omega > 9°$, an insignificant amount of interpenetration of the delamination faces was observed at the outer surfaces of specimens where $x_3/B = 0, 1$. The interpenetration occurred for $r/a \leq 5\%$ of the distance from the delamination front, where $\theta = \pm\pi$ and r is shown in Fig. 1.1b, and a denotes the half delamination length. For all other specimens, no interpenetration of the delamination faces was observed throughout the model thickness.

4.5 Fracture criteria

A two-dimensional energy-based fracture toughness criterion was presented in Banks-Sills and Ashkenazi (2000) for a crack along a bimaterial interface between two dissimilar linear elastic, isotropic and homogeneous materials. In that study, other fracture criteria, such as the critical hoop stress and critical shear stress, were examined by means of best-fit comparisons with obtained experimental data from tests on glass//epoxy interface BD specimens. The criterion that was well suited to the experimental data and required determination of a minimum number of free parameters is given as

$$\mathcal{G}_{ic} = \overline{\mathcal{G}}_{1c}\left(1 + \tan^2\hat{\psi}\right) \tag{4.10}$$

where

$$\overline{\mathcal{G}}_{1c} = \frac{\left[\text{avg}(\hat{K}_1)\right]^2}{H_1} = \frac{\hat{K}_{1c}^2}{H_1}, \tag{4.11}$$

$\hat{K}_1$ is given in eq. (4.9), H_1 is given in eq. $(3.16)_1$ and $\hat{\psi}$ is given in eq. (1.12). The only free parameter is the normalization length $\hat{L}$. To obtain $\hat{K}_{1c}$, values of $\hat{K}_1$ from each test were plotted as a function of $\hat{K}_2$ as shown in Fig. 4.11a. This criterion was extended in Banks-Sills et al. (2005) to the case of a delamination along the $0°//90°$ interface; it was further extended to a three-dimensional energy-based fracture criterion in Banks-Sills et al. (2006) for a delamination along the $+45°//-45°$ interface. In both cases an MD laminate was fabricated from UD plies.

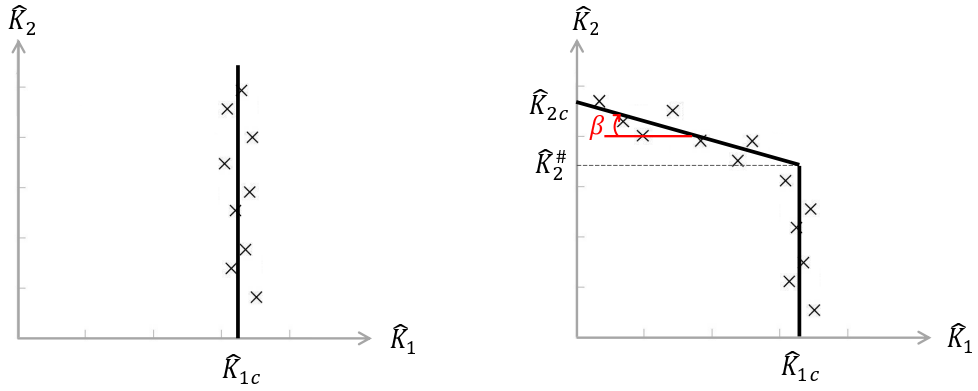

(a) (b)

Figure 4.11: Schematic plot of experimental data set in the $\hat{K}_1$-$\hat{K}_2$ plane: (a) $\hat{K}_1$ is constant for all test specimens, and (b) $\hat{K}_1$ is nearly constant until $\hat{K}_2 = \hat{K}_2^{\sharp}$, then reduction in mode 1 begins.

It may be noted that the criterion given in eqs. (4.10) and (4.11) was also presented in Wang (1997), where an additional approach was taken for experimental data sets with a behavior schematically shown in Fig. 4.11b. Several pairs of materials were considered in Wang (1997) (aluminum//epoxy, steel//epoxy, brass//epoxy interfaces), in which some of the experimental results (obtained from BD and asymmetrical DCB tests) were found in the literature. It was found that the data fit $\hat{K}_1 = \hat{K}_{1c}$ for values of $\hat{K}_2$ less than some value say $\hat{K}_2^{\sharp}$, but for $\hat{K}_2$ greater than that value

$$\hat{K}_2 = \beta \hat{K}_1 + \hat{K}_{2c} \tag{4.12}$$

fit the experimental data as shown in Fig. 4.11b. In eq. (4.12), $\hat{K}_{2c}$ is the critical value of $\hat{K}_2$ obtained when $\hat{K}_1 = 0$ and β is the slope of the oblique line. Combining the two lines in Fig. 4.11b, a fracture criterion may be written as

$$\hat{K}_1 = \min\left(\hat{K}_{1c}, \frac{\hat{K}_2 - \hat{K}_{2c}}{\beta}\right). \tag{4.13}$$

Thus, it is possible to write a two-dimensional energy based criterion, similar to the one presented in eq. (4.10), with the new definition of $\hat{K}_1$ in eq. (4.13) substituted into eq. (4.11). It may be noted that the data presented in Wang (1997) in deriving eq. (4.13) included only data for which $\hat{K}_2$ was positive. Here, $\hat{K}_2 > 0$ for negative loading angles, that is $\omega < 0$; $\hat{K}_2 < 0$ for positive loading angles, $\omega > 0$.

The two-dimensional fracture criterion in eq. (4.10) may be extended to three-dimensions as

$$\mathcal{G}_{ic} = \overline{\mathcal{G}}_{1c}\left(1 + \tan^2\hat{\psi}\right)\left(1 + \tan^2\phi\right) \tag{4.14}$$

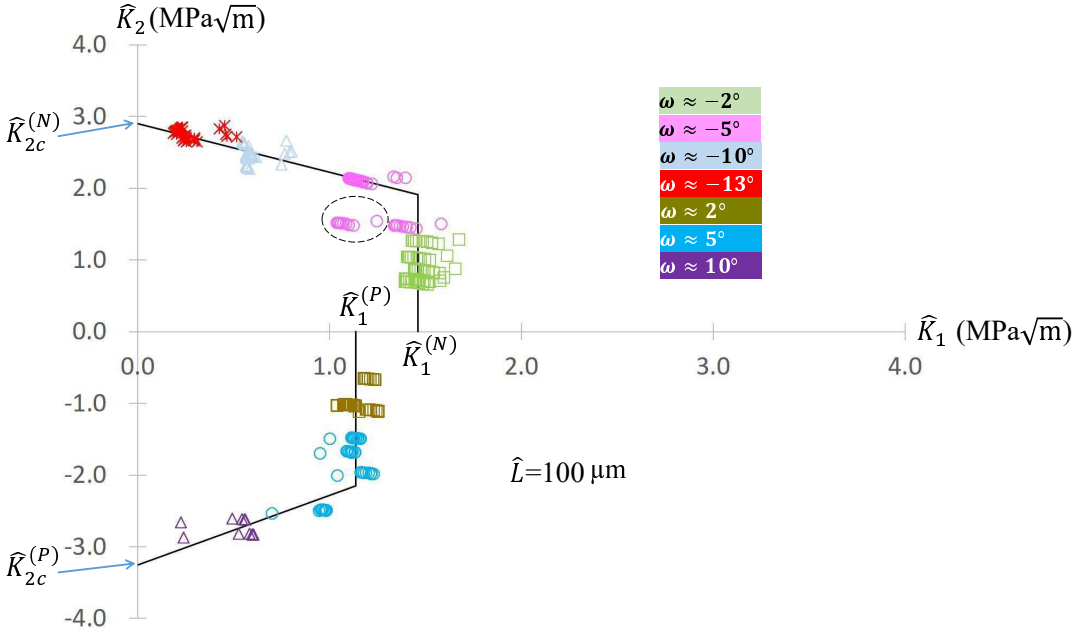

Figure 4.12: The stress intensity factor $\hat{K}_2$ versus $\hat{K}_1$ as described in eq. (4.17) for $\hat{L} = 100$ μm.

where $\overline{\mathcal{G}}_{1c}$ is defined in eq. (4.11). This criterion was presented in Banks-Sills et al. (2006) and in Banks-Sills et al. (2010). It is also possible to use $\hat{K}_1$ in eq. (4.13) in place of $\hat{K}_{1c}$ in eq. (4.11). Therefore, eq. (4.14) may be rewritten as

$$\mathcal{G}_{ic} = \mathcal{G}_1 \left(1 + \tan^2 \hat{\psi}\right) \left(1 + \tan^2 \phi\right), \tag{4.15}$$

where $\mathcal{G}_1$ is defined as

$$\mathcal{G}_1 = \frac{\hat{K}_1^2}{H_1}, \tag{4.16}$$

with the new definition of $\hat{K}_1$ in eq. (4.13).

Use of the same approach presented in eq. (4.13) results in the following expression for $\hat{K}_1$ for positive and negative $\hat{K}_2$ where

$$\hat{K}_1 = \begin{cases} \min\left(\hat{K}_1^{(N)}, \dfrac{\hat{K}_2 - \hat{K}_{2c}^{(N)}}{\beta^{(N)}}\right) & \text{for } \hat{K}_2 > 0 \\ \min\left(\hat{K}_1^{(P)}, \dfrac{\hat{K}_2 - \hat{K}_{2c}^{(P)}}{\beta^{(P)}}\right) & \text{for } \hat{K}_2 < 0. \end{cases} \tag{4.17}$$

In Fig. 4.12, eq. (4.17) is plotted for a normalized length parameter $\hat{L} = 100$ μm. In eq. (4.17) and Fig. 4.12, the superscripts (N) and (P) represent the sign of the loading angle applied during testing. The data points shown in Fig. 4.12 are projected onto the $\hat{K}_1$ - $\hat{K}_2$ plane for $K_{III} = 0$. Recall that for each BD specimen, 20 $(\hat{K}_1, \hat{K}_2)$ points

Table 4.11: Parameters of eq. (4.17) obtained for $\hat{L} = 100$ μm.

ω	$\hat{K}_1$ (MPa$\sqrt{\text{m}}$)	$\hat{K}_2$ (MPa$\sqrt{\text{m}}$)	β
$\omega < 0$	$\hat{K}_1^{(N)} = 1.46$	$\hat{K}_{2c}^{(N)} = 2.90$	$\beta^{(N)} = -0.67$
$\omega > 0$	$\hat{K}_1^{(P)} = 1.14$	$\hat{K}_{2c}^{(P)} = -3.25$	$\beta^{(P)} = 0.97$

were obtained along the delamination front. The value of $\hat{K}_1^{(N)}$ was determined as the average value of all $\hat{K}_1$ obtained at failure from specimens **sp8.2**, **sp9.1**, **sp3.1**, **sp1.1**, **sp14.1**, where $\omega \approx -2°$, and **sp7.2**, where $\omega \approx -4°$. In the same manner, the value of $\hat{K}_1^{(P)}$ was determined by using the $\hat{K}_1$ data obtained at failure from specimens **sp10.1**, **sp14.2**, **sp10.2**, **sp16.1**, where $\omega \approx +2°$, and **sp15.1** and **sp9.2**, where $\omega \approx +4°$. The value of $\hat{K}_{2c}^{(N)}$ was determined from the intersection point between the oblique line obtained by means of a linear regression applied to the rest of the $(\hat{K}_1, \hat{K}_2)$ points, where $\omega \approx -5°, \ -10°, \ -13°$, and the vertical axis, where $\hat{K}_1 = 0$. In a similar manner, the value of $\hat{K}_{2c}^{(P)}$ was determined. The values of $\beta^{(N)}$ and $\beta^{(P)}$ were determined by calculating the slopes of the oblique lines from linear regression. The obtained parameters determined for $\hat{L} = 100$ μm are listed in Table 4.11. Since specimen **sp1.2** was found to contain pores, it was excluded from determination of the parameters in eq. (4.17). Nevertheless, these points are shown in Fig. 4.12 and are surrounded by a dashed ellipse.

The fact that $\hat{K}_1^{(P)} \neq \hat{K}_1^{(N)}$ motivates consideration of another value of $\hat{L}$ for which $\hat{K}_1^{(N)} = \hat{K}_1^{(P)} \equiv \hat{K}_{1c}$. If the value of $\hat{L}$ is chosen to be $2,900$ m, $\hat{K}_{1c}$ is found as 1.30 MPa$\sqrt{\text{m}}$, as shown in Fig. 4.13. Indeed, $\hat{L} = 2,900$ m is an unrealistic physical length scale. Thus, the

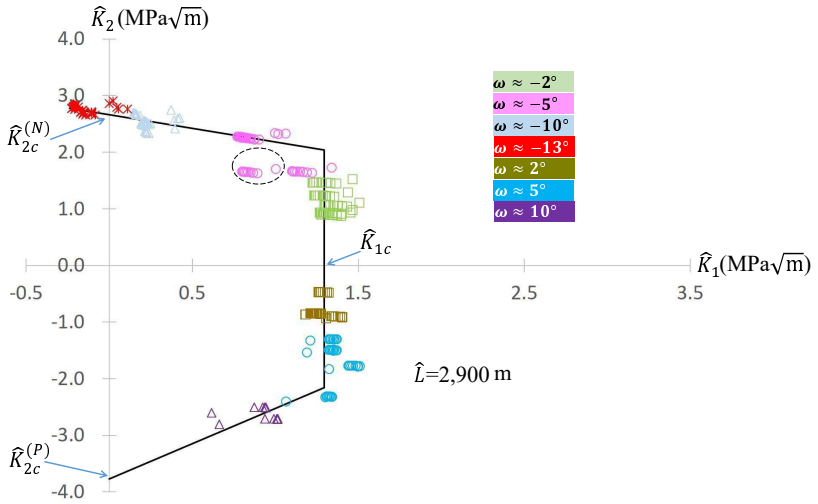

Figure 4.13: The stress intensity factor $\hat{K}_2$ versus $\hat{K}_1$ as described in eq. (4.17) for $\hat{L} = 2,900$ m.

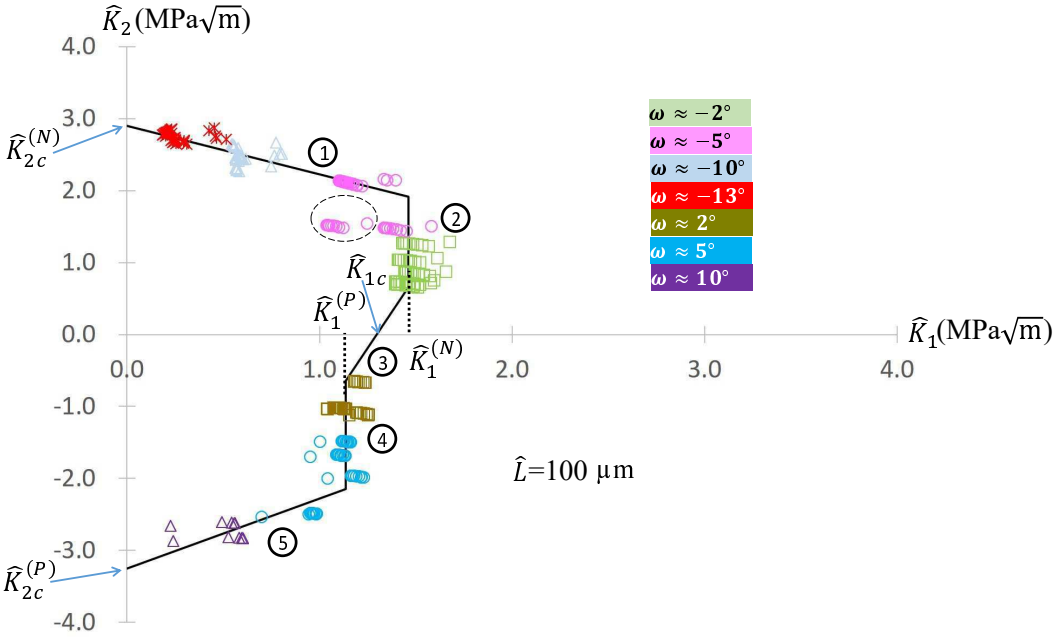

Figure 4.14: The stress intensity factor $\hat{K}_2$ versus $\hat{K}_1$ as described in eq. (4.18) for $\hat{L} = 100$ μm.

approach presented in the work of Mega and Banks-Sills (2019) is used here. In that study, a fracture toughness criterion was obtained for a delamination along an MD composite with an interface between a UD ply with fibers in the 0°-direction and a plain, balanced woven ply with tows in the $+45°/-45°$-direction. According to Mega and Banks-Sills (2019), another segment within the range of $\hat{K}_1^{(P)} \le \hat{K}_1 \le \hat{K}_1^{(N)}$ in the $\hat{K}_1$-$\hat{K}_2$ plane should be introduced, so that

$$\hat{K}_1 = \begin{cases} \min\left[\min\left(\hat{K}_1^{(N)}, \dfrac{\hat{K}_2 - I}{S}\right), \dfrac{\hat{K}_2 - \hat{K}_{2c}^{(N)}}{\beta^{(N)}}\right] & \text{for } \hat{K}_2 > 0 \\ \min\left[\max\left(\hat{K}_1^{(P)}, \dfrac{\hat{K}_2 - I}{S}\right), \dfrac{\hat{K}_2 - \hat{K}_{2c}^{(P)}}{\beta^{(P)}}\right] & \text{for } \hat{K}_2 < 0. \end{cases} \tag{4.18}$$

This criterion is shown in Fig. 4.14. In eq. (4.18), the intercept and slope of the new segment/line are denoted by I and S, respectively, and found to be $I = -5.22$ MPa$\sqrt{\text{m}}$ and $S = 4.02$. The new segment, branch number 3, was determined by means of linear interpolation between the two known points, which are $\left(\hat{K}_1^{(N)}, \min\left(\hat{K}_2^{(N)}\right)\right)$ and $\left(\hat{K}_1^{(P)}, \max\left(\hat{K}_2^{(P)}\right)\right)$, in the $\hat{K}_1$-$\hat{K}_2$ plane. It should be noted that the minimum absolute values of $\hat{K}_2^{(N)}$ and $\hat{K}_2^{(P)}$ were determined based upon the $(\hat{K}_1, \hat{K}_2)$ data of the BD specimens which were employed in the derivation of $\hat{K}_1^{(N)}$ and $\hat{K}_1^{(P)}$, respectively. For a normalizing length parameter of $\hat{L} = 100$ μm, those values of $\hat{K}_2$ were found to be $\hat{K}_2^{(N)} = 0.66$ MPa$\sqrt{\text{m}}$ and $\hat{K}_2^{(P)} = -0.65$ MPa$\sqrt{\text{m}}$, respectively. The point of intersection

between the introduced straight line and the $\hat{K}_1$-axis (where $\hat{K}_2 = 0$) determines the value of $\hat{K}_{1c}$, as may be seen in Fig. 4.14, where it was obtained as $\hat{K}_{1c} = 1.30$ MPa$\sqrt{\text{m}}$. Coincidentally, this is the same value as that for the criterion shown in Fig. 4.13.

As may be seen in Figs. 4.12 through 4.14, there is much scatter in the data about the criteria. To employ such criteria for a structure fabricated from this laminate with a straight through delamination as that considered here, one calculates the stress intensity factors $\hat{K}_1$, $\hat{K}_2$ and K_{III}. Neglecting K_{III}, if the points $(\hat{K}_1, \hat{K}_2)$ are within the criterion, one may assume that catastrophic failure will not occur. If the points are outside the criterion, then failure is expected. For all of the criteria, considering each specimen individually, it was observed that all the $(\hat{K}_1, \hat{K}_2)$ points of specimens **sp6.2**, **sp8.1**, **sp10.1** and **sp14.2** are outside the failure criteria, where failure is assumed to occur. However, all data points of specimens **sp12.2**, **sp6.1**, **sp10.2**, **sp15.1** and **sp16.1** are inside the criteria, where failure is unexpected. For all other specimens, considering each specimen individually, it was observed that the $(\hat{K}_1, \hat{K}_2)$ points along the delamination front cut through the failure curve. It is postulated that once some of the points along the delamination front are critical, the delamination will propagate carrying the remainder of the points to failure. The specimens for which all points are within the failure criterion, are a motivating factor to carry out a statistical analysis. Later, a three-dimensional criterion will be treated, in which the values of K_{III} are also considered.

In Banks-Sills (2015), two statistical models, the t-distribution for statistical intervals (Whitmore, 1986; Luko and Neubauer, 2011) and the z-variate for determination of a probability and confidence interval (Natrella, 1963), were employed for the case of 10% probability of unexpected failure. These statistical tools were applied to different bimaterial interfaces for which the BD specimen with delamination/crack along an interface was introduced. It should be noted that for each case of a bimaterial interface presented in Banks-Sills (2015), the statistical analyses were imposed upon the average value of $\overline{\mathcal{G}}_{1c}$ in eq. (4.11). It was shown in Banks-Sills (2015) that a failure curve determined by means of the z-variate model is more conservative than that obtained by means of the t-distribution for all examined bimaterial interfaces. Thus, it is proposed here to apply the z-variate probability analysis to the criterion given in eq. (4.18), with some required adaptations.

Since in this investigation $\hat{K}_1$ in eq. (4.18) depends upon $\hat{K}_2$, unlike the cases presented in Banks-Sills (2015) where $\hat{K}_{1c}$ was found to be constant for all values of $\hat{K}_2$, the procedure must be extended. For simplicity, an auxiliary right-hand coordinate system may be defined, as shown schematically in Fig. 4.15, so that the experimental data may be described by both $\hat{K}_1$-$\hat{K}_2$ and $\hat{K}_1'$-$\hat{K}_2'$ axes. For the region where $\hat{K}_2 < \hat{K}_2^\sharp$, as shown in Fig. 4.15, $\hat{K}_1$ is nearly constant in the $\hat{K}_1$-$\hat{K}_2$ plane, whereas for the region where $\hat{K}_2 > \hat{K}_2^\sharp$, $\hat{K}_1'$ is nearly constant in the $\hat{K}_1'$-$\hat{K}_2'$ plane. The values of these constants are required. To this

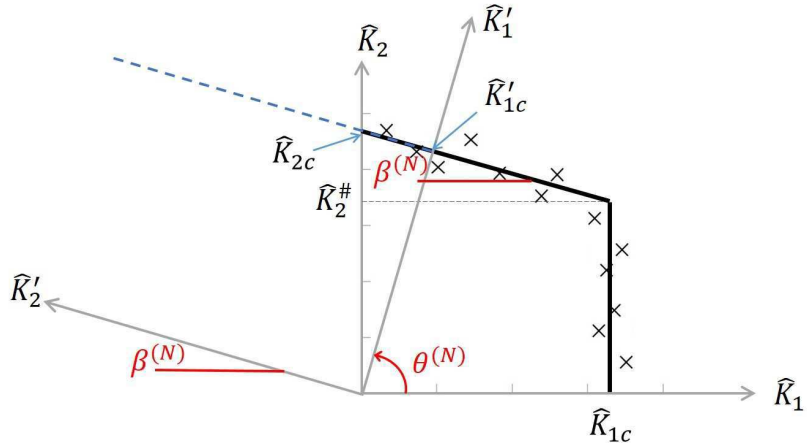

Figure 4.15: Schematic plot of experimental data set for $\hat{K}_2 > 0$ in the $\hat{K}_1$-$\hat{K}_2$ plane and in the auxiliary $\hat{K}_1'$-$\hat{K}_2'$ plane: $\hat{K}_1$ is nearly constant until $\hat{K}_2 = \hat{K}_2^{\sharp}$, then $\hat{K}_1'$ is nearly constant.

end, it may be seen that the slope of the $\hat{K}_2'$-axis is the same as the slope of the oblique criterion line, namely, $\beta^{(N)}$. Hence, the relationship between the angle of rotation $\theta^{(N)}$, which is shown in Fig. 4.15, and the slope of the oblique line $\beta^{(N)}$ is given by

$$\beta^{(N)} = -\cot\theta^{(N)} \qquad \text{for } \hat{K}_2 > \hat{K}_2^{\sharp}\,. \tag{4.19}$$

For $\hat{K}_2 < 0$,

$$\beta^{(P)} = \cot\theta^{(P)} \qquad \text{for } \hat{K}_2 < \hat{K}_2^{\sharp}\,, \tag{4.20}$$

where $\theta^{(P)}$ is the rotation angle of the $\hat{K}_1'$-$\hat{K}_2'$-axes for $\hat{K}_2 < 0$. Rotation of the $\hat{K}_1$-$\hat{K}_2$ coordinate system to the $\hat{K}_1'$-$\hat{K}_2'$ coordinate system, for $\hat{K}_2$ both positive and negative, results in the following expressions

$$\begin{Bmatrix} \hat{K}_1' \\ \hat{K}_2' \end{Bmatrix} = \begin{cases} \begin{bmatrix} \cos\theta^{(N)} & \sin\theta^{(N)} \\ -\sin\theta^{(N)} & \cos\theta^{(N)} \end{bmatrix} \begin{Bmatrix} \hat{K}_1 \\ \hat{K}_2 \end{Bmatrix} & \text{for } \hat{K}_2 > 0 \\ \begin{bmatrix} \cos\theta^{(P)} & -\sin\theta^{(P)} \\ \sin\theta^{(P)} & \cos\theta^{(P)} \end{bmatrix} \begin{Bmatrix} \hat{K}_1 \\ \hat{K}_2 \end{Bmatrix} & \text{for } \hat{K}_2 < 0. \end{cases} \tag{4.21}$$

Using the relationships in eqs (4.19) and (4.20), it may be shown that

$$\begin{Bmatrix} \hat{K}_1' \\ \hat{K}_2' \end{Bmatrix} = \begin{cases} \dfrac{1}{\sqrt{1+\beta^{(N)2}}} \begin{bmatrix} -\beta^{(N)} & 1 \\ -1 & -\beta^{(N)} \end{bmatrix} \begin{Bmatrix} \hat{K}_1 \\ \hat{K}_2 \end{Bmatrix} & \text{for } \hat{K}_2 > 0 \\ \dfrac{1}{\sqrt{1+\beta^{(P)2}}} \begin{bmatrix} \beta^{(P)} & -1 \\ 1 & \beta^{(P)} \end{bmatrix} \begin{Bmatrix} \hat{K}_1 \\ \hat{K}_2 \end{Bmatrix} & \text{for } \hat{K}_2 < 0. \end{cases} \tag{4.22}$$

The reader may recall that $\beta^{(N)} < 0$ and $\beta^{(P)} > 0$.

Table 4.12: Parameters of eq. (4.23) obtained for $\hat{L} = 100$ μm.

$\hat{K}_1$ (MPa$\sqrt{\text{m}}$)	N	K	s (MPa$\sqrt{\text{m}}$)	$\hat{K}_1^*$ (MPa$\sqrt{\text{m}}$)	n
$\hat{K}_1^{'(N)} = 2.40$	260	1.42	0.08	$\hat{K}_1^{'(N)*} = 2.29$	18
$\hat{K}_1^{(N)} = 1.46$	120	1.50	0.07	$\hat{K}_1^{(N)*} = 1.35$	6
$\hat{K}_1^{(P)} = 1.14$	120	1.50	0.06	$\hat{K}_1^{(P)*} = 1.04$	8
$\hat{K}_1^{'(P)} = 2.33$	80	1.55	0.11	$\hat{K}_1^{'(P)*} = 2.16$	4

For a normalizing length parameter of $\hat{L} = 100$ μm, the values of $\hat{K}_1^{'(N)}$ and $\hat{K}_1^{'(P)}$ are obtained. For $\hat{K}_1^{'(N)}$, the $\hat{K}_1$ and $\hat{K}_2$ values of data points from specimens **sp12.1**, **sp2.1**, **sp11.2**, **sp12.2**, **sp13.2**, **sp3.2**, **sp8.1** and **sp11.1** were substituted into eq. $(4.22)_1$ to determine the value of $\hat{K}_1'$. These were averaged to obtain $\hat{K}_1^{'(N)} = 2.40$ MPa$\sqrt{\text{m}}$. Similarly, the value of $\hat{K}_1^{'(P)}$ was found as 2.33 MPa$\sqrt{\text{m}}$, from specimens **sp15.2**, **sp7.1**, **sp6.1** and **sp5.2**. Use was made of eq. $(4.22)_2$. These values are shown in column 1 of Table 4.12. Values found earlier for $\hat{K}_1^{(N)}$ and $\hat{K}_1^{(P)}$ in Table 4.11 are also displayed in Table 4.12.

In a similar manner to that presented in Banks-Sills (2015), where a reduced value of $\overline{\mathcal{G}}_{1c}$ was introduced, the value of $\hat{K}_1^{(j)}$ for $j = N, P$ in eq. (4.18) is reduced by a factor proportional to its standard deviation s given as

$$\hat{K}_1^{(j)*} = \hat{K}_1^{(j)} - Ks. \tag{4.23}$$

In eq. (4.23), $\hat{K}_1^{(j)*}$ is the reduced value of $\hat{K}_1^{(j)}$ in the $\hat{K}_1$-$\hat{K}_2$ coordinate systems, for both positive and negative values of $\hat{K}_2$. In the auxiliary $\hat{K}_1'$-$\hat{K}_2'$ coordinate systems, a reduced value of $\hat{K}_1^{'(j)}$ is denoted by $\hat{K}_1^{'(j)*}$. It may be quantified in a similar manner to that expressed in eq. (4.23). The statistical factor K is determined according to the statistical model used in the probability analysis calculation. For the z-variate model,

$$K \simeq \frac{|z_P| + \sqrt{z_P^2 - ab}}{a} \tag{4.24}$$

where

$$a = 1 - \frac{z_\gamma^2}{2(N-1)} \qquad \text{and} \qquad b = z_P^2 - \frac{z_\gamma^2}{N}. \tag{4.25}$$

The number of data points/samples is denoted by N, z is the standard variate and the subscripts P and γ in eqs. (4.24) and (4.25) represent probability and confidence, respectively. For the case of only a 10% probability that a failed $(\hat{K}_1, \hat{K}_2)$ data point will be obtained within the safe zone, with a confidence of 95%, one may choose $P = 0.1$ and $\gamma = 0.95$. Consequently, $z_P = z_{0.1} = -1.2816$ and $z_\gamma = z_{0.95} = 1.6448$ (Anderson et al., 2015). The values of the z-variate parametres used in the statistical analysis, are detailed

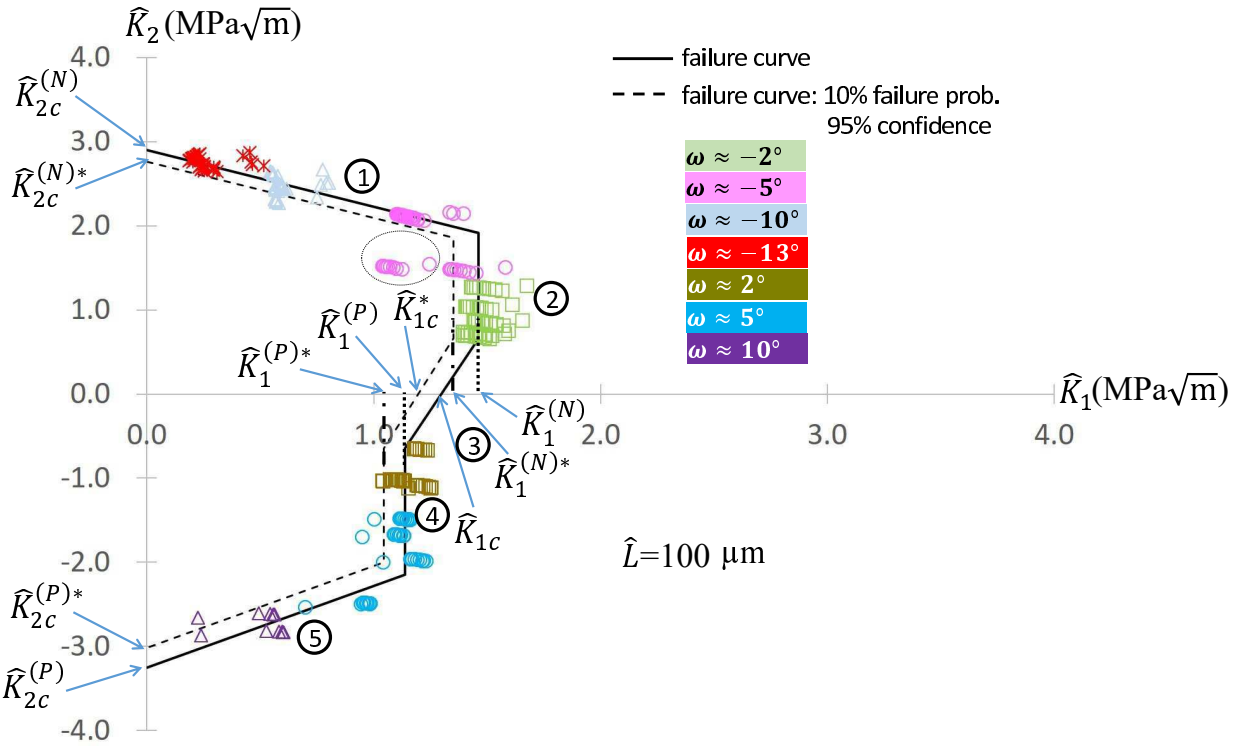

Figure 4.16: The stress intensity factor $\hat{K}_2$ versus $\hat{K}_1$ as described in eq. (4.18) and the reduced failure curve based upon eq. (4.26) for a 10% probability of unexpected failure with a 95% confidence; both for $\hat{L} = 100$ μm.

in Table 4.12. For each group of specimens in a calculation, the sample number N is presented in column 2. Using eqs. (4.24) and (4.25), values of K are found and are given in column 3 of Table 4.12. The standard deviation s, for each average value in column 1, is presented in column 4 of Table 4.12. By employing eq. (4.23), the reduced values of $\hat{K}_1^{(j)*}$ and $\hat{K}_1^{\prime(j)*}$ may be calculated. Those values are also presented in Table 4.12, for $\hat{L} = 100$ μm.

Based upon the reduced values obtained for $\hat{K}_1^{(j)*}$ and $\hat{K}_1^{\prime(j)*}$ and while using the proper transformation (rotation) between the $\hat{K}_1'$-$\hat{K}_2'$ coordinate systems and the $\hat{K}_1$-$\hat{K}_2$ coordinate system, which may be retrieved from eqs. (4.22), the reduced fracture criterion of eq. (4.18) may be determined as

$$\hat{K}_1 = \begin{cases} \min\left[\min\left(\hat{K}_1^{(N)*}, \dfrac{\hat{K}_2 - I^*}{S^*}\right), \dfrac{\hat{K}_2 - \hat{K}_{2c}^{(N)*}}{\beta^{(N)}}\right] & \text{for } \hat{K}_2 > 0 \\ \min\left[\max\left(\hat{K}_1^{(P)*}, \dfrac{\hat{K}_2 - I^*}{S^*}\right), \dfrac{\hat{K}_2 - \hat{K}_{2c}^{(P)*}}{\beta^{(P)}}\right] & \text{for } \hat{K}_2 < 0, \end{cases} \tag{4.26}$$

which is plotted as the dashed curve in Fig. 4.16 for $\hat{L} = 100$ μm.

Table 4.13: Additional parameters used in the determination of the fracture criteria (before and after the statistical analysis) presented in Fig. 4.16 and obtained for $\hat{L} = 100$ μm.

statistical analysis	$\hat{K}_{1c}$ (MPa$\sqrt{\text{m}}$)	I (MPa$\sqrt{\text{m}}$)	S	$\hat{K}_{2c}^{(N)}$ (MPa$\sqrt{\text{m}}$)	$\hat{K}_{2c}^{(P)}$ (MPa$\sqrt{\text{m}}$)	$\hat{K}_{2}^{(N)\sharp}$ (MPa$\sqrt{\text{m}}$)	$\hat{K}_{2}^{(P)\sharp}$ (MPa$\sqrt{\text{m}}$)
before	1.30	-5.22	4.02	2.90	-3.25	1.91	-2.15
after (with *)	1.20	-5.10	4.27	2.76	-3.01	1.86	-2.00

In eq. (4.26), $\hat{K}_{2c}^{(N)*}$ and $\hat{K}_{2c}^{(P)*}$ are the reduced values of $\hat{K}_{2c}^{(N)}$ and $\hat{K}_{2c}^{(P)}$, respectively, on branches 1 and 5. The value of $\hat{K}_{2c}^{(N)*}$ was determined from the intersection point between the reduced oblique line, obtained by means of $\hat{K}_1^{\prime(N)*}$, and the vertical axis, where $\hat{K}_1 = 0$, as may be observed in Fig. 4.16. In a similar manner, the value of $\hat{K}_{2c}^{(P)*}$ was determined. In eq. (4.26), the intercept and slope of the reduced introduced segment, the dashed line denoted as branch 3 in Fig. 4.16, was determined. A line was drawn between the two known points, $\left(\hat{K}_1^{(N)*}, \min\left(\hat{K}_2^{(N)}\right)\right)$ and $\left(\hat{K}_1^{(P)*}, \max\left(\hat{K}_2^{(P)}\right)\right)$. For $\hat{L} = 100$ μm, their values were found to be $I^* = -5.10$ MPa$\sqrt{\text{m}}$ and $S^* = 4.27$. The point of intersection between the dashed branch 3 in Fig. 4.16 and the $\hat{K}_1$-axis (where $\hat{K}_2 = 0$) determines the value of $\hat{K}_{1c}^*$, as may be seen in Fig. 4.16, where it was obtained as $\hat{K}_{1c}^* = 1.20$ MPa$\sqrt{\text{m}}$. The values of some additional parameters, which were used in the determination of the fracture criteria shown in Fig. 4.16, before and after the statistical analysis, are listed in Table 4.13, for $\hat{L} = 100$ μm. While neglecting specimen **sp1.2**, from the dashed curve in Fig. 4.16, there is a 10% probability with a 95% confidence that the next data point will be within this curve and still the specimen will fail unexpectedly. The number of $(\hat{K}_1, \hat{K}_2)$ data points within the reduced failure curve is denoted by n and is shown in column 6 of Table 4.12. Indeed, it may be observed (also in Table 4.12) that less than 6.2% of the $(\hat{K}_1, \hat{K}_2)$ data points are within the reduced fracture criterion given in eq. (4.26). Thus, it may be concluded that the probability analysis that was carried out reduced the chance for an unexpected failure. It may be assumed that the region within the reduced fracture criterion is safe with a 90% probability with a 95% confidence. It should be noted that there is no specimen for which all points along the delamination front are within the statistically obtained failure curve.

Next, a three-dimensional failure surface is developed in terms of the critical interface energy release rate $\mathcal{G}_{ic}$ given in eq. (4.15), with $\hat{K}_1$ in eq. (4.18) substituted in eq. (4.16) and the phase angles $\hat{\psi}$ and ϕ defined in eqs. (1.12) and (1.14), respectively, with $L = \hat{L}$.

The criterion in eq. (4.18) may be expressed in terms of $\hat{K}_1$ and the phase angle $\hat{\psi}$ as

$$\hat{K}_1 = \begin{cases} \min\left(\hat{K}_1^{(N)}, \dfrac{\hat{K}_{2c}^{(N)}}{\tan\hat{\psi} - \beta^{(N)}}\right) & \text{for } \hat{\psi}^{(N)} \leq \hat{\psi} \\ \dfrac{I}{\tan\hat{\psi} - S} & \text{for } \hat{\psi}^{(P)} \leq \hat{\psi} \leq \hat{\psi}^{(N)} \\ \min\left(\hat{K}_1^{(P)}, \dfrac{\hat{K}_{2c}^{(P)}}{\tan\hat{\psi} - \beta^{(P)}}\right) & \text{for } \hat{\psi} \leq \hat{\psi}^{(P)}. \end{cases} \tag{4.27}$$

In eq. (4.27), the values of $\hat{K}_1^{(j)}$, $\hat{K}_{2c}^{(j)}$ and $\beta^{(j)}$ for $j = N, P$ may be found in Table 4.11, whereas the values of $\hat{K}_{1c}$, I and S may be found in Table 4.13. The phase angles $\hat{\psi}^{(j)}$ may be obtained as

$$\hat{\psi}^{(j)} = \arctan\left(\frac{I}{\hat{K}_1^{(j)}} + S\right) \qquad \text{for } j = N, P. \tag{4.28}$$

The reduced criterion in eq. (4.26) also may be expressed in terms of $\hat{K}_1$ and $\hat{\psi}$. To this end, the relations as presented in eq.(4.28) are rewritten in terms of the reduced parameters I^*, S^* and $\hat{K}_1^{(j)*}$. These are substituted into eq. (4.26) to obtain

$$\hat{K}_1 = \begin{cases} \min\left(\hat{K}_1^{(N)*}, \dfrac{\hat{K}_{2c}^{(N)*}}{\tan\hat{\psi} - \beta^{(N)}}\right) & \text{for } \hat{\psi}^{(N)*} \leq \hat{\psi} \\ \dfrac{I^*}{\tan\hat{\psi} - S^*} & \text{for } \hat{\psi}^{(P)*} \leq \hat{\psi} \leq \hat{\psi}^{(N)*} \\ \min\left(\hat{K}_1^{(P)*}, \dfrac{\hat{K}_{2c}^{(P)*}}{\tan\hat{\psi} - \beta^{(P)}}\right) & \text{for } \hat{\psi} \leq \hat{\psi}^{(P)*}. \end{cases} \tag{4.29}$$

In eq. (4.29), the values of $\beta^{(j)}$ for $j = N, P$ may be found in Table 4.11, whereas the values of $\hat{K}_1^{(j)*}$ are listed in Table 4.12. The values of $\hat{K}_{1c}^*$, $\hat{K}_{2c}^{(j)*}$, I^* and S^* may be found in Table 4.13.

The criterion in eq. (4.27) may be rewritten in terms of the in-plane phase angle $\hat{\psi}$, so that each of the branches in Fig. 4.16 is explicitly given as

$$\hat{K}_1 = \begin{cases} \dfrac{\hat{K}_{2c}^{(N)}}{\tan\hat{\psi} - \beta^{(N)}} & \text{for } \hat{\psi}^{(N)\sharp} \leq \hat{\psi} < \pi/2 \\ \hat{K}_1^{(N)} & \text{for } \hat{\psi}^{(N)} \leq \hat{\psi} \leq \hat{\psi}^{(N)\sharp} \\ \dfrac{I}{\tan\hat{\psi} - S} & \text{for } \hat{\psi}^{(P)} \leq \hat{\psi} \leq \hat{\psi}^{(N)} \\ \hat{K}_1^{(P)} & \text{for } \hat{\psi}^{(P)\sharp} \leq \hat{\psi} \leq \hat{\psi}^{(P)} \\ \dfrac{\hat{K}_{2c}^{(P)}}{\tan\hat{\psi} - \beta^{(P)}} & \text{for } -\pi/2 < \hat{\psi} \leq \hat{\psi}^{(P)\sharp}, \end{cases} \tag{4.30}$$

Table 4.14: Values of $\hat{\psi}$ used in the determination of the fracture criteria in eqs. (4.30) and (4.32) before and after the statistical analysis, respectively, obtained for $\hat{L} = 100$ μm.

statistical analysis	$\hat{\psi}^{(P)\sharp}$ (rad)	$\hat{\psi}^{(P)}$ (rad)	$\hat{\psi}^{(N)}$ (rad)	$\hat{\psi}^{(N)\sharp}$ (rad)
before	-1.08	-0.52	0.42	0.92
after (with *)	-1.09	-0.55	0.46	0.94

where

$$\hat{\psi}^{(j)\sharp} = \arctan\left(\frac{\hat{K}_{2c}^{(j)}}{\hat{K}_1^{(j)}} + \beta^{(j)}\right) = \arctan\left(\frac{\hat{K}_2^{(j)\sharp}}{\hat{K}_1^{(j)}}\right) \qquad \text{for } j = N, P. \tag{4.31}$$

In eq. (4.31), $\hat{K}_2^{(j)\sharp}$ for $j = N, P$ are the positive and negative values of $\hat{K}_2$, respectively, for which a reduction in mode 1 begins. Such behavior of the experimental data sets is schematically shown in Fig. 4.11b for positive values of $\hat{K}_2$, where $\hat{K}_2^{(N)\sharp} = \hat{K}_2^{\sharp}$. The values of $\hat{K}_2^{(j)\sharp}$ for $j = N, P$ may be found in Table 4.13. In a similar manner, eq. (4.29) is rewritten to obtain

$$\hat{K}_1 = \begin{cases} \dfrac{\hat{K}_{2c}^{(N)*}}{\tan\hat{\psi} - \beta^{(N)}} & \text{for } \hat{\psi}^{(N)\sharp *} \le \hat{\psi} < \pi/2 \\ \hat{K}_1^{(N)*} & \text{for } \hat{\psi}^{(N)*} \le \hat{\psi} \le \hat{\psi}^{(N)\sharp *} \\ \dfrac{I^*}{\tan\hat{\psi} - S^*} & \text{for } \hat{\psi}^{(P)*} \le \hat{\psi} \le \hat{\psi}^{(N)*} \\ \hat{K}_1^{(P)*} & \text{for } \hat{\psi}^{(P)\sharp *} \le \hat{\psi} \le \hat{\psi}^{(P)*} \\ \dfrac{\hat{K}_{2c}^{(P)*}}{\tan\hat{\psi} - \beta^{(P)}} & \text{for } -\pi/2 < \hat{\psi} \le \hat{\psi}^{(P)\sharp *}, \end{cases} \tag{4.32}$$

where

$$\hat{\psi}^{(j)\sharp *} = \arctan\left(\frac{\hat{K}_{2c}^{(j)*}}{\hat{K}_1^{(j)*}} + \beta^{(j)}\right) = \arctan\left(\frac{\hat{K}_2^{(j)\sharp *}}{\hat{K}_1^{(j)*}}\right) \qquad \text{for } j = N, P. \tag{4.33}$$

In eq. (4.33), $\hat{K}_2^{(j)\sharp *}$ for $j = N, P$ is the value of $\hat{K}_2$ at the intersection between the lines $\hat{K}_2 = \hat{K}_1\beta^{(j)} + \hat{K}_{2c}^{(j)*}$ and $\hat{K}_1 = \hat{K}_1^{(j)*}$. It may be noted that $|\hat{K}_2^{(j)\sharp *}| < |\hat{K}_2^{(j)\sharp}|$, however, $|\hat{K}_1^{(j)*}|$ is sufficiently smaller than $|\hat{K}_1^{(j)}|$, so that $|\hat{\psi}^{(j)\sharp *}| > |\hat{\psi}^{(j)\sharp}|$. The important values of $\hat{\psi}$ for both the original and statistical curves may be found in Table 4.14.

In Fig. 4.17a, the curves of $\hat{K}_1$ in eqs. (4.30) and (4.32) as a function of the in-plane phase angle $\hat{\psi}$ are plotted, for a normalizing length parameter of $\hat{L} = 100$ μm. The mode 1 energy release rate $\mathcal{G}_1$ in eq. (4.16), with the new definitions of $\hat{K}_1$ in eqs. (4.30) and (4.32) substituted into eq. (4.16), are presented in Fig. 4.17b as a function of $\hat{\psi}$ for

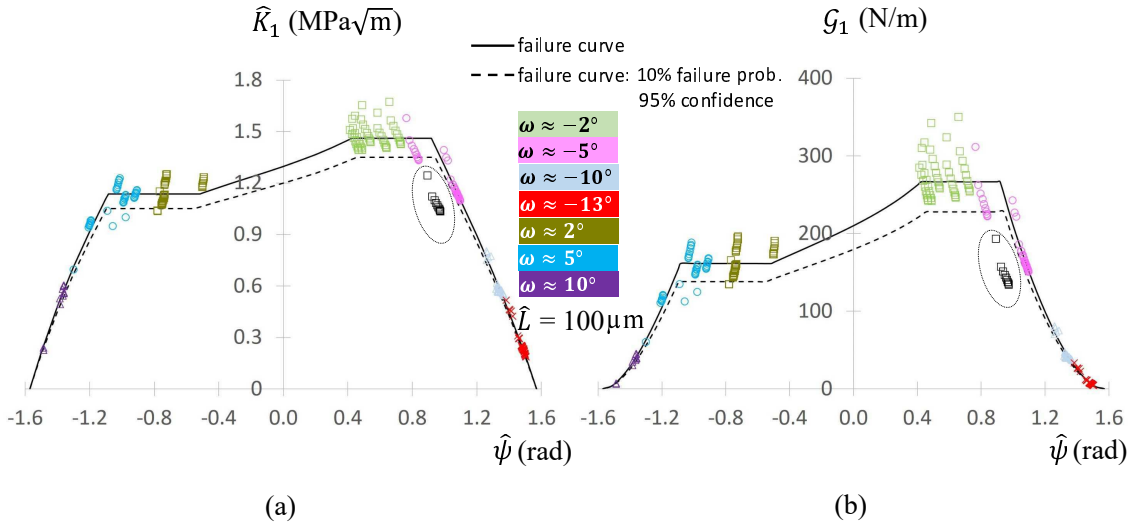

Figure 4.17: (a) $\hat{K}_1$ from eqs. (4.30) and (4.32) as a function of the in-plane phase angle $\hat{\psi}$, and (b) the derived mode 1 energy release rate $\mathcal{G}_1$ in eq. (4.16) versus $\hat{\psi}$ ($\hat{L} = 100$ μm).

$\hat{L} = 100$ μm. Recall that since specimen **sp1.2** was found to have pores, its data points were excluded from the determination of the parameters in eq. (4.18). Thus, they are also excluded from the determination of $\hat{K}_1$ and $\mathcal{G}_1$ versus ψ. Nevertheless, these points are shown in Figs. 4.17a and 4.17b and are surrounded by an ellipse.

Based upon the relationship between $\hat{K}_1$ and $\hat{K}_2$ in eq. (4.18), and the definitions of the in-plane mode mixity angle $\hat{\psi}$ in eq. (1.12) and the mode 1 energy release rate $\mathcal{G}_1$ in eq. (4.16), with the new definition of $\hat{K}_1$ in eq. (4.30) substituted into eq. (4.16), quantification of the in-plane energy release rate $\mathcal{G}_{i-2D}$ may be made, as presented in Fig. 4.18. In Fig. 4.18, the values of the energy release rate calculated from 20 slices, one element thick, along the delamination front of each BD specimen presented in Table 4.10 are projected onto the $\mathcal{G}_i, \hat{\psi}$-plane, where $K_{III} = \phi = 0$. As may be observed, the failure curve in eq. (4.15) with $\phi = 0$, and $\hat{K}_1$ in eq. (4.30) substituted into eq. (4.16), fits well the in-plane energy release rate data calculated from eq. (1.17) with $K_{III} = 0$ and the $(\hat{K}_1, \hat{K}_2)$ data of the BD specimens at failure. Also, it may be observed in Fig. 4.18 that there is scatter about this solid curve and that the values of the in-plane energy release rate of specimen **sp1.2**, shown with an ellipse, are below the 2D failure curve at a location which is supposed to be safe from failure.

The statistically obtained $\mathcal{G}_{i-2D}$ failure curve is also plotted in Fig. 4.18 as the dashed curve, which was obtained by using eq. (4.15) with $\phi = 0$ and $\hat{K}_1$ in eq. (4.32) substituted into eq. (4.16). While ignoring specimen **sp1.2**, it may be observed that less than 6.2% of the $(\hat{K}_1, \hat{K}_2)$ data points, a total of 36 points, are below the statistical failure curve, which is based upon the statistically obtained fracture criterion given in eq. (4.32). For

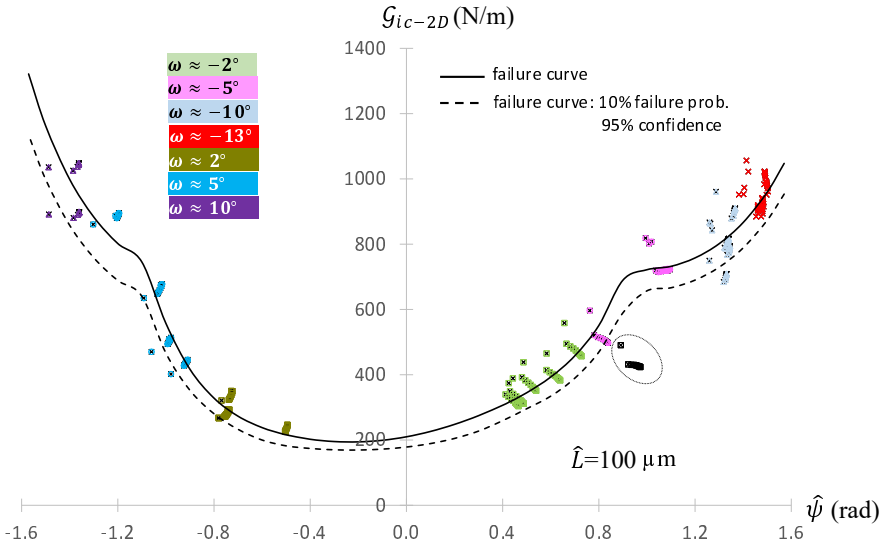

Figure 4.18: The in-plane energy release rate $\mathcal{G}_{i-2D}(\hat{\psi})$ for $\hat{L} = 100$ μm, given in eq. (4.15) with $\phi = 0$

.

each specimen, all data from points along the delamination front or some data is above the dashed curve, implying that failure has taken place.

It should be noted that there are materials which are $\hat{L}$ sensitive, such as the glass/epoxy pair in Banks-Sills et al. (1999); but the current pair of materials was not. When comparing the value obtained for $\mathcal{G}_{1c}$ with $\hat{L} = 0.1$ mm, 0.5 mm, 1 mm and 10 mm, $\mathcal{G}_{1c}$ changes by a maximum of 1% for $\hat{L} = 10$ mm as compared to that obtained with $\hat{L} = 0.1$ mm. This indicates that this material pair is not sensitive to changes in $\hat{L}$. It is also possible to examine other quantities, such as $\hat{K}_{2c}^{(N)}$, $\hat{K}_{1}^{(N)}$, $\hat{K}_{1}^{(P)}$, $\hat{K}_{2c}^{(P)}$ and $\hat{K}_{1c}$. A maximum percent difference of 4% was obtained for $\hat{K}_{1}^{(P)}$ calculated with $\hat{L} = 10$ mm as compared to that calculated with $\hat{L} = 0.1$ mm; lower percent of differences were obtained for the other quantities.

The three-dimensional criterion in eq. (4.15), with $\hat{K}_1$ in eq. (4.30) substituted into eq. (4.16) and the phase angles $\hat{\psi}$ and ϕ defined in eqs. (1.12) and (1.14), respectively, with $L = \hat{L}$, is plotted; several views are shown in Fig. 4.19. The $(\mathcal{G}_{ic}, \hat{\psi}, \phi)$ data of the BD specimens at failure are also shown in Fig. 4.19. For the criterion presented in Fig. 4.19, considering each specimen individually, it was observed that not all of the $(\mathcal{G}_{ic}, \hat{\psi}, \phi)$ points along the delamination front are above the criterion, in the failure region. It was found that all data points of specimens **sp6.2**, **sp8.1**, **sp10.1** and **sp14.2** are above the failure surface, where failure is assumed to occur, as expected. All data points of specimens **sp12.2**, **sp6.1**, **sp10.2**, **sp15.1** and **sp16.1** are below the surface, in the safe zone; this is considered as scatter in experimental data. For all other specimens, the data points

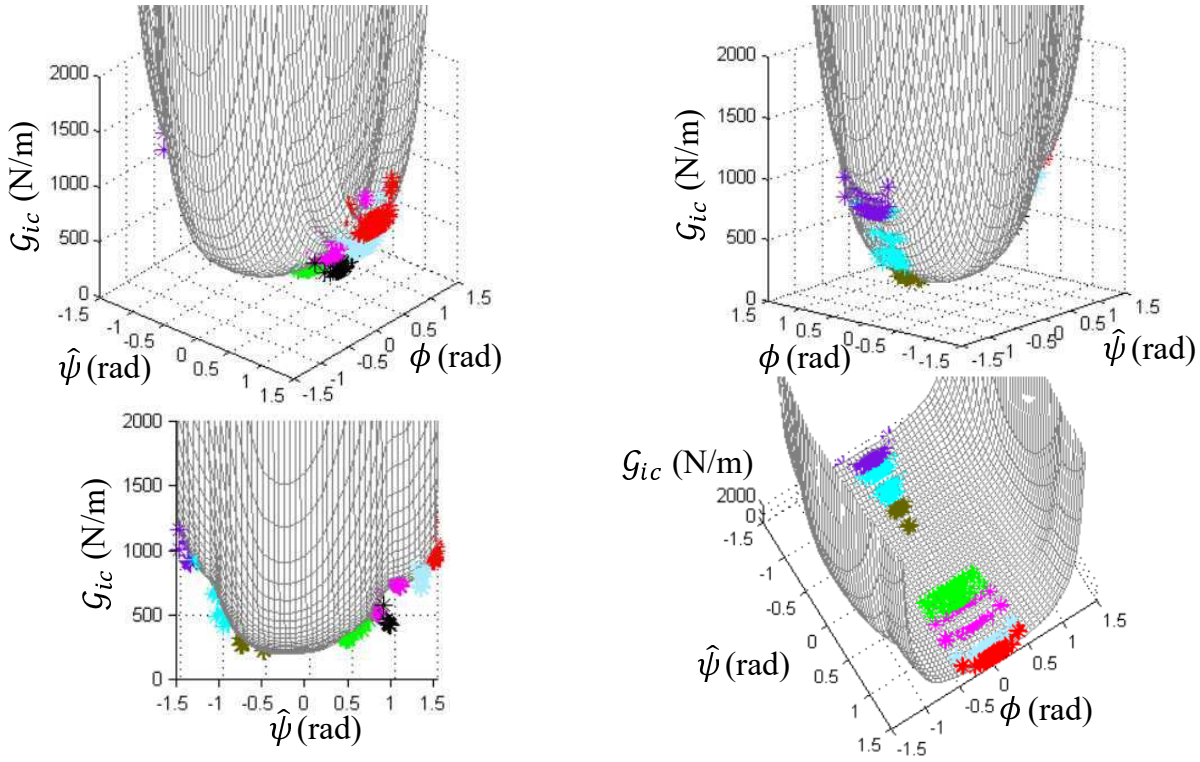

Figure 4.19: Different views of the three-dimensional failure surface obtained for a delamination along an interface between a plain woven fabric with yarn in the 0°/90°-directions and in the $+45°/-45°$-directions ($\hat{L} = 100$ μm).

cut through the failure surface. Recall, that it is postulated that once some of the points along the delamination front are critical, the delamination will propagate carrying the remainder of the points to failure.

It may be noted that for each BD specimen, the interface energy release rate related to the in-plane stress intensity factors, $\mathcal{G}_{i-2D}$, is dominant throughout the specimen thickness. Its contribution to the total and critical interface energy release rate $\mathcal{G}_{ic}$, which was found to be nearly constant throughout the specimen thickness in Fig. 4.10, is significant; varying from 100% at the specimen mid-thickness (where $K_{III} = \phi = 0$) to more than 93% at $x_3/B = 0.075$ and 0.925, which are very close to the specimen outer surfaces. For all specimens, the contribution of $\mathcal{G}_{i-2D}$ to $\mathcal{G}_{ic}$ at specimen outer surfaces, where $x_3/B = 0$ and 1, was found to be greater than 84.3%. Thus, it is concluded that $\mathcal{G}_{i-2D}$ governs the failure of the examined BD specimens.

A statistically obtained three-dimensional failure surface may be generated from the three-dimensional criterion in eq. (4.15), while substituting the statistically obtained fracture criterion given in eq. (4.32) into eq. (4.16). This failure surface is plotted with different views shown in Fig. 4.20. While considering each specimen individually, it was observed

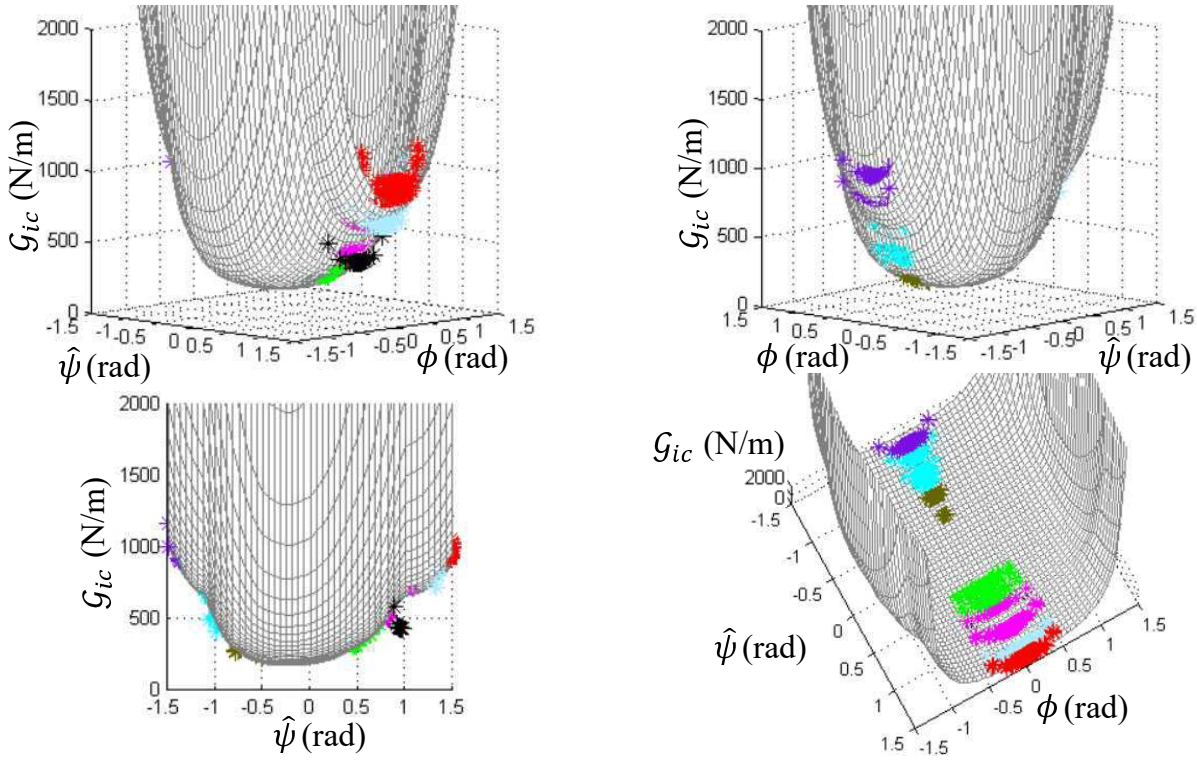

Figure 4.20: Different views of the statistically obtained three-dimensional failure surface based upon eq. (4.32), for a 10% probability of unexpected failure with a 95% confidence ($\hat{L} = 100$ μm).

that not all, but most, of the $(\mathcal{G}_{ic}, \hat{\psi}, \phi)$ points along the delamination front are above the statistical failure surface, where failure is assumed to occur. The number of experimental data points $(\mathcal{G}_{ic}, \hat{\psi}, \phi)$ which are below the statistical failure surface is the same as presented in Table 4.12, noted by n, which is for both two and three dimensions. It may also be observed in Fig. 4.20 that there is scatter about this surface too and that the values of the interface energy release rate data points of specimen **sp1.2**, which are marked by the black stars in Figs. 4.19 and 4.20, are all below the statistical 3D-criterion at a location which is supposed to be safe from failure. While ignoring specimen **sp1.2**, it may be observed that less than 6.2% of the $(\mathcal{G}_{ic}, \hat{\psi}, \phi)$ data points, a total of 36 points, are below the statistical failure surface, which is based upon the statistical fracture criterion given in eq. (4.32). Again, it may be concluded that the probability analysis, that was carried out, reduced the chance for an unexpected/premature failure. It may be assumed that the region below the reduced 3D-surface is safe from failure with a 90% probability and 95% confidence. This assumption is correct as long as the specimen or structure is free of pores or other initial damage as with specimen **sp1.2**.

It may be noted that the mixed-mode fracture toughness measured by means of the BD test specimen, as detailed in this chapter, has been published in Banks-Sills and Dolev

(2020). In Mega et al. (2020), a summary and comparison of test results obtained from BD mixed-mode fracture toughness tests of two different material systems, the MD carbon/epoxy prepreg plain woven plies considered here and the MD carbon/epoxy wet-layup composite studied in Mega and Banks-Sills (2019), have been presented. The delamination initiation deterministic failure criteria (2D and 3D) given in eqs. (4.18) and (4.27) and shown in Figs. 4.16, 4.18 and 4.19, as well as statistically obtained fracture initiation criteria (2D and 3D) given in eqs. (4.26) and (4.29) and shown in Figs. 4.16, 4.18 and 4.20, have been also published in Mega et al. (2020).

Chapter 5

Beam-type specimens: quasi-static tests

In this investigation, the double cantilever beam (DCB), calibrated-end loaded split (C-ELS) and mixed-mode end loaded split (MMELS) specimens were used for measuring the interface fracture toughness $\mathcal{G}_{ic}$ and R-curve behavior for nearly mode I, nearly mode II and in-plane mixed mode ratios, respectively, for a delamination between two plain balanced woven plies. The interface is the same as that investigated for the BD specimens and discussed at the very beginning of Chapters 1 and 4. As mentioned in Section 1.3, for woven MD laminate composites, there are no standardized fracture toughness test methods. Here, the existing standardized interlaminar fracture toughness test methods for unidirectional fiber reinforced laminate composites were used for guidance. These include the ASTM Standard D 5528-13 (2014) and ISO 15024 (2011) for mode I deformation and the ISO 15114 (2014) for mode II deformation. It should be noted here that, in general, for a delamination between plies with tows in different directions pure deformation modes cannot be attained. For DCB specimens there will be a small in-plane sliding component; for C-ELS specimens, a small opening component; and for MMELS, the modes 1 and 2 components will vary with delamination length.

The layup of all MD laminate composite beam-type configurations, is shown in Fig. 5.1, in which the red and gray layers represent the weave in the $0°/90°$ and $+45°/-45°$ directions, respectively. The composite strips containing an artificial delamination, which were used in preparing the different beam-type specimens, were cut via a water-jet machine from a composite plate, which was fabricated and autoclave cured. The $530\times885\times5$ mm^3 laminate composite plate was hand layered with 23 carbon/epoxy (G0814/913) prepreg plain woven plies, each $\sim$0.22 mm thick. The initial delamination length a_0, which was set to about 50 mm long, was introduced by means of a non-adhesive thin PTFE film, $\sim$12.8 μm thick. The material properties used to model the plain woven plies

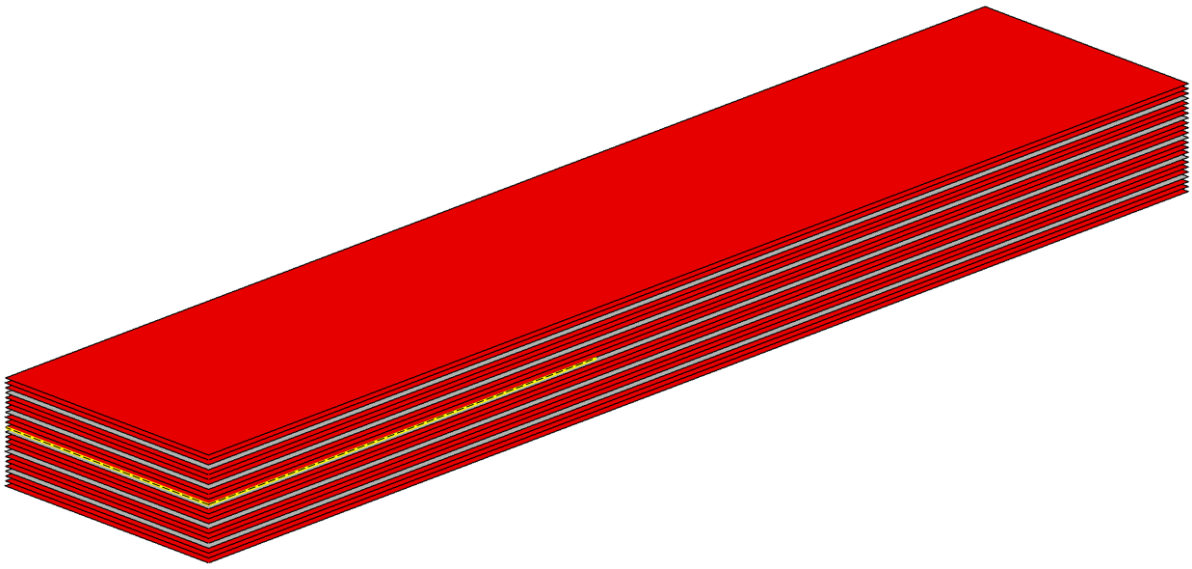

Figure 5.1: Beam-type specimen of an MD laminate composite layup. Position of delamination is illustrated in yellow.

with yarn in the 0°/90°-directions are presented in Table 2.1. The properties of the ply with yarn in the +45°/-45°-directions were obtained by rotating the properties of the 0°/90° ply about the x_2-axis shown in Fig. 1.1b by 45° (Ting, 1996, pp.54-55), and are also presented in Table 2.1. A ply group or stack constructed from the same plain woven plies has the same material properties as a single ply with its total thickness the sum of thicknesses of each ply within the ply group. The layup contains 23 carbon/epoxy (G0814/913) prepreg plain woven plies in the following stacking sequence: $[(0°/90°)_3, (+45°/-45°), (0°/90°)_3, (+45°/-45°), (0°/90°)_3$ // $(+45°/-45°), (0°/90°)_3, (+45°/-45°), (0°/90°)_3, (+45°/-45°), (0°/90°)_3]$ as shown in Fig. 5.1. The gray ply consists of a +45°/-45° plain woven ply; the red stacks are 0°/90° plies.

The three specimens used in this study are shown in Figs. 5.2a, 5.2b and 5.2c for the DCB, C-ELS and MMELS specimens, respectively. A test protocol is described in Sections 5.1.1, 5.2.1 and 5.3.1, for each specimen, respectively. A total of thirteen tests were performed with the three configurations to obtain approximately three distinct mode mixities, so that the failure behavior at various mode mixities was achieved. The specimens were analyzed by means of the FE method. Analyses are presented in Sections 5.1.2, 5.2.2 and 5.3.2 for each specimen type, respectively, and results are described in Sections 5.1.3, 5.2.3 and 5.3.3, respectively.

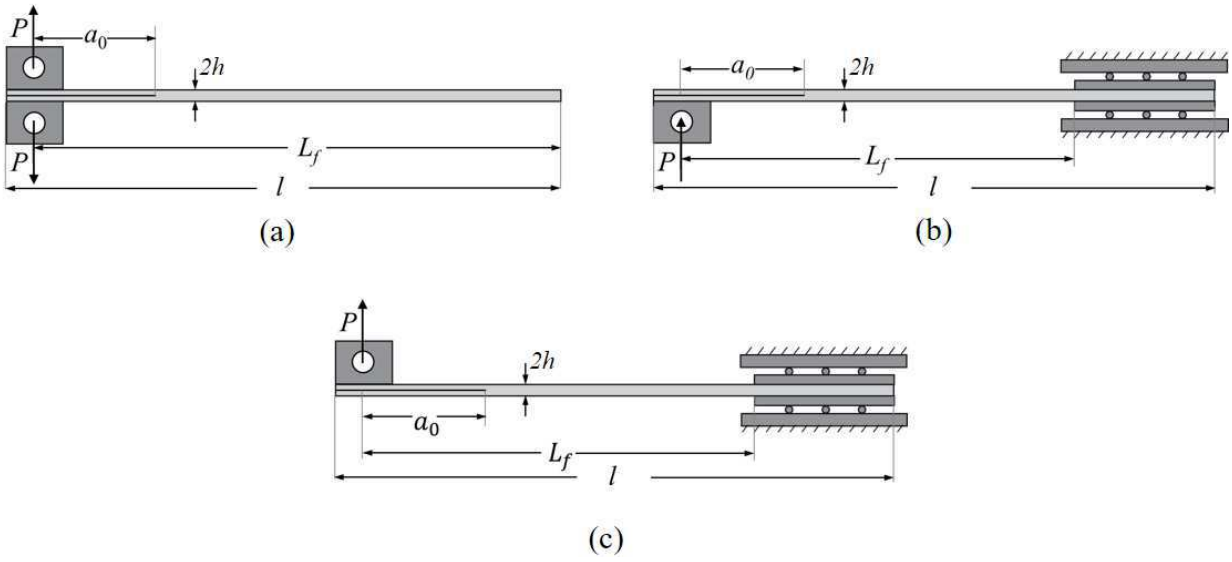

Figure 5.2: Illustration of beam-type specimens with load blocks: (a) DCB, (b) C-ELS and (c) MMELS.

5.1 DCB

Three quasi-static tests of delamination initiation and propagation were carried out on DCB specimens with the layup shown in Fig. 5.1. An illustration of a DCB specimen, is presented in Figs. 5.2a and 5.3a, where the geometric parameters l, b and $2h$ are the specimen length, width and height, respectively. Note that in the ASTM Standard D 5528-13 (2014), the height is denoted by h. The initial delamination length a_0 is measured from the artificially introduced delamination front to the load line. It should be noted that the currently considered interface was already investigated in Banks-Sills et al. (2013) and Simon et al. (2017), in which DCB quasi-static tests were carried out on quasi-isotropic laminate specimens made of the same plain woven composite material (G0814/913 carbon/epoxy) with the same interface, as presented in Fig. 1.1b. Those specimens contained 15 plies alternating between 0°/90° and +45°/-45°-directions. In Banks-Sills et al. (2013), the first specimen batch was used for measuring the nearly mode I fracture toughness of the 15 ply laminate; whereas, the second specimen batch was used in Ishbir et al. (2014) for measuring the nearly mode I fatigue delamination propagation rate, da/dN, under constant amplitude displacement cycles with a constant displacement ratio of $R_d = 0.1$. The third, fourth and fifth specimen batches were used in Simon et al. (2017) in order to develop a methodology for predicting the nearly mode I delamination growth rate under various R-ratios. The sixth specimen batch, with 69 woven plies was used in Chapter 4 for measuring the mixed mode interface fracture toughness $\mathcal{G}_{ic}$ while employing the BD test

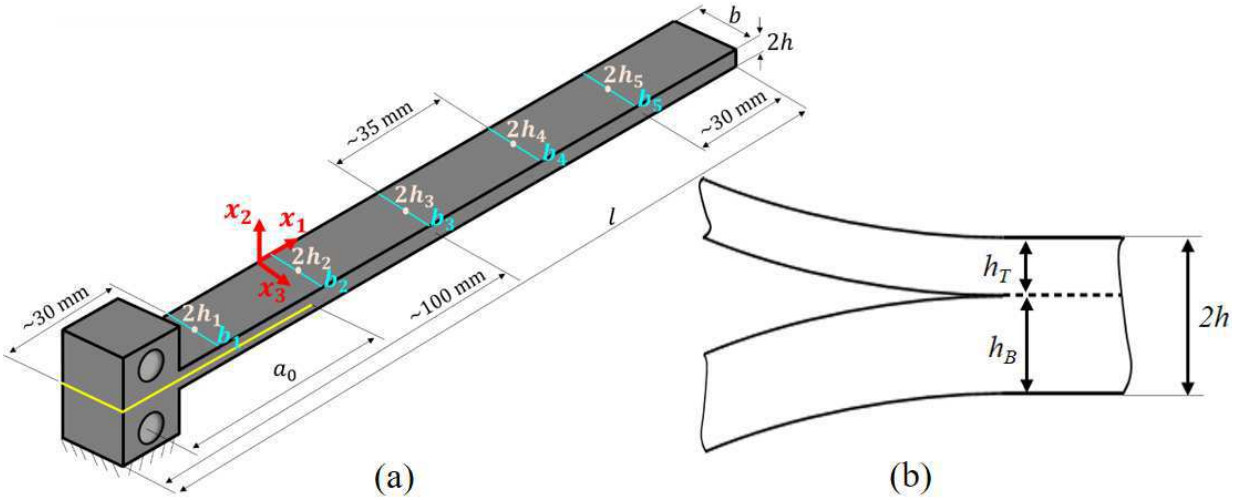

Figure 5.3: (a) Measurement locations for DCB specimens. (b) Illustration of DCB specimen heights (interface location is marked by the dashed line): $2h$ - total height; h_T and h_B - upper and lower specimen sub-laminate heights, respectively.

specimen. Another MD laminate composite plate was manufactured from 15 alternating woven plies, and was found to be too flexible for carrying out the C-ELS tests. Thus, a stiffer layup was designed as shown in Fig. 5.1, which is considered as the seventh specimen batch. The DCB tests were carried out to compare results obtained here to those in Simon et al. (2017). The plates from which the specimens were fabricated were different.

5.1.1 Delamination propagation test protocol

In this section, the DCB test protocol is presented. Specimen dimensions were measured in the spirit of the ASTM Standard D 5528-13 (2014) and ISO 15024 (2011) Standard. Measurements of the geometric parameters of each DCB specimen, some of which are presented in Figs. 5.2a and 5.3a, were made. The specimen height $2h$ was measured along the specimen center-line at five locations. One location is behind the delamination front (about 30 mm from the end of the specimen where load blocks are attached). There are four locations ahead of the delamination front: near the end of the PTFE film, about 30 mm from the other end of the specimen and at two equally spaced locations in between, as presented schematically in Fig. 5.3a. These measurements were made with a digital micrometer, which has a resolution of 0.001 mm. At these locations, the specimen width b was measured with an electronic digital caliper of resolution 0.01 mm. These measurements were carried out before a test was conducted. According to the ASTM Standard D 5528-13 (2014), the length of the specimen l should be at least 125 mm. It

may be noted that the ASTM Standard D 5528-13 (2014) recommends making only three measurements, at specimen midpoint and next to each edge of the specimen; meaning, at b_1 and b_5 and one measurement at the specimen midpoint b_3. In addition, at these locations, the thickness measurements should be performed, along the specimen center-line. The variation in thickness along the specimen length shall not exceed 0.1 mm. The ISO 15024 (2011) Standard recommends measuring the specimen width b at three evenly spaced points along the specimen length. At these locations, thickness measurements should be made along the specimen center-line. In addition, specimen thickness should be measured next to each edge of the specimen at width midpoint. It may be noted that here the measurements were performed at locations of interest, combining both standards recommendations. The initial delamination length a_0 was measured from the center of the loading holes to the end of delamination front on both specimen sides, front and back, with the Vision Measuring Machine (model number iMS-2010; DongGuang, China), with a resolution of 0.0001 mm. The length of the specimen l was measured with a ruler.

White acrylic paint was applied to both sides of each specimen for easier delamination front tracking. Prior to specimen painting, the delamination tip (PTFE end) was detected and marked with the aid of a Carl Zeiss™ microscope (model Stemi 2000-C stereomicroscope, Göttingen, Germany).

After the acrylic paint dried, the specimens were placed in a conditioning chamber (M.R.C. BTH80/-20, Holon, Israel) at least one week before a test was carried out. The chamber conditions are $23 \pm 1^\circ$ C and $50 \pm 3\%$ relative humidity (RH), which is within the requirements of the ASTM Standard D5528-13 (2014). According to the ASTM Standard D5528-13 (2014), specimens should be tested at conditions of $23 \pm 3^\circ$ C and $50 \pm 10\%$ RH. At the beginning of each test, the temperature and the RH in the Instron work area were noted and their values were monitored continuously (every 5 min) throughout a test.

A load P was applied normal to the specimen thickness, through the upper load block using an Instron loading machine (model number 8872, Bucks, UK), according to the recommendations presented in the ASTM Standard D 5528-13 (2014) and ISO 15024 (2011) Standard. The lower load block was fixed. The load cell with a maximum load of 250 N and a resolution of $\pm 0.25\%$ of the reading for a load greater than 2.5 N was used. The tests were carried out in displacement control. The ASTM Standard D 5528-13 (2014) and ISO 15024 (2011) Standard recommend a displacement rate of between 0.5 and 5 mm/min for specimen loading; for unloading, the displacement rate should not exceed 25 mm/min. Automatic test instructions were written via the Instron WaveMatrix computer software, which controls the Instron loading machine. In the first test stage, in which the delamination propagated for a short distance from the artificial delamination of an initial length a_0, the cross-head displacement of the Instron was increased quasi-statically at a rate of 1 mm/min. If there was a load drop of 5 N, the Instron automatically

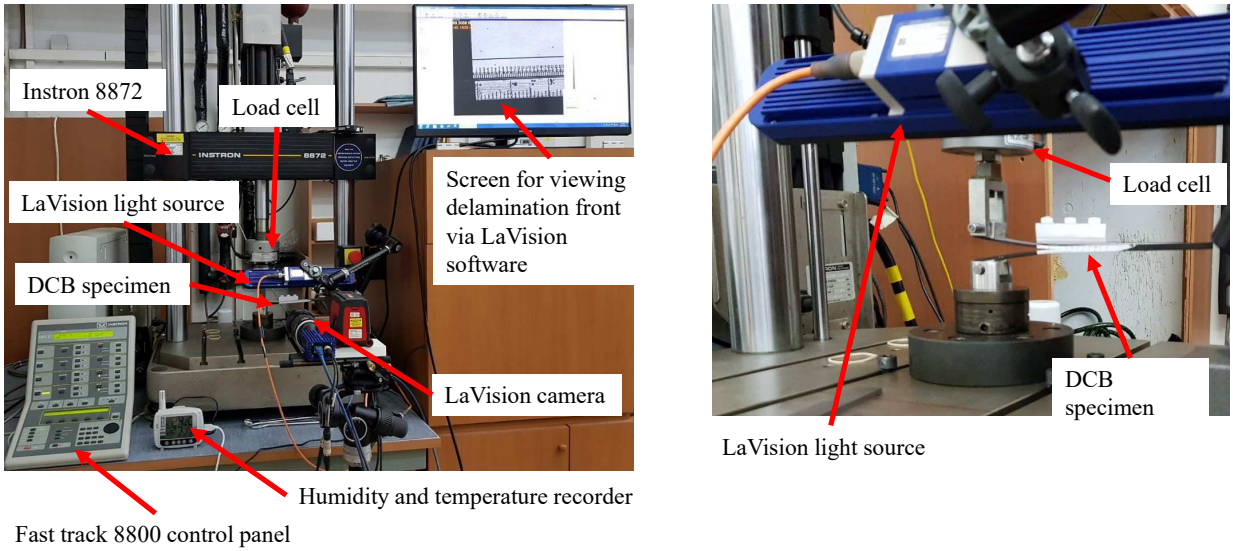

Figure 5.4: DCB fracture toughness test setup: (a) general view and (b) close-up.

unloaded at a rate of 5 mm/min. Otherwise, the delamination propagation was monitored. For a propagation of between 3 to 5 mm, unloading was induced at a rate of 5 mm/min. In either case of unloading, a residual load of about 3 N remained on the specimen. A small residual opening load was chosen to prevent accidental application of a compressive load. In the next stage, in which the delamination propagates from the pre-delamination length a_p derived in the first stage, the cross-head displacement of the Instron was increased quasi-statically at a rate of 1 mm/min until the delamination propagated 60 mm. Next, the specimen was unloaded to about 3 N at a rate of 5 mm/min.

The test setup is shown in Fig. 5.4. The cross-head displacement and the applied load are obtained by a computer which monitors the Instron machine. A LaVision system, described in Section 4.1, is employed during the test. Prior to testing, the camera is aligned using a level. During a test, images of the test specimen are taken at a rate of 2 Hz. The LaVision system enables synchronization between the Instron machine cross-head displacement and load and the images of the specimen acquired by the LaVision camera. In this way, the instantaneous applied load and displacement are displayed on the appropriate image of the test specimen. A paper ruler is attached to each specimen prior to testing. When test analysis is performed, the ruler is used for calibration and delamination tip tracking along with the reference tracking marks, as presented in Fig. 5.5 for specimen DCB-7-1.1. The specimen identifier includes DCB which represents the test type; 7 which represents the batch number; and 1.1, where the first number represents

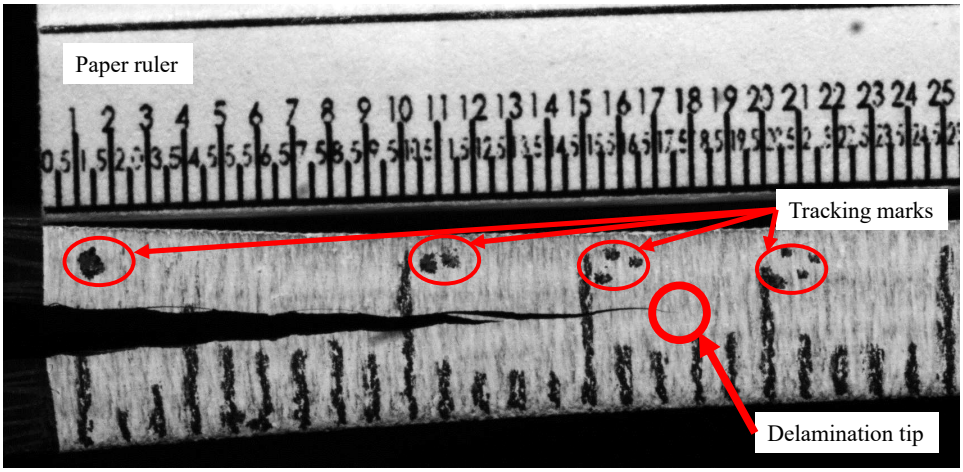

Figure 5.5: Image of the delamination in a DCB specimen (DCB-7-1.1) during a fracture toughness test, captured via the LaVision digital camera.

the row from which the specimen was fabricated and the second number represents the position in the row.

At the end of each test, the total length of the delamination a was determined. The total delamination propagation length is measured from the end of the PTFE film to the delamination tip on both specimen sides (front and back) with the optical mode of an Olympus Confocal Microscope (model number OLS4100; Tokyo, Japan), with a resolution of 0.16 $(\text{pixel}/\mu\text{m})^2$. Then, the appropriate value was added to the corresponding initial delamination length a_0. All geometric parameters are used in the FE model of each DCB specimen.

Since in each specimen the upper and lower arms are of different heights, these were measured after a test was performed. It was not possible to measure them before a test. In Figs. 5.6a and 5.6b, the variation in the height of the specimen arms or sub-laminates along the interface is shown for two different specimens MMELS-7-1.7 and C-ELS-7-1.13, respectively. In Figs. 5.6, the pictures are of two arbitrary tested beam-type specimens, which were photographed while their final delamination length was measured by means of the optical mode of the Olympus confocal microscope. The height variation of the specimen arms, which may be observed in Figs. 5.6, was common to all beam-type specimens, regardless of the test method; it was observed in the DCB, C-ELS and MMELS test specimens. The height of the upper and lower sub-laminates h_T and h_B, respectively, as illustrated in Fig. 5.3b, is measured at the approximate specimen center-line at five locations along the specimen length with a digital micrometer. These measurements are made at the same location at which the total height of the specimen, $2h$, was previously measured. The measured values of the height of the upper and lower arms are sensitive to

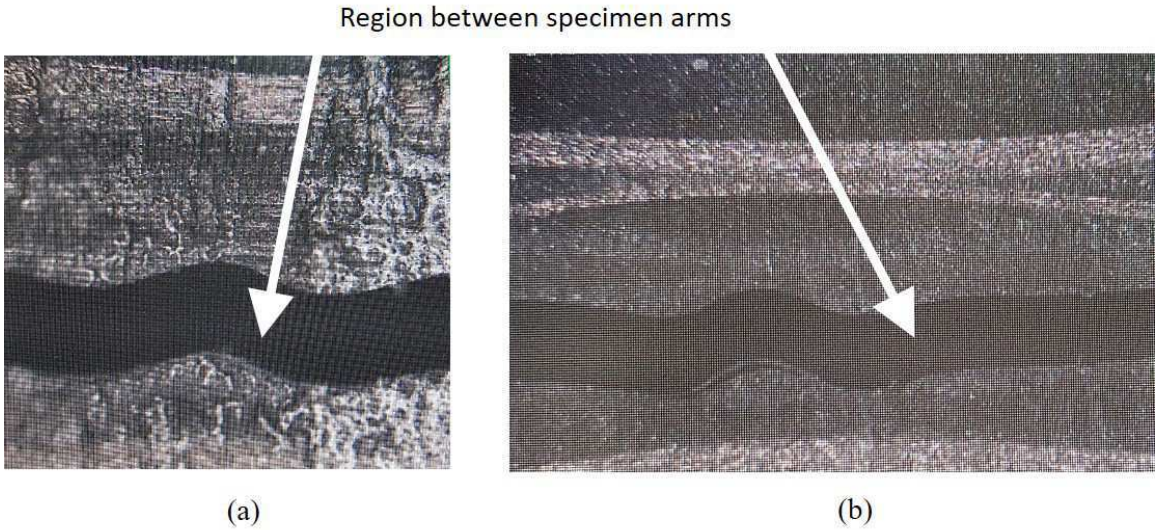

Figure 5.6: Representative examples of the height variation of specimen arms or sub-laminates along the interface in two different beam-type specimens: (a) MMELS-7-1.7 and (b) C-ELS-7-1.13.

the location at which the measurement is taken, whether it is a localized peak or valley. This phenomenon does not occur on the outer surfaces of each specimen, as a result of the manufacturing process of the composite plate, where the bottom of the composite plate is placed on a flat aluminum plate and the MD laminate composite is uniformly compressed by the pressurized environment applied during the thermal cycle in the autoclave.

The upper sub-laminate consists of 11 plies; whereas, the lower sub-laminate consists of 12 plies. Average values of h_T and h_B, $\overline{h}_T$ and $\overline{h}_B$, were found. It was seen that $\overline{h}_T$ was thinner than $\overline{h}_B$ but not in proportion to the fewer number of plies in that arm. It was also observed that the sum of $\overline{h}_T$ and $\overline{h}_B$ was not equal to $\overline{2h}$. Hence, $\overline{h}_T$ and $\overline{h}_B$ were scaled. Scaling $\overline{h}_T$ and $\overline{h}_B$ assisted in overcoming these differences. The scaled parameters at various points along the specimen length are given as

$$\begin{aligned} h_T^{(sc)} &= \frac{\overline{2h}}{\overline{h}_T + \overline{h}_B} \cdot h_T \\ h_B^{(sc)} &= \frac{\overline{2h}}{\overline{h}_T + \overline{h}_B} \cdot h_B. \end{aligned} \tag{5.1}$$

In this way,

$$\overline{2h} = \overline{h}_T^{(sc)} + \overline{h}_B^{(sc)}, \tag{5.2}$$

where $\overline{h}_T^{(sc)}$ and $\overline{h}_B^{(sc)}$ are the averaged values of the scaled parameters $h_T^{(sc)}$ and $h_B^{(sc)}$, respectively.

5.1.2 Analysis

Three DCB specimens containing an artificial delamination were tested based on the protocol presented in Section 5.1.1. The geometric parameters of the tested specimens, which are shown in Figs. 5.2a and 5.3a, are presented in Table 5.1. The parameters with subscript 1 represent measurements behind the artificial delamination front, whereas parameters with subscripts 2 to 5 represent measurements length ahead of the delamination front. Average values of specimen height and width denoted by $\overline{2h}$ and $\overline{b}$, respectively, are presented in Table 5.1. It should be noted that the low values of the standard deviation (STD) demonstrate the repeatability in specimen fabrication. Recall that according to the ASTM Standard D 5528-13 (2014), the thickness variation along the specimen length shall not exceed 0.1 mm; whereas, the ISO 15024 (2011) Standard recommends that the variation in thickness and width along the specimen length should be limited to ±1% of the mean value of the measured dimension obtained for that specimen. It may be found that all specimens comply with both standards. The measured values for the upper and lower sub-laminates of the DCB specimens are presented in Tables G.1 and G.2. The scaled values appear in Tables G.3 and G.4. Their averages, which also appear in Tables G.3 and G.4, were used in the FE model of each DCB specimen. It should be noted that the evaluated average ply thickness of the 11 plies in the upper specimen arm or sub-laminate, which is calculated as $\overline{h}_T/11$, is thinner than the evaluated average ply thickness of the 12 plies in the lower specimen sub-laminate, which is calculated as $\overline{h}_B/12$. A typical difference of about 0.03 mm in the average ply thickness between the upper and lower sub-laminates was obtained. Recall that the nominal ply thickness is 0.22 mm. Nevertheless, those evaluated ply thicknesses are within the valid range acceptable for this material and manufacturing process.

Table 5.1: Geometric parameters of the DCB specimens.

specimen no.	$2h_1$ (mm)	$2h_2$ (mm)	$2h_3$ (mm)	$2h_4$ (mm)	$2h_5$ (mm)	$\overline{2h}$ (mm)	STD (mm)
DCB-7-1.1	5.00	5.00	4.97	4.98	4.99	4.99	0.01
DCB-7-1.2	5.08	5.05	5.04	5.04	5.06	5.05	0.01
DCB-7-1.3	5.05	5.05	5.04	5.04	5.07	5.05	0.01
specimen no.	b_1 (mm)	b_2 (mm)	b_3 (mm)	b_4 (mm)	b_5 (mm)	$\overline{b}$ (mm)	STD (mm)
DCB-7-1.1	20.47	20.45	20.51	20.42	20.34	20.44	0.06
DCB-7-1.2	20.47	20.42	20.42	20.36	20.36	20.41	0.04
DCB-7-1.3	20.34	20.32	20.33	20.32	20.32	20.33	0.01
specimen no.	$a_0^{(f)}$ (mm)	$a_0^{(b)}$ (mm)	$\overline{a}_0$ (mm)	$\lvert\Delta_0\rvert$ (mm)	l (mm)		
DCB-7-1.1	50.30	50.78	50.54	0.48	200.5		
DCB-7-1.2	51.54	51.49	51.52	0.05	199.5		
DCB-7-1.3	50.87	50.59	50.73	0.28	200.0		

Table 5.2: Failure load at initial delamination propagation and final delamination length of the DCB specimens.

specimen no.	P_i	$a_f^{(f)}$ (mm)	$a_f^{(b)}$ (mm)	$\overline{a}_f$ (mm)	$\lvert\Delta_f\rvert$ (mm)
DCB-7-1.1	53.6	112.04	112.66	112.35	0.62
DCB-7-1.2	63.0	111.31	111.81	111.56	0.50
DCB-7-1.3	56.7	110.60	110.12	110.36	0.48

The initial delamination length on the front and back sides of the specimen, $a_0^{(f)}$ and $a_0^{(b)}$, respectively, as well as the average value of the initial delamination length $\overline{a}_0$ are also presented in Table 5.1. It is observed that the absolute difference between $a_0^{(f)}$ and $a_0^{(b)}$, denoted as $|\Delta_0|$ in Table 5.1, for each specimen is less than 2 mm, which complies with the ASTM Standard D 5528-13 (2014) and ISO 15024 (2011) Standard. According to those standards, a_0 should be approximately 50 mm long. Here it is a little longer. The length of the specimens, l, is also presented in Table 5.1, and is seen to be approximately 200 mm, which conforms with both standards. After the tests were carried out, the delamination length was measured on both sides of each specimen by means of the optical mode of the Olympus confocal microscope. These values are presented in Table 5.2, as $a_f^{(f)}$ and $a_f^{(b)}$, respectively. It may be observed that the absolute difference between the final delamination length on both sides of each specimen, denoted by $|\Delta_f|$, is less than 2 mm for all specimens, as required in the standards.

The room temperature and relative humidity (RH) were recorded during the tests, where each lasted about 1 hour. The initial and final environmental conditions of each test are presented in Table 5.3. Recall that the ASTM Standard D 5528-13 (2014) requires that the test temperature be $23 \pm 3^\circ$ C and the RH be $50 \pm 10\%$. In Table 5.3, it may be observed that the RH was generally less than the recommended values, whereas the temperatures were within the required range.

The load-displacement curves obtained for the three DCB fracture toughness tests are shown in Fig. 5.7. It is seen that the initial propagation load P_i seen visually in the images and coinciding with the first load drop are presented in Table 5.2. In Fig. 5.7, each abrupt load drop in the curve implies unstable delamination propagation. It may be seen that almost no stable delamination propagation, which is characterised by a

Table 5.3: Temperature and relative humidity during DCB tests.

specimen no.	$\vartheta_{initial}$ (°C)	$\mathrm{RH}_{initial}$ (%)	ϑ_{final} (°C)	RH_{final} (%)
DCB-7-1.1	22.6	34.4	21.9	29.4
DCB-7-1.2	22.7	40.0	22.5	39.3
DCB-7-1.3	22.7	32.5	24.6	23.4

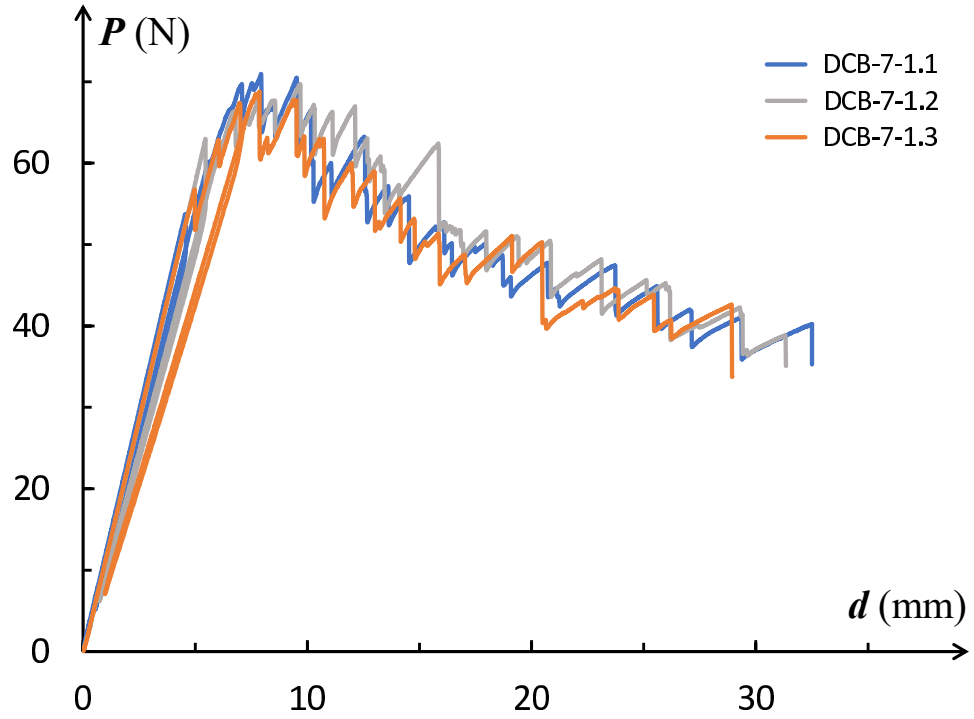

Figure 5.7: Load versus displacement curves from fracture toughness tests of DCB specimens: DCB-7-1.1, DCB-7-1.2 and DCB-7-1.3.

continuous load decrease, was detected. The same behavior was observed for all three DCB specimens. It should be noted that in Ishbir et al. (2014) and Simon et al. (2017), where a different layup but the same interface for the DCB specimens was considered, similar behavior of delamination propagation was reported.

After the test, the recorded load-displacement data along with the specimen photographs captured during the test were analyzed to obtain a relationship between delamination length, a, and the compliance C. Recall that the compliance is given by

$$C = \frac{d}{P} \tag{5.3}$$

where d is the loading machine actuator displacement and P is the applied load, as may be seen in Fig. 5.7. As verified and mentioned by Simon et al. (2017) and Chocron and Banks-Sills (2019), the loading machine compliance without the specimen was found to be very small. Since the same loading machine was used here with a similar DCB specimen, it was also assumed that the specimen opening displacement could be approximated by the loading machine actuator displacement.

It should be noted that delamination propagation, as observed in the images, was not always straight forward; sometimes there was a bifurcation of the delamination tip on the specimen edge. At other locations, the delamination tip jumped several millimeters ahead. Nevertheless, although it was sometimes difficult to determine the position of the

Table 5.4: Detected delamination propagation parameters for specimen DCB-7-1.1.

a (mm)	Δa (mm)	C (mm/N)	P (N)	image no.
50.54	0.0	0.085	53.6	546
51.44	0.9	0.092	58.6	1259
55.54	5.0	0.119	69.8	1507
59.24	8.7	0.155	70.5	1738
74.34	23.8	0.282	55.6	2326
78.04	27.5	0.300	52.0	2487
82.54	32.0	0.358	49.7	2702
85.14	34.6	0.409	48.6	2838
104.54	54.0	0.748	40.8	4105

delamination tip from the specimen photographs, curve fitting of specimen compliance versus delamination length was performed based upon the data obtained for visually detected delamination lengths. In a similar manner as suggested in Simon et al. (2017) and Chocron and Banks-Sills (2019), and following the ASTM Standard D 5528-13 (2014) and ISO 15024 (2011) Standard regarding beam theory, it may be shown that $C \propto a^3$. Thus, the relationship between the delamination length and specimen compliance may be expressed by a power law of the form

$$a = g(C - C_0)^{1/3}. \tag{5.4}$$

In eq. (5.4), parameters g and C_0 are fitting parameters of the power law which fits the empirical data. In Table 5.4, some delamination propagation parameters are presented for specimen DCB-7-1.1. These parameters are for delamination lengths that were visually detected within the recorded data of a P versus d curve and the photographs. The experimental data in Table 5.4 was used along with eq. (5.4) to generate the a versus C fitting curve presented in Fig. 5.8. The values of g and C_0 and the coefficient of determination R^2

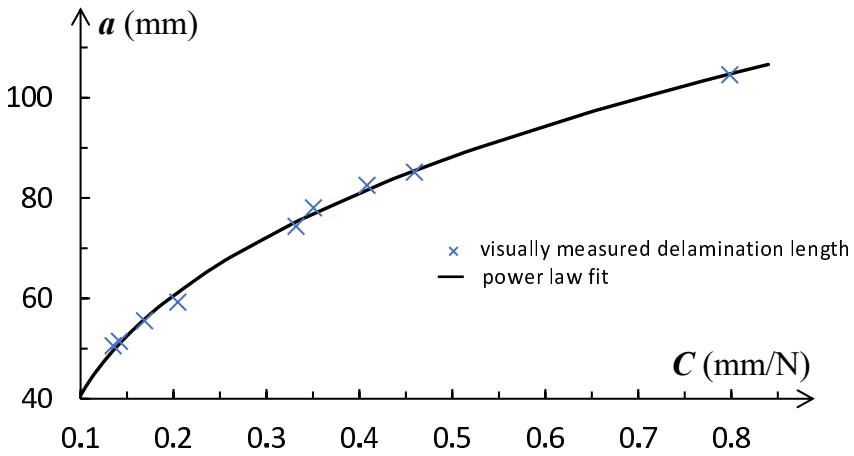

Figure 5.8: Correlation between delamination length and test compliance for specimen DCB-7-1.1.

were found as 115.66 $(\mathrm{N} \cdot \mathrm{mm}^2)^{1/3}$, $6.23{\cdot}10^{-3}$ mm/N and 0.998, respectively. In Fig. 5.8, it may be observed that there is good agreement between the measured and evaluated values of a. The same procedure was performed separately with the experimental data of specimens DCB-7-1.2 and DCB-7-1.3. The delamination propagation data of specimens DCB-7-1.1, DCB-7-1.2 and DCB-7-1.3 is presented in Tables G.5, G.6 and G.7, respectively, for visually detected and evaluated delamination lengths. In those tables, the values of the parameters of eq. (5.4), g and C_0, as well as the coefficient of determination R^2, are shown for each DCB specimen.

All DCB specimens were analyzed by means of the FE method using the ADINA (Bathe, 2011) software. The three-dimensional FE models contained twenty noded isoparametric, brick elements. In order to model the square-root singularity along the delamination front, quarter-point elements were used. The oscillatory part of the singularity was not modeled. The material properties used to characterize the plain woven plies with the yarn in the $0°/90°$ and $+45°/-45°$ directions are presented in Table 2.1. An example of a three-dimensional FE model is presented in Fig. 5.9a, where the FE model was used in analyzing specimen DCB-7-1.1.

To demonstrate mesh convergence of the FE model inner mesh, as well as domain independence, a coarse, fine and finer mesh were used with the geometric parameters of specimen DCB-7-1.1 in Table 5.1 with a representative delamination length of $a = 80$ mm. The in-plane dimensions of the elements in the vicinity of the delamination front were set to $1.03 \cdot 10^{-4} \times 1.03 \cdot 10^{-4}$ m^2, $5.14 \cdot 10^{-5} \times 5.14 \cdot 10^{-5}$ m^2 and $2.57 \cdot 10^{-5} \times 2.57 \cdot 10^{-5}$ m^2, as shown in Figs. 5.10a, 5.10b and 5.10c, respectively. A modified fine mesh shown in Fig. 5.10d, in which the ply thickness of the upper and lower plies which define the interface were divided into 4 elements along their thickness, was also generated. In that mesh,

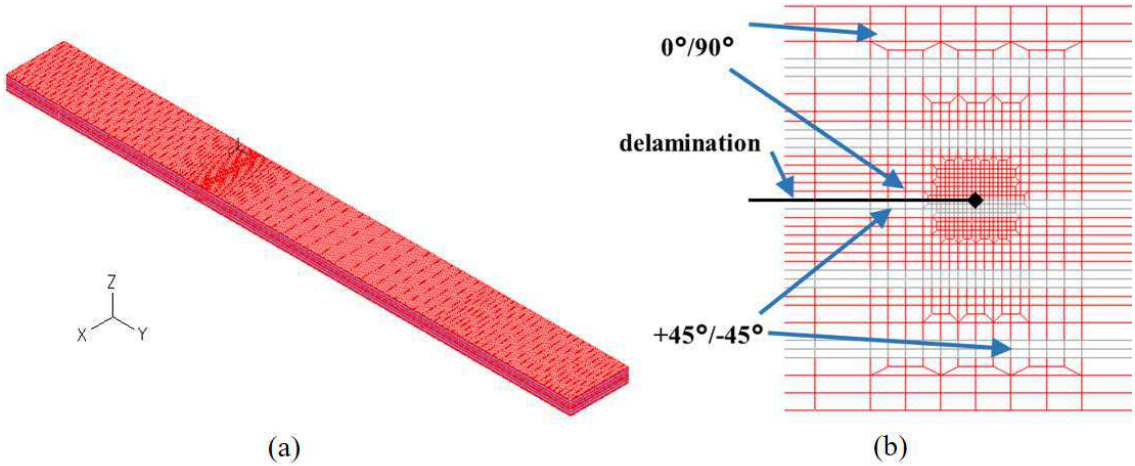

Figure 5.9: (a) Mesh of the DCB specimen. (b) Detailed front view near the delamination tip.

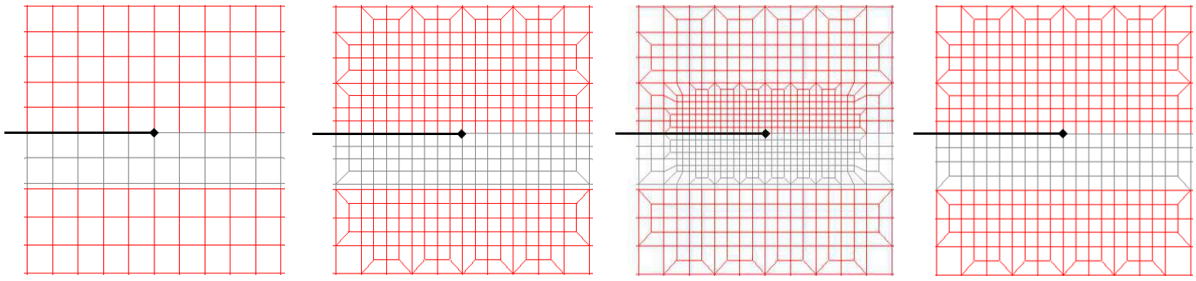

Figure 5.10: Detailed front-view of FE models of one delamination tip region of specimen DCB-7-1.1 used in convergence study: (a) coarse mesh, (b) fine mesh, (c) finer mesh and (d) modified fine mesh.

the in-plane dimensions of the elements in the vicinity of the delamination front were set to $5.14 \cdot 10^{-5} \times 5.14 \cdot 10^{-5}$ m^2 in the upper ply and $5.14 \cdot 10^{-5} \times 5.69 \cdot 10^{-5}$ m^2 in the lower ply. Thus, an in-plane aspect ratio of 1.0 and 1.11 was obtained, respectively, as shown in Figs. 5.9b and 5.10d. It may be noted that the in-plane aspect ratio of the elements at the bottom of the lower ply in the coarse mesh in Fig. 5.10a is 5.04; for the fine and finer meshes in Figs. 5.10b and 5.10c, the in-plane aspect ratio of some of those elements is 2.52 and 5.04. In all meshes there were 40 elements along the delamination front, each $5.1 \cdot 10^{-4}$ m thick. The delamination front is assumed to be straight through the model width. Some characteristics of the FE meshes which were used in the convergence study are given in Table 5.5.

An arbitrary constant load of $P^{FEA} = 20$ N was applied in all FE analyses for simplicity. The stress intensity factors were calculated along the delamination front of each mesh by means of the three-dimensional M-integral, which was described in Section 3.2. The stress intensity factors obtained for the modified fine mesh were also verified by means of the DE

Table 5.5: Characteristics of the four meshes which were used in the convergence study of the DCB specimen.

mesh	no. of elements	no. of nodes	element in-plane size near delamination front (m^2)	in-plane aspect ratio	no. of integration domains
coarse	167,600	706,719	$1.03 \cdot 10^{-4} \times 1.03 \cdot 10^{-4}$	1.0	2
fine	178,560	752,113	$5.14 \cdot 10^{-5} \times 5.14 \cdot 10^{-5}$	1.0	4
finer	191,440	805,453	$2.57 \cdot 10^{-5} \times 2.57 \cdot 10^{-5}$	1.0	5
modified fine	177,760	748,975	$5.14 \cdot 10^{-5} \times 5.14 \cdot 10^{-5}$ upper ply elements	1.0	4
			$5.14 \cdot 10^{-5} \times 5.69 \cdot 10^{-5}$ lower ply elements	1.11	

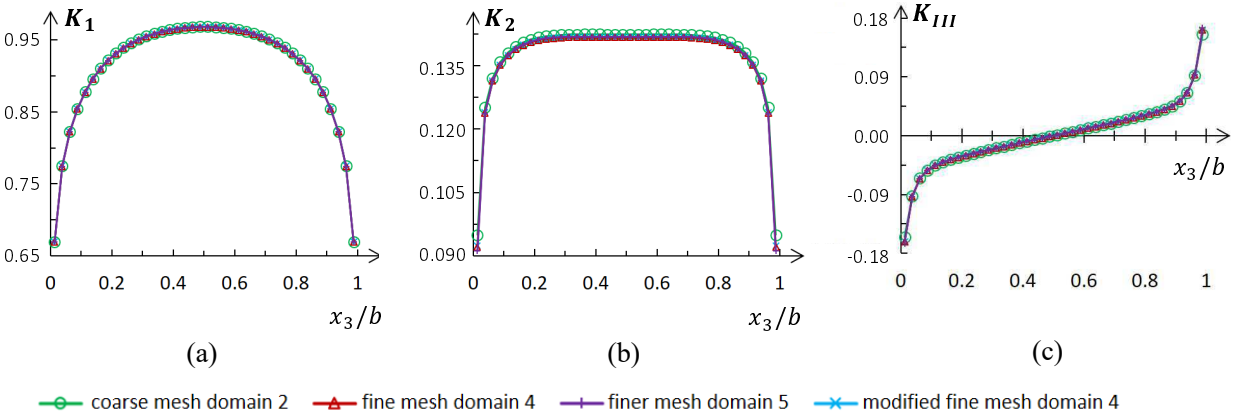

Figure 5.11: Stress intensity factors calculated along the delamination front by means of the three-dimensional M-integral for the largest domain of each FE mesh used to analyze specimen DCB-7-1.1 (coarse, fine and finer meshes). (a) K_1 in MPa$\sqrt{\text{m}} \cdot \text{m}^{-i\varepsilon}$, (b) K_2 in MPa$\sqrt{\text{m}} \cdot \text{m}^{-i\varepsilon}$ and (c) K_{III} in MPa$\sqrt{\text{m}}$.

method, which was presented in Section 3.1. The stress intensity factors obtained for the largest domain of each mesh as a function of the normalized delamination front coordinate (x_3/b) are shown in Fig. 5.11. Recall that the dimensions of the complex in-plane stress intensity factor components are F$\times$L$^{-(3/2+i\varepsilon)}$, where F and L represent force and length, respectively. The oscillatory parameter, ε, depends upon the mechanical properties of both materials on either side of the interface and for the investigated interface is presented in Table 4.9 and given in eq. (2.46). Both in-plane stress intensity factor components, K_1 and K_2, have units of MPa$\sqrt{\text{m}} \cdot \text{m}^{-i\varepsilon}$ and are shown, respectively, in Figs. 5.11a and 5.11b. The dimensions of the out-of-plane stress intensity factor, K_{III}, are F$\times$L$^{-3/2}$ with units of MPa$\sqrt{\text{m}}$; it is presented in Fig. 5.11c. It may be observed that the in-plane stress intensity factors shown in Figs. 5.11a and 5.11b, respectively, are symmetric with respect to specimen mid-thickness ($x_3/b = 0.5$), whereas the out-of-plane stress intensity factor shown in Fig. 5.11c is anti-symmetric. Differences between the various results are discussed in the sequel.

To demonstrate domain independence with the finer mesh shown in Fig. 5.10c, the stress intensity factors obtained by means of the M-integral in domain 5, which is shown in Fig. 3.2e, served as reference values and were used for comparison. In order to quantify the change in the calculated stress intensity factors obtained for each domain, the percent difference defined in eq. (4.8) was used. In Table 5.6, the differences between the stress intensity factors obtained for the fifth (reference) and other domains of integration (see Fig. 3.2) are presented. It should be noted that the maximum percent difference shown in Table 5.6 occurred at different positions along the delamination front. The values obtained for the different integration domains demonstrate domain independence. In a

Table 5.6: Maximum percent difference (in absolute value) between the stress intensity factors calculated for the fifth integration domain (reference) and domains 2, 3 and 4 of the finer mesh shown in Fig. 5.10c.

percent difference								
domain 2			domain 3			domain 4		
K_1	K_2	K_{III}	K_1	K_2	K_{III}	K_1	K_2	K_{III}
0.101	0.495	0.288	0.062	0.261	0.091	0.017	0.119	0.022

similar manner, demonstration of domain independence with the modified fine mesh shown in Fig. 5.10d, is presented in Table 5.7, in which the stress intensity factors obtained by means of the M-integral in domain 4 (shown in Fig. 3.2d) served as reference values and were used for comparison. Note, that the maximum percent difference shown in Table 5.7 occurred at different positions along the delamination front. The differences were less than 0.2% for domain 3.

In addition to Fig. 5.11, solution convergence is examined in Table 5.8, in which the differences between the stress intensity factors obtained for pairs of meshes are presented. For each pair of meshes, the mesh which is more refined in the vicinity of the delamination front serves as the reference (ref) in eq. (4.8). It should be noted that the maximum percent differences shown in Table 5.8 occurred at different positions along the delamination front. It may be observed that convergence is obtained for both ranges of x_3/b. Results for $x_3/b = 0.0125$ and 0.9875, that is for the domain in the outermost elements, deteriorate as compared to the other domains. Recall that in the development of the first term of the asymptotic stress and displacement fields, conditions of plane deformation were assumed, as may be seen in Section 2.2. This assumption is common in cases of through cracks/delaminations, so that the singularity related to body/medium free surface is not represented. Moreover, the assumption of plane deformation over constrains the free surface. Therefore, the values calculated by means of the M-integral and the DE method at FE model outer faces are inaccurate. Since the absolute value of the maximum percent difference within the range of $0.0375 \leq x_3/b \leq 0.9625$ between the fine and the finer mesh and also between the modified fine and the finer mesh is less than 0.3%, it

Table 5.7: Maximum percent difference (in absolute value) between the stress intensity factors calculated for the fourth integration domain (reference) and domains 2 and 3 of the modified fine mesh shown in Fig. 5.10d.

percent difference					
domain 2			domain 3		
K_1	K_2	K_{III}	K_1	K_2	K_{III}
0.096	0.411	0.353	0.064	0.180	0.088

Table 5.8: Maximum percent difference (in absolute value) between the stress intensity factors for pairs of meshes, along the delamination front, calculated for the largest integration domain of each mesh.

percent difference									
meshes	coarse and fine			fine and finer			modified fine and finer		
range	K_1	K_2	K_{III}	K_1	K_2	K_{III}	K_1	K_2	K_{III}
$0.0375 \leq x_3/b \leq 0.9625$	0.045	1.043	0.473	0.004	0.125	0.202	0.006	0.186	0.194
$0.0125 \leq x_3/b \leq 0.9875$	0.045	3.062	4.370	0.015	1.070	1.518	0.022	1.336	1.692

may be concluded that the fine mesh (typical side view of one delamination tip region is shown in Fig. 5.10b) and the modified fine mesh (typical side view of one delamination tip region is shown in Fig. 5.10d) may be used in all FE models in this study.

The stress intensity factors obtained for the largest domain of the finer and modified fine meshes as a function of the normalized delamination front coordinate x_3/b, as well as the stress intensity factors obtained for the modified fine mesh by means of the DE method, are shown in Fig. 5.12. Although the values of the stress intensity factors are calculated at different locations along the normalized delamination front coordinate x_3/b, it may be observed in Fig. 5.12 that the behavior of each stress intensity factor obtained by means of the DE method is similar to the corresponding stress intensity factor calculated by means of the three-dimensional M-integral. It may be noted that at model mid-width where $x_3/b = 0.5$, the maximum percent differences between the fine and the finer mesh are less than 0.004%, 0.12% and 0.008% for K_1, K_2 and K_{III}, respectively. Between the modified

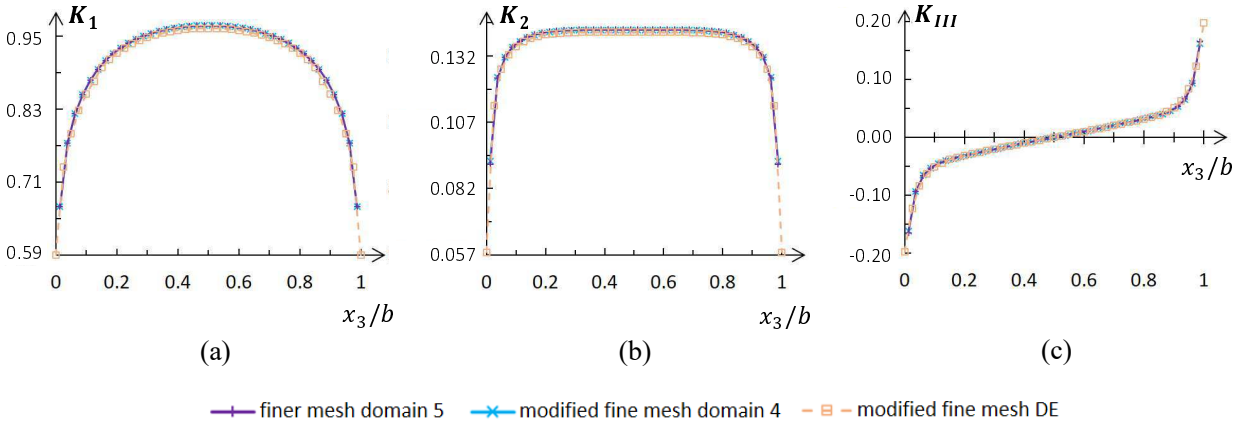

Figure 5.12: Stress intensity factors calculated along the delamination front by means of the three-dimensional M-integral for the largest domain of the finer and modified fine meshes and those calculated by means of the DE method for the modified fine mesh. (a) K_1 in MPa$\sqrt{\text{m}} \cdot \text{m}^{-i\varepsilon}$, (b) K_2 in MPa$\sqrt{\text{m}} \cdot \text{m}^{-i\varepsilon}$ and (c) K_{III} in MPa$\sqrt{\text{m}}$.

fine and the finer mesh, they are less than 0.006%, 0.1% and 0.001% for K_1, K_2 and K_{III}, respectively. The maximum percent differences for K_1 and K_2 between the modified fine mesh extracted by means of the DE method and the finer mesh are less than 0.5% and 0.7%, respectively. The maximum percent difference for K_{III} is meaningless at this point, since the value obtained by means of the DE method is less than $1.6 \cdot 10^{-7}$ MPa$\sqrt{\text{m}}$, whereas the value retrieved by means of the M-integral for the finer mesh is less than $6.0 \cdot 10^{-12}$ MPa$\sqrt{\text{m}}$.

It may be pointed out that for the in-plane phase angle $\hat{\psi}$, which characterizes the in-plane mode mixity, at model mid-width where $x_3/b = 0.5$, the maximum percent difference between the fine and the finer mesh is less than 0.12%; between the modified fine and the finer mesh it is less than 0.11%. The maximum percent difference for $\hat{\psi}$ between the modified fine mesh extracted by means of the DE method and the finer mesh is less than 0.19%. As expected, the DE method is less accurate than the three-dimensional M-integral, but still reproduces relatively satisfying results especially in cases where the three-dimensional M-integral may not be applied.

It should be noted that another FE model of the modified fine mesh in Fig. 5.10d was generated for specimen DCB-7-1.1 with a delamination length of $a = 80$ mm. This is the same specimen and same delamination length used in the convergence study in the region of the delamination front. Mesh refinement was performed in regions that are relatively far from the delamination front; additional nodal points were encountered far from the delamination front, at a distance which is more than the thickness of 54 plies ahead and behind the delamination front. This refined model contained 229,600 brick elements and 966,811 nodal points with a delamination tip region as shown in Fig. 5.10d. Far from the delamination front, a maximum in-plane element aspect ratio of 1 to 15.6 throughout the FE model was permitted. The properties of this mesh may be compared to that of the modified fine mesh in Table 5.5. For the strain energy release rate calculated by ADINA (Bathe, 2011) within the range of $0.0 \leq x_3/b \leq 1.0$, it was found that the maximum percent difference between this mesh, with more nodal points far from the delamination front, and the original modified fine mesh is less than $5.0 \cdot 10^{-5}$ %. Thus, it was concluded that the bending motion is sufficiently characterized by the original modified fine mesh.

Based upon domain independence and the convergence study for the inner and outer FE meshes presented above, the modified fine mesh is employed for the DCB specimens. Recall that in the modified fine mesh the in-plane dimensions of the elements in the vicinity of the delamination front were set to $5.14 \cdot 10^{-5} \times 5.14 \cdot 10^{-5}$ m^2 in the upper ply and $5.14 \cdot 10^{-5} \times 5.69 \cdot 10^{-5}$ m^2 in the lower ply. Thus, an in-plane aspect ratio of 1.0 and 1.11 was obtained, respectively, as shown in Fig. 5.9b. In all meshes there were 40 elements along the delamination front, each approximately $5.1 \cdot 10^{-4}$ m thick. Finite element models were generated for eight delamination lengths of each DCB specimen, while assuming that the delamination front is straight through the model width. The

delamination lengths, which were modeled, varied for the range 40 mm $\leq a \leq$ 110 mm with an increment of approximately 10 mm in order to cover the span of the experimentally obtained delamination lengths. An arbitrary constant load of $P^{FEA} = 20$ N was applied in all FE analyses for simplicity. All FE meshes contained 177,760 brick elements and 748,975 nodal points. A maximum in-plane element aspect ratio of 1 to 11.9 was permitted away from the delamination front, at a distance of 54 ply thicknesses ahead and behind the delamination front. In regions very far from expected stress concentrations (such as load application points, reactions, delamination front, etc.), an in-plane element aspect ratio varied between 1 to 30.6 and 1 to 44.2 was permitted. It may be noted that in the modified fine mesh for $a = 80$ mm, this in-plane aspect ratio was 1 to 31.4. It is recalled that a ply group consisting of several plies of the same plain woven material is assumed to serve as a single plain woven ply with the same material properties as described above, with a total thickness of all plies in the ply group.

The stress intensity factors were calculated by means of the three-dimensional M-integral, described in Section 3.2, for each slice of elements within domain 4, one element thick through the model thickness as shown in Fig. 3.2d. As described in Section 4.4.2, in order to resolve the complicated units of the in-plane stress intensity factors, K_1 and K_2, eq. (4.9) was used with length parameter $\hat{L} = 100$ μm. The normalized in-plane stress intensity factors, $\hat{K}_1$ and $\hat{K}_2$, as well as the out-of-plane stress intensity factor, K_{III}, for different delamination lengths but the same applied load $P^{FEA} = 20$ N, as a function of the normalized delamination front coordinate x_3/b are shown in Figs. 5.13a to 5.13c, respectively. The mesh in the neighborhood of the delamination front is translated and the remainder of the mesh follows the same principles as that used for the mesh for $a = 80$ mm. Recall that the number of elements for these meshes was fixed, 177,760 elements with 748,975 nodal points; the in-plane aspect ratio of elements far away from the delamination front and model restraints was readjusted and varied between 1 to 30.6 and 1 to 44.2. It may be observed that the in-plane stress intensity factor components are symmetric with respect to specimen mid-thickness $x_3/b = 0.5$, whereas the out-of-plane stress intensity factor is anti-symmetric. This behavior of the stress intensity factors was observed in every analysis that was performed for each DCB FE model.

Based upon these results, the interface energy release rate $\mathcal{G}_i$ using eq. (1.17), as well as the two phase angles, $\hat{\psi}$ in eq. (1.12) and ϕ in eq. (1.14), were also calculated. The in-plane phase angle $\hat{\psi}$ and the out-of-plane phase angle ϕ, for different delamination lengths but the same applied load $P^{FEA} = 20$ N as a function of the normalized delamination front coordinate x_3/b are presented in Figs. 5.13d and 5.13e, respectively. It may be observed that the values of $\hat{\psi}$ in Fig. 5.13d are relatively small for every value of a through the specimen width. Hence, the contribution of $\hat{K}_2$ to the total interface energy release rate $\mathcal{G}_i$ is negligible. In Fig. 5.13e, the values of ϕ are shown, where it may be observed that ϕ

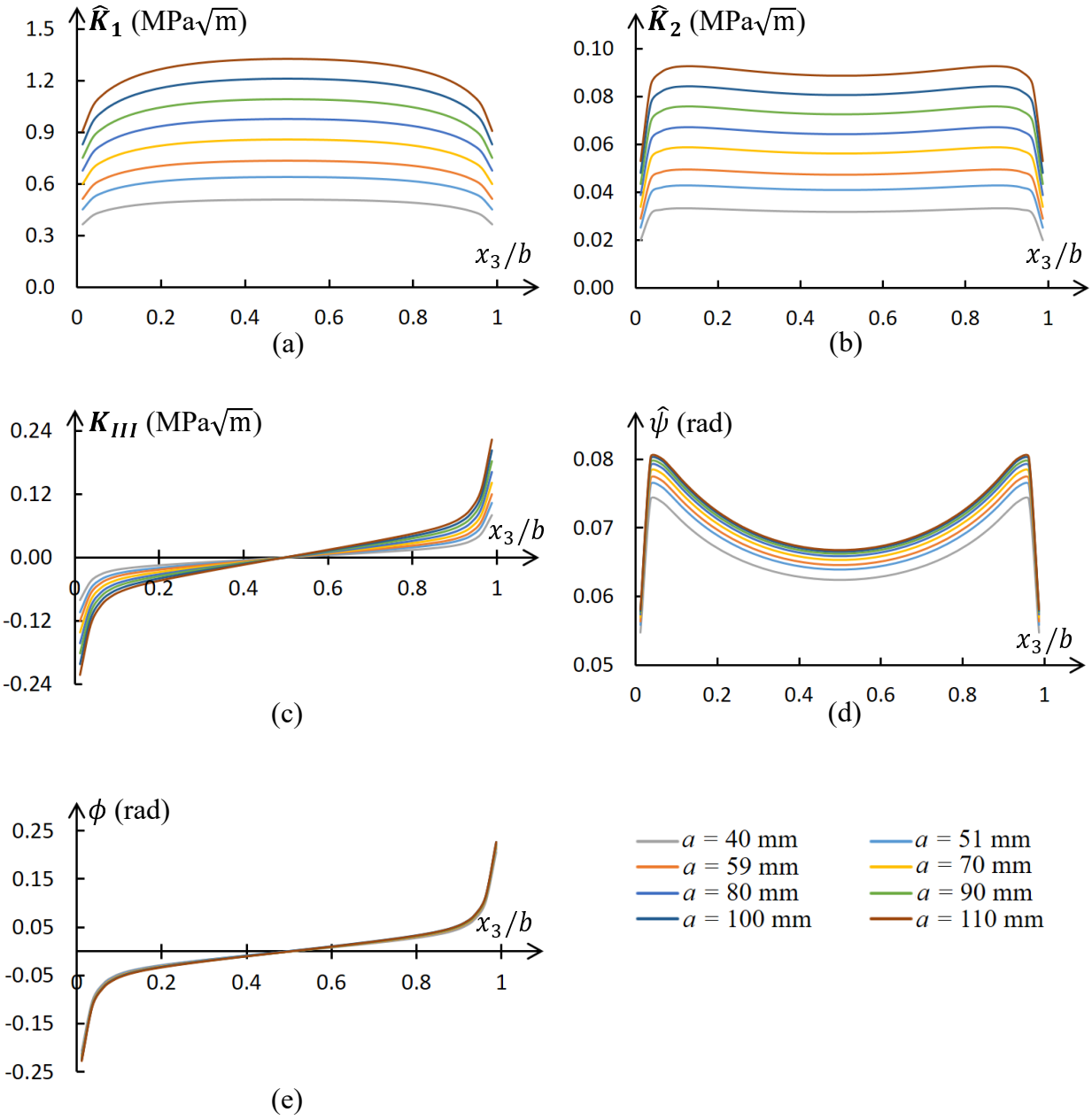

Figure 5.13: Normalized in-plane stress intensity factors (a) $\hat{K}_1$ and (b) $\hat{K}_2$ ($\hat{L} = 100$ μm); (c) out-of-plane stress intensity factor K_{III}; and the two phase angles (d) $\hat{\psi}$ and (e) ϕ as a function of normalized delamination front coordinate x_3/b for different delamination lengths for specimen DCB-7-1.1 with an applied load $P^{FEA} = 20$ N.

is essentially the same value for every value of a. In addition, it is seen that the values of ϕ are relatively small as well, except near the specimen outer edges. Hence, the contribution of K_{III} to the total interface energy release rate $\mathcal{G}_i$ is also negligible. Nonetheless, $\hat{K}_2$ and K_{III} are included in the calculation of $\mathcal{G}_i$.

Since linear elastic behavior of the specimen was assumed, as in the ASTM Standard D 5528-13 (2014) and ISO 15024 (2011) Standard, the stress intensity factors K_j, for $j = 1, 2, III$, as well as the interface energy release rate $\mathcal{G}_i$ are dependent upon the applied load P as

$$\begin{aligned} K_j &\propto P \\ \mathcal{G}_i &\propto P^2. \end{aligned} \tag{5.5}$$

Recall that an arbitrary constant load of $P^{FEA} = 20$ N was applied in all FE analyses for simplicity. Thus, based upon the obtained FEA results with $P^{FEA} = 20$ N, the values of the stress intensity factors K_j, for $j = 1, 2, III$ and the interface energy release rate $\mathcal{G}_i$ may be calculated, while employing the proper failure load that was measured in the test. The relationship between the experimental data and the FE analyses is given by

$$\begin{aligned} K_j^{Test} &= K_j^{FEA}\left(\frac{P^{Test}}{P^{FEA}}\right) \\ \mathcal{G}_i^{Test} &= \mathcal{G}_i^{FEA}\left(\frac{P^{Test}}{P^{FEA}}\right)^2. \end{aligned} \tag{5.6}$$

In eq. (5.6), the superscript FEA represents values employed or calculated from the FE analyses; whereas the superscript $Test$ represents values measured from the DCB test. It may be noted that the normalized in-plane stress intensity factors, $\hat{K}_1$ and $\hat{K}_2$, are also linearly dependent on P. It may be recalled that the phase angles $\hat{\psi}$ and ϕ remain the same, since the behavior of each stress intensity factor is linear with P.

Since it was found that for the DCB specimens $\hat{K}_1$ is dominant whereas the other stress intensity factors may be neglected, the interface energy release rate $\mathcal{G}_i$ may be treated as the mode I energy release rate $\mathcal{G}_I$. The mode I interface energy release rate $\mathcal{G}_I^{FEA}$, for different delamination lengths but the same applied load $P^{FEA} = 20$ N as a function of the normalized delamination front coordinate x_3/b, is presented in Fig. 5.14. It may be observed that for a constant value of the applied load, the interface energy release rate increases with a. When using the ASTM Standard D 5528-13 (2014) or ISO 15024 (2011) Standard to calculate the energy release rate for UD laminates, a global value is obtained. Thus here, an average through the width is found as

$$\mathcal{G}_I \equiv \int_0^1 \mathcal{G}_i(x_3/b)d(x_3/b). \tag{5.7}$$

It may be noted that the $\mathcal{G}_i^{FEA}(x_3/b, a)$ curves used in calculating the average mode I energy release rate $\mathcal{G}_I^{FEA}(a)$ were those obtained via the J-integral calculation embedded

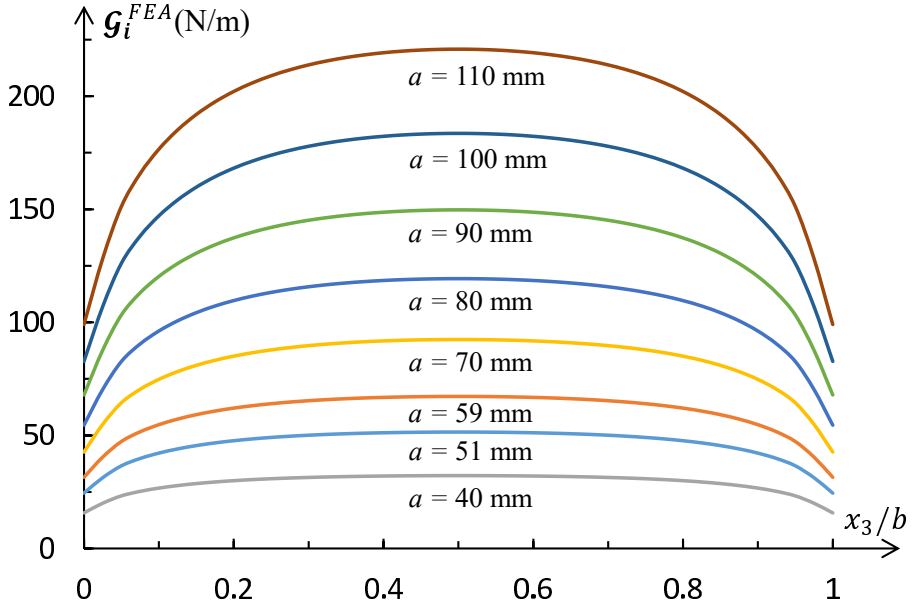

Figure 5.14: The interface energy release rate $\mathcal{G}_i^{FEA}$ as a function of the normalized delamination front coordinate x_3/b for different delamination lengths for specimen DCB-7-1.1 with an applied load $P^{FEA} = 20$ N.

within ADINA (Bathe, 2011) software, which is based upon the Gaussian surface integration, as may be found in Murakami and Sato (1983). Although the J-integral calculations are retrieved at the vertices of the elements along the delamination front and not at the mid-size of these elements, the averaged through the width values are being compared. For specimen DCB-7-1.1 with a delamination length of $a = 80$ mm, the difference between the $\mathcal{G}_I^{FEA}$ value calculated by means of the stress intensity factors which were extracted via the M-integral and the $\mathcal{G}_I^{FEA}$ value obtained by the J-integral in ADINA (Bathe, 2011) is less than 0.01%.

A second order polynomial curve fit given by

$$\mathcal{G}_I(a) = C_1 a^2 + C_2 a + C_3, \tag{5.8}$$

was employed in order to characterize the relationship between the calculated $\mathcal{G}_I^{FEA}$ from eq. (5.7) and the corresponding delamination length a. For specimen DCB-7-1.1, the values of the fitting parameters are given in Table 5.9.

Table 5.9: Values of the fitting parameters in eq. (5.8) for the DCB specimens.

specimen no.	C_1 (N/m^3)	C_2 (N/m^2)	C_3 (N/m)	R^2
DCB-7-1.1	$1.52 \cdot 10^4$	$1.16 \cdot 10^2$	$2.47 \cdot 10^{-1}$	1.0
DCB-7-1.2	$1.42 \cdot 10^4$	$1.64 \cdot 10^2$	1.16	1.0
DCB-7-1.3	$1.51 \cdot 10^4$	$1.17 \cdot 10^2$	$2.40 \cdot 10^{-1}$	1.0

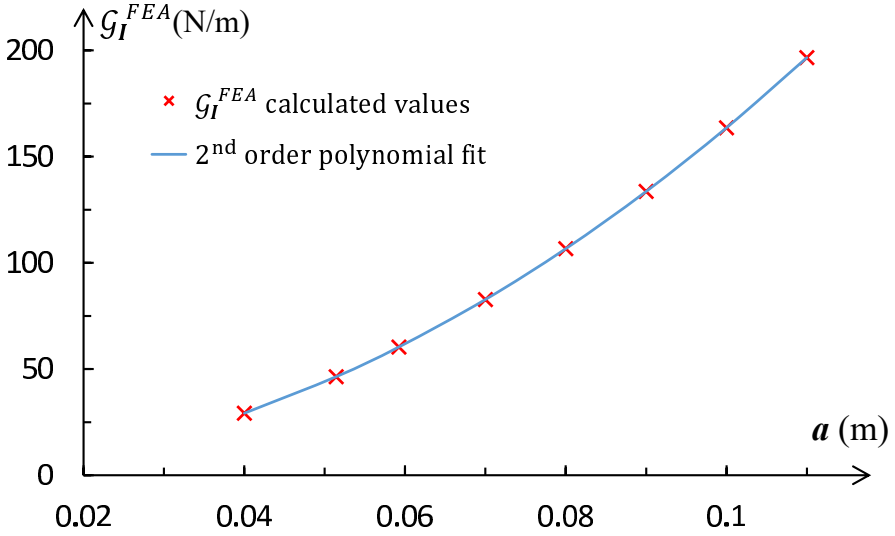

Figure 5.15: The averaged mode I interface energy release rate $\mathcal{G}_I^{FEA}$ as a function of delamination length for specimen DCB-7-1.1 with an applied load $P^{FEA} = 20$ N.

In Fig. 5.15, the $\mathcal{G}_I^{FEA}(a)$ fitting curve obtained for specimen DCB-7-1.1 is presented along with the values of $\mathcal{G}_I^{FEA}$ in eq. (5.7) calculated for different delamination lengths a. It may be seen that excellent agreement exists between the fitted curve and calculated values. The same procedure was performed separately with the experimental data of specimens DCB-7-1.2 and DCB-7-1.3 and their FEA results. For specimens DCB-7-1.2 and DCB-7-1.3, the values of the fitting parameters in eq. (5.8) are shown in Table 5.9. In Tables G.5 through G.7 in Appendix G, the calculated values of $\mathcal{G}_{IR}$, which were obtained by means of the FE method are presented for both experimentally detected and evaluated delamination lengths of the corresponding DCB specimen. It may be recalled that in order to obtain these values curve fitting in eq. (5.8) and load adjustment of the FEA applied load to the experimentally obtained failure load in eq. (5.6) were performed.

5.1.3 Results

Based upon the data in Tables G.5 through G.7, a $\mathcal{G}_{IR}$-curve was generated. The $\mathcal{G}_{IR}$ versus $\Delta a = a - a_0$ data points are plotted in Fig. 5.16. An initiation fracture toughness is shown for $\Delta a = 0$ as $\mathcal{G}_{Ic} = 376.3$ N/m, which is the average of the critical interface energy release rate values for delamination growth from the PTFE insert obtained for specimens DCB-7-1.1, DCB-7-1.2 and DCB-7-1.3. It may be seen that the values of $\mathcal{G}_{IR}$ increase with Δa until a steady state value of $\mathcal{G}_{Iss} = 715.5$ N/m is reached for $\Delta a = 14$ mm. Fitting the points between $0 \leq \Delta a \leq 14$ mm results in the power law given by

$$\mathcal{G}_{IR} = 118.0(\Delta a)^{0.4} + 376.3 \tag{5.9}$$

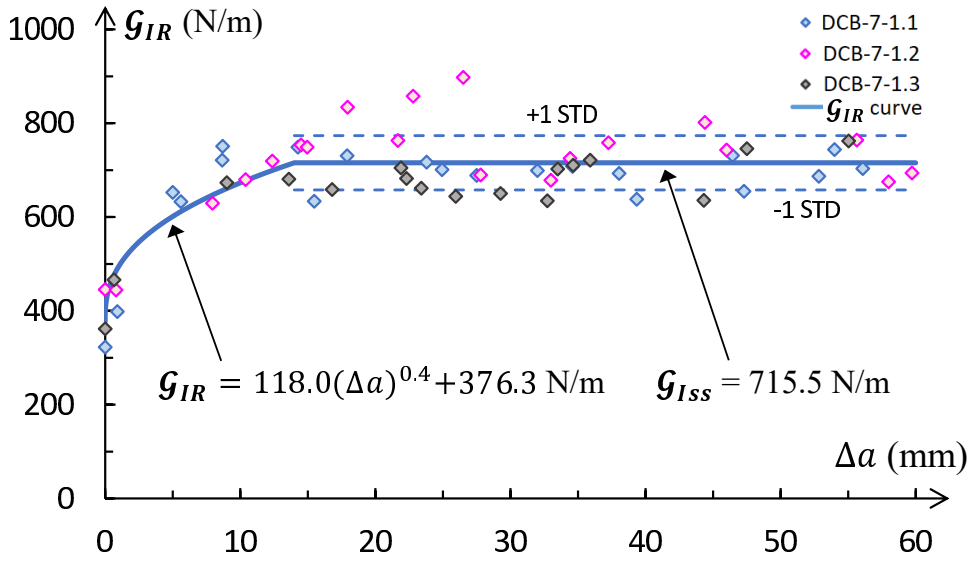

Figure 5.16: Fracture resistance curve: the average critical interface energy release rate, referred as $\mathcal{G}_{IR}$, as a function of delamination propagation length $\Delta a = a - a_0$.

where Δa in eq. (5.9) is measured in millimeters. The coefficient of determination R^2 of the power law in eq. (5.9) and the plotted points where $0 \leq \Delta a \leq 14$ mm was found as 0.89. Also, it may be observed that for 14 mm $\leq \Delta a \leq 60$ mm, most of the $\mathcal{G}_{IR}$ data points are within one standard deviation from the $\mathcal{G}_{Iss}$ line; the value of one STD was found to be 57.8 N/m.

A comparison was made between the results obtained in the current investigation with those obtained in Simon et al. (2017). In that study, the same layup was used, the same interface but two different batches. For batch 1, the specimens had thicknesses which varied between 3.7 mm and 3.9 mm and an artificial delamination length of approximately 24 mm; the second batch had an average thickness of 3.45 mm and an artificial delamination length of approximately 47.5 mm. The data obtained here is for the same interface, but a different and thicker layup of approximate thickness 5.0 mm and artificial delamination length of approximately 51 mm. It may be noted that the fracture toughness resistance data presented in Banks-Sills et al. (2013) and Ishbir et al. (2014) was obtained with a different test protocol, which did not follow that presented in Simon et al. (2017). In the current study the test protocol followed the fracture resistance test protocol presented in Simon et al. (2017). Thus, the comparison is made only to the data presented in Simon et al. (2017).

In Fig. 5.17, despite the scatter in the region where $\mathcal{G}_{IR}$ increases with Δa, it may be seen that the $\mathcal{G}_{Ic}$ values at delamination initiation and $\mathcal{G}_{IR}$ values for propagation of specimens DCB-7-1.1, DCB-7-1.2 and DCB-7-1.3 up to $\mathcal{G}_{Iss}$ are lower than those obtained in Simon et al. (2017), where $\mathcal{G}_{Ic} = 507.5$ N/m. The behavior in which specimens of greater thickness

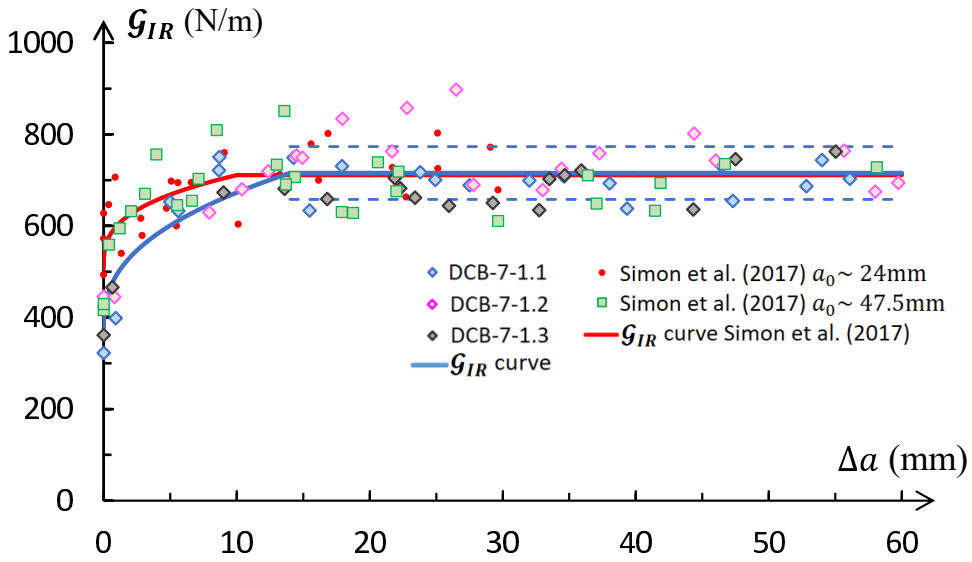

Figure 5.17: Fracture toughness resistance curves: comparison between results from the current investigation and results presented in Simon et al. (2017).

have lower fracture toughness values was observed in other studies. In Kravchenko et al. (2017), UD, CFRP DCB specimens were tested with four different thickness between 2.0 mm and 8.4 mm. The critical mode I energy release rate $\mathcal{G}_{Ic}$ varied between 192 N/m for the thickest specimen and 277 N/m for the thinnest. Moreover, the BD specimens tested in Section 4.5 had an approximate composite strip height of 15.6 mm with a critical mode 1 energy release rate of 210.2 N/m. Another example is the MD carbon/epoxy composite studied in Mega and Banks-Sills (2019) with $\mathcal{G}_{1c}$ = 114.4 N/m obtained by means of BD specimens with an approximate height of 16.6 mm. In Chocron and Banks-Sills (2019), DCB specimens which were 5 mm thick and fabricated from the same material and interface as in Mega and Banks-Sills (2019) were tested with a critical mode I energy release rate of 357.9 N/m. In addition, it may be seen in Fig. 5.17, that at the plateau region, almost the same $\mathcal{G}_{Iss}$ value was obtained here as $\mathcal{G}_{Iss}$ = 715.5 N/m; in Simon et al. (2017), $\mathcal{G}_{Iss}$ = 710.9 N/m. Thus, it appears that in the steady state region the delamination propagation mode I energy release rate $\mathcal{G}_{IR}$ values are relatively insensitive to the height/thickness of the DCB specimens. This is supported by the behavior of R-curves for thermoset UD laminate specimens as discussed in Suo et al. (1992) for the case in which fiber bridging occurs.

5.2 C-ELS

Five quasi-static tests of delamination initiation and propagation were carried out on C-ELS specimens with the layup shown in Fig. 5.1. An illustration of a C-ELS specimen is presented in Fig. 5.2b, where the geometric parameters l, b and $2h$ are the specimen length, width and height, respectively. In Fig. 5.2b, the right side of the specimen is constrained by means of a clamping fixture, so that free horizontal sliding is allowed but rotation and vertical movement are prohibited; the specimen free length L_f is measured from the load line to the edge of the clamping fixture. The C-ELS specimen is loaded normal to its thickness by a single vertical load P. The initial delamination length a_0 is measured from the load line to the artificially introduced delamination front. The C-ELS tests were carried out in order to measure the nearly mode II fracture toughness of the interface, which is shown in Fig. 1.1b. Note that the C-ELS specimens used here were fabricated from the same seventh batch of material tested in Section 5.1 for the DCB specimens.

5.2.1 Fracture test protocol

In this section, the C-ELS test protocol is presented. Specimen dimensions were measured in the spirit of the ISO 15114 (2014) Standard. Measurements of the geometric parameters of each C-ELS specimen, some of which are presented in Figs. 5.2b and 5.3a, were made. It may be noted that in Fig. 5.3a, a DCB specimen is schematically presented. Nevertheless, except for the upper load block, the geometric parameters of both specimens are the same. The specimen height $2h$ was measured along the specimen center-line at five locations. One location is behind the delamination front about 30 mm from the end of the specimen where load blocks are attached. There are four locations ahead of the delamination front: near the end of the PTFE film, about 30 mm from the other end of the specimen and at two equally spaced locations in between, as presented schematically in Fig. 5.3a. These measurements were made with a digital micrometer, which has a resolution of 0.001 mm. At these locations, the specimen width b was measured with an electronic digital caliper of resolution 0.01 mm. These measurements were carried out before a test was conducted. According to the ISO 15114 (2014) Standard for UD material, the initial delamination length a_0 should be greater than 50 mm, so that the influence of the load block may be neglected. In addition, the length of the specimen l should be at least $a_0 + 110$ mm long, meaning at least 160 mm long.

The ISO 15114 (2014) Standard recommends measuring the specimen width b at three evenly spaced points along the specimen length. At these locations, thickness measurements should be made along the specimen center-line. The variation in thickness along

the specimen length shall not exceed 0.1 mm. It may be noted that here the measurements were performed at locations of interest, as in the case of the DCB specimens in Section 5.1. The initial delamination length a_0 was measured from the center of the loading holes to the end of delamination front on both specimen sides, front and back, with the Vision Measuring Machine (model number iMS-2010; DongGuang, China), with a resolution of 0.0001 mm. The length of the specimen l was measured with a ruler.

White acrylic paint was applied to both sides of each specimen for easier delamination front tracking. Prior to specimen painting, the delamination tip PTFE end was detected and marked with the aid of a Carl Zeiss™ microscope (model Stemi 2000-C stereomicroscope, Göttingen, Germany). After the acrylic paint dried, the specimens were placed in a conditioning chamber (M.R.C. BTH80/-20, Holon, Israel) at least one week before a test was carried out. This chamber was described in Section 5.1.1.

The C-ELS tests were carried out in two stages. In the first stage, an initial monotonically rising displacement was applied at 1 mm/min to induce a natural delamination. This pre-cracking procedure was carried out in nearly mode II deformation. After the delamination propagates between 2 to 5 mm, unloading takes place at a rate of 5 mm/min. Unloading is interrupted when the load reaches 3 N. A small residual load was chosen to prevent accidental application of a load in the opposite direction. In the second stage, nearly mode II deformation is applied to cause initiation and propagation of the natural pre-cracked delamination. The displacement rate in this part of the test is 0.5 mm/min. At the beginning of each test stage, the temperature and the RH in the Instron work area were noted and their values were monitored continuously every 5 min throughout a test.

The displacement is controlled by an Instron loading machine (model number 8872, Bucks, UK), according to the recommendations presented in the ISO 15114 (2014) Standard. The load cell with a maximum load of 1000 N and a resolution of $\pm 0.25\%$ of the reading for a load greater than 10 N was used. Automatic test instructions were written via the Instron WaveMatrix computer software, which controls the Instron loading machine.

The free length for the pre-cracking stage, denoted by L_0 and shown in Fig. 5.2b as L_f, was chosen as

$$L_0 \simeq \frac{4}{3} a_0, \tag{5.10}$$

in order to promote stable delamination propagation, as recommended in the ISO 15114 (2014) Standard. Prior to testing, the bolts of the clamping fixture were tightened according to the ISO 15114 (2014) Standard recommendations with a torque of 8 Nm obtained by means of a torque wrench and a level.

In the second stage of the test, the free length denoted by L_p and shown in Fig. 5.2b as L_f, was chosen as

$$\frac{4}{3} a_p < L_p < \frac{5}{3} a_p, \tag{5.11}$$

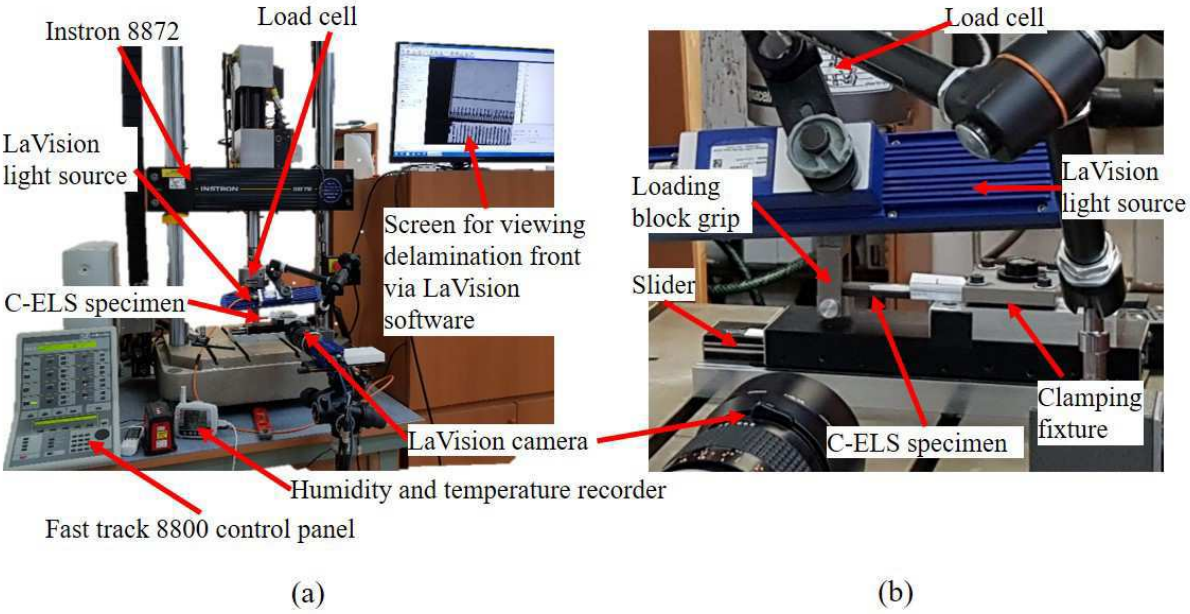

Figure 5.18: C-ELS fracture toughness test setup: (a) general view and (b) close-up.

where a_p is the natural pre-delamination length that was obtained at the end of the first stage of the test. This choice is made to provide sufficient length for delamination propagation, as well as relatively stable delamination growth. The test is interrupted when the delamination front is within 10 mm from the clamp. Next, the specimen was unloaded to about 3 N at a rate of 5 mm/min.

The test setup is presented in Fig. 5.18. A close-up of the C-ELS test rig with a mounted specimen is shown in Fig. 5.18b. The cross-head displacement and the applied load are obtained by a computer which monitors the Instron machine. A LaVision system, described in Section 4.1, is employed during the test. Prior to testing, the camera is aligned using a level. During a test, images of the test specimen are taken at a rate of 2 Hz. The LaVision system enables synchronization between the Instron machine cross-head displacement and load and the images of the specimen acquired by the LaVision camera. In this way, the instantaneous applied load and displacement are displayed on the appropriate image of the test specimen. A paper ruler is attached to each specimen prior to testing. When the test analysis is performed, the ruler is used for calibration and delamination tip tracking, as presented in Fig. 5.19 for specimen C-ELS-7-1.11. The specimen identifier includes C-ELS which represents the test type; 7 which represents the batch number; and 1.11, where the first number represents the row from which the specimen was fabricated and the second number represents the position in the row.

At the end of each test stage, the total length of the delamination a was determined. The total delamination propagation length is measured from the end of the PTFE film

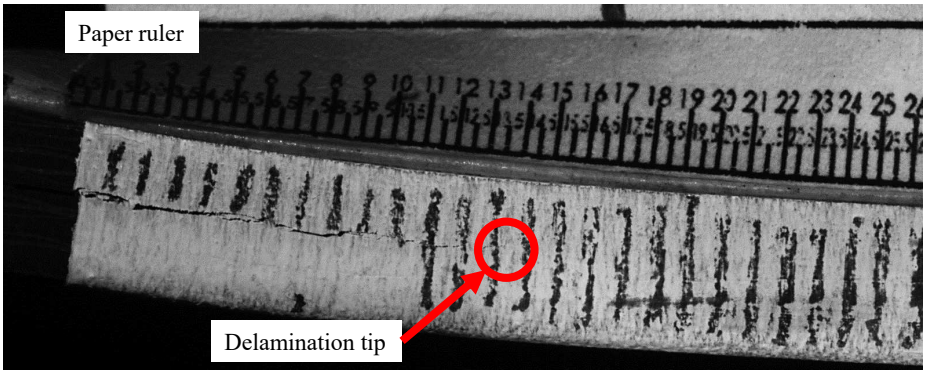

Figure 5.19: Image of the delamination in specimen C-ELS-7-1.11 during the second stage of the C-ELS test, in which delamination is propagated from a natural delamination front, captured via the LaVision digital camera.

to the delamination tip on both specimen sides, front and back, with the optical mode of the Olympus confocal microscope. Then, the appropriate value was added to the corresponding initial delamination length a_0. All geometric parameters are used in the FE model of each C-ELS specimen.

Prior to testing, calibration of the ELS fixture is recommended in the ISO 15114 (2014) Standard. This procedure is performed by using a C-ELS specimen with a load block attached to the bottom of its intact part, so that the delamination front is fully confined within the clamping fixture and the specimen may be treated as one beam. It is suggested to carry out this procedure with a beam free length of $L_f = 110$ mm and then to repeat the procedure six more times with the beam clamped with free lengths of $L_f = 100$, 90, 80, 70, 60 and 50 mm. A cross-head displacement rate of 1 mm/min is recommended for loading; the unloading rate of up to 10 mm/min is suggested. Here, the unloading part was carried out at a rate of 5 mm/min. In addition, the specimen used for the calibration may be reused for mode II testing, by bonding a load block to the bottom of the delamination edge of the specimen. The suggested maximum applied load for the calibration procedure is 250 N for CFRPs. Note that the ISO 15114 (2014) Standard recommends a specimen thickness of 3 mm for specimens having a fiber volume fraction of 60% for UD carbon fiber specimens. Here the specimens are made of MD carbon/epoxy plain woven plies, where each ply has less than the 60% fiber volume fraction. It may be noted that here the calibration procedure was performed with six beam free lengths of $L_f = 100$, 90, 80, 70, 60 and 50 mm; this specimen was not used again to avoid undesirable discrepancies. In addition, the maximum applied load for the calibration procedure was set to 190 N. At this load, a deflection of more than 10% of the beam free length was obtained for $L_f = 100$ mm.

The experimental data obtained from the ELS fixture calibration is analyzed for each specimen free length L_f. The specimen compliance C for each value of L_f is calculated from the linear slope of the loading part of each load-displacement curve. Then, values of C are used to plot $C^{1/3}$ versus L_f. A linear regression of the data points is performed while extending the regression back to $C^{1/3} = 0$. The obtained line is expressed as

$$C^{1/3} = slope \cdot L + slope \cdot |\Delta_{clamp}| \tag{5.12}$$

where

$$slope = \left(\frac{1}{2bh^3 E_{1f}} \right)^{1/3} \tag{5.13}$$

and Δ_{clamp} and E_{1f} are the clamp correction parameter and the beam flexural modulus, respectively. It may be recalled that the delamination considered here is along an interface between two plain woven plies of different orientations in an MD laminate, where the specimen arms or sub-laminates are of different thicknesses and different effective mechanical properties, such as axial and flexural moduli. Therefore, some of the methods presented in the ISO 15114 (2014) Standard, which rely upon beam theory where identical flexural moduli in all specimen laminate segments (upper sublaminate, lower sublaminate and intact laminate) occur, are not applicable for determining the critical interface energy release rate $\mathcal{G}_{ic}$ for near mode II deformation. The calibration described here is used for calibration of the FE models. The values for Δ_{clamp} and E_{1f} determined experimentally serve as reference values in the adjustments of the FE models, which are needed for correct representation of the clamping fixture in the FE analyses.

Since in each specimen the upper and lower arms are of different heights, these were measured after a test was performed. It was not possible to measure them before a test. The variation in the height of the specimen arms or sub-laminates along the interface is presented in Fig. 5.6b, for specimen C-ELS-7-1.13. Recall that this was common to all beam-type specimens. The height of the upper and lower sub-laminates h_T and h_B, respectively, as illustrated in Fig. 5.3b, is measured at the approximate specimen center-line at five locations along the specimen length with a digital micrometer. These measurements are made at the same location at which the total height of the specimen, $2h$, was previously measured. As indicated in Section 5.1.1, the upper sub-laminate consists of 11 plies; whereas, the lower sub-laminate consists of 12 plies. Also, the measured values of the height of the upper and lower arms are sensitive to the location at which the measurement is taken, whether it is a localized peak or valley. Recall that this phenomenon does not occur on the outer surfaces of each specimen, as a result of the manufacturing process of the composite plate. Thus, the measured values of h_T and h_B were scaled according to eqs. (5.1) and (5.2).

5.2.2 Analysis

Five C-ELS specimens containing an artificial delamination and one specimen utilized for calibration of the ELS fixture were tested based upon the protocol presented in Section 5.2.1. The geometric parameters of the tested specimens, which are shown in Figs. 5.2b and 5.3a, are presented in Table 5.10. The parameters with subscript 1 represent measurements behind the artificial delamination front, whereas parameters with subscripts 2 to 5 represent measurements ahead of the delamination front. Average values of specimen height and width denoted by $\overline{2h}$ and $\overline{b}$, respectively, are presented in Table 5.10. It should be noted that the low values of the standard deviation (STD) demonstrate the repeatability in specimen fabrication. According to the ISO 15114 (2014) Standard, the thickness variation along the specimen length shall not exceed 0.1 mm. It may be found that all specimens comply with this requirement. The measured values for the upper and lower sub-laminates of the C-ELS specimens are presented in Tables G.1 and G.2. The scaled values calculated by means of eqs. (5.1) and (5.2) appear in Tables G.3 and G.4. Their averages, which also appear in Tables G.3 and G.4, were used in the FE model of each C-ELS specimen. It should be noted that the evaluated average ply thickness of

Table 5.10: Geometric parameters of the C-ELS specimens.

specimen no.	$2h_1$ (mm)	$2h_2$ (mm)	$2h_3$ (mm)	$2h_4$ (mm)	$2h_5$ (mm)	$\overline{2h}$ (mm)	STD (mm)
C-ELS-7-1.4	5.02	4.98	4.97	4.99	4.99	4.99	0.02
C-ELS-7-1.10	4.94	4.96	4.94	4.96	4.96	4.95	0.01
C-ELS-7-1.11	4.97	4.98	4.98	4.97	4.98	4.98	0.00
C-ELS-7-1.12	4.97	4.98	4.96	4.97	4.98	4.97	0.01
C-ELS-7-1.13	4.98	4.99	4.96	5.00	4.99	4.98	0.01
C-ELS-7-1.14	4.99	4.98	4.95	4.97	4.98	4.97	0.01
specimen no.	b_1 (mm)	b_2 (mm)	b_3 (mm)	b_4 (mm)	b_5 (mm)	$\overline{b}$ (mm)	STD (mm)
C-ELS-7-1.4	20.14	20.25	20.32	20.33	20.35	20.28	0.08
C-ELS-7-1.10	20.26	20.29	20.29	20.26	20.25	20.27	0.02
C-ELS-7-1.11	20.40	20.41	20.40	20.38	20.25	20.37	0.06
C-ELS-7-1.12	20.36	20.33	20.31	20.31	20.27	20.32	0.03
C-ELS-7-1.13	20.32	20.29	20.3	20.25	20.26	20.28	0.03
C-ELS-7-1.14	20.30	20.29	20.25	20.30	20.28	20.28	0.02
specimen no.	$a_0^{(f)}$ (mm)	$a_0^{(b)}$ (mm)	$\overline{a}_0$ (mm)	$\lvert\Delta_0\rvert$ (mm)	L_0 (mm)	l (mm)	
C-ELS-7-1.4	-	-	-	-	-	199.5	
C-ELS-7-1.10	50.58	50.30	50.44	0.28	67.0	199.5	
C-ELS-7-1.11	50.26	50.50	50.13	0.26	66.5	200.0	
C-ELS-7-1.12	49.82	50.26	50.04	0.44	67.0	200.0	
C-ELS-7-1.13	49.80	49.51	49.66	0.29	66.0	199.5	
C-ELS-7-1.14	49.38	49.57	49.47	0.19	66.0	200.0	

Table 5.11: Failure load at initial delamination propagation and final delamination length of the C-ELS specimens for both test stages: first stage - initiation from the PTFE film (APC), and second stage - initiation and propagation from the natural delamination.

	Stage I: pre-cracking					Stage II: propagation					
specimen no.	P_{NL} (N)	P_{vis} (N)	$P_{5\%/\max}$ (N)	$\overline{a}_p$ (mm)	$\lvert\Delta_p\rvert$ (mm)	P_{NL} (N)	P_{vis} (N)	$P_{5\%/\max}$ (N)	L_p (mm)	$\overline{a}_f$ (mm)	$\lvert\Delta_f\rvert$ (mm)
C-ELS-7-1.10	239.9	251.8	268.7	53.74	1.62	260.0	274.7	302.3	83.0	81.78	1.45
C-ELS-7-1.11	207.1	247.7	264.1	52.09	0.16	251.0	270.0	309.3	82.0	76.88	1.37
C-ELS-7-1.12	189.2	208.0	248.2	53.04	0.31	248.4	261.3	310.5	83.0	77.64	0.44
C-ELS-7-1.13	227.3	243.0	275.4	54.72	0.24	259.5	272.3	306.0	85.0	79.90	1.65
C-ELS-7-1.14	196.3	229.5	245.1	51.06	0.20	237.2	261.1	300.4*	81.0	73.43	0.64
Average	212.0	236.0	260.3			251.2	267.9	305.7			
STD	19.0	15.9	11.8			8.4	5.7	3.9			
CV	8.96%	6.73%	4.51%			3.33%	2.11%	1.27%			

the 11 plies in the upper specimen arm or sub-laminate, which is calculated as $\overline{h}_T/11$, is thinner than the evaluated average ply thickness of the 12 plies in the lower specimen sub-laminate, which is calculated as $\overline{h}_B/12$. A typical difference of about 0.03 mm in the average ply thickness between the upper and lower sub-laminates was obtained. Recall that the nominal ply thickness is 0.22 mm. Nevertheless, those evaluated ply thicknesses are within the valid range acceptable for this material and manufacturing process. In addition, it may be noted that the dimensions of the C-ELS specimens as well as the geometry of the load blocks were chosen so that the correction factors F and N presented in the ISO 15114 (2014) Standard may be taken as unity.

The initial delamination length on the front and back sides of the specimen, $a_0^{(f)}$ and $a_0^{(b)}$, respectively, as well as the average values of the initial delamination length $\overline{a}_0$ are also presented in Table 5.10. It is observed that the absolute difference between $a_0^{(f)}$ and $a_0^{(b)}$, denoted as $|\Delta_0|$ in Table 5.10, for each specimen is less than 2 mm. According to the ISO 15114 (2014) Standard, a_0 should be approximately 50 mm long. Here, it satisfies this requirement. The length of the specimens, l, is also presented in Table 5.10, and is seen to be approximately 200 mm, which conforms with the standard. After each test stage was carried out, the delamination length was measured on both sides of each specimen by means of the optical mode of the Olympus confocal microscope. The average delamination lengths which were measured at the end of each test stage, artificial pre-crack (APC) and pre-crack (PC), are presented in Table 5.11, as $\overline{a}_p$ and $\overline{a}_f$, respectively. For each test stage, it may be observed that the absolute difference between the final delamination length on both sides of each specimen, denoted by $|\Delta_p|$ and $|\Delta_f|$, is less than 2 mm for all specimens.

Note, that for all C-ELS specimens the experimental data obtained for $\overline{a}_f$ was not used since all average final delamination lengths were within less than 10 mm of the edge of

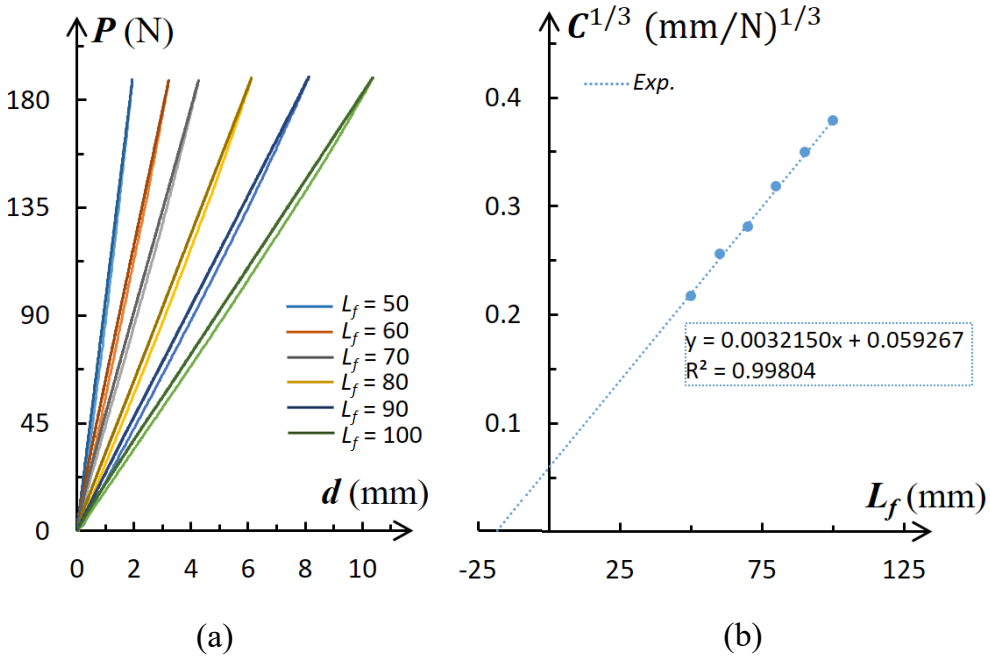

Figure 5.20: (a) Load versus displacement curves for the ELS fixture calibration procedure. (b) Plot of $C^{1/3}$ versus L_f.

the clamping fixture. The ISO 15114 (2014) Standard recommends using data which is further away from the clamp. Nonetheless, the values related to $\overline{a}_f$ are presented, as well as the absolute difference in the final delamination lengths $|\Delta_f|$ measured on both sides of each specimen; they were seen to be less than 2 mm.

As recommended in the ISO 15114 (2014) Standard, prior to C-ELS testing a calibration procedure of the ELS fixture was performed according to the protocol presented in Section 5.2.1. The experimental data obtained for each specimen free length L_f was analyzed and the specimen compliance C for each value of L_f was calculated from the linear portion of the slope of the loading part of each load-displacement curve. The load-displacement curves obtained for the procedure of the ELS fixture calibration are presented in Fig. 5.20a. Values of C were used to plot $C^{1/3}$ versus L_f, as shown in Fig. 5.20b. As may be observed, a linear regression of the data points was performed extending the regression back to $C^{1/3} = 0$. For specimen C-ELS-7-1.4 used for clamp calibration, the value of the clamp correction parameter in eq. (5.12) was found to be $\Delta_{clamp} = 18.43$ mm; the value of the beam flexural modulus in eq. (5.13) was found to be $E_{1f} = 47.72$ GPa. These values were used as reference values in calibration of the FE model.

The room temperature and relative humidity (RH) were recorded during the two stages of the C-ELS tests, where each APC stage lasted about 15 minutes and each PC stage lasted about an hour. The initial and final environmental conditions of each test stage

Table 5.12: Temperature and relative humidity during C-ELS APC and PC test stages.

	Stage I: pre-cracking				Stage II: propagation			
specimen no.	$\vartheta_{initial}$ (°C)	$\mathrm{RH}_{initial}$ (%)	ϑ_{final} (°C)	RH_{final} (%)	$\vartheta_{initial}$ (°C)	$\mathrm{RH}_{initial}$ (%)	ϑ_{final} (°C)	RH_{final} (%)
C-ELS-7-1.4	22.4	36.3	22.5	36.0				
C-ELS-7-1.10	22.3	42.5	23.6	48.4	23.3	46.4	23.4	49.1
C-ELS-7-1.11	23.2	39.3	23.1	38.4	23.8	39.2	23.8	41.9
C-ELS-7-1.12	23.5	38.2	23.8	41.4	23.8	37.1	24.9	39.2
C-ELS-7-1.13	23.4	42.5	23.3	43.9	23.4	44.2	23.3	48.8
C-ELS-7-1.14	22.5	44.2	23.1	46.1	22.9	47.5	23.1	45.0

are presented in Table 5.12. Recall that the ASTM Standard D 5528-13 (2014) requires that the test temperature be $23 \pm 3°$ C and the RH be $50 \pm 10\%$. In Table 5.12, it may be observed that eight out of the twenty two readings of the RH were below the recommended values, whereas the temperature readings were within the required range.

The load-displacement curves obtained for the five C-ELS fracture toughness tests are shown in Figs. 5.21a and 5.21b for the APC and PC stages, respectively. It may be observed in Fig. 5.21b that there are regions of unstable delamination propagation, which is characterized by a sharp decrease in the load. However, it is also observed that the

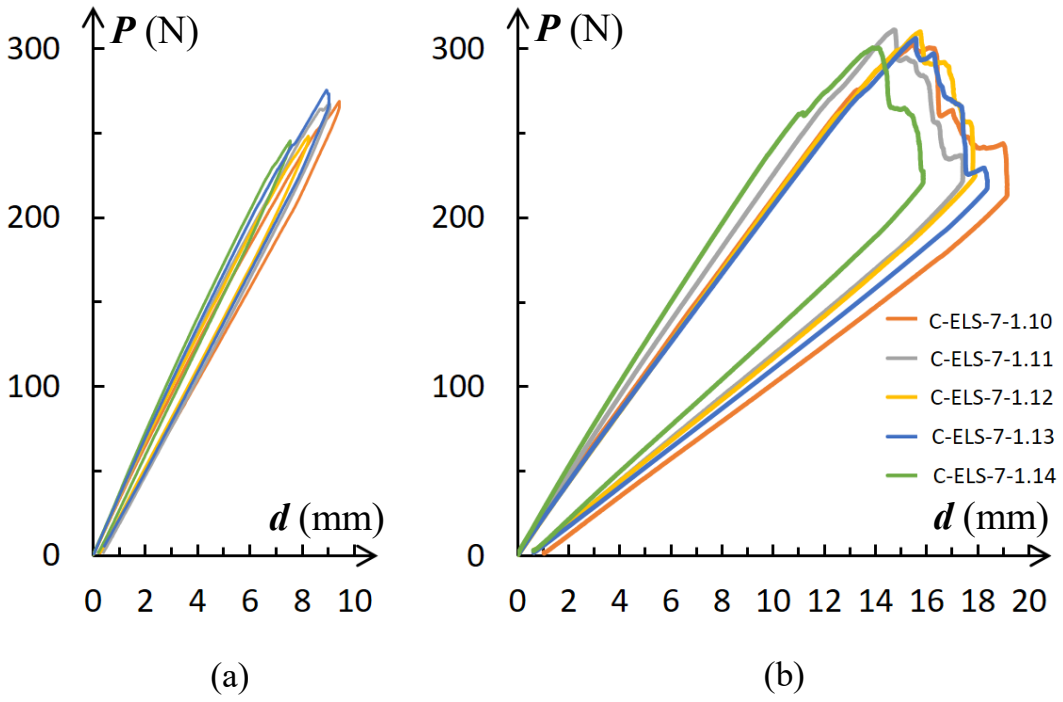

Figure 5.21: Load versus displacement curves from fracture toughness tests of C-ELS specimens, C-ELS-7-1.10 to C-ELS-7-1.14: (a) first test stage for delamination initiation from PTFE film (APC) and (b) second test stage for initiation and propagation from natural delamination (PC).

delamination propagation in the C-ELS specimens is more stable than that within the DCB specimens as shown in Fig. 5.7. According to the ISO 15114 (2014) Standard, the initiation load at failure is determined in three ways: non-linear (NL), which is defined as the point where a deviation from the linear load-displacement curve is observed while ignoring any changes related to the initial activation of the loading system; visual (vis); and 5% offset or maximum load (5%/max), whichever of the two occurs first. The 5% offset represents an increase of 5% in the compliance from its initial value. The initiation loads at failure, denoted by P_{NL}, P_{vis} and $P_{5\%/\mathrm{max}}$, are shown in Table 5.11 for each test stage of the C-ELS specimens. The coefficient of variation (CV) is given by

$$\mathrm{CV} = \frac{\mathrm{STD}}{\overline{P}} \ , \tag{5.14}$$

where $\overline{P}$ is the average value of the loads and STD is its standard deviation. These values are also presented in Table 5.11 for P_{NL}, P_{vis} and $P_{5\%/\mathrm{max}}$ calculated for each of the C-ELS test stages. As may be observed in Table 5.11, the variation in the loads decreases as the average load value increases, i.e. the CV value of $P_{5\%/\mathrm{max}}$ is less than that of P_{vis}, which is less than that calculated for P_{NL}. It is also seen that the CV values of those loads decrease in the second stage of the C-ELS test, in which the initiation and propagation are obtained for specimens with a natural delamination front.

It should be noted that delamination propagation, as observed in the images, was not always straight forward; sometimes the delamination tip jumped several millimeters ahead. It was found to be more stable than that for the DCB specimens, but still there were load drops, corresponding to delamination propagation jumps as the delamination propagated. Nevertheless, although it was sometimes difficult to determine the position of the delamination tip from the specimen photographs, curve fitting of specimen compliance versus delamination length was performed based upon the data obtained for visually detected delamination lengths.

In a similar manner as that performed for the DCB specimens in Section 5.1.2, and following the ISO 15114 (2014) Standard regarding beam theory, it may be shown that $C \propto a^3$. Thus, the relationship between the delamination length and specimen compliance may be expressed according to the experimental compliance method (ECM) presented in the ISO 15114 (2014) Standard. The ECM expression may be rewritten as a power law as given in eq. (5.4). The experimental data in Table G.8 was used along with eq. (5.4) to generate the a versus C curve presented in Fig. 5.22. The values of g and C_0 and the coefficient of determination R^2 were found as 206.36 $(\mathrm{N} \cdot \mathrm{mm}^2)^{1/3}$, $2.95{\cdot}10^{-2}$ mm/N and 0.993, respectively. In Fig. 5.22, it may be observed that there is good agreement between the measured and evaluated values of a. In addition, it may be seen from Figs. 5.22 and 5.8 that C for the C-ELS specimen is one order of magnitude less than that obtained for the DCB specimens. The same procedure was performed separately with the experimental

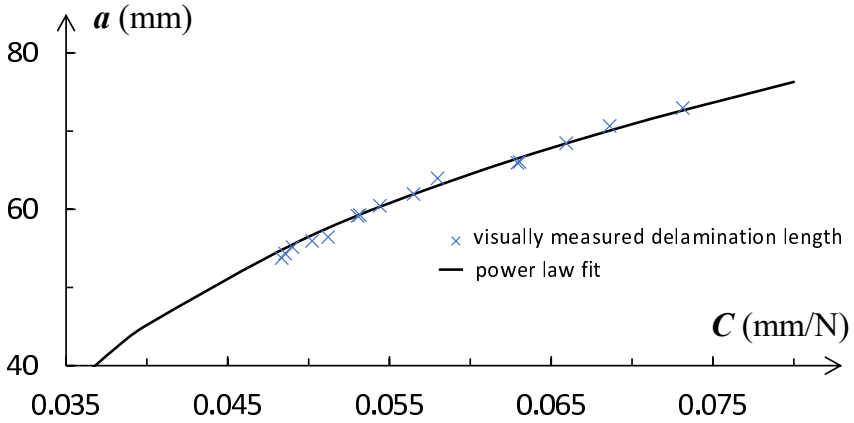

Figure 5.22: Correlation between delamination length and test compliance for specimen C-ELS-7-1.10.

data of specimens C-ELS-7-1.10 to C-ELS-7-1.14. The delamination propagation data of specimens C-ELS-7-1.10 to C-ELS-7-1.14 is presented in Tables G.8 through G.12, for visually detected delamination lengths. It may be noted that in all C-ELS specimens, the compliance obtained in the first stage of the C-ELS test was higher than that obtained in the second stage of the test, in which the delamination propagated from a natural delamination front, as mentioned in Davies et al. (1998). In Tables G.8 through G.12, as well as in Table 5.13, the values of the parameters of eq. (5.4), g and C_0, as well as the coefficient of determination R^2, are shown for each C-ELS specimen.

To analyze the C-ELS specimens by means of the FE method, several contact surfaces were used. These include the delamination faces, as well as the specimen outer surfaces where it was confined within the ELS clamping fixture. Two-dimensional FE analyses with plane strain conditions were implemented by means of the ADINA (Bathe, 2011) software. Use was made of eight noded isoparametric, quadrilateral elements. The square-root singularity along the delamination front was modeled with quarter-point elements. The oscillatory part of the singularity was not modeled. The material properties used to characterize the plain woven plies with the yarn in the $0°/90°$ and $+45°/-45°$ directions

Table 5.13: Values of the fitting parameters in eq. (5.4) for the C-ELS specimens.

specimen no.	$g\left(\left[\mathrm{N}\cdot\mathrm{mm}^2\right]^{1/3}\right)$	C_0 (mm/N)	R^2
C-ELS-7-1.10	206.36	$2.95\cdot10^{-2}$	0.993
C-ELS-7-1.11	217.32	$3.13\cdot10^{-2}$	0.995
C-ELS-7-1.12	219.38	$3.24\cdot10^{-2}$	0.993
C-ELS-7-1.13	214.47	$3.26\cdot10^{-2}$	0.996
C-ELS-7-1.14	218.44	$2.98\cdot10^{-2}$	0.997

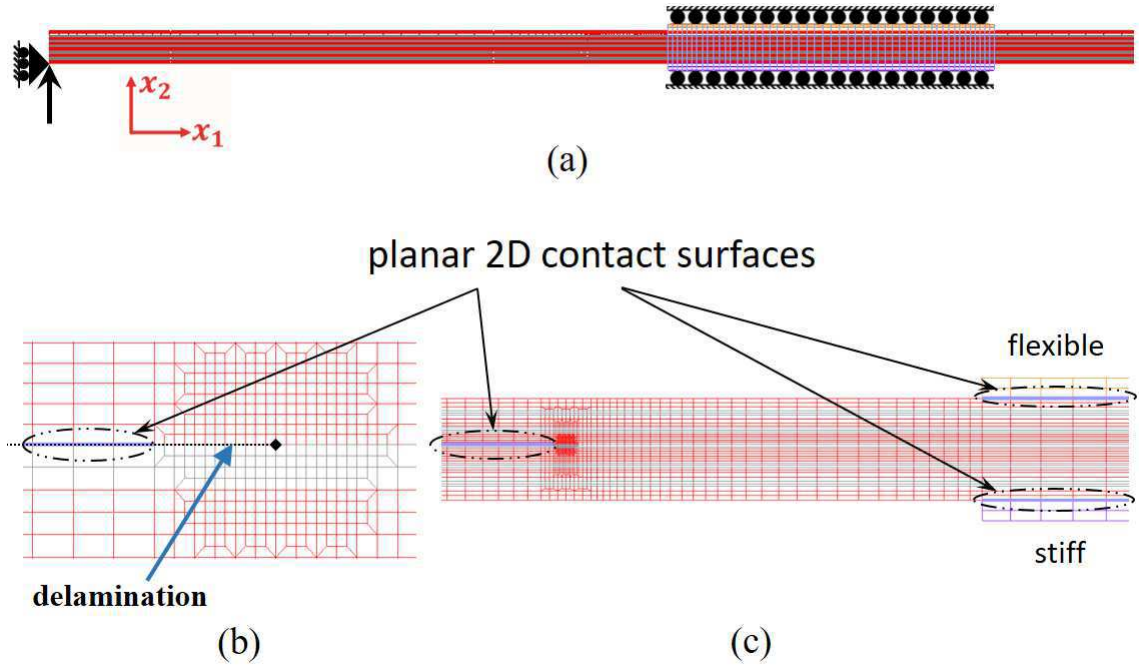

Figure 5.23: Mesh of the C-ELS specimen: (a) illustration of the FE model constraints, (b) detailed front view near the delamination tip, and (c) detailed view indicating the locations where contact boundaries are applied; contact is implemented along the remainder of delamination faces and along both sides of the specimen where it is confined within the clamping fixture.

are presented in Table 2.1. An example of a two-dimensional FE model is presented in Fig. 5.23a, where the FE model was used in analyzing specimen C-ELS-7-1.10. The ELS clamp fixture was modeled as shown in Figs. 5.23a and 5.23c, in which two rectangular bodies are referred to as being flexible and stiff. Surface-to-surface contact interaction was introduced along both sides of the specimen model between the stiff and flexible clamps. The clamps were constrained to have the same displacement in the x_1-direction; displacement in the x_2-direction was prohibited.

The lower clamp was modeled to be steel as shown in Table 5.14. At the first trial of calibrating the FE model, the upper clamp was modeled to be steel and then its properties were adjusted iteratively/manually. It should be noted that adjustment of the FE model

Table 5.14: Mechanical properties of the stiff and flexible clamps in Figs. 5.23a and 5.23c.

clamp	$E_{11} = E_{33}$ (GPa)	E_{22} (GPa)	G_{13} (GPa)	$G_{23} = G_{12}$ (GPa)	ν_{13}	$\nu_{23} = \nu_{21}$
lower (stiff)	205.0	205.0	78.8	78.8	0.3	0.3
upper (flexible)	205.0	$341.6 \cdot 10^{-3}$	205.0	102.2	0.0	0.0

for the upper clamp, was performed with the model generated for specimen C-ELS-7-1.4, for which the calibration procedure was carried out. Recall that the artificial delamination of specimen C-ELS-7-1.4 was confined within the ELS clamping fixture, so that only the intact beam region of the specimen was examined. Thus in the FE model for specimen C-ELS-7-1.4, contact surfaces were applied only where the specimen was between the clamps.

The material properties of the upper clamp in the x_1 and x_3-directions were taken to be stiff in order to avoid undesirable deformations that did not occur in the C-ELS tests. Thus, the upper clamp was modeled to be tetragonal, where its material properties were modified until reasonable agreement was obtained between the FEA results and the calibration experimental data. These material properties are presented in Table 5.14. The value of E_{22} was found to be equivalent to application of linear springs of stiffness of 17.1 N/m.

The FE models were analyzed for different values of model free length L_f. Although the FE analyses for specimen C-ELS-7-1.4 were non-linear due to the contact surfaces and large displacement, a linear relationship between the applied load and obtained deflection was found. It may be noted that in each two-dimensional FE analysis, the applied load from the calibration procedure $P = 190$ N was translated into a uniform distributed load $P/\overline{b}$, where $\overline{b} = 0.02028$ m as given in Table 5.10, and then applied as a concentrated load at the bottom of the specimen model, as schematically shown in Fig. 5.23a.

The FEA results for each model free length L_f were used to determine the corresponding compliance C. The load-displacement curves obtained by means of the FEAs for the ELS fixture calibration procedure are presented in Fig. 5.24a, in which the loading part of each load-displacement curve obtained experimentally is also shown. The absolute percent difference between the FE curves and the experimentally obtained curves varied between 1.0% and 4.4%. It may be noted that in Fig. 5.24a, for $L_f = 70$ mm, the experimentally obtained curve is covered by the curve obtained from the FEA for this value of free length. Next, values of C were used to plot $C^{1/3}$ versus L_f, as shown in Fig. 5.24b.

As performed for the experimental data of specimen C-ELS-7-1.4, the values from the FEAs for the flexural modulus E_{1f} in eq. (5.13) and the clamp correction parameter Δ_{clamp} in eq. (5.12) for $C^{1/3} = 0$ were determined as $E_{1f} = 53.69$ GPa and $\Delta_{clamp} = 21.45$ mm. It may be recalled that these parameters were found as $E_{1f} = 47.72$ GPa and $\Delta_{clamp} = 18.43$ mm from the analysis of the experimental data of specimen C-ELS-7-1.4. Although the flexural modulus is not applicable for determining the critical interface energy release rate for the interface investigated here, it may be noted that this value is close to the axial modulus $E_{11} = E_{33}$ of the $0°/90°$ direction plain woven ply in Table 2.1 given by $E_{11} = 57.3$ GPa. Since the content of the $0°/90°$ direction plies in specimen

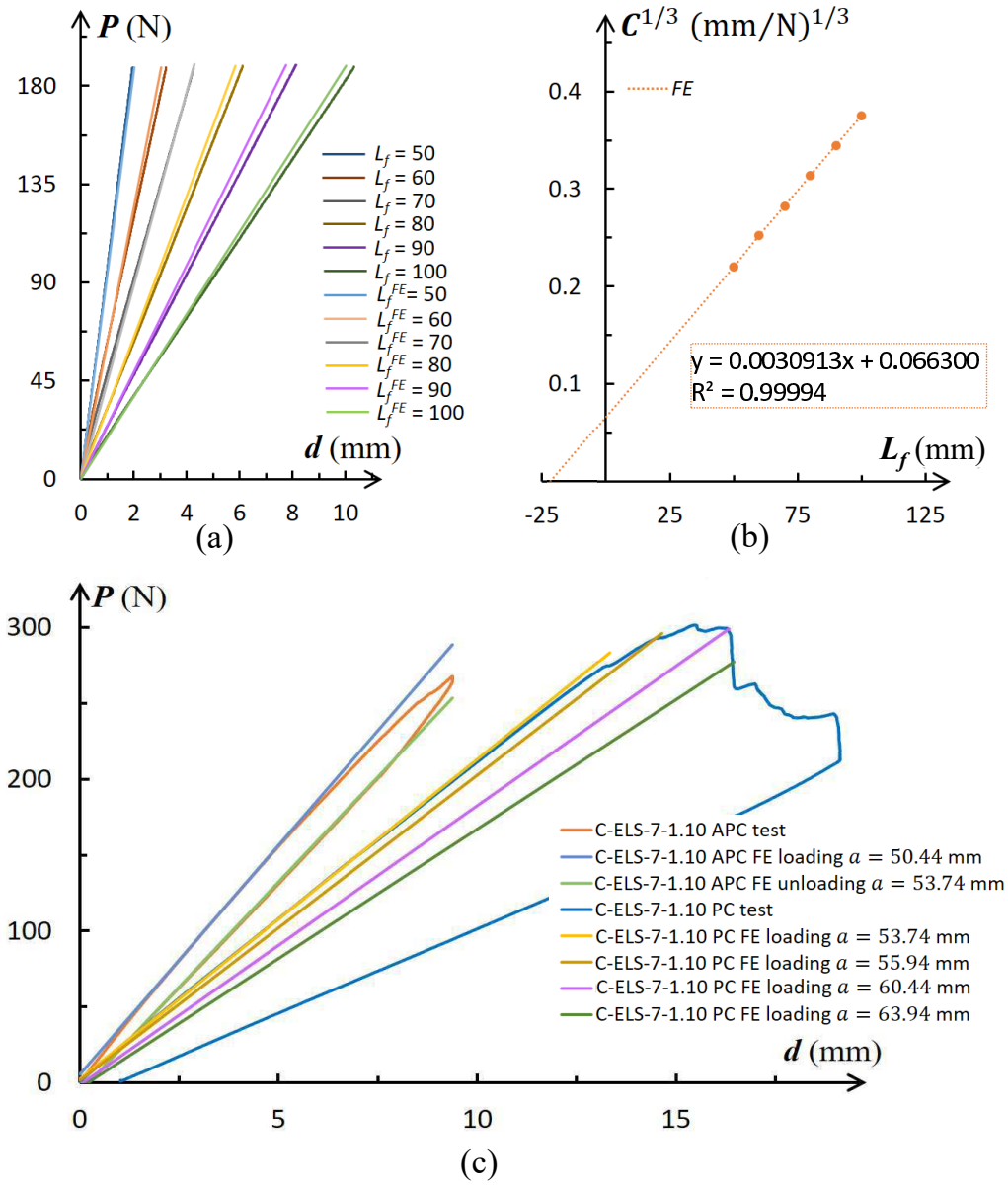

Figure 5.24: (a) Comparison between the loading curves experimentally obtained from the ELS clamp calibration procedure for specimen C-ELS-7-1.4 and load-displacement curves obtained for specimen C-ELS-7-1.4 by means of FE analyses; (b) plot of $C^{1/3}$ versus L_f for the FEA calibration procedure. (c) Comparison between the load-displacement curves obtained for specimen C-ELS-7-1.10 from both test stages, APC and PC, experimental data and FEA results.

layup is high, this is a reasonable result. In addition, this value is close to the flexural modulus $E_{1f} = 52.95$ GPa of the intact beam segment of specimen C-ELS-7-1.4, which was calculated by means of classical laminate plate theory, as may be found in Ashton and Whitney (1970).

In Fig. 5.24c the load-displacement curves are presented for two stages of the C-ELS tests: APC and PC. These curves are for specimen C-ELS-7-1.10 which were obtained from the experimental data and via the FEAs. In the FEAs, the maximum value of the experimentally measured displacement was applied. In Fig. 5.24c, relatively good agreement is observed between the experimental data and the FE results, in the linear regions of the curves where delamination initiation or propagation are not suspected to occur. In addition, in the second stage of the C-ELS test, it is observed that the FEA load-displacement curve for specific values of visually detected delamination lengths coincide with the experimental delamination propagation load-displacement curve at almost the same locations. That is, for the same applied displacement, the value of the obtained force calculated by means of the FEA is very close to the value of the force which was measured during the test. The failure loads which were obtained by means of the FEAs for the C-ELS specimens are also presented in Tables G.8 through G.12 for visually detected delamination lengths. In Tables G.8 through G.12, it may be observed that good agreement between the load values, obtained experimentally and by FEA, was found for most delamination lengths in each C-ELS specimen. The maximum and minimum percent differences between the values of these loads are summarized in Table 5.15. The largest difference is 6%. Thus, it was concluded that the measured applied displacement and load, as well as specimen attributes, were well represented and modeled in the FE analyses.

To demonstrate mesh convergence of the FE model inner mesh, a coarse, fine and finer mesh were used with the geometric parameters of specimen C-ELS-7-1.10 in Table 5.10 with representative delamination lengths of $a = 54.34$ mm and $a = 72.94$ mm. The in-plane dimensions of the elements in the vicinity of the delamination front were set to $1.02 \cdot 10^{-4} \times 1.02 \cdot 10^{-4}$ m^2, $5.09 \cdot 10^{-5} \times 5.09 \cdot 10^{-5}$ m^2 and $2.55 \cdot 10^{-5} \times 2.55 \cdot 10^{-5}$ m^2,

Table 5.15: Maximum and minimum percent difference (in absolute value) between the values of the load obtained experimentally and by FEA for visually detected delamination lengths in the C-ELS specimens, as presented in Tables G.8 through G.12.

specimen no.	max. %	min. %
C-ELS-7-1.10	6.0	0.4
C-ELS-7-1.11	4.2	0.2
C-ELS-7-1.12	3.7	0.0
C-ELS-7-1.13	4.7	0.2
C-ELS-7-1.14	4.2	0.6

Table 5.16: Characteristics of the four meshes which were used in the convergence study of the C-ELS specimen.

mesh	no. of elements	no. of nodes	element in-plane size near delamination front (m^2)	in-plane aspect ratio
coarse	4,942	15,366	$1.02 \cdot 10^{-4} \times 1.02 \cdot 10^{-4}$	1.0
fine	5,218	16,206	$5.09 \cdot 10^{-5} \times 5.09 \cdot 10^{-5}$	1.0
finer	5,538	17,180	$2.55 \cdot 10^{-5} \times 2.55 \cdot 10^{-5}$	1.0
modified fine	5,196	16,142	$5.09 \cdot 10^{-5} \times 5.09 \cdot 10^{-5}$ upper ply elements	1.0
			$5.09 \cdot 10^{-5} \times 5.65 \cdot 10^{-5}$ lower ply elements	1.11

in a similar manner as shown in Figs. 5.10a, 5.10b and 5.10c, respectively. A modified fine mesh similar to that shown in Fig. 5.10d, in which the ply thickness of the upper and lower plies which define the interface were divided into 4 elements along their thickness, was also generated. In that mesh, the in-plane dimensions of the elements in the vicinity of the delamination front were set to $5.09 \cdot 10^{-5} \times 5.09 \cdot 10^{-5}$ m^2 in the upper ply and $5.09 \cdot 10^{-5} \times 5.65 \cdot 10^{-5}$ m^2 in the lower ply. Thus, an in-plane aspect ratio of 1.0 and 1.11 was obtained, respectively, as shown in Figs. 5.23b and 5.10d. Since each specimen arm was of different height and the upper and lower arms of each specimen were found to be of different ply thicknesses, as discussed in the beginning of Sections 5.1.2 and 5.2.2, the sizes of the elements were appropriately adjusted in each specimen model. The in-plane aspect ratio of the elements at the bottom of the lower ply in the coarse mesh as shown in Fig. 5.10a is 4.59; for the fine and finer meshes as shown in Figs. 5.10b and 5.10c, the in-plane aspect ratio of some of those elements is 2.29 and 4.59. Some characteristics of the FE meshes which were used in the convergence study are given in Table 5.16.

The stress intensity factors were calculated for each mesh by means of the DE method, which was presented in Section 3.1. The displacement from the experimental data was applied in all FEAs, each model with a suitable displacement according to its delamination length. The stress intensity factors were calculated for each delamination length and each mesh type. The location in which the square-root of the sum of the coefficient of determination of both in-plane stress intensity factors, K_1 and K_2, was the closest to value of $\sqrt{2}$ was chosen for determination of the values of K_1 and K_2. It may be noted that the distance from the delamination tip, in which the values of K_1 and K_2 were chosen, occurred at different positions along the delamination. Ordinary units for the in-plane stress intensity factors $\hat{K}_1$ and $\hat{K}_2$ were obtained by employing eq. (4.9) with length parameter $\hat{L} = 100$ μm, as described in Section 4.4.2. Since plane strain conditions were

assumed, which means that $K_{III} = 0$, the out-of-plane phase angle ϕ in eq. (1.14) was determined as $\phi = 0$. The in-plane phase angle $\hat{\psi}$ in eq. (1.12) was calculated for each mesh type and each delamination length a.

Solution convergence is examined in Table 5.17, in which the differences between the interface energy release rate $\mathcal{G}_i$ calculated by means of the J-integral in Adina (Bathe, 2011). It may be noted that delamination face opening was obtained near the delamination tip for at least a distance of 2.95 mm and 3.21 mm from the delamination tip with a delamination length of $a = 54.34$ mm and $a = 72.94$ mm, respectively. The normalized in-plane stress intensity factors and the corresponding in-plane phase angle $\hat{\psi}$ obtained for pairs of meshes are also presented. For each pair of meshes, the mesh which is more refined in the vicinity of the delamination front serves as the reference (ref) in eq. (4.8). It should be noted that the maximum percent differences shown in Table 5.17 occurred at different positions along the delamination faces. It may be observed that convergence is obtained for both delamination lengths $a = 54.34$ mm and $a = 72.94$ mm. It may be recalled that the values calculated by means of the DE method are less accurate. Nonetheless, the differences in all parameter values presented in Table 5.17 are relatively small, especially the values for $\hat{\psi}$. Since the absolute value of the maximum percent difference for both delamination lengths between the fine and the finer mesh and also between the modified fine and the finer mesh is less than 0.2%, it may be concluded that the modified fine mesh shown in Fig. 5.10d may be used in all FE models in this study. Although, the DE method is less accurate than the M-integral, it still reproduces relatively satisfying results.

It should be noted that another FE model of the modified fine mesh in Fig. 5.23b was generated for specimen C-ELS-7-1.10 with delamination lengths of $a = 54.34$ mm and $a = 72.94$ mm. This is the same specimen and the same delamination lengths used in the convergence study in the region of the delamination tip. Mesh refinement was performed in regions away from the delamination tip; additional elements were included, at a distance which is between 6 to 61 ply thicknesses behind the delamination tip. These

Table 5.17: Maximum percent difference (in absolute value) between the energy release rate $\mathcal{G}_i$ calculated by means of the J-integral in Adina (Bathe, 2011), normalized in-plane stress intensity factors with $\hat{L} = 100$ μm calculated by DE and in-plane phase angle $\hat{\psi}$ for pairs of meshes.

percent difference												
meshes	coarse and fine				fine and finer				modified fine and finer			
delamination	$\mathcal{G}_i$	$\hat{K}_1$	$\hat{K}_2$	$\hat{\psi}$	$\mathcal{G}_i$	$\hat{K}_1$	$\hat{K}_2$	$\hat{\psi}$	$\mathcal{G}_i$	$\hat{K}_1$	$\hat{K}_2$	$\hat{\psi}$
$a = 54.34$ mm	0.15	0.15	0.12	0.0011	0.0040	0.084	0.067	0.0006	0.0043	0.098	0.078	0.0007
$a = 72.94$ mm	0.16	0.19	0.12	0.0014	0.0067	0.130	0.085	0.0010	0.0072	0.143	0.094	0.0011

refined models contained 5,484 plane strain 2D solid elements and 17,038 nodal points with a delamination tip region as shown in Fig. 5.23b. Far from the delamination front, a maximum in-plane element aspect ratio of 1 to 17.5 and 1 to 27.6 throughout the FE model was permitted, for the FE models with delamination lengths of $a = 54.34$ mm and $a = 72.94$ mm, respectively. The properties of these meshes may be compared to that of the modified fine meshes in Table 5.16. For the strain energy release rate calculated by ADINA (Bathe, 2011), for both delamination lengths, it was found that the maximum percent difference between the refined mesh and the original modified fine mesh is less than $8.0 \cdot 10^{-4}$ %. Thus, it was concluded that the bending motion is sufficiently characterized by the original modified fine mesh.

Based upon the convergence study for the inner and outer FE meshes presented above, the modified fine mesh is employed for all C-ELS specimens. In the same manner as for the DCB FE models, the modified fine mesh as shown in Figs. 5.9b and 5.23 was employed, as detailed in Table 5.16. Finite element models were generated for all delamination lengths, which were visually observed in the images of each C-ELS specimen, as acquired during the tests. The delamination lengths, which were modeled, varied between 49.47 mm $\leq a \leq$ 74.66 mm. In each C-ELS FE model, for each delamination length a, the appropriate displacement value from the experimental data, was applied incrementally on the bottom of the FE model; each displacement increment was 10% of the total displacement. The FE model boundary conditions and restraints are illustrated in Fig. 5.23a. In order to eliminate delamination face interpenetration, surface-to-surface contact interaction was introduced along most of the span of the delamination faces, except for the region in the vicinity of the delamination tip as shown in Fig. 5.23b in which the contact regions are surrounded by the dashed ellipses. This is in addition to the contact interaction implemented along the specimen confinement region, which is characterized by the flexible and stiff clamps in Fig. 5.23c. All FE meshes contained 5,196 plane strain 2D solid elements and 16,142 nodal points. A maximum element aspect ratio of 1 to 12.7 was permitted between the delamination front and a distance of about 61 ply thicknesses ahead and behind the delamination front. In regions very far from expected stress concentrations (such as load application points, reactions, delamination front, etc.), an element aspect ratio varied between 1 to 15.8 and 1 to 28.3 was permitted. It is recalled that ply groups consisting of several plies of the same plain woven material is assumed to serve as a single plain woven ply with the same mechanical properties presented in Table 2.1, with a total thickness of all plies in the ply group.

For each FE analysis of each C-ELS specimen model, the resultant load was calculated by multiplying the FE result for the uniformly distributed load with the specimen average width $\overline{b}$ in Table 5.10. It may be noted that a linear relationship between the displacement and resultant load was found in each step of each FE analysis, as may be seen in Fig. 5.24c

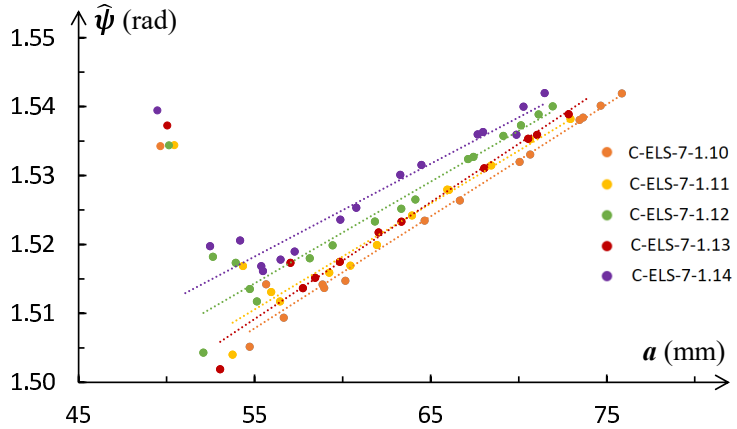

Figure 5.25: The in-plane phase angle $\hat{\psi}$ versus a with $\hat{L} = 100$ μm obtained by means of the DE method for the C-ELS specimens.

for specimen C-ELS-7-1.10. In addition, it was observed that the value of the compliance in eq. (5.4) obtained by means of the FEM was very close to the value retrieved from the experimental data.

The stress intensity factors, obtained for the modified fine mesh, were calculated by means of the DE method, which was presented in Section 3.1. Ordinary units for the in-plane stress intensity factors $\hat{K}_1$ and $\hat{K}_2$ were obtained by employing eq. (4.9) with length parameter $\hat{L} = 100$ μm, as described in Section 4.4.2. Recall that plane strain conditions were assumed, hence $K_{III} = \phi = 0$. The in-plane phase angle $\hat{\psi}$ in eq. (1.12) was calculated for each delamination length a of each C-ELS specimen. Despite the scatter, it may be observed that the values of $\hat{\psi}$ in Fig. 5.25 are relatively close to the value of $\pi/2$ for every value of a. Hence, the contribution of $\hat{K}_1$ to the total interface energy release rate $\mathcal{G}_i$ is negligible. It may be noted that the upper left most points in Fig. 5.25 are the obtained values of $\hat{\psi}$ which are related to the APC stage of the test of each C-ELS specimen. Since it was found that for the C-ELS specimens $\hat{K}_2$ is dominant, whereas the other stress intensity factors may be neglected, the interface energy release rate $\mathcal{G}_i$ may be treated as the mode II energy release rate $\mathcal{G}_{II}$.

It may be noted that the $\mathcal{G}_i(a)$ values, which are used, were those obtained via the J-integral calculation embedded within ADINA software (Bathe, 2011). Despite the inaccuracies that might be encountered by using the DE method, the maximum percent differences (in absolute value) between the values of $\mathcal{G}_i(a)$ obtained via the J-integral in ADINA and those calculated by means of the DE method and eq. (1.17) with $K_{III} = 0$ were found to be less than 0.4%. Nonetheless, the $\mathcal{G}_i(a)$ obtained via the J-integral in ADINA were used for determining the values of $\mathcal{G}_{IIc}$, as well as $\mathcal{G}_{IIR}$.

It may be noted that non-linear FEAs including contact interaction surfaces and large

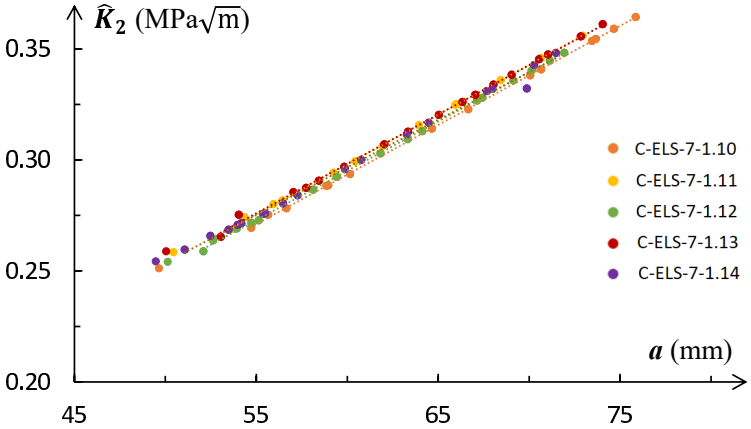

Figure 5.26: The scaled in-plane stress intensity $\hat{K}_2$ versus a with an applied load $P^{FEA} =$ 20 N and $\hat{L} = 100$ μm obtained by means of the DE method for the C-ELS specimens.

displacements were performed for each C-ELS specimen. As mentioned above, a linear relationship between the displacement and resultant load was found in each step of each FEA, as presented for specimen C-ELS-7-1.10 in Fig. 5.24c. Thus, it is interesting to note that a linear relationship was found between the delamination length a and the normalized in-plane stress intensity $\hat{K}_2$ calculated by means of the DE method, as presented in Fig. 5.26. To this end, the values of $\hat{K}_2$ were scaled; the maximum load obtained in the FEA was used as P^{Test} with $P^{FEA} = 20$ N in eq. $(5.6)_1$. The lower left most points in Fig. 5.26 are those obtained in the APC stage of the C-ELS test. The location of each of these points seems to be along the linear relation, which was obtained from the PC stage experimental data of the C-ELS test.

5.2.3 Results

Based upon the data in Tables G.8 to G.12, a $\mathcal{G}_{IIR}$-curve was generated. The values of $\mathcal{G}_{IIR}$ versus $\Delta a = a - a_0$ are plotted in Fig. 5.27. An initiation fracture toughness is shown for $\Delta a = 0$ as $\mathcal{G}_{IIc} = 889.1$ N/m, which is the nearly mode II average critical interface energy release rate for delamination growth from the PTFE insert obtained for specimens C-ELS-7-1.10 through C-ELS-7-1.14. It may be observed that the values of $\mathcal{G}_{IIR}$ increase with Δa until a steady state value of $\mathcal{G}_{IIss} = 2352.6$ N/m is reached for $\Delta a = 9$ mm. Fitting the points between $0 \leq \Delta a \leq 9$ mm results in the expression given by

$$\mathcal{G}_{IIR} = 162.6 \cdot \Delta a + 889.1 \tag{5.15}$$

where Δa in eq. (5.15) is measured in millimeters. The coefficient of determination R^2 for eq. (5.15) and the plotted points was found to be 0.84. Also, it may be observed that

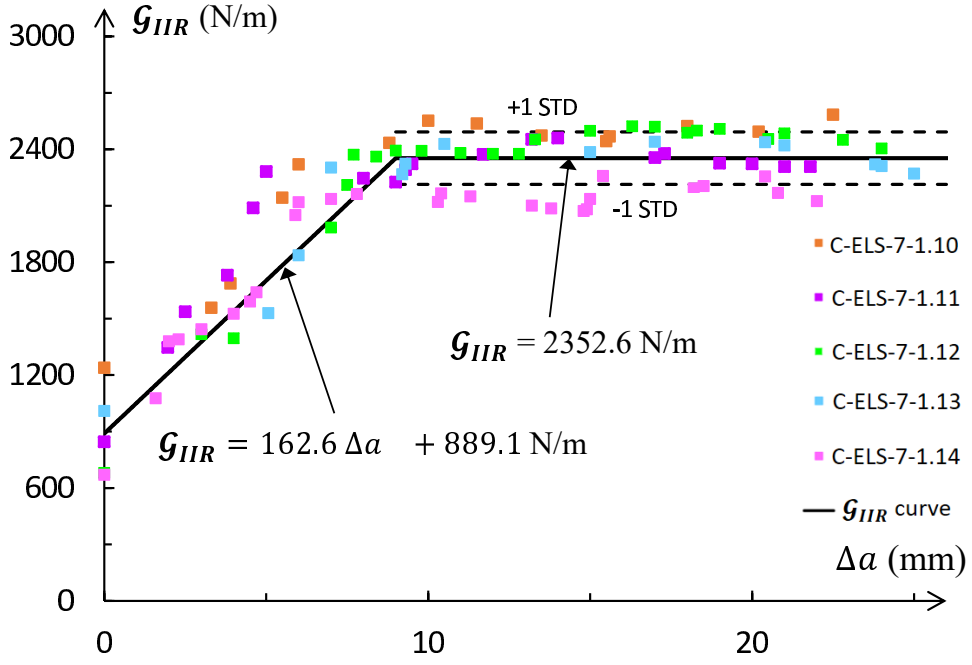

Figure 5.27: Fracture resistance curve: the critical interface energy release rate, referred as $\mathcal{G}_{IIR}$, as a function of delamination propagation length $\Delta a = a - a_0$.

for 9 mm $\leq \Delta a \leq$ 25 mm, most of the $\mathcal{G}_{IIR}$ data points are within one standard deviation from the $\mathcal{G}_{IIss}$ line; the value of one STD was found to be 139.5 N/m.

For the C-ELS specimens, an average value of $\mathcal{G}_{IIc} = 889.1$ N/m was obtained with $\hat{\psi} = 0.49\pi$. It may be noted that this value is somewhat lower than the average critical value for fracture toughness $\mathcal{G}_{ic} = 1006.8$ N/m for this phase angle obtained by means of the BD tests in Section 4.5. This value may be observed in the failure curve presented in Fig. 4.18. In Mega and Banks-Sills (2019), an MD carbon/epoxy composite was studied. There, the value of the average critical energy release rate $\mathcal{G}_{ic} = 1002.5$ N/m for $\hat{\psi} = 0.46\pi$ obtained by means of BD specimens with an approximate thickness of 16.6 mm. Furthermore, in Mega and Banks-Sills (2020), C-ELS specimens which were 5 mm thick and fabricated from the same material and interface as in Mega and Banks-Sills (2019) were tested. The average critical energy release rate $\mathcal{G}_{ic} = 829.9$ N/m was found for $\hat{\psi} = 0.46\pi$.

Despite the differences which may be related to the scatter, it appears that for nearly mode II deformation, the values of the critical energy release rate for initiation $\mathcal{G}_{IIc}$ are less affected by specimen thickness. This is in contrast to the nearly mode I deformation, where $\mathcal{G}_{Ic}$ was found to be sensitive to specimen thickness.

5.3 MMELS

Five quasi-static tests of delamination initiation and propagation were carried out on MMELS specimens with the layup shown in Fig. 5.1. An illustration of a MMELS specimen is presented in Fig. 5.2c, where the geometric parameters l, b and $2h$ are the specimen length, width and height, respectively. In Fig. 5.2c, the right side of the specimen is constrained by means of a clamping fixture, so that free horizontal sliding is allowed but rotation and vertical movement are prohibited; the specimen free length L_f is measured from the load line to the edge of the clamping fixture. The MMELS specimen is loaded normal to its upper arm through displacement control. The initial delamination length a_0 is measured from the load line to the artificially introduced delamination front. The MMELS tests were carried out in order to measure the fracture toughness for one mixed mode ratio of the interface, which is shown in Fig. 1.1b. Note that the MMELS specimens used here were fabricated from the same seventh batch of material tested in Sections 5.1 and 5.2 for the DCB and C-ELS specimens, respectively. In Section 5.3.1, the fracture test protocol is presented. The specimens were analyzed by means of the FEM and three-dimensional M-integral. Analyses are presented in Section 5.3.2; whereas, the results are described in Section 5.3.3.

5.3.1 Fracture test protocol

In this section, the MMELS test protocol is presented. It is based upon the procedure presented in Blackman et al. (2001), which is used for determining the mixed mode I/II delamination resistance of UD FRP laminates by means of the asymmetric double cantilever beam (ADCB). It may be noted that the MMELS test is also called the ADCB or fixed-ratio mixed-mode (FRMM) test.

The C-ELS fracture test protocol in Section 5.2.1 was followed here except for several differences mentioned below. The length of the specimen l should be greater than $a_0 +$ 110 mm long, meaning greater than 160 mm long. A length of 170 mm is recommended in Blackman et al. (2001).

The Instron loading machine used for all other tests was used here, as well. The load cell with a maximum load of 250 N and a resolution of $\pm 0.25\%$ of the reading for a load greater than 2.5 N was used. Prior to testing, the bolts of the clamping fixture were tightened as specified in Section 5.2.1 for the C-ELS specimens. The MMELS tests were carried out in two stages. The free length for both test stages, denoted by L_f and shown in Fig. 5.2c is 100 mm, which corresponds to the suggestion in Blackman et al. (2001) regarding promotion of stable delamination propagation for $L_f < 2.44a$. In the first stage, an initial monotonically increasing displacement was applied at 0.5 mm/min to induce a natural

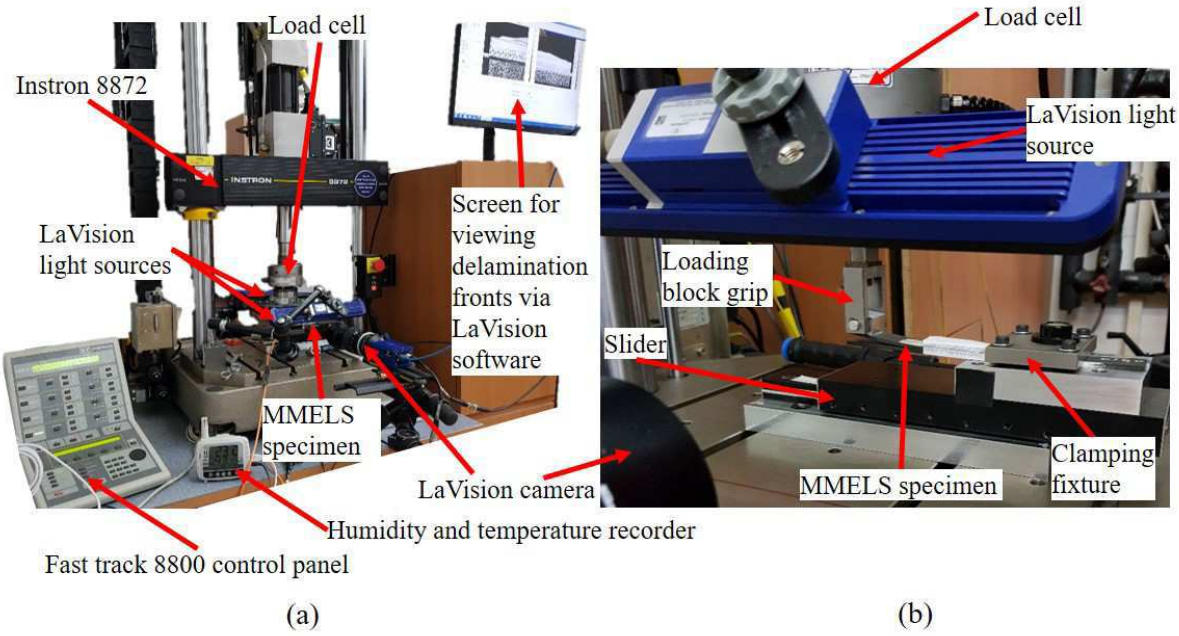

Figure 5.28: MMELS fracture toughness test setup: (a) general view and (b) close-up.

delamination. After delamination propagation was observed, unloading took place at a rate of 5 mm/min. Unloading was interrupted when the load reached 3 N. In the second stage, with propagation from the natural delamination, the displacement rate was the same as for the initial stage. The test was interrupted when the delamination front was within 10 mm from the clamp. Next, the specimen was unloaded to about 3 N at a rate of 5 mm/min. It may be noted that in both test stages, a constant cross-head rate between 1 and 5 mm/min is recommended in Blackman et al. (2001) for loading; for unloading, the displacement rate should be limited to 25 mm/min. Since it was found to be very difficult to follow delamination propagation in both test stages, the displacement rate of 0.5 mm/min was employed here. At the beginning of each test stage, the temperature and the RH in the Instron work area were noted and their values were monitored continuously every 5 min throughout a test.

The test setup is presented in Fig. 5.28. A close-up of the MMELS test rig with a mounted specimen is shown in Fig. 5.28b. The test system for the MMELS tests is similar to that used in the C-ELS tests, as described in Section 5.2.1. Here, another LaVision camera was employed in order to capture the delamination tip from both sides of the specimen. During a test, images of the test specimen were taken at a rate of 3 Hz.

In Fig. 5.29a, specimen MMELS-7-1.9 with the delamination tip captured from its front side, as well as the paper ruler attached to the specimen, are shown. The specimen identifier includes MMELS which represents the test type; 7 which represents the batch number; and 1.9, where the first number represents the row from which the specimen

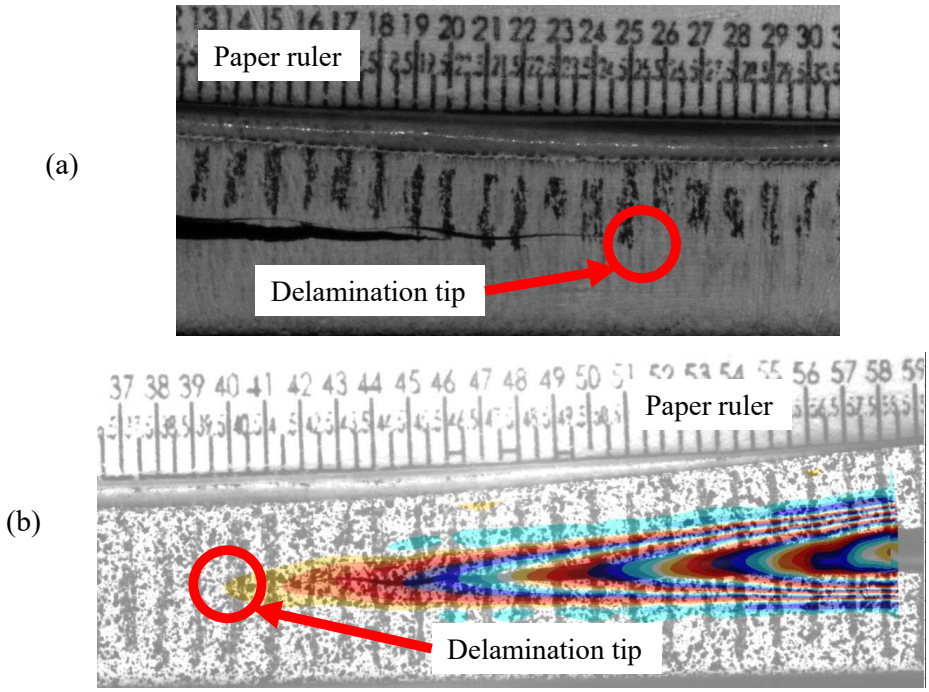

Figure 5.29: Images of the delamination in specimens (a) MMELS-7-1.9 and (b) MMELS-7-1.5 during the second stage of the MMELS test, in which delamination is propagated from a natural delamination front, captured via the LaVision digital camera.

was fabricated and the second number represents the position in the row. Speckles, which were used in the digital image correlation (DIC) method, were spread over the front and back sides of the remaining four MMELS specimens. The program used for DIC analysis is an additional modula within DaVis (2015) software. The DIC was not employed for determining the displacement or strain fields quantitatively in the vicinity of the delamination tip. It was applied only for easier tracking and detection of the delamination tip in the images of the specimen acquired during the test, since it was found difficult to locate the correct position of the delamination tip. The back side of specimen MMELS-7-1.5 is presented in Fig. 5.29b, in which the strain field in the opening direction was adjusted manually in order to capture the delamination tip while minimizing inaccuracies.

For the specimen without speckles, the total length of the delamination a was determined at the end of each test stage, as done for the C-ELS specimens in Section 5.2.1. For specimens with speckles on both sides of each specimen, the delamination length a for the first and the second stages of the test was determined from the images taken from both sides of the specimen. The total delamination length a was verified at the end of second test stage by means of the Olympus confocal microscope. All geometric parameters are used in the FE model of each MMELS specimen.

As with the DCB and C-ELS specimens, in each specimen the upper and lower arms are of different heights, these were measured after a test was performed. The variation in the height of the specimen arms or sub-laminates along the interface is presented in Fig. 5.6a, for specimen MMELS-7-1.7. Recall that this was common to all beam-type specimens. The height of the upper and lower sub-laminates h_T and h_B, respectively, as illustrated in Fig. 5.3b, was measured as presented in Sections 5.1.1 and 5.2.1 for the DCB and C-ELS specimens, respectively.

5.3.2 Analysis

Five MMELS specimens containing an artificial delamination were tested based upon the protocol presented in Section 5.3.1. The geometric parameters of the tested specimens, which are shown in Figs. 5.2c and 5.3a, are presented in Table 5.18. The parameters with subscript 1 represent measurements behind the artificial delamination front, whereas parameters with subscripts 2 to 5 represent measurements ahead of the delamination front. Average values of specimen height and width denoted by $\overline{2h}$ and $\overline{b}$, respectively, are presented in Table 5.18. It should be noted that the low values of the standard deviation (STD) demonstrate the repeatability in specimen fabrication. According to Blackman et al. (2001), the thickness variation along the specimen length shall not

Table 5.18: Geometric parameters of the MMELS specimens.

specimen no.	$2h_1$ (mm)	$2h_2$ (mm)	$2h_3$ (mm)	$2h_4$ (mm)	$2h_5$ (mm)	$\overline{2h}$ (mm)	STD (mm)
MMELS-7-1.5	5.04	5.03	5.01	5.01	5.03	5.02	0.01
MMELS-7-1.7	5.00	4.98	4.95	4.96	4.97	4.97	0.02
MMELS-7-1.9	4.95	4.98	4.95	4.96	4.95	4.96	0.01
MMELS-7-1.17	4.94	4.94	4.94	4.94	4.95	4.94	0.00
MMELS-7-1.18	4.99	4.97	4.95	4.98	4.97	4.97	0.01
specimen no.	b_1 (mm)	b_2 (mm)	b_3 (mm)	b_4 (mm)	b_5 (mm)	$\overline{b}$ (mm)	STD (mm)
MMELS-7-1.5	20.42	20.40	20.42	20.33	20.32	20.38	0.04
MMELS-7-1.7	20.30	20.32	20.32	20.29	20.27	20.30	0.02
MMELS-7-1.9	20.37	20.39	20.35	20.32	20.31	20.35	0.03
MMELS-7-1.17	20.24	20.24	20.23	20.22	20.21	20.23	0.01
MMELS-7-1.18	20.38	20.39	20.35	20.35	20.21	20.34	0.06
specimen no.	$a_0^{(f)}$ (mm)	$a_0^{(b)}$ (mm)	$\overline{a}_0$ (mm)	$\lvert\Delta_0\rvert$ (mm)	L_f (mm)	l (mm)	
MMELS-7-1.5	50.78	50.23	50.50	0.55	100.0	200.0	
MMELS-7-1.7	51.24	51.16	51.20	0.08	100.0	199.8	
MMELS-7-1.9	50.58	50.80	50.69	0.12	100.0	200.0	
MMELS-7-1.17	51.10	51.31	51.20	0.21	100.0	200.0	
MMELS-7-1.18	51.33	51.12	51.22	0.21	100.0	199.5	

Table 5.19: Failure load at initial delamination propagation and final delamination length of the MMELS specimens for both test stages: first stage - initiation from the PTFE film (APC), and second stage - initiation and propagation from the natural delamination.

	Stage I: pre-cracking					Stage II: propagation				
specimen no.	P_{NL} (N)	P_{vis} (N)	$P_{5\%/\max}$ (N)	$\overline{a}_p$ (mm)	$\lvert\Delta_p\rvert$ (mm)	P_{NL} (N)	P_{vis} (N)	$P_{5\%/\max}$ (N)	$\overline{a}_f$ (mm)	$\lvert\Delta_f\rvert$ (mm)
MMELS-7-1.5	78.5	96.0	109.3	54.05	0.55	99.5	102.3	106.2	92.52	1.20
MMELS-7-1.7	79.9	89.1	107.2	54.95	0.43	92.3	102.9	103.5	93.30	0.28
MMELS-7-1.9	80.8	81.1	95.5	54.29	0.27	99.8	101.7	112.4	90.15	0.18
MMELS-7-1.17	79.1	89.7	98.3	52.10	0.01	93.8	98.4	105.2	93.56	0.34
MMELS-7-1.18	84.2	98.8	106.9	54.27	0.52	89.5	93.9	110.0	91.95	0.37
Average	80.5	90.9	103.4			95.0	99.8	107.5		
STD	2.0	6.2	5.5			4.1	3.4	3.3		
CV	2.49%	6.76%	5.29%			4.27%	3.36%	3.04%		

exceed 0.1 mm. It may be found that all specimens comply with this requirement. The measured values for the upper and lower sub-laminates of the MMELS specimens are presented in Tables G.1 and G.2. The scaled values calculated by means of eqs. (5.1) and (5.2) appear in Tables G.3 and G.4. Their averages, which also appear in Tables G.3 and G.4, were used in the FE model of each MMELS specimen. It should be noted that the evaluated average ply thickness of the 11 plies in the upper specimen arm or sub-laminate, which is calculated as $\overline{h}_T/11$, is thinner than the evaluated average ply thickness of the 12 plies in the lower specimen sub-laminate, which is calculated as $\overline{h}_B/12$. A typical difference of about 0.03 mm in the average ply thickness between the upper and lower sub-laminates was obtained. Recall that the nominal ply thickness is 0.22 mm. Nevertheless, those evaluated ply thicknesses are within the valid range acceptable for this material and manufacturing process. In addition, it may be noted that the dimensions of the MMELS specimens as well as the geometry of the load blocks were chosen so that the correction factors F and N presented in Blackman et al. (2001) may be taken as unity.

The initial delamination length on the front and back sides of the specimen, $a_0^{(f)}$ and $a_0^{(b)}$, respectively, as well as the average values of the initial delamination length $\overline{a}_0$ are also presented in Table 5.18. It is observed that the absolute difference between $a_0^{(f)}$ and $a_0^{(b)}$, denoted as $|\Delta_0|$ in Table 5.18, for each specimen is less than 2 mm, which complies with Blackman et al. (2001). According to Blackman et al. (2001), a_0 should be approximately 50 mm. Here, it satisfies this requirement. The length of the specimens, l, is also presented in Table 5.18, and is seen to be approximately 200 mm, which conforms with Blackman et al. (2001). After each test stage was carried out, the delamination length was measured on both sides of each specimen by means of the optical mode of the Olympus confocal microscope. The average delamination lengths at the end of each test stage, artificial pre-crack (APC) and pre-crack (PC), are presented in Table 5.19, as $\overline{a}_p$ and $\overline{a}_f$, respectively. For each test stage, it may be observed that the absolute difference

Table 5.20: Temperature and relative humidity during MMELS APC and PC test stages.

	Stage I: pre-cracking				Stage II: propagation			
specimen no.	$\vartheta_{initial}$ (°C)	$\mathrm{RH}_{initial}$ (%)	ϑ_{final} (°C)	RH_{final} (%)	$\vartheta_{initial}$ (°C)	$\mathrm{RH}_{initial}$ (%)	ϑ_{final} (°C)	RH_{final} (%)
MMELS-7-1.5	22.2	43.9	22.2	43.3	22.4	43.2	22.7	42.8
MMELS-7-1.7	22.4	44.3	22.3	44.8	22.3	45.7	22.2	44.1
MMELS-7-1.9	23.2	50.8	22.9	45.9	23.1	45.2	23.5	47.6
MMELS-7-1.17	23.2	43.9	23.3	43.3	23.1	43.4	22.9	44.4
MMELS-7-1.18	23.1	44.6	23.3	43.6	23.0	44.7	23.2	45.0

between the final delamination length on both sides of each specimen, denoted by $|\Delta_p|$ and $|\Delta_f|$, is less than 2 mm for all specimens, as required in Blackman et al. (2001).

Note, that for all MMELS specimens the experimental data obtained for $\overline{a}_f$ was not used since all average final delamination lengths were within less than 10 mm of the edge of the clamping fixture. In Blackman et al. (2001) it is recommended using data which is further away from the clamp. Nonetheless, the values related to $\overline{a}_f$ are presented, as well as the absolute difference in the final delamination lengths $|\Delta_f|$ measured on both sides of each specimen; they were seen to be less than 2 mm.

The room temperature and relative humidity (RH) were recorded during the two stages of the MMELS tests, where each APC stage lasted about 20 minutes and each PC stage lasted about an hour. The initial and final environmental conditions of each test stage are presented in Table 5.20. The test temperature should be $23 \pm 3°$ C and the RH, $50 \pm 10\%$, according to Blackman et al. (2001). In Table 5.20, it may be observed that the readings of the temperature and RH were within the required range.

The load-displacement curves obtained for the five MMELS fracture toughness tests are shown in Figs. 5.30a and 5.30b for the APC and PC stages, respectively. It may be observed in Fig. 5.30b that there are regions of unstable delamination propagation, which is characterized by a sharp decrease in the load. However, it is also observed that the delamination propagation in the MMELS specimens is less stable than that within the C-ELS specimens as shown in Fig. 5.21. The abrupt load drops in the curves in Fig. 5.30b are similar to those observed in the DCB specimens, as presented in Fig. 5.7. According to Blackman et al. (2001), the initiation load at failure is determined in three ways: NL, vis and 5%/max, in the same manner as was determined for the C-ELS specimens in Section 5.2.2. The initiation loads at failure, denoted by P_{NL}, P_{vis} and $P_{5\%/\mathrm{max}}$, are shown in Table 5.19 for each test stage of the MMELS specimens.

In a similar manner as that performed for the DCB and C-ELS specimens in Sections 5.1.2 and 5.2.2, respectively, and following Blackman et al. (2001) regarding beam theory, it may be shown that the compliance $C \propto a^3$. Thus, the relationship between the delamination length and specimen compliance may be expressed according to the experimental

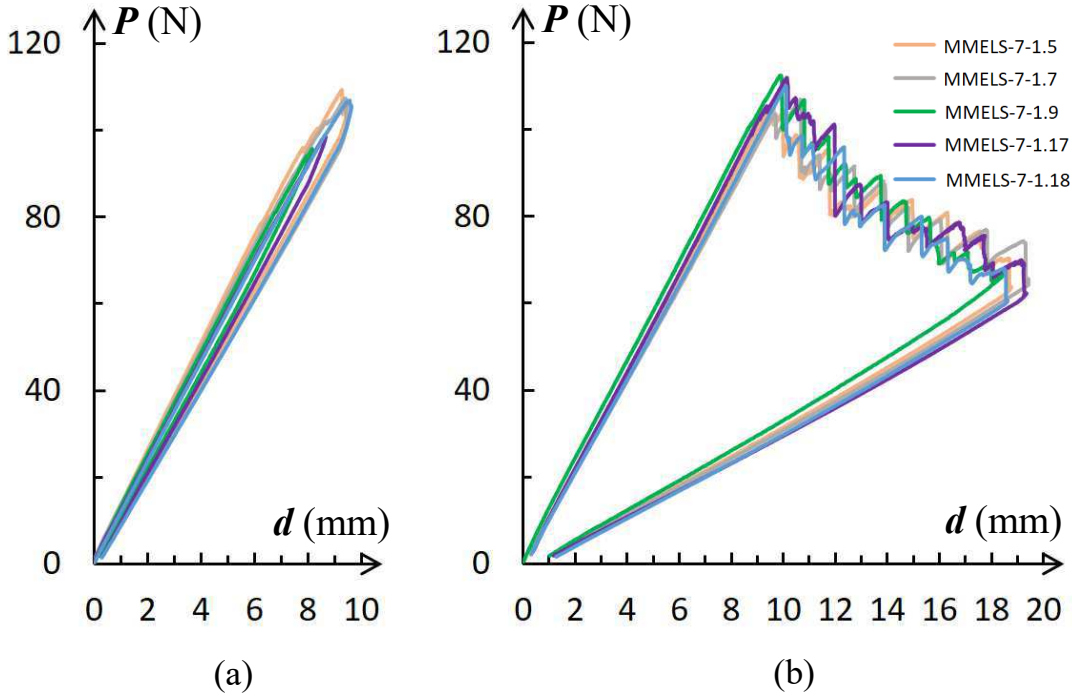

Figure 5.30: Load versus displacement curves from fracture toughness tests of MMELS specimens, MMELS-7-1.5, MMELS-7-1.7, MMELS-7-1.9, MMELS-7-1.17 and MMELS-7-1.18: (a) first test stage for delamination initiation from PTFE film (APC) and (b) second test stage for initiation and propagation from the natural delamination (PC).

compliance method (ECM) presented in Blackman et al. (2001). The ECM expression may be rewritten as a cube root power law as given in eq. (5.4). The experimental data in Table G.13 was used along with eq. (5.4) to generate the a versus C curve presented in Fig. 5.31. The values of g and C_0 and the coefficient of determination R^2 were found as 146.66 $(\mathrm{N} \cdot \mathrm{mm}^2)^{1/3}$, $4.10 \cdot 10^{-2}$ mm/N and 0.998, respectively. In Fig. 5.31, it may be observed that there is good agreement between the measured and evaluated values of a. In addition, it may be observed in Figs. 5.31 and 5.8 that C for the MMELS specimen is smaller than that for the DCB specimens. However, the compliance of the MMELS specimen is greater than that obtained for the C-ELS specimen in Fig. 5.22. The same procedure of curve fitting to eq. (5.4) was performed separately with the experimental data of specimens MMELS-7-1.7, MMELS-7-1.9, MMELS-7-1.17 and MMELS-7-1.18. The delamination propagation data for all MMELS specimens is presented in Tables G.13 through G.17, for visually detected and for a few evaluated delamination lengths. In Tables G.13 through G.17, as well as in Table 5.26, the values of the parameters of eq. (5.4), g and C_0, and the coefficient of determination R^2, are shown for each MMELS specimen.

All MMELS specimens were analyzed by means of the FE method using the ADINA

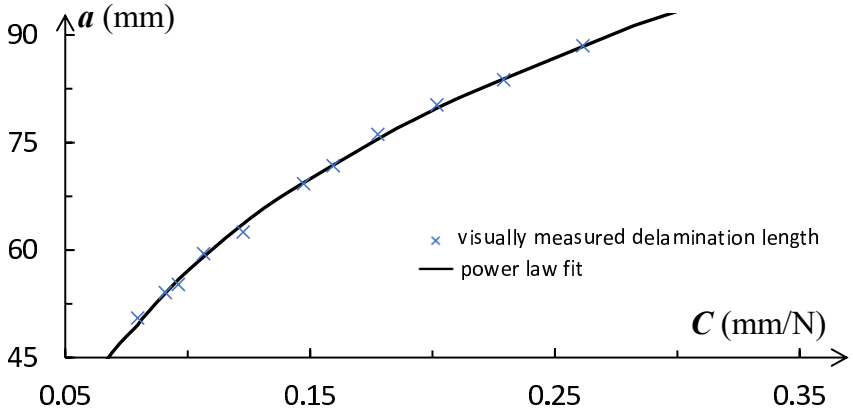

Figure 5.31: Correlation between delamination length and test compliance for specimen MMELS-7-1.5.

(Bathe, 2011) software. The three-dimensional FE models contained twenty noded isoparametric, brick elements. In order to model the square-root singularity along the delamination front, quarter-point elements were used. The oscillatory part of the singularity was not modeled. The mechanical properties used to characterize the plain woven plies with the yarn in the $0°/90°$ and $+45°/-45°$ directions are presented in Table 2.1. An example of a three-dimensional FE model is presented in Fig. 5.32c, where the FE model was used in analyzing specimen MMELS-7-1.5. The in-plane dimensions of the elements in the vicinity of the delamination front of the specimen MMELS-7-1.5 model were set to $5.16 \cdot 10^{-5} \times 5.16 \cdot 10^{-5}$ m^2 in the upper ply and $5.16 \cdot 10^{-5} \times 5.73 \cdot 10^{-5}$ m^2 in the lower ply. Thus, an in-plane aspect ratio of 1.0 and 1.11 was obtained, respectively, as shown in Fig. 5.32b. The FE model boundary conditions and restraints are illustrated in Fig. 5.32a. Contact interaction was implemented along the specimen and clamps; one of which is flexible and one is stiff as seen in Fig. 5.32c. The mechanical properties of the clamps are the same as employed in the FEAs of the C-ELS specimens, as those presented in Table 5.14.

Table 5.21: Values of the fitting parameters in eq. (5.4) for the MMELS specimens.

specimen no.	$g\left(\left[\mathrm{N}\cdot\mathrm{mm}^2\right]^{1/3}\right)$	C_0 (mm/N)	R^2
MMELS-7-1.5	146.66	$4.10 \cdot 10^{-2}$	0.998
MMELS-7-1.7	147.04	$4.36 \cdot 10^{-2}$	0.997
MMELS-7-1.9	148.96	$4.05 \cdot 10^{-2}$	0.999
MMELS-7-1.17	146.01	$4.48 \cdot 10^{-2}$	0.999
MMELS-7-1.18	144.91	$4.16 \cdot 10^{-2}$	0.999

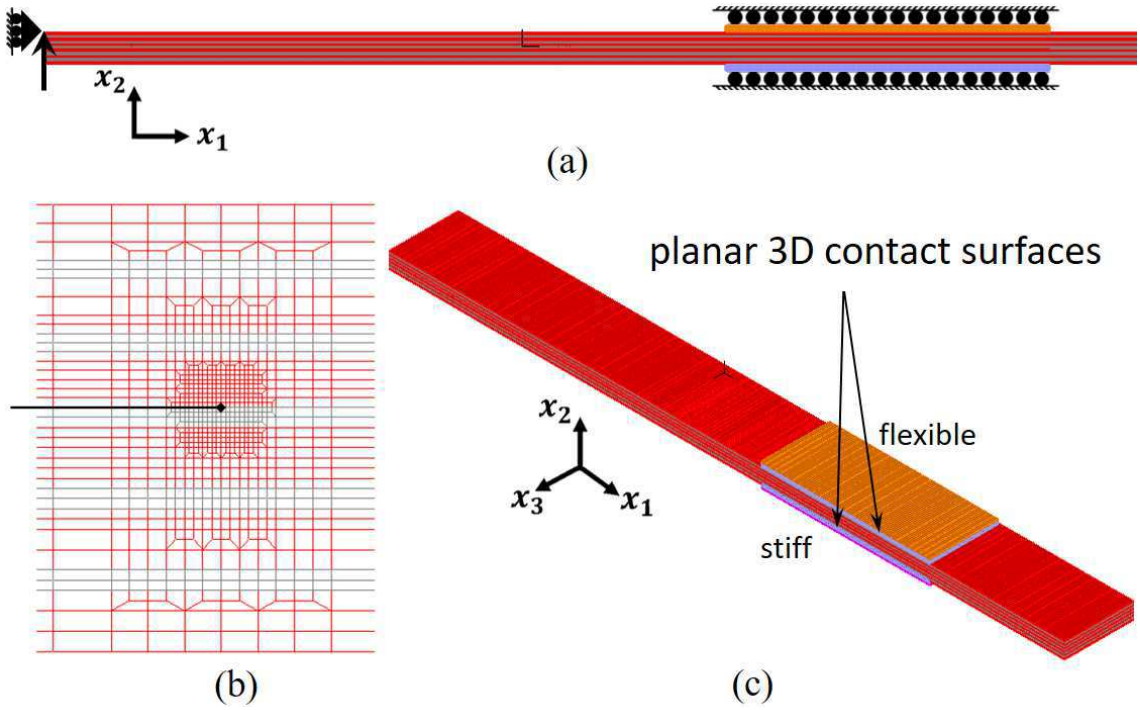

Figure 5.32: Mesh of the MMELS specimen: (a) illustration of the FE model constraints, (b) detailed front view near the delamination tip, and (c) isometric view indicating the locations where contact boundaries are applied; contact is implemented along both sides of the specimen where it is confined within the clamping fixture.

To demonstrate mesh convergence of the FE model inner mesh, as well as domain independence, a coarse, fine and finer mesh were used with the geometric parameters of specimen MMELS-7-1.5 in Table 5.18 with a representative delamination length of $a = 76.15$ mm. The in-plane dimensions of the elements in the vicinity of the delamination front are presented in Table 5.22. These were obtained in a similar manner to the DCB specimens as presented in Figs. 5.10a, 5.10b and 5.10c, respectively. It may be noted that the in-plane aspect ratio of the elements at the bottom of the lower ply in the coarse mesh as in Fig. 5.10a is 4.52; for the fine and finer meshes as in Figs. 5.10b and 5.10c, the in-plane aspect ratio of some of those elements is 2.26 and 4.52. In all meshes, there were 40 elements along the delamination front, each approximately $5.1 \cdot 10^{-4}$ m thick. The delamination front is assumed to be straight through the model width.

An arbitrary constant load of $P^{FEA} = 20$ N was applied in all FE analyses for simplicity. The stress intensity factors were calculated along the delamination front of each mesh by means of the three-dimensional M-integral, which was described in Section 3.2. The stress intensity factors obtained for the largest domain of each mesh as a function of the normalized delamination front coordinate (x_3/b) are shown in Fig. 5.33. Recall that the dimensions of the complex in-plane stress intensity factor components are $\mathrm{F}\times\mathrm{L}^{-(3/2+i\varepsilon)}$,

Table 5.22: Characteristics of the four meshes which were used in the convergence study of the MMELS specimen.

mesh	no. of elements	no. of nodes	element in-plane size near delamination front (m^2)	in-plane aspect ratio	no. of integration domains
coarse	197,680	838,486	$1.03 \cdot 10^{-4} \times 1.03 \cdot 10^{-4}$	1.0	2
fine	208,720	884,206	$5.16 \cdot 10^{-5} \times 5.16 \cdot 10^{-5}$	1.0	4
finer	221,520	937,220	$2.58 \cdot 10^{-5} \times 2.58 \cdot 10^{-5}$	1.0	5
modified fine	207,840	880,742	$5.16 \cdot 10^{-5} \times 5.16 \cdot 10^{-5}$ upper ply elements	1.0	4
			$5.16 \cdot 10^{-5} \times 5.73 \cdot 10^{-5}$ lower ply elements	1.11	

where F and L represent force and length, respectively; so that their units are $\mathrm{MPa}\sqrt{\mathrm{m}} \cdot \mathrm{m}^{-i\varepsilon}$. The oscillatory parameter, ε, depends upon the mechanical properties of both materials on either side of the interface and for the investigated interface is presented in Table 4.9 and given in eq. (2.46). Both in-plane stress intensity factors, K_1 and K_2 are shown, respectively, in Figs. 5.33a and 5.33b. The dimensions of the out-of-plane stress intensity factor, K_{III}, are $\mathrm{F}\times\mathrm{L}^{-3/2}$ with units of $\mathrm{MPa}\sqrt{\mathrm{m}}$; it is presented in Fig. 5.33c. It may be observed that the in-plane stress intensity factors shown in Figs. 5.33a and 5.33b, respectively, are symmetric with respect to specimen mid-thickness ($x_3/b = 0.5$), whereas the out-of-plane stress intensity factor shown in Fig. 5.33c is anti-symmetric. Differences between the various results are discussed in the sequel.

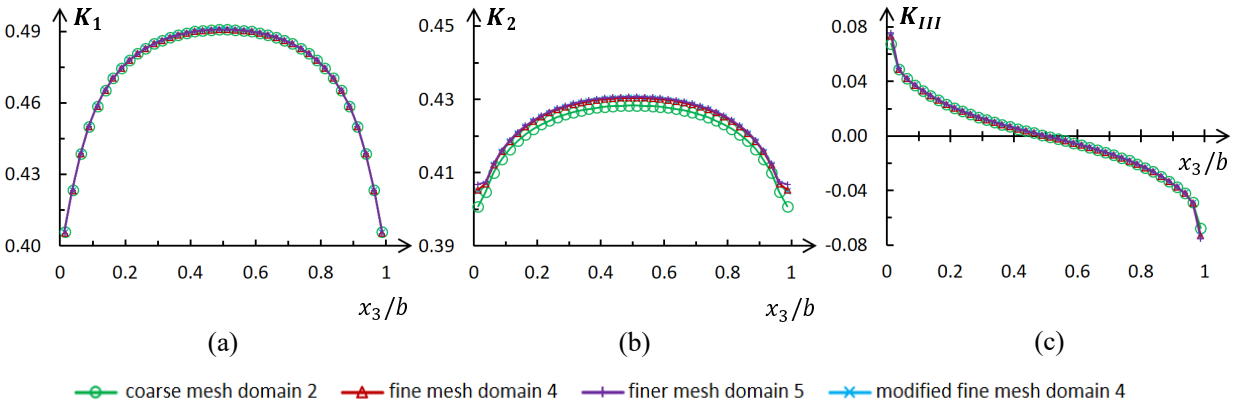

Figure 5.33: Stress intensity factors calculated along the delamination front by means of the three-dimensional M-integral for the largest domain of each FE mesh used to analyze specimen MMELS-7-1.5 (coarse, fine and finer meshes). (a) K_1 in $\mathrm{MPa}\sqrt{\mathrm{m}} \cdot \mathrm{m}^{-i\varepsilon}$, (b) K_2 in $\mathrm{MPa}\sqrt{\mathrm{m}} \cdot \mathrm{m}^{-i\varepsilon}$ and (c) K_{III} in $\mathrm{MPa}\sqrt{\mathrm{m}}$.

Table 5.23: Maximum percent difference (in absolute value) between the stress intensity factors calculated for the fifth integration domain (reference) and domains 2, 3 and 4 of the finer mesh, as shown in Fig. 5.10c.

percent difference								
domain 2			domain 3			domain 4		
K_1	K_2	K_{III}	K_1	K_2	K_{III}	K_1	K_2	K_{III}
0.083	0.538	0.202	0.065	0.219	0.054	0.019	0.052	0.012

To demonstrate domain independence with the finer mesh similar to that shown in Fig. 5.10c, the stress intensity factors obtained by means of the M-integral in domain 5, which is shown in Fig. 3.2e, served as reference values and were used for comparison. In order to quantify the change in the calculated stress intensity factors obtained for each domain, the percent difference defined in eq. (4.8) was used. In Table 5.23, the differences between the stress intensity factors obtained for the fifth (reference) and other domains of integration (see Fig. 3.2) are presented. It should be noted that the maximum percent difference shown in Table 5.23 occurred at different positions along the delamination front. The values obtained for the different integration domains demonstrate domain independence. In a similar manner, demonstration of domain independence with the modified fine mesh as shown in Figs. 5.32b and 5.10d, is presented in Table 5.24, in which the stress intensity factors obtained by means of the M-integral in domain 4 (shown in Fig. 3.2d) served as reference values and were used for comparison. Note, that the maximum percent difference shown in Table 5.24 occurred at different positions along the delamination front. The differences were less than 0.3% for domain 3.

In addition to Fig. 5.33, solution convergence is examined in Table 5.25, in which the differences between the stress intensity factors obtained for pairs of meshes are presented. For each pair of meshes, the mesh which is more refined in the vicinity of the delamination front serves as the reference (ref) in eq. (4.8). It should be noted that the maximum percent differences shown in Table 5.25 occurred at different positions along the delamination front. It may be observed that convergence is obtained for both ranges of x_3/b. Results for

Table 5.24: Maximum percent difference (in absolute value) between the stress intensity factors calculated for the fourth integration domain (reference) and domains 2 and 3 of the modified fine mesh, as shown in Fig. 5.10d.

percent difference					
domain 2			domain 3		
K_1	K_2	K_{III}	K_1	K_2	K_{III}
0.112	0.618	0.349	0.065	0.209	0.117

Table 5.25: Maximum percent difference (in absolute value) between the stress intensity factors for pairs of meshes, along the delamination front, calculated for the largest integration domain of each mesh.

percent difference									
meshes	coarse and fine			fine and finer			modified fine and finer		
range	K_1	K_2	K_{III}	K_1	K_2	K_{III}	K_1	K_2	K_{III}
$0.0375 \leq x_3/b \leq 0.9625$	0.012	0.554	0.585	0.013	0.105	0.380	0.020	0.119	0.419
$0.0125 \leq x_3/b \leq 0.9875$	0.115	1.124	7.600	0.055	0.362	3.051	0.073	0.440	3.395

$x_3/b = 0.0125$ and 0.9875, that is for the domain in the outermost elements, deteriorate as compared to the other domains. The error in K_{III} is somewhat higher than expected as compared to the value obtained for the DCB specimen in Table 5.8. Recall that in the development of the first term of the asymptotic stress and displacement fields, conditions of plane deformation were assumed, as may be seen in Section 2.2. This assumption is common in cases of through cracks/delaminations, so that the singularity related to the free surface is not represented. Moreover, the assumption of plane deformation over constrains the free surface. Therefore, the values calculated by means of the M-integral and the DE method at the FE model outer faces are inaccurate. Since the absolute value of the maximum percent difference within the range of $0.0375 \leq x_3/b \leq 0.9625$ between the fine and the finer mesh, and also between the modified fine and the finer mesh is less than 0.5%, it may be concluded that the modified fine mesh shown in Fig. 5.10d may be used in all FE models in this study.

Based upon domain independence and the convergence study for the inner FE mesh of the MMELS model and the outer FE mesh convergence study performed for the DCB and C-ELS FE models in Sections 5.1.2 and 5.2.2, respectively, the modified fine mesh, as shown in Figs. 5.32b and 5.10d, was employed for the MMELS specimens. Finite element models were generated for delamination lengths, which were visually observed in the images of each MMELS specimen, as acquired during the tests. The delamination lengths, which were modeled, varied within the range 50.50 mm $\leq a \leq$ 89.69 mm. Two types of FE meshes were used for the analyses of the MMELS specimens: a mesh for short delamination lengths where $a < 80$ mm, and a mesh for long delamination lengths where $a > 80$ mm. These are referred to as the short delamination mesh and the long delamination mesh, respectively.

The FE short delamination meshes contained 207,840 brick elements and 880,742 nodal points, as shown in Table 5.22. A maximum in-plane element aspect ratio of 1 to 12.7 was permitted away from the delamination front, at a distance of 61 ply thicknesses ahead and behind the delamination front. In regions very far from expected stress concentrations, such as load application points, reactions, delamination front, etc., an in-plane element

aspect ratio no greater than 1 to 28.8 was permitted. The mesh in the neighborhood of the delamination front was translated and the remainder of the mesh followed the same principles as that used for the mesh for $a = 76.15$ mm. The FE long delamination meshes contained 187,680 brick elements and 796,882 nodal points. A maximum in-plane element aspect ratio of 1 to 12.7 and 1 to 13.4 was permitted away from the delamination front, at a distance of 61 and 45 ply thicknesses behind and ahead the delamination front, respectively. In regions very far from expected stress concentrations, an in-plane element aspect ratio no greater than 1 to 35.5 was permitted. In a similar manner as with the short mesh, here, the mesh in the vicinity of the delamination front was translated.

The stress intensity factors were calculated by means of the three-dimensional M-integral, described in Section 3.2, for each slice of elements within domain 4, one element thick through the model thickness as shown in Fig. 3.2d. Ordinary units for the in-plane stress intensity factors $\hat{K}_1$ and $\hat{K}_2$ were obtained by employing eq. (4.9) with the length parameter $\hat{L} = 100$ μm, as described in Section 4.4.2. The normalized in-plane stress intensity factors, $\hat{K}_1$ and $\hat{K}_2$, as well as the out-of-plane stress intensity factor, K_{III}, for different delamination lengths, but for the same applied load $P^{FEA} = 20$ N, as a function of the normalized delamination front coordinate x_3/b are shown in Figs. 5.34a to 5.34c, respectively. It may be observed that the in-plane stress intensity factor components are symmetric with respect to specimen mid-thickness $x_3/b = 0.5$, whereas the out-of-plane stress intensity factor is anti-symmetric. In addition, the values of $\hat{K}_1$ and $\hat{K}_2$ increase with a; the absolute value of K_{III}, also increases with a. It may be noted that for each MMELS specimen another FE model was generated with a delamination length $a = 45$ mm, as discussed in the sequel.

Based upon these results, the two phase angles, $\hat{\psi}$ in eq. (1.12) and ϕ in eq. (1.14), were also calculated. The in-plane phase angle $\hat{\psi}$ and the out-of-plane phase angle ϕ, for different delamination lengths but the same applied load $P^{FEA} = 20$ N as a function of the normalized delamination front coordinate x_3/b are presented in Figs. 5.34d and 5.34e, respectively. It may be observed that the values of $\hat{\psi}$ in Fig. 5.34d increase with a; at model mid-width, the values of $\hat{\psi}$ vary between 0.633 rad and 0.642 rad for $a = 50.50$ mm and $a = 88.50$ mm, respectively. For each value of a, $\hat{\psi}$ is nearly constant with a less than 1% change within the range of $0.2125 < x_3/b < 0.7875$. Near the model outer surfaces, a maximum percent difference of 10.2% is obtained between the values of $\hat{\psi}$ at the mid-width and $x_3/b = 0.0125$ and 0.9875. The contributions of both $\hat{K}_1$ and $\hat{K}_2$ to the total interface energy release rate $\mathcal{G}_i$ are important. In Fig. 5.34e, the values of ϕ are shown, where it may be observed that ϕ is essentially the same value for each value of a. In addition, it is seen that the values of ϕ are relatively small except near the specimen outer edges. For each value of a, within the range of $0.1125 < x_3/b < 0.8875$, the absolute value of ϕ is less than 0.05 rad, which is somewhat similar to the absolute value of ϕ for specimen

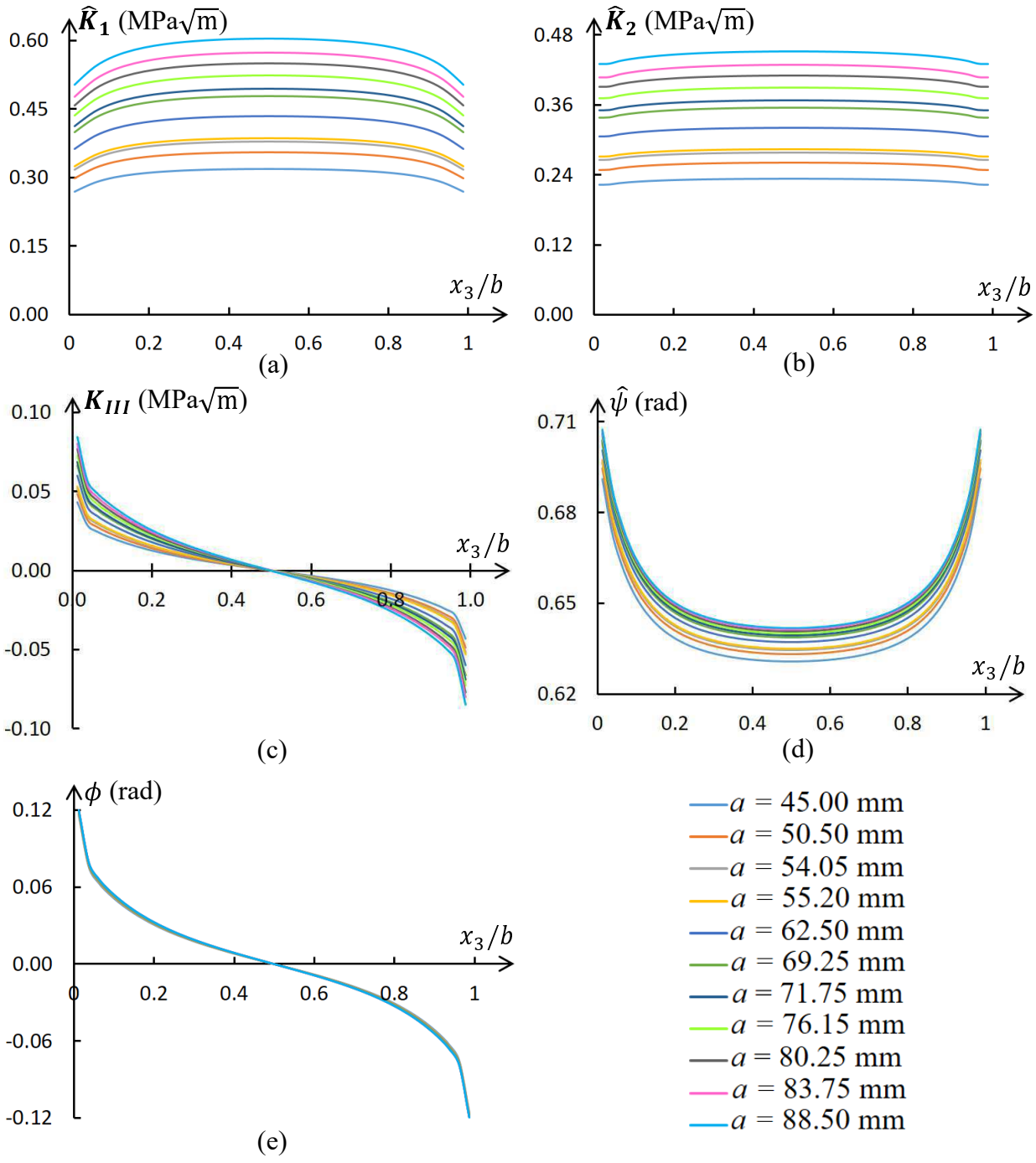

Figure 5.34: Normalized in-plane stress intensity factors (a) $\hat{K}_1$ and (b) $\hat{K}_2$ ($\hat{L} = 100$ μm); (c) out-of-plane stress intensity factor K_{III}; and the two phase angles (d) $\hat{\psi}$ and (e) ϕ as a function of normalized delamination front coordinate x_3/b for different delamination lengths for specimen MMELS-7-1.5 with an applied load $P^{FEA} = 20$ N.

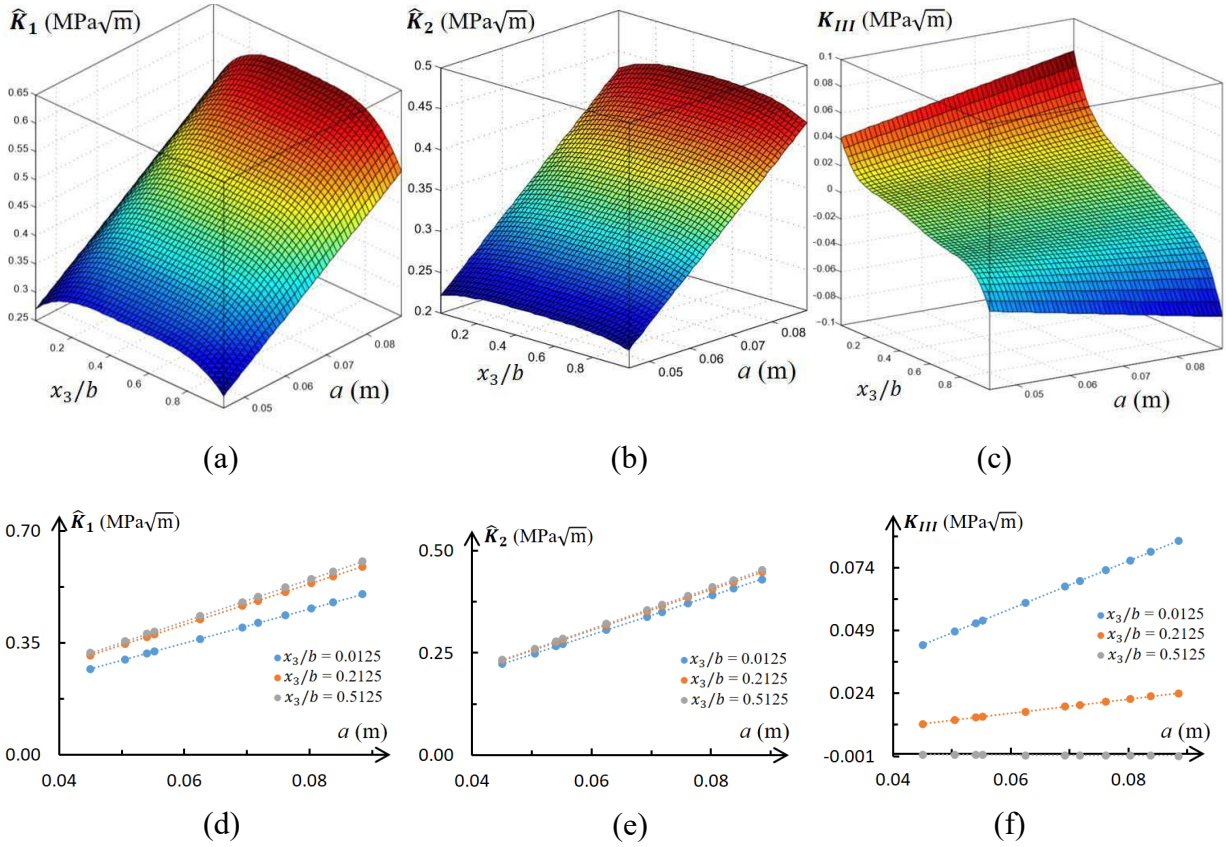

Figure 5.35: Three-dimensional surfaces of the normalized in-plane stress intensity factors (a) $\hat{K}_1$ and (b) $\hat{K}_2$ ($\hat{L} = 100$ μm); and (c) out-of-plane stress intensity factor K_{III} as a function of normalized delamination front coordinate x_3/b and delamination length a. The normalized in-plane stress intensity factors (d) $\hat{K}_1$ and (e) $\hat{K}_2$ ($\hat{L} = 100$ μm); and (f) out-of-plane stress intensity factor K_{III} as a function of delamination length a for different values of x_3/b for specimen MMELS-7-1.5 with an applied load $P^{FEA} = 20$ N.

DCB-7-1.1 presented in Fig. 5.13e. Near the model outer surfaces, the absolute value of ϕ increases until an absolute value of 0.12 rad is reached. Hence, the contribution of K_{III} to the total interface energy release rate $\mathcal{G}_i$ is less than that of $\hat{K}_1$ and $\hat{K}_2$. Nonetheless, its contribution is included in the calculation of $\mathcal{G}_i$.

The three-dimensional surface of each of the stress intensity factors, $\hat{K}_1$, $\hat{K}_2$ and K_{III}, as a function of the delamination length a is plotted in Figs. 5.35a to 5.35c, respectively. In Figs. 5.35d to 5.35f, the stress intensity factors, $\hat{K}_1$, $\hat{K}_2$ and K_{III}, are plotted as a function of delamination length a for specific values of x_3/b for an applied load $P^{FEA} = 20$ N. Although the FEAs were non-linear, it may be observed that for each value of x_3/b along the delamination front, a linear relationship was found between each of the stress intensity factors and the delamination length a. This behavior was observed in every analysis that

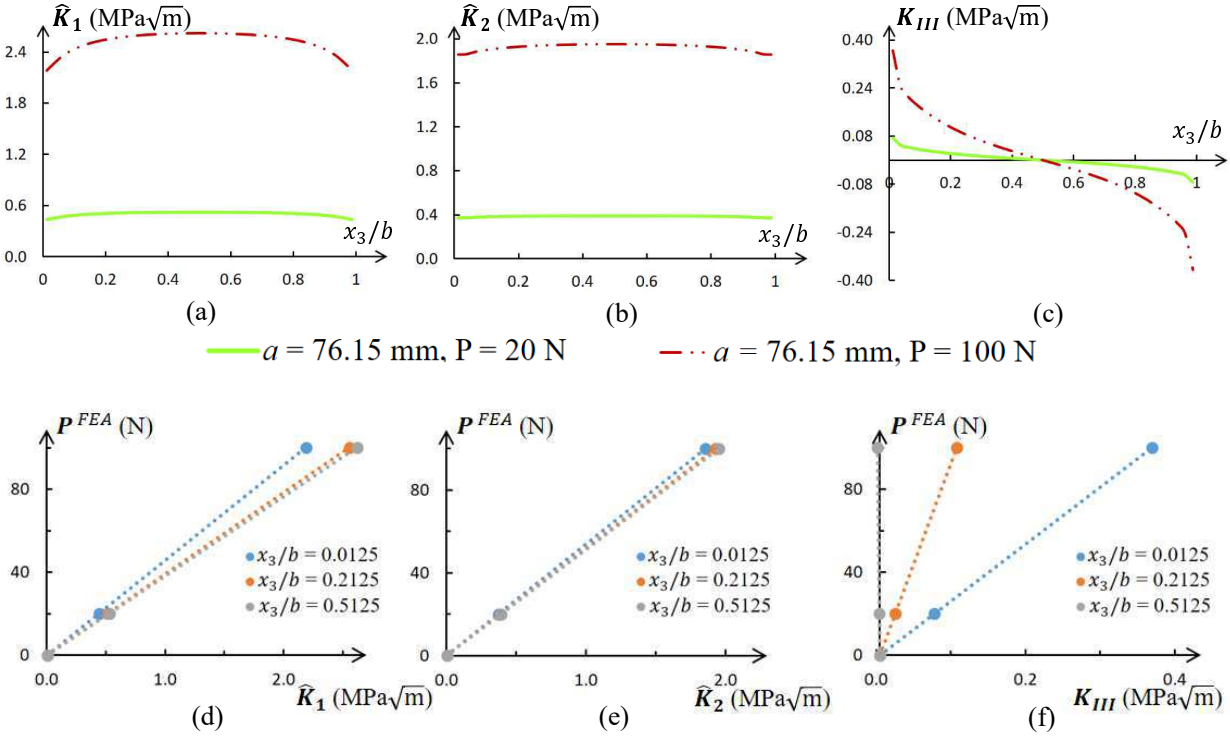

Figure 5.36: Normalized in-plane stress intensity factors (a) $\hat{K}_1$ and (b) $\hat{K}_2$ ($\hat{L} = 100$ μm); (c) out-of-plane stress intensity factor K_{III} as a function of normalized delamination front coordinate x_3/b for specimen MMELS-7-1.5 with a delamination length $a = 76.15$ mm and different applied loads $P^{FEA} = 20$ N and $P^{FEA} = 100$ N. The relationship between the applied load P^{FEA} and (d) $\hat{K}_1$, (e) $\hat{K}_2$ ($\hat{L} = 100$ μm), and (f) K_{III} for different values of x_3/b for a delamination length $a = 76.15$ mm.

was performed for each MMELS FE model. Thus, for each MMELS specimen in this particular case, two FEAs at $a = 45$ mm and 90 mm would have been sufficient for determining the value of the stress intensity factors, $\hat{K}_1$, $\hat{K}_2$ and K_{III}, by means of linear interpolation. But it is retrospective wisdom.

Although the FEAs for specimen MMELS-7-1.5 were non-linear, as a result of the contact surfaces and large displacements, a linear relationship was found between the load applied in the FEA and the corresponding stress intensity factors, as may be observed in Figs. 5.36a through 5.36c and in Figs. 5.36d through 5.36f. For the stress intensity factors in Figs. 5.36a to 5.36c, which are plotted with respect to the normalized delamination front coordinate x_3/b, the results for $P^{FEA} = 100$ N are 5.00 times greater than those for $P^{FEA} = 20$ N. Note that the two FEAs are for specimen MMELS-7-1.5 with a delamination length $a = 76.15$ mm; they only differ in the load applied on the FE model. For each stress intensity factor, it was found that the ratio between the values calculated

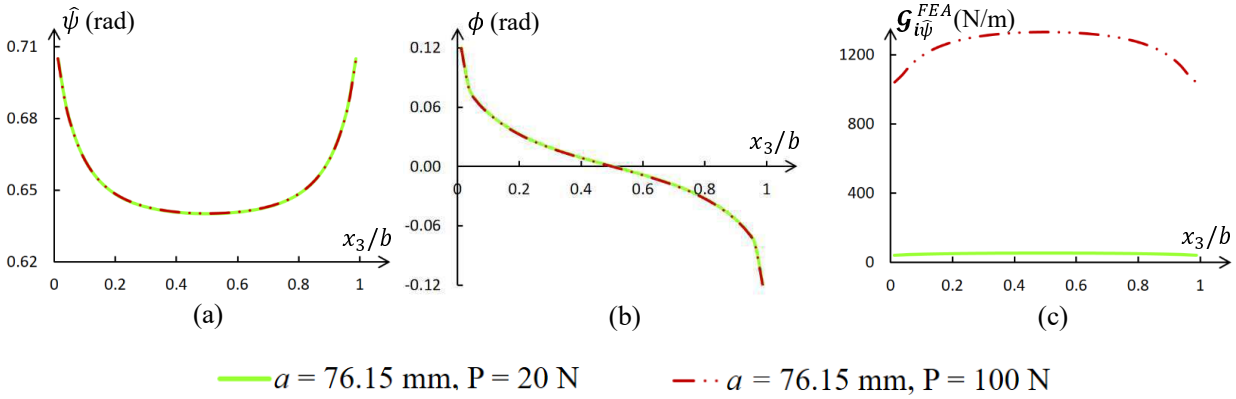

Figure 5.37: The two phase angles (a) $\hat{\psi}$ and (b) ϕ; and (c) the interface energy release rate $\mathcal{G}_{i\hat{\psi}}^{FEA}$ as a function of normalized delamination front coordinate x_3/b for a delamination length $a = 76.15$ mm and different applied loads $P^{FEA} = 20$ N and $P^{FEA} = 100$ N.

from these two FEAs is the same as that exists for the applied loads, meaning a ratio of 5.00. The plots of P^{FEA} versus each stress intensity factor $\hat{K}_1$, $\hat{K}_2$ and K_{III}, are presented for different values of x_3/b in Figs. 5.36d to 5.36f, respectively. In each of these plots, it may be observed that the stress intensity factor calculated for $P^{FEA} = 100$ N is 5.00 times greater than that for $P^{FEA} = 20$ N. The values of the stress intensity factors, $\hat{K}_1$ and $\hat{K}_2$, are quite similar for $x_3/b = 0.2125$ and 0.5125, as may be observed in Figs. 5.36a and 5.36b. It may be noted that for K_{III} and $x_3/b = 0.5125$ in Fig. 5.36f, the values are along the ordinate, that is $K_{III} \approx 0$.

In Figs. 5.37a and 5.37b, the phase angles $\hat{\psi}$ and ϕ are plotted as a function of x_3/b for $a = 76.15$ mm and two values of P^{FEA}. It may be observed that the relationship between the in-plane normalized stress intensity factors, represented by $\hat{\psi}$ in eq. (1.12), remained unchanged, as well as the relationship between the out-of-plane to in-plane stress intensity factors, which is represented by ϕ in eq. (1.14). The energy release rate $\mathcal{G}_{i\hat{\psi}}^{FEA}$ along the delamination front is presented in Fig. 5.37c. It may be seen that an increase of 500% of the initial value the applied load results in an increase of 2500% from the initial value of the interface energy release rate, as indicated in eq. $(5.6)_2$.

The existence of a linear relationship between the stress intensity factors and the FE applied load was further exploited for simplicity in all MMELS FE models. Since eq. (5.6) was found to be applicable for analyzing the MMELS specimens by means of the FE method, in each MMELS FE model, for each delamination length a, a normalized load $P^{FEA} = 20$ N was applied in the FE model. The actual results were obtained by using eqs. (5.6).

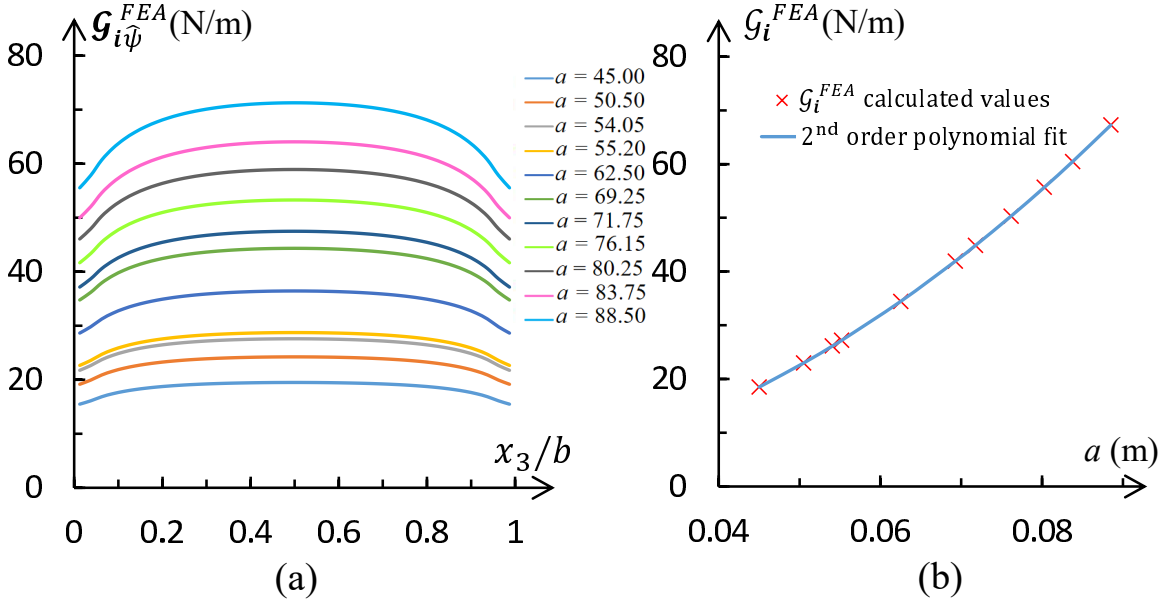

Figure 5.38: (a) The interface energy release rate $\mathcal{G}_{i\hat{\psi}}^{FEA}$ as a function of the normalized delamination front coordinate x_3/b for different delamination lengths for specimen MMELS-7-1.5 with an applied load $P^{FEA} = 20$ N. (b) The averaged interface energy release rate $\mathcal{G}_i^{FEA}$ as a function of delamination length for specimen MMELS-7-1.5 with an applied load $P^{FEA} = 20$ N.

The interface energy release rate $\mathcal{G}_{i\hat{\psi}}^{FEA}$, for different delamination lengths but the same applied load $P^{FEA} = 20$ N as a function of the normalized delamination front coordinate x_3/b, is presented in Fig. 5.38a. The i in the subscript of $\mathcal{G}_{i\hat{\psi}}^{FEA}$ represents interface; $\hat{\psi}$ denotes the dependence of this value upon the in-plane phase angle, which varies along the delamination front. It may be observed that for a constant value of the applied load, the interface energy release rate increases with a. When using methods presented in Blackman et al. (2001) to calculate the energy release rate for UD laminates, a global value is obtained. Thus here, an average through the width is found as

$$\mathcal{G}_i(a) = \int_0^1 \mathcal{G}_{i\hat{\psi}}(x_3/b, a) d(x_3/b). \tag{5.16}$$

It may be noted that the $\mathcal{G}_{i\hat{\psi}}^{FEA}(x_3/b, a)$ curves used in calculating the average interface energy release rate $\mathcal{G}_i^{FEA}(a)$ were those obtained via the stress intensity factors using eq. (1.17) which were extracted by means of the M-integral.

A second order polynomial curve fit given by

$$\mathcal{G}_i(a) = C_1 a^2 + C_2 a + C_3 \tag{5.17}$$

was employed in order to characterize the relationship between the calculated $\mathcal{G}_i^{FEA}$ from eq. (5.16) and the corresponding delamination length a. For specimen MMELS-7-1.5, the

Table 5.26: Values of the fitting parameters in eq. (5.17) for the MMELS specimens.

specimen no.	C_1 (N/m^3)	C_2 (N/m^2)	C_3 (N/m)	R^2
MMELS-7-1.5	$8.07 \cdot 10^3$	$4.38 \cdot 10^1$	$1.83 \cdot 10^{-1}$	1.0
MMELS-7-1.7	$8.32 \cdot 10^3$	$4.34 \cdot 10^1$	$1.67 \cdot 10^{-1}$	1.0
MMELS-7-1.9	$8.29 \cdot 10^3$	$4.72 \cdot 10^1$	$1.26 \cdot 10^{-1}$	1.0
MMELS-7-1.17	$8.62 \cdot 10^3$	$4.43 \cdot 10^1$	$2.05 \cdot 10^{-1}$	1.0
MMELS-7-1.18	$8.63 \cdot 10^3$	$4.56 \cdot 10^1$	$1.72 \cdot 10^{-1}$	1.0

values of the fitting parameters are given in Table 5.26. In Fig. 5.38b, the $\mathcal{G}_i^{FEA}(a)$ fitting curve obtained for specimen MMELS-7-1.5 is presented along with the values of $\mathcal{G}_i^{FEA}$ in eq. (5.16) calculated for different delamination lengths a. It may be observed that excellent agreement exists between the fitted curve and calculated values. The additional FEA result, with a delamination length $a = 45$ mm, was needed for better fitting of the $\mathcal{G}_i(a)$ function. The same procedure was performed separately with the experimental data of specimens MMELS-7-1.7, MMELS-7-1.9, MMELS-7-1.17 and MMELS-7-1.18 and their FEA results; the values of the fitting parameters in eq. (5.17) are also shown for these specimens in Table 5.26. It may be noted that in all MMELS specimens the values of the in-plane phase angle $\hat{\psi}$, given in eq. (1.12), were found to vary within a relatively narrow range of $0.20\pi < \hat{\psi} < 0.23\pi$.

In Tables G.13 through G.17 in Appendix G, the calculated values of the fracture toughness resistance $\mathcal{G}_{iR}$, as a function of the delamination length a, are presented for both experimentally detected and evaluated delamination lengths of the corresponding MMELS specimen. It may be recalled that in order to obtain these values curve fitting in eq. (5.17) and load adjustment of the FEA applied load to the experimentally obtained failure load in eq. (5.6) were performed, so that an average through the thickness fracture resistance value, based on the actual load in the experiment, is obtained.

5.3.3 Results

Based upon the data in Tables G.13 through G.17, a $\mathcal{G}_{iR}$-curve was generated. The $\mathcal{G}_{iR}$ versus $\Delta a = a - a_0$ data points are plotted in Fig. 5.39 An initiation fracture toughness is shown for $\Delta a = 0$ as $\mathcal{G}_{ic} = 393.3$ N/m, which is the critical interface energy release rate value for delamination growth from the PTFE insert obtained for specimens MMELS-7-1.5, MMELS-7-1.7, MMELS-7-1.9, MMELS-7-1.17 and MMELS-7-1.18. It may be seen that the values of the fracture toughness resistance $\mathcal{G}_{iR}$ increase with Δa until a steady state value of $\mathcal{G}_{iss} = 836.3$ N/m is reached for $\Delta a = 14$ mm. Fitting the points between

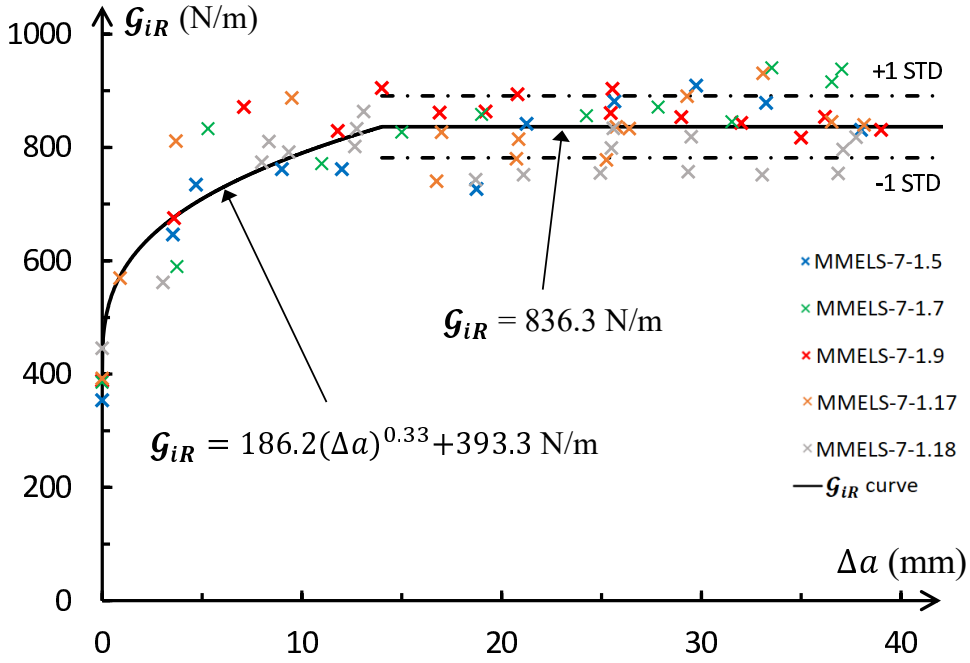

Figure 5.39: Fracture resistance curve: the critical interface energy release rate $\mathcal{G}_{iR}$ as a function of delamination propagation length $\Delta a = a - a_0$.

$0 \leq \Delta a \leq 14$ mm results in the power law given by

$$\mathcal{G}_{iR} = 186.2 \cdot (\Delta a)^{0.33} + 393.3 \tag{5.18}$$

where Δa in eq. (5.18) is measured in millimeters. The coefficient of determination R^2 of the power law in eq. (5.18) and the plotted points where $0 \leq \Delta a \leq 14$ mm was found as 0.88. Also, it may be observed that for 14 mm $\leq \Delta a \leq 40$ mm, most of the $\mathcal{G}_{iR}$ data points are within one standard deviation from the $\mathcal{G}_{iss}$ line; the value of one STD was found to be 54.8 N/m.

It may be noted that the obtained value of $\mathcal{G}_{ic} = 393.3$ N/m is close to the critical value for fracture initiation for an in-plane phase angle $\hat{\psi}$ which approaches $\pi/5$ obtained by means of the BD tests in Section 4.5. This value was found as $\mathcal{G}_{ic} = 407.6$ N/m as may be observed from the failure curve presented in Fig. 4.18.

Moreover, for beam-type specimens, the value of $\mathcal{G}_{ic}$ for mixed-mode in-plane deformation is close to that obtained for mode I. Here, an initiation fracture toughness value of $\mathcal{G}_{ic} = 393.3$ N/m was obtained for $\hat{\psi} \approx \pi/5$, whereas in Section 5.1.3, a value of $\mathcal{G}_{Ic} = 376.3$ N/m for nearly mode I deformation was determined. The behavior of R-curves for thermoset and thermoplastic UD laminate specimens was presented in Albertsen et al. (1995). In that work, the fracture toughness for different deformation modes was examined, as well as the influence of the fiber surface treatment upon the fracture toughness values at

initiation and propagation. The mode mixity in Albertsen et al. (1995) was expressed in terms of the $\mathcal{G}_I/\mathcal{G}_{II}$ ratio. In order to compare between the obtained results with respect to the mixed-mode ratio expressed by $\hat{\psi}$, use of eq. (1.12) with $\epsilon = 0$ was made. Since the delamination in Albertsen et al. (1995) is located between two adjacent UD plies of the same orientation, the value of $\hat{L}$ in eq. (1.12) is not required. For the thermoset beam-type specimens made from UD carbon/epoxy (C/HG9106) with commercially treated fibers, the value for delamination initiation obtained for the DCB tests was $\mathcal{G}_{Ic} = 400$ N/m. The delamination initiation value obtained for the mixed-mode flexure (MMF) tests, shown in Fig. 1.9a in which $\hat{\psi} \simeq 0.23\pi$, was $\mathcal{G}_{I/IIc} = 410$ N/m. This result of Albertsen et al. (1995), where $\mathcal{G}_{Ic}$ and $\mathcal{G}_{I/IIc}$ are close to each other for a relatively small mixed mode ratio, supports the results obtained in the current investigation for $\mathcal{G}_{Ic}$ and $\mathcal{G}_{ic}$.

Chapter 6

Discussion and Conclusions

This investigation focused on the mixed mode I/II fracture behavior at initiation, as well as for propagation under quasi-static loading, of a carbon/epoxy MD woven composite containing an interlaminar delamination between two plain woven plies. The tows in the upper ply are in the $0°/90°$-directions, and for the lower ply, the tows are in the $+45°/-45°$-directions. The investigation involved analytical, numerical and experimental work. It may be noted that the methodology developed here is transferable to other MD laminate composites, but it requires adaptations and much analytical, numerical and experimental work.

In Chapter 1, a literature review was presented. A brief introduction to the field of polymer-fiber composites was given in Section 1.1, where some of the difficulties raised by the composite structure manufacturing process were described. The stress and displacement fields near the tip of an interface crack, which is located between two linear elastic isotopic materials, were described in Section 1.2. A literature review regarding pure deformation modes, as well as in-plane mixed mode fracture toughness measurement methods was presented in Section 1.3, where examples of various bimaterial interface delaminations within an MD composite laminate were also described. Many test techniques and specimens, which were used during the last fifteen years, were examined. Only a few test methods were approved to serve as standards. Furthermore, although the composite structure architecture, its constituents and applied in-service loads are complicated in most cases, the standards are limited to UD carbon or glass FRP specimens, which are subjected to quasi-static loading conditions. Among these standards are the three mode I test standards, ASTM Standard D 5528-13 (2014), ISO 15024 (2011) and JIS K 7086 published in 1993 (Hojo et al., 1995) employing the DCB specimen. The three mode II test standards include the ISO 15114 (2014) standard employing the C-ELS test configuration; and the two standards in which the three-point bending ENF test configuration is employed; these are the ASTM standard D 7905 (2014) and the JIS K 7086 established in

March 1993 (Tanaka et al., 1995). There is currently one international standard for the mixed mode I/II test method which is the ASTM standard D 6671-13 (2014), in which the MMB test configuration is employed.

In Chapter 2, the first term of the asymptotic expansion for the stress and displacement fields in the neighborhood of the delamination front, for the interface studied here, was presented. Use was made of the formalisms of Lekhnitskii (1950) and Stroh (1958), in which plane deformations are assumed. The expressions for the in-plane stress and displacement components were obtained; those were related to the complex in-plane stress intensity factor $K = K_1 + iK_2$, which is the amplitude of the oscillatory, square-root singular stress components. The expressions for the out-of-plane stress and displacement components were also obtained; those were related to the real out-of-plane stress intensity factor K_{III}, which is the amplitude of the square-root singular stress component. It may be pointed out that the mechanical and thermal properties of the $0°/90°$ woven ply were obtained by Ishbir (2014) via the High Fidelity Generalized Method of Cells (HFGMC), described in detail in Aboudi (2004). In addition, the residual stresses were found to be minimal since both plies, $0°/90°$ and $+45°/-45°$, have the same coefficients of thermal expansion. Hence, the stress intensity factors result only from mechanical loading.

Next, methods for extraction and calculation of the stress intensity factors were presented in Chapter 3. The DE method, which is considered a straightforward method, was presented in Section 3.1. It is based upon the relative displacement of the crack faces or the "jump" in the crack face displacements within the neighborhood of the delamination front. Thus, the first term of the asymptotic expansion for the displacement field was employed. Use is made of the expressions in eqs. (3.7) and (3.8). An interaction energy or M-integral for mechanical loading was extended for the investigated interface and was presented in Section 3.2. The M-integral is based on conservative integrals and therefore it is a more complicated but accurate method. A solution being sought, in which the stress and displacement fields may be obtained via the FEM, along with a known auxiliary solution, in which the first term of the asymptotic expansion for the displacement field was employed, resulted in separate expressions for the stress intensity factors given in eqs. (3.17) to (3.19). Three benchmark problems were solved by performing numerical analyses in Section 3.3, while using the known asymptotic solutions in eqs. (2.64) and (2.65) with the stress intensity factors in Table 3.1. These were employed to obtain the displacement vector of each nodal point located on the outer surfaces of each benchmark FE model, which served as boundary conditions in the FEA. The FEA result (displacement field throughout the FE model) together with the M-integral were employed for calculating the stress intensity factors. These were also calculated by means of the FEA and the DE method. Comparison of the calculated and exact values of the stress intensity factors (analytic solution) was quantified for both methods and excellent agreement was found,

so that the software written for the M-integral and the DE method, as well as the first term of the asymptotic displacement field, were verified and both methods were validated.

Mixed-mode fracture toughness tests were carried out on the MD laminate studied here making use of a BD specimen. Tests at various loading angles were performed in order to obtain a wide range of mode mixities, as presented in Chapter 4. The test procedure was based upon the protocol described in Section 4.1, in which specimen dimensions were measured in the spirit of the ASTM E 399-12$^{\varepsilon 1}$ (2013) standard. The materials and methods were presented in Section 4.2, in which the manufacturing process and stacking sequence of the 69 carbon/epoxy (G0814/913) prepreg plain woven plies were described. The specimens were analyzed by means of the FEM and the M-integral to obtaine the stress intensity factors; these were used to determine the critical interface energy release rate and two phase angles (mode mixities). The obtained results were discussed in Section 4.3, in which verification of FE mesh convergence and domain independence was also included. Finally, a two and three-dimensional failure criterion were presented in Section 4.5. A statistical analysis with a 10% probability of unexpected failure and a 95% confidence was carried out for each criterion, in order to account for scatter in the results. The statistical curve and surface, which were presented in Section 4.5, predicted, as expected, that all specimens fail. The statistical curve and surface obtained may be used for safer design purposes for the investigated interface.

Fracture toughness tests for delamination initiation and propagation under quasi-static loading were carried out making use of three beam-type specimens: DCB, C-ELS and MMELS. Results were presented in Chapter 5. A carbon/epoxy (G0814/913) prepreg plain woven plate containing 23 plies was fabricated. Specimens were cut from the plate by means of a water-jet machine. The specimens were used to measure the fracture toughness $\mathcal{G}_{ic}$ of the investigated interface, as well as the R-curve behavior. The deformation modes considered were nearly mode I, nearly mode II and one in-plane mixed mode ratio. The DCB specimen was presented in Section 5.1. Three fracture toughness tests were carried out based upon the protocol described in Section 5.1.1. The DCB specimens were analyzed by means of the FEM and the M-integral to determine the stress intensity factors, as described in Section 5.1.2. A fracture toughness resistance $\mathcal{G}_{IR}$-curve was generated, as presented in Section 5.1.3, and the critical values of the interface energy release rate for initiation $\mathcal{G}_{Ic} = 376.3$ N/m and steady-state propagation $\mathcal{G}_{Iss} = 715.5$ N/m were determined.

The C-ELS specimen was presented in Section 5.2. Five fracture toughness tests, as well as ELS clamping fixture calibration procedure were carried out based upon the protocol described in Section 5.2.1. The C-ELS specimens were analyzed by means of the FEM and the DE method to determine the in-plane stress intensity factors, as described in Section 5.2.2. A fracture toughness resistance $\mathcal{G}_{IIR}$-curve was generated, as presented in

Section 5.2.3, and the critical values of the interface energy release rate for initiation $\mathcal{G}_{IIc} = 889.1$ N/m and steady-state propagation $\mathcal{G}_{IIss} = 2352.6$ N/m were determined.

The MMELS specimen was presented in Section 5.3. Five fracture toughness test were carried out based upon the protocol described in Section 5.3.1. The MMELS specimens were analyzed by means of the FEM and the three-dimensional M-integral to determine the stress intensity factors. These were further used, along with the analyzed experimental data, to determine the critical interface energy release rate and two phase angles (mode mixities), as described in Section 5.3.2. Finally, a fracture toughness resistance $\mathcal{G}_{iR}$-curve was generated, as presented in Section 5.3.3, and the critical values of the interface energy release rate for initiation $\mathcal{G}_{ic} = 393.3$ N/m and steady-state propagation $\mathcal{G}_{iss} = 836.3$ N/m were determined for the MMELS specimen.

Two approaches, global and local, may be found in the literature for calculating the critical energy release rate. The global approach, as advocated by the standards, is appropriate for calculating the fracture toughness with respect to the entire region mechanically affected by the delamination. The local approach is more complicated. The interface energy release rate is calculated along the delamination front. The delamination considered here is along an interface between two plain woven plies of different orientations in an MD laminate, where the specimen arms or sub-laminates are of different thicknesses and different effective mechanical properties, such as axial and flexural moduli. Therefore, some of the methods presented in the standards, which rely upon beam theory where identical flexural moduli in all specimen laminate segments (upper sublaminate, lower sublaminate and intact laminate) occur, are not applicable for determining the critical interface energy release rate $\mathcal{G}_{ic}$. Also, for the BD specimens tested here, no appropriate global expression for determining $\mathcal{G}_{ic}$ is available. Hence, the local approach was implemented.

It may be noted that the stress intensity factor K_{III} was much smaller than $\hat{K}_1$ and $\hat{K}_2$, except at the specimen edges. This appears to be the result of a Poisson effect. Nonetheless, in calculating the total interface energy release rate $\mathcal{G}_i$, it was taken into consideration for all the three-dimensional analyses carried out.

Quantification of the critical energy release rate $\mathcal{G}_{ic}$ values obtained for delamination initiation in all test specimens as a function of the in-plane phase angle $\hat{\psi}$ are presented in Fig. 6.1. The data shown in Fig. 6.1 is a major result of this comprehensive investigation. This plot was originally generated for the BD fracture toughness tests discussed in Section 4.5 and shown in Fig. 4.18. The fracture toughness values for delamination initiation obtained by means of the beam-type specimens, DCB, MMELS and C-ELS, are also plotted in Fig. 6.1, where it is clear that for the DCB specimens with $\hat{\psi} \approx 0$, a higher value of $\mathcal{G}_{ic}$ was obtained as compared to the BD specimens. However, the value for $\mathcal{G}_{Ic}$ was found to be less than that obtained in Simon et al. (2017), in which the same

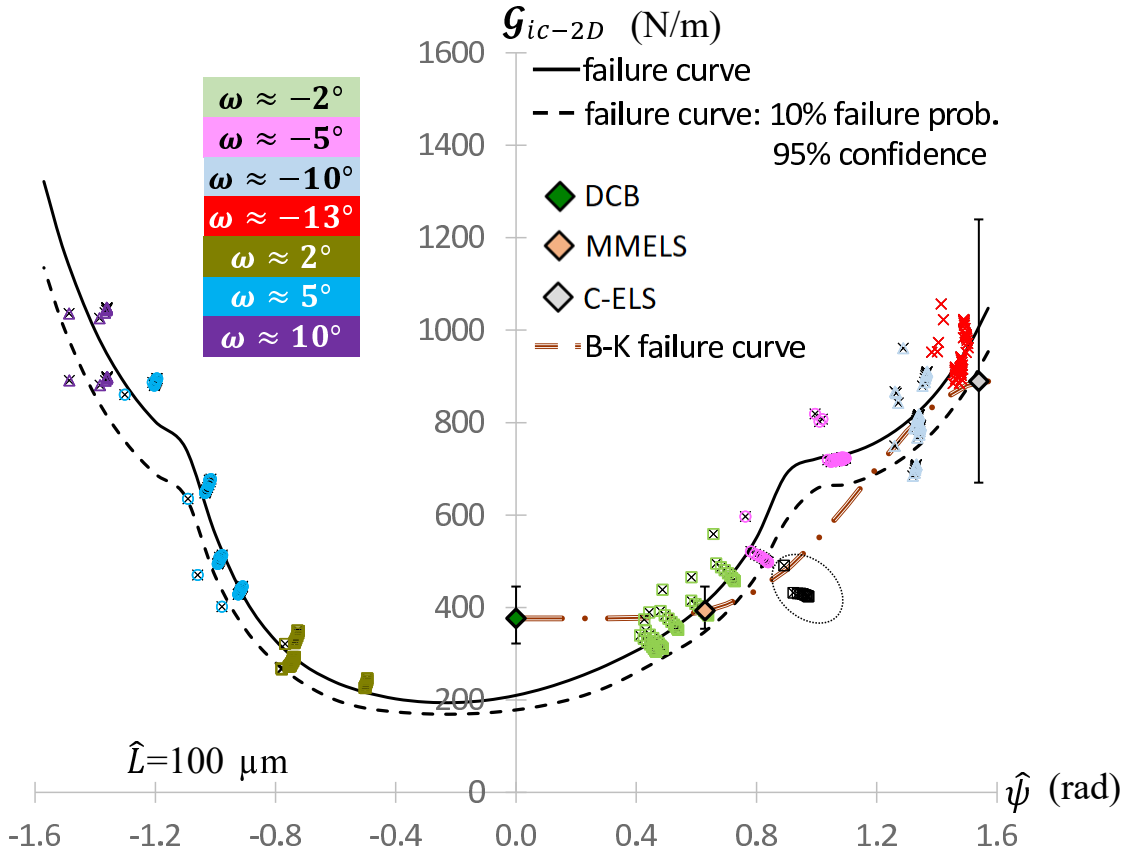

Figure 6.1: The in-plane energy release rate $\mathcal{G}_{i-2D}(\hat{\psi})$ for $\hat{L} = 100$ μm, given in eq. (4.15) with $\phi = 0$ for the BD test specimen. The beam-type specimen $\mathcal{G}_{ic}$ values for initiation and their obtained B-K failure curve (plotted in brown), given in eq. (6.1) with $m = 3.22$

.

interface was investigated, but thinner specimens with a different stacking sequence, was employed. In some previous works, such as in that of Hojo and Aoki (1993), where DCB specimens composed of UD AS4/PEEK laminates and of UD T800/3631 laminates with nominal thicknesses of $2h = 3, 4, 5$ and 8 mm were tested, it was observed that there was no thickness effect upon the value of the fracture toughness at initiation. It should be noted that in order to attain those thicknesses, the DCB specimens were milled from a thickness of 8 mm to their final thickness. Milling down the specimen may have affected the initiation energy release rate values that obtained.

The behavior in which DCB specimens of greater thickness have lower fracture toughness initiation values was also observed in other recent studies, in which thermoset UD laminate specimens were investigated, such as in Kravchenko et al. (2017) and Kumar et al. (2018). Another example is the MD carbon/epoxy composite studied in Mega and Banks-Sills (2019) in comparison to Chocron and Banks-Sills (2019), as discussed at the end of Section 5.1.3. In order to emphasize the effect of specimen nominal thickness upon the

Table 6.1: Values of $\mathcal{G}_{Ic}$ as a function of specimen thickness, $2h$, as obtained for a UD CFRP from Kumar et al. (2018) and from Kravchenko et al. (2017), for a delamination along a 0° UD fabric and $+45°/-45°$ (weave) interface from Chocron and Banks-Sills (2019) and Mega and Banks-Sills (2019), as well as for a delamination along a 0°/90° and $+45°/-45°$ (weaves) interface from Simon et al. (2017) and as investigated here in Chapters 4 and 5.

	$2h$ (mm)	$\mathcal{G}_{Ic}$ (N/m)
Kumar et al. (2018)	4.0	170
	5.3	144
	6.7	102
Kravchenko et al. (2017)	2.0	277
	4.1	233
	6.1	184
	8.2	192
	15.6*	110
Chocron and Banks-Sills (2019)	5.0	358
Mega and Banks-Sills (2019)	16.6	114
Simon et al. (2017)	3.7	508
Chapter 5	5.0	376
Chapter 4	15.6	210

*The extrapolated value obtained by considering the initiation values of specimens for which K-dominance was verified in Kravchenko et al. (2017) (with nominal thickness of 4.1, 6.1 and 8.2 mm).

initiation energy release rate value, a summary is presented in Table 6.1, and also plotted in Fig. 6.2. Since linear elastic behavior of the specimen is recommended in the ASTM Standard D 5528-13 (2014) and ISO Standard 15024 (2011), the value of $\mathcal{G}_{Ic}$ for the specimen 2.0 mm thick, given in Fig. 6.2 and in Table 6.1, was excluded from the calculation of the extrapolated value of $\mathcal{G}_{Ic}$ for a thickness of 15.6 mm. The extrapolated value of 110 N/m is marked with an x in Fig. 6.2. In Fig. 6.2, it is clearly observed that there is a relationship between specimen nominal thickness and the initiation energy release rate value, where higher $\mathcal{G}_{Ic}$ values are obtained for thinner specimens. The differences in the initiation toughness values obtained for nearly mode I deformation may be explained by the different levels of constraint in the two specimens. In Kravchenko et al. (2017), it was shown that the size of the K-dominant zone is the same order of magnitude as the fracture process zone reported in the literature for brittle thermosets and thermoplastics. Thus, for thin DCB specimens, higher initiation energy release rate values are expected.

Referring to Fig. 6.1, it is observed that there is relatively good agreement between the critical values for delamination onset obtained with both specimen types, the BD and the beam-type specimens, when $\hat{\psi} > 0.20\pi$. Thus, despite the scatter, it appears that increasing the mode II deformation results in values of the critical energy release rate for

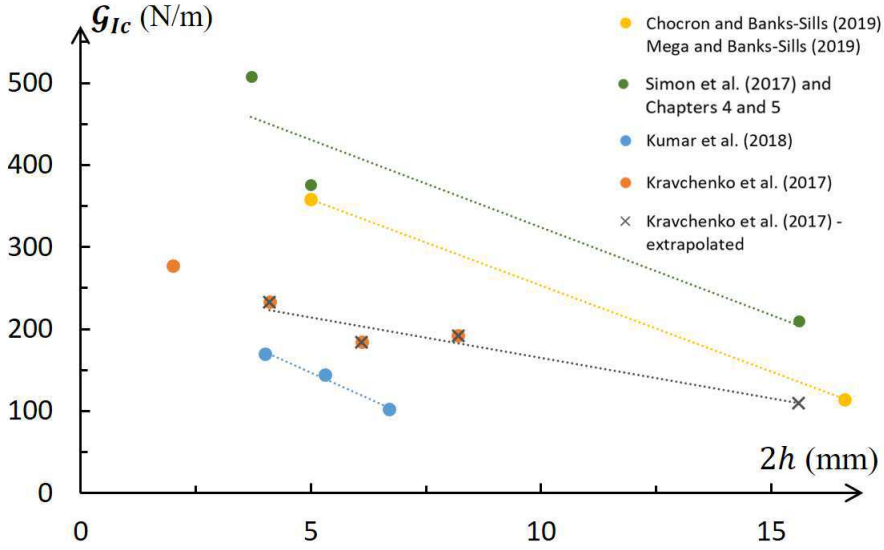

Figure 6.2: Values of $\mathcal{G}_{Ic}$ plotted as a function of specimen thickness, $2h$, for different material systems as obtained for a UD CFRP from Kumar et al. (2018) and from Kravchenko et al. (2017), for a delamination along a $0°$ and $+45°/-45°$ interface from Chocron and Banks-Sills (2019) and Mega and Banks-Sills (2019), as well as for a delamination along a $0°/90°$ and $+45°/-45°$ interface from Simon et al. (2017) and as investigated here in Chapters 4 and 5.

initiation $\mathcal{G}_{ic}$ which are less sensitive to specimen thickness. This is in contrast to the nearly mode I deformation, where $\mathcal{G}_{Ic}$ was found to be affected by the specimen thickness.

Another failure criterion is used with beam-type specimens. As proposed by Benzeggagh and Kenane (1996), an empirical failure criterion given as

$$\mathcal{G}_{Tc} = \mathcal{G}_{Ic} + (\mathcal{G}_{IIc} - \mathcal{G}_{Ic}) \left(\frac{\mathcal{G}_{II}}{\mathcal{G}_T} \right)^m \tag{6.1}$$

where

$$\mathcal{G}_T = \mathcal{G}_I + \mathcal{G}_{II} \tag{6.2}$$

may be used for characterizing the relationship between the critical values of the energy release rate experimentally obtained and the corresponding mode mixity. The latter may also be expressed in terms of the mode mixity ratio $\mathcal{G}_{II}/\mathcal{G}_T$, where the total energy release rate is given in eq. (6.2). In eq. (6.1), c in the subscripts denotes the critical value for the energy release rate obtained for different mode mixities. Employing the criterion in eq. (6.1) with the beam-type specimen test results shown in Fig. 6.1, leads to $m = 3.22$. It is assumed here that

$$\tan^2\hat{\psi} = \mathcal{G}_{II}/\mathcal{G}_I \tag{6.3}$$

which is an extension of the definition of $\hat{\psi}$ in eq. (1.12). The B-K failure curve is also plotted in Fig. 6.1 as a function of $\hat{\psi}$. It may be observed that the B-K curve is conservative

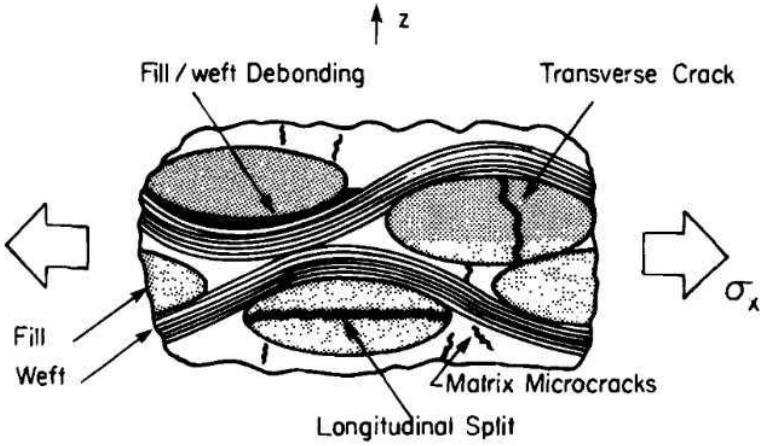

Figure 6.3: Schematic illustration of damage observed on the outer side of a dog-bone specimen made of woven fabric composites loaded in tension as presented in Alif and Carlsson (1997).

for the region where $0.23\pi < \hat{\psi} < 0.35\pi$, while it is not conservative for the region where $\hat{\psi} < 0.16\pi$. Thus, for thick structural composites, the fracture initiation values for mode I deformation should be determined by means of thick specimen test methods. Otherwise, "optimistic" values may result in improper design, which may end in catastrophic events.

For the investigated interface, a plateau region of the $\mathcal{G}_{IR}$-curve was obtained, in which almost the same delamination propagation resistance value was determined here and in Simon et al. (2017). Here, $\mathcal{G}_{Iss} = 715.5$ N/m, whereas in Simon et al. (2017), $\mathcal{G}_{Iss} = 710.9$ N/m. Thus, it appears that in the steady state region the delamination propagation mode I energy release rate $\mathcal{G}_{IR}$ values are relatively insensitive to the thickness of the DCB specimens. This was supported by the behavior of R-curves for thermoset UD laminate specimens as discussed in Suo et al. (1992).

Although here the specimens are made of plain woven plies, it is interesting to explore some of the failure mechanisms in woven composites. In Alif and Carlsson (1997), failure mechanisms of a carbon/epoxy 5-harness weave and a glass/epoxy 4-harness weave were investigated. A schematic illustration of damage observed on the outer side of a dog-bone tensile test specimen made of the woven fabric composites is shown in Fig. 6.3, as presented in Alif and Carlsson (1997). It is interesting to note that in the tensile tests of the carbon/epoxy weave specimens in Alif and Carlsson (1997), the sequence of damage evolution was found as: initial cracking of the pure matrix regions, transverse yarn (fill) bundle cracking, fill/weft debonding and longitudinal splits of the fill bundles close to ultimate failure. However, in the glass/epoxy weave specimens, the sequence of damage formation was found as: initial cracking of the pure matrix regions, fill/weft debonding and longitudinal splits of the fill bundles close to ultimate failure, without transverse yarn

bundle cracking. The absence of transverse yarn bundle cracking may be attributed to the improved constraint of fill tows by weft tows within the 4-harness weave pattern. In addition, it may be pointed out that the compression and shear strengths of the weaves examined in Alif and Carlsson (1997) were found to be lower than their tensile strength. For the $0°/90°$ plain woven ply used here, the shear strength is less than 20% of the strength in tension and compression, which may also support the difference between the results obtained for the DCB and BD specimens with a low loading angle.

As presented in the literature regarding fracture toughness of composites, for UD DCB specimens, phenomena such as fiber bridging and matrix cracking tend to occur. For woven fabric composites, phenomena such as matrix cracking, bifurcation of the delamination front and other failure mechanisms as shown in Fig. 6.3, are typically observed. All of these phenomena result in a rising R-curve. However, some of them, such as fiber bridging in UD DCB specimens, do not occur in structural composites (Davies et al., 1998). Moreover, in the case of woven fabric composites, the increase in fracture resistance is attributed to mechanisms other than those which occur in UD DCB specimens. For woven composites, as observed in Hojo et al. (1995) and in Alif et al. (1997), a "stick-slip" behavior of the mode I delamination propagation was obtained. Following the "stick-slip" characteristic, the delamination temporarily arrests by a transverse fiber bundle, which serves as an obstacle or barrier oriented in the 90°-direction. With further load application, a small delamination is formed ahead of the transverse (fill/warp) tow together with further backward delamination propagation around the fill yarn, sometimes with additional longitudinal separation of the fill yarn fiber bundle on the outer sides of the DCB specimen, as schematically shown in Fig. 6.3. This behavior of crack arrest, debonding of fill yarns and longitudinal splitting was also observed in other works that may be found in the literature, such as Alif et al. (1998), Ogasawara et al.(2012), Banks-Sills et al. (2013) and Fanteria et al. (2017).

Regarding the current investigated interface, scanning electron microscopy (SEM) analyses were performed in Banks-Sills et al. (2013), in which the same interface was studied, with different DCB specimen thickness and stacking sequence, as discussed in Section 5.1. Based upon the SEM analyses in Banks-Sills et al. (2013), it was found that the delamination propagated along the $0°/90°//+45°/-45°$ interface. As also occurred in the current study, partial delamination of yarn at the outer sides (front and back) of the DCB specimen was observed during the tests. It may be noted that the initial increase in mode I fracture toughness was attributed in Alif et al. (1998) to the damage progression associated with the twisting delamination path through the woven fabric microstructure. In that work, the effect of weave pattern on the interlaminar fracture toughness for mode I deformation was investigated in plain, twill and satin weave DCB specimens. According

to Alif et al. (1998), the delamination resistance was increased as the complexity of the weave increases.

It may be pointed out that a "stick-slip" delamination propagation was observed in the MMELS specimen tests, in which the mode I deformation was found to be dominant. This behavior was also observed in Alif et al. (1997), in which the mode I, mode II and mixed mode fracture of a carbon/epoxy 5-harness weave was investigated by means of the DCB, ENF and MMB specimens. It was observed in Alif et al. (1997), that in mixed mode deformation in which mode I was dominant, the behavior of crack propagation was similar to the "stick-slip" characteristic of mode I. For the C-ELS specimens tested here with nearly mode II deformation, the delamination propagation was found to be more stable than that obtained for the DCB and MMELS specimens.

Quantification of the critical energy release rate $\mathcal{G}_{ic}$ values obtained for delamination initiation in all test specimens and the steady-state interface energy release rate $\mathcal{G}_{iss}$ values obtained for the beam-type test specimens as a function of the in-plane phase angle $\hat{\psi}$ are presented in Fig. 6.4. This plot is the same as that given in Fig. 6.1, except that it includes the $\mathcal{G}_{iss}$ values. It is observed that for each value of $\hat{\psi}$, a higher value of $\mathcal{G}_{iss}$ was obtained as compared to the initiation value $\mathcal{G}_{ic}$. Use of the B-K criterion given in eq. (6.1) was made for characterizing the relationship between the steady-state propagation values of the energy release rate experimentally obtained and the corresponding mode mixity. The latter is expressed in terms of the mode mixity ratio $\mathcal{G}_{II}/\mathcal{G}_T$, where the total energy release rate is given in eq. (6.2). Again, it is assumed here that $\hat{\psi}$ is expressed by means of eq. (6.3). In eq. (6.1), the subscript c is replaced by ss so that the steady-state propagation values for the energy release rate obtained for different mode mixities are used. Note that $\mathcal{G}_{Iss} = 715.5$ N/m, $\mathcal{G}_{IIss} = 2352.6$ N/m and $\mathcal{G}_{iss} = 836.3$ N/m. Employing the criterion in eq. (6.1) with the beam-type specimen test results for steady-state delamination growth shown in Fig. 6.4, leads to $m = 2.60$, which is less than the value obtained for delamination initiation. Nevertheless, the behavior of both B-K failure curves, at delamination initiation and delamination steady-state propagation, is relatively similar. It may be noted that the steady-state delamination growth values are approximately twice as high as the delamination initiation values, varying from $\mathcal{G}_{iss}/\mathcal{G}_{ic} = 1.9$ for the DCB specimens, through $\mathcal{G}_{iss}/\mathcal{G}_{ic} = 2.1$ for the MMELS specimens, to $\mathcal{G}_{iss}/\mathcal{G}_{ic} = 2.6$ for the C-ELS specimens. In all beam-type specimens, an increase in the fracture toughness resistance was observed as delamination propagated until a steady-state value was reached. That increase is attributed to the "stick-slip" behavior, as discussed above. It is observed on the specimen edges that the tows are separating in the process of delamination propagation, both ahead and behind the delamination front, which was affected by the woven fabric microstructure. Fill tows, which are close to delamination surface, are separating and contributing more energy as the delamination grows. Micro-computerized tomography on

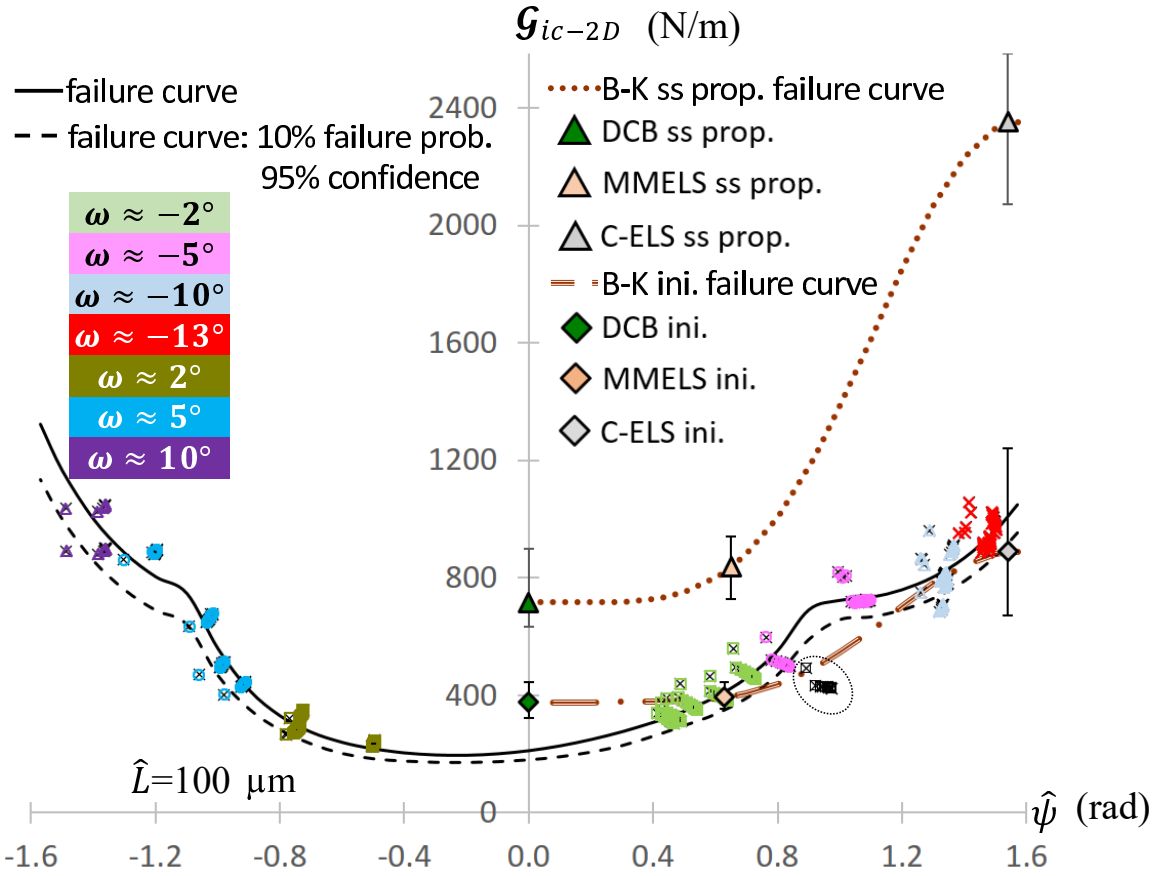

Figure 6.4: The in-plane energy release rate $\mathcal{G}_{i-2D}(\hat{\psi})$ for $\hat{L} = 100$ μm, given in eq. (4.15) with $\phi = 0$ for the BD test specimen. The beam-type specimen $\mathcal{G}_{ic}$ values for initiation (ini.) and their obtained B-K failure curve (plotted in brown), given in eq. (6.1) with $m = 3.22$. The beam-type specimen $\mathcal{G}_{iss}$ values for steady-state propagation (ss prop.) and their obtained B-K failure curve (plotted in brown dots), given in eq. (6.1) with $m = 2.60$.

another set of specimens, composed of a twill weave, showed tow separation to occur also within the specimen.

It is worth mentioning that despite the fact that the FEAs for the C-ELS and MMELS specimens were non-linear, as a result of the contact surfaces and large displacements, a linear relationship was found between the delamination length in the second stage of the C-ELS test and the corresponding in-plane phase angle $\hat{\psi}$. Demonstration of the linear relationship between the normalized in-plane stress intensity factor $\hat{K}_2$ and the delamination length was also presented in Section 5.2.2. Regarding the MMELS FEAs, a linear relationship between the delamination length and each of the stress intensity factors at the same location along the delamination front (same value of the normalized delamination front coordinate x_3/b) was found, as presented in Section 5.3.2.

As future work, this thesis may be extended in several directions. A new look at the large amount of data obtained for the three beam-type specimens tested here would be the first step. Data analysis in a manner similar to that employed with the data obtained for the BD test specimens is recommended. It is suggested to examine and analyse both the fracture onset data, as well as the steady state delamination propagation data, so that two criteria may be determined by means of the beam-type specimens. The criterion for delamination initiation will serve as a lower bound, as performed with the data obtained for the BD specimens, whereas the the criterion for a steady state delamination propagation will serve as an upper bound. SEM analyses of the BD and the beam-type specimens may also be performed. Since there was only one ratio of mode mixity that was examined here with the beam-type specimens, it is suggested, as a second direction, to carry out additional beam-type fracture toughness tests with specimens of mode mixity of $\hat{\psi} \approx 0.12\pi$, 0.28π and 0.35π, in which the beam-type specimen arms are of different thicknesses than those of the MMELS specimen examined here. In this way a complete beam-type failure curve may be determined for delamination initiation and propagation. Indeed, a statistical analysis should be applied to all analyzed data. It is also suggested to examine the effect of porosity upon the investigated interface fracture toughness for several mode mixities. As observed in Section 4.5, for specimen **sp1.2** which was found to have pores in it, the obtained critical energy release rate was found to be lower than that obtained for specimens without voids, as may be also seen in Fig. 6.1. That region was considered to be safe from delamination initiation, but the fracture toughness calculated for specimen **sp1.2** was more than 4 STDs away from the failure curve determined for valid BD specimens. Finally, measurement of the interlaminar fatigue delamination growth rate by means of the beam-type specimens with the same interface as examined here at different mode mixities may be carried out. In this way, generation of a master curve for delamination growth rate versus normalized energy release rate, may be obtained for various mode mixities.

Bibliography

[1] Aboudi, J. The generalized method of cells and the high-fidelity generalized method of cells micromechanical models–a review. *Mech. Adv. Mater. Struc.*, 11: 329-366, 2004.

[2] Albertsen, H., Ivens, J., Peters, P., Wevers, M., and Verpoest, I. Interlaminar fracture toughness of CFRP influenced by fibre surface treatment: part 1. Experimental results. *Compos. Sci. Technol.*, 54: 133-145, 1995.

[3] Alif, N., and Carlsson, L.A. Failure mechanisms of woven carbon and glass composites. *Composite Materials, Fatigue and Fracture (Sixth Volume), ASTM STP 1285*, Armanios, E.A. (ed.), American Society for Testing and Materials, West Conshohocken, PA, pp. 471-493, 1997.

[4] Alif, N., Carlsson, L.A., and Gillespie, J.W. Mode I, mode II and mixed mode fracture of woven fabric carbon/epoxy. *Composite Materials, Testing and Design, Thirteenth Volume, ASTM STP 1242*, Hooper, S.J. (ed.), American Society for Testing and Materials, West Conshohocken, PA, pp. 82-106, 1997.

[5] Alif, N., Carlsson, L.A., and Boogh, L. The effect of weave pattern and crack propagation direction on mode I delamination resistance of woven glass and carbon composites. *Compos. Part B: Eng.*, 29: 603-611, 1998.

[6] Allegri, G., Winson, M.R., and Hallett, S.R. A new semi-empirical law for variable stress-ratio and mixed-mode fatigue delamination growth. *Compos. Part A: Appl. Sci. Manuf.*, 48: 192-200, 2013.

[7] Anderson, D.R., Sweeney, D.J., Williams, T.A., Camm, J.D., Cochran, J.J., Fry, M.J., and Ohlmann, J.W. Quantitative Methods for Business, Thirteenth Edition. Cengage Learning, Boston, pp. 83-84, 2015.

[8] Arcan, M., Hashin, Z., and Voloshin, A. A method to produce uniform plane-stress states with applications to fiber-reinforced materials. *Exp. Mech.*, 18: 141-146, 1978.

[9] Atkinson, C. On stress singularities and interfaces in linear elastic fracture mechanics. *Int. J. Fract.*, 13: 807-820, 1977.

[10] Atkinson, C., Smelser, R.E., and Sanchez, J. Combined mode fracture via the cracked Brazilian disk test. *Int. J. Fract.*, 18: 279-291, 1982.

[11] Ashton, J.E., and Whitney, J.M. Theory of Laminated Plates. Technomic publication, Connecticut, pp. 7-18, 1970.

[12] ASTM D5229/D5229M-92 (reapproved 2010). Test method for moisture absorption properties and equilibrium conditioning of polymer matrix composites. *Space Simulation; Aerospace and Aircraft; Composite Materials, Vol. 15.03*, American Society for Testing and Materials, West Conshohocken, PA, 2011.

[13] ASTM Standard D 5528-13. Standard test method for mode I interlaminar fracture toughness of unidirectional fiber-reinforced polymer matrix composites. *Space Simulation; Aerospace and Aircraft; Composite Materials, Vol. 15.03*, American Society for Testing and Materials, West Conshohocken, PA, pp. 289-301, 2014.

[14] ASTM Standard D 6671-13. Standard test method for mixed mode I-mode II interlaminar fracture toughness of unidirectional fiber-reinforced polymer matrix composites. *Space Simulation; Aerospace and Aircraft; Composite Materials, Vol. 15.03*, American Society for Testing and Materials, West Conshohocken, PA, pp. 429-443, 2014.

[15] ASTM Standard E 399-12$^{\varepsilon 1}$. Test method for linear-elastic plane-strain fracture toughness K_{Ic} of metallic materials. Metals-Mechanical Testing Elavated and Low-Tempurture Tests; Metallography, Vol. 03.01, ASTM International, West Conshohocken, PA, pp. 519-551, 2013.

[16] ASTM Standard D 7905-14. Standard Test Method for Determination of the Mode II Interlaminar Fracture Toughness of Unidirectional Fiber-Reinforced Polymer Matrix Composites. *Space Simulation; Aerospace and Aircraft; Composite Materials, Vol. 15.03*, American Society for Testing and Materials, West Conshohocken, PA, 2014.

[17] Balzani, C., Wagner, W., Wilckens, D., Degenhardt, R., Büsing, S., and Reimerdes, H.-G. Adhesive joints in composite laminates - A combined numerical/ experimental estimate of critical energy release rates. *Int. J. Adhes. Adhes.*, 32: 23-38, 2012.

[18] Banks-Sills, L., and Bortman, Y. Reappraisal of the quarter-point quadrilateral element in linear elastic fracture mechanics, *Int. J. Fract.*, 25: 169-180, 1984.

[19] Banks-Sills, L., Travitzky, N., Ashkenazi, D., and Eliasi, R. A methodology for measuring interface fracture properties of composite materials. *Int. J. Fract.*, 99: 143-160, 1999.

[20] Banks-Sills, L., and Ashkenazi, D. A note on fracture criteria for interface fracture. *Int. J. Fract.*, 103: 177-188, 2000.

[21] Banks-Sills, L., Travitzky, N., and Ashkenazi, D. Interface fracture properties of a bimaterial ceramic composite. *Mech. Mater.*, 32: 711-722, 2000.

[22] Banks-Sills, L., and Boniface, V. Fracture mechanics for an interface crack between a special pair of transversely isotropic materials. *Multiscale Deformation and Fracture in Materials and Structures–The James R. Rice 60th Anniversary Volume,* eds. Chuang T.-J. and Rudnicki J.W., Kluwer Academic Publishers, The Netherlands, pp. 183-204, 2000.

[23] Banks-Sills, L., and Dolev, O. The conservative M-integral for thermal-elastic problems. *Int. J. Fract.*, 125: 149-170, 2004.

[24] Banks-Sills, L., Boniface, V., and Eliasi, R. Development of a methodology for determination of interface fracture toughness of laminate composites - the 0°/90° pair. *Int. J. Solids Struct.*, 42: 663-680, 2005.

[25] Banks-Sills, L., Freed, Y., Eliasi, R., and Fourman, V. Fracture toughness of the $+45°/-45°$ interface of a laminate composite. *Int. J. Fract.*, 141: 195-210, 2006.

[26] Banks-Sills, L., Konovalov, N., and Fliesher, A. Comparison of two- and three-dimensional analyses of interface fracture data obtained from Brazilian disk specimens. *Int. J. Struct. Integr.*, 1: 20-42, 2010.

[27] Banks-Sills, L., Ishbir, C., Fourman, V., Rogel, L., and Eliasi, R. Interface fracture toughness of a multi-directional woven composite *Int. J. Fract.*, 182: 187-207, 2013.

[28] Banks-Sills, L. Interface fracture mechanics: theory and experiment. *Int. J. Fract.*, 191: 131-146, 2015.

[29] Banks-Sills, L., and Dolev, O. Mixed mode testing of a multi-directional woven laminate. *Int. J. Fract.*, doi:10.1007/s10704-020-00429-3, 2020.

[30] Barnett, D.M., and Kirchner, H.O.K. A proof of the equivalence of the Stroh and Lekhnitskii sextic equations for plane anisotropic elastostatics. *Philos. Mag. A*, 76: 231-239, 1997.

[31] Bartlett, D.W., (Ed.) Advanced aerodynamics - selected NASA research. NASA Conference Publication, NASA/CP-2208, 1981.

[32] Bathe, K.J. *ADINA–Automatic Dynamic Incremental Nonlinear Analysis*, Version 8.8.0, ADINA R&D, Inc. Watertown, Massachusetts, 2011.

[33] Benzeggagh, M.L., and Kenane, M. Measurement of mixed-mode delamination fracture toughness of unidirectional glass/epoxy composites with mixed-mode bending apparatus. *Compos. Sci. Technol.*, 56: 439-449, 1996.

[34] Blackman, B.R.K., Brunner, A.J., and Davies, P. Delamination fracture of continuous fibre composites: mixed-mode fracture. In: Moore, D., Williams, J., Pavan, A., editors. Fracture Mechanics Testing Methods for Polymers, Adhesives and Composite, Oxford, UK. ESIS, 28: 335-367, 2001.

[35] Blanco, N., Gamstedt, E.K., Asp, L.E., and Costa, J. Mixed-mode delamination growth in carbon-fibre composite laminates under cyclic loading. *Int. J. Solids Struct.*, 41: 4219-4235, 2004.

[36] Blankenship, C.P., and Teichman, L.A., (compilers) Advanced materials technology. NASA/AIAA Advanced materials technology seminar. NASA/CP-2251, 1982.

[37] Bowles M.D. The "Apollo" of aeronautics: NASA's aircraft energy efficiency program 1973-1987. NASA/SP-2009-574, 2010.

[38] Brandt, F. New load introduction concept for improved and simplified delamination beam testing. *Exp. Tech.*, 22: 17-20, 1998.

[39] Brunner, A.J., Blackman, B.R.K., and Davies, P. A status report on delamination resistance testing of polymer-matrix composites. *Eng. Fract. Mech.*, 75: 2779-2794, 2008.

[40] Carlone, P., Dragan, A., Velimir, Ć., and Gaetano, S.P. Meta-modeling of the curing process of thermoset matrix composites by means of a FEM-ANN approach. *Compos. Part B: Eng.*, 67: 441-448, 2014.

[41] Charalambides, P.G., Lund, J., Evans, A.G., and McMeeking, R.M. A test specimen for determining the fracture resistance of bimaterial interfaces. *J. Appl. Mech.*, 56: 77-82, 1989.

[42] Charalambous, G., Allegri, G., Lander, J.K., and Hallett, S.R. A cut-ply specimen for the mixed mode fracture toughness and fatigue characterisation of FRPs. *Compos. Part A: Appl. Sci. Manuf.*, 74: 77-87, 2015a.

[43] Charalambous, G., Allegri, G., and Hallett, S.R. Temperature effects on mixed mode I/II delamination under quasi-static and fatigue loading of a carbon/epoxy composite. *Compos. Part A: Appl. Sci. Manuf.*, 77: 75-86, 2015b.

[44] Chen, F.H.K., and Shield, R.T. Conservation laws in elasticity of the J-integral type. *ZAMP*, 28: 1-22, 1977.

[45] Chocron, T., and Banks-Sills, L. Nearly mode I fracture toughness and tatigue delamination propagation in a multidirectional laminate fabricated by a wet-layup. *Phys. Mesomech.*, 22: 107-140, 2019.

[46] Ciepluch, C.C., Davis, D.Y., and Gray, D.E. Results of NASA's energy efficient engine program. *J. Propuls.*, 3: 560-568, 1987.

[47] Comninou, M. The interface crack. *J. Appl. Mech.*, 44: 631-636, 1977.

[48] Comninou, M. The interface crack in a shear field. *J. Appl. Mech.*, 45: 287-290, 1978.

[49] Comninou, M., and Schmueser, D. The interface crack in a combined tension-compression and shear field. *J. Appl. Mech.*, 46: 345-348, 1979.

[50] Conroy, M., Kinloch, A.J., Williams, J.G., and Ivankovic, A. Mixed mode partitioning of beam-like geometries: a damage dependent solution. *Eng. Fract. Mech.*, 149: 351-367, 2015.

[51] Davidson B.D. Standard test method for determination of the mode II interlaminar fracture toughness of unidirectional fiber-reinforced polymer matrix composites. *Preliminary Standard*, pp. 1-23, received - 2014, issued - June 2013.

[52] Davies, P., Blackman, B.R.K., and Brunner, A.J. Standard test methods for delamination resistance of composite materials: Current status. *Appl. Compos. Mater.*, 5: 345-364, 1998.

[53] DaVis, Version 8.3. LaVision, Göttingen, Germany, 2015.

[54] de Oliveira, R., Lavanchy, S., Chatton, R., Costantini, D., Michaud, V., Salathé, R., and Månson, J.-A.E. Experimental investigation of the effect of the mould thermal expansion on the development of internal stresses during carbon fiber composite processing. *Compos. Part A: Appl. Sci. Manuf.*, 39: 1083-1090, 2008.

[55] Deng, X. General crack-tip fields for stationary and steadily growing interface cracks in anisotropic bimaterials. *J. Appl. Mech.*, 60: 183-189, 1993.

[56] Dow, M.B., and Dexter, H.B. Development of stitched, braided and woven composite structures in the ACT program and at Langley Research Center (1985 to 1997) summary and bibliography. NASA/TP-97-206234, 1997.

[57] Dundurs, J. Edge-bonded dissimilar orthogonal elastic wedges under normal and shear loading. *J. Appl. Mech.*, 36: 650-652, 1969.

[58] El-Hajjar, R., and Haj-Ali, R. In-plane shear testing of thick-section pultruded FRP composites using a modified Arcan fixture. *Compos. Part B: Eng.*, 35: 421-428, 2004.

[59] Fanteria, D., Lazzeri, L., Panettieri, E., Mariani, U., and Rigamonti, M. Experimental characterization of the interlaminar fracture toughness of a woven and a unidirectional carbon/epoxy composite. *Compos. Sci. Technol.*, 142: 20-29, 2017.

[60] Freed, Y., and Banks-Sills, L. A through interface crack between a ± 45 transversely isotropic pair of materials. *Int. J. Fract.*, 133: 1-41, 2005.

[61] Garg, D.P., Zikry, M.A., and Anderson, G.L. Current and potential future research activities in adaptive structures: an ARO perspective. *J. Smart Mater. Struct.*, 10: 610-623, 2001.

[62] Giannis, S. Utilising fracture mechanics principles for predicting the mixed-mode delamination onset and growth in tapered composite laminates. *Compos. Struct.*, 102: 294-305, 2013.

[63] Golestanian, H., and El-Gizawy, A.S. Cure dependent lamina stiffness matrices of resin transfer molded composite parts with woven fiber mats. *J. Compos. Mater.*, 31: 2402-2423, 1997.

[64] Golestanian, H., and El-Gizawy, A.S. Modeling of process induced residual stresses in resin transfer molded composites with woven fiber mats. *J. Compos. Mater.*, 35: 1513-1528, 2001.

[65] Heydari, M.H., Choupani, N., and Shameli, M. Experimental and numerical investigation of mixed-mode interlaminar fracture of carbon-polyester laminated woven composite by using Arcan set-up. *Appl. Compos. Mater.*, 18: 499-511, 2011.

[66] Hojo, M., and Aoki, T. Thickness effect of double cantilever beam specimen on interlaminar fracture toughness of AS4/PEEK and T800/epoxy laminates. In: ASTM-STP 1156, *Composite Materials: Fatigue and Fracture, Fourth Volume.*, Eds. Stinchcomb W., and Ashbaugh N., American Society for Testing and Materials International, West Conshohocken, PA, pp. 281-298, 1993.

[67] Hojo, M., Kageyama, K., and Tanaka, K. Prestandardization study on mode I interlaminar fracture toughness test for CFRP in Japan. *Compos.*, 26: 243-255, 1995.

[68] Hung, S.-C., and Liechti, K.M. An evaluation of the Arcan specimen for determining the shear moduli of fiber-reinforced composites. *Exp. Mech.*, 37: 460-468, 1997.

[69] Ishbir, C. Fracture and fatigue behavior of plain laminate multi-directional woven composites (the $0^\circ/90^\circ$ and $+45^\circ/-45^\circ$ interface). Ph.D. Thesis, Tel Aviv University, submitted 2014.

[70] Ishbir, C., Banks-Sills, L., Fourman, V., and Eliasi, R. Delamination propagation in a multi-directional woven composite DCB specimen subjected to fatigue loading. *Compos. Part B: Eng.*, 66: 180-189, 2014.

[71] ISO 15024:2001(E). Fibre-reinforced plastic composites - Determination of mode I interlaminar fracture toughness, $\mathcal{G}_{Ic}$, for unidirectionally reinforced materials. International Organization for Standardization, Geneva, Switzerland, downloaded - Jan 2011, issued - 2001.

[72] ISO 15114:2014(E). Fibre-reinforced plastic composites - determination of the mode II fracture resistance for unidirectionally reinforced materials using the calibrated end-loaded split (C-ELS) test and an effective crack length approach. International Organization for Standardization, Geneva, Switzerland, 2014.

[73] Khan, I.A. Prediction of elastic properties of 2D orthogonal plain weave fabric composite. Ph.D. Thesis, National Institute of Technology Rourkela, India, 2009.

[74] Kinloch, A.J., Wang, Y., Williams, J.G., and Yayla, P. The mixed-mode delamination of fiber composite materials. *Compos. Sci. Technol.*, 47: 225-237, 1993.

[75] Kravchenko, O.G., Kravchenko, S.G., and Sun, C.T. Thickness dependence of mode I interlaminar fracture toughness in a carbon fiber thermosetting composite. *Compos. Struct.*, 160: 538-546, 2017.

[76] Kumar, A.P., Pinninti, R.R., and Gupta, A. Thickness effect of DCB specimen on interlaminar fracture toughness in carbon/epoxy composites. *Int. J. Mech. Prod. Eng. Res. Dev.*, 8: 541-548, 2018.

[77] Lekhnitskii, S.G. *Theory of Elasticity of an Anisotropic Body.* Holden-Day, San Francisco, 1950, in Russian; translated by P. Fern, 1963, in English.

[78] Luko, S.N., and Neubauer, D.V. Statistical intervals-Part 2: the predicition interval. Stand News, Sept/Oct 1415, 2011.

[79] Mega, M., and Banks-Sills, L. Mixed mode interface fracture toughness of a multi-directional composite - UD/woven pair. *Theor. Appl. Fract. Mech.*, 104: 102323, 2019.

[80] Mega, M., Dolev, O., and Banks-Sills, L. Two and three - dimensional failure criteria for laminate composites. *J. Appl. Mech.*, 87: 021001-1-021001-11, 2020.

[81] Mega, M., and Banks-Sills, L. Comparison of methods for determination of fracture toughness in a multi-directional CFRP laminate. Submitted to publication: *Procedia Struct. Integr.*, 2020.

[82] Mollón, V., Bonhomme, J., Viña, J., and Argüelles, A. Theoretical and experimental analysis of carbon epoxy asymmetric dcb specimens to characterize mixed mode fracture toughness. *Polym. Test.*, 29: 766-770, 2010.

[83] Murakami, T., and Sato, T. Three-dimensional J-integral calculations of part-through surface crack problems. *Comput. Struct.*, 17: 731-736, 1983.

[84] Nagai, M., Ikeda, T., and Miyazaki, N. Stress intensity factor analysis of a three-dimensional interface crack between dissimilar anisotropic materials. *Eng. Fract. Mech.*, 74: 2481-2497, 2007.

[85] Nagai, M., Ikeda, T., and Miyazaki, N. Stress intensity factor analysis of a three-dimensional interface crack between dissimilar anisotropic materials under thermal stress. *Eng. Fract. Mech.*, 91: 14-36, 2012.

[86] Nagai, M., Ikeda, T., and Miyazaki, N. Stress intensity factor analyses of three-dimensional interface cracks using tetrahedral finite elements. *Comput. Mech.*, 51: 603-615, 2013.

[87] Natrella, M.G. Experimental statistics. National Bureau of Standards Handbook 91, U.S. Government Printing Office, Washington, DC, pp. 2-13−2-15, 1963.

[88] O'Brien, T.K. Interlaminar fracture toughness: the long and winding road to standardization. *Compos. Part B: Eng.*, 29: 57-62, 1998.

[89] Ogasawara, T., Yoshimure, A., Ishikawa, T., Takahashi, R., Sasakib, N., and Ogawa, T. Interlaminar fracture toughness of 5 harness satin woven fabric carbon/epoxy composites. *Adv. Compos. Mater.*, 21: 45-56, 2012.

[90] Peng, L., Xu, J., Zhang, J., and Zhao, L. Mixed mode delamination growth of multi-directional composite laminates under fatigue loading. *Eng. Fract. Mech.*, 96: 676-686, 2012.

[91] Poe, C.C., Dexter, H.B., and Raju, I.S. Review of the NASA textile composites research. *J. Aircr.*, 36: 876-884, 1999.

[92] Reeder, J.R., and Crews, J.R. Mixed-mode bending method for delamination testing. *AIAA J.*, 28: 1270-1276, 1990.

[93] Rice, J.R. Elastic fracture mechanics concepts for interfacial cracks. *J. Appl. Mech.*, 55: 98-103, 1988.

[94] Rice, J.R., Sou, Z., and Wang, J.S. Mechanics and thermodynamics of brittle interfacial failure in bimaterial systems. *Metal Ceramic Interfaces*, eds. Rühle, M., Evans, A.G., Ashby, M.F. and Hirth, J.P., Pergamon Press, New York, pp. 269-294, 1990.

[95] Rogel, L., and Banks-Sills, L. A through interface crack between a transversely isotropic pair of materials ($+30°/-60°$ and $-30°/+60°$). *Eng. Fract. Mech.*, 77: 3261-3291, 2010.

[96] Sakata, I.F., and Ostrom, R.B. Study on utilization of advanced composites in commercial aircraft wing structures - final report. NASA Contractor Report 145381-2, 1978.

[97] Schwartz, M. Encyclopedia of materials, parts, and finishes. CRC Press, Boca Raton, Florida, 2002.

[98] Shankar, B.V., and Marrey, R.V. Analytical method for micromechanics of textile composite. *Compos. Sci. Technol.*, 57: 703-713, 1997.

[99] Simon, I., Banks-Sills, L. and Fourman, V. Mode I delamination propagation and R-ratio effects in woven composite DCB specimens for a multi-directional layup. *Int. J. Fatigue*, 96: 237-251, 2017.

[100] Stroh, A.N. Dislocations and cracks in anisotropic elasticity. *Philos. Mag.*, 3: 625-646, 1958.

[101] Suo, Z., Bao, G., and Fan, B. Delamination R-curve phenomena due to damage. *J. Mech. Phys. Solids*, 40: 1-16, 1992.

[102] Szekrényes, A., and Uj, J. Beam and finite element analysis of quasi-unidirectional composite SLB and ELS specimens. *Compos. Sci. Technol.*, 64: 2393-2406, 2004.

[103] Taher, S.T., Thomsen, O.T., Dulieu-Barton, J.M., and Zhang, S. Modelling for predicting the mechanical properties of textile composites - a review. *Compos. Part A: Appl. Sci. Manuf.*, 43: 1698-1708, 2012.

[104] Tan, P., Tong, L., and Steven, G.P. Modelling for predicting the mechanical properties of textile composites - a review. *Compos. Part B: Eng.*, 28: 903-922, 1997.

[105] Tanaka, K., Kageyama, K., and Hojo, M. Prestandardization study on mode II interlaminar fracture toughness test for CFRP in Japan. *Compos.*, 26: 257-267, 1995.

[106] Ting, T.C.T. Anisotropic Elasticity: Theory and Applications. Oxford University Press, New York, 1996.

[107] Vision Assistant, Version 8.0. National Instruments Corporation, Austin, TX, 2005.

[108] Wang, C.H. Fracture of interface cracks under combined loading. *Eng. Fract. Mech.*, 56: 77-86, 1997.

[109] Wang, S.S., and Yau, J.F., Interfacial cracks in adhesively bonded scarf joints. *AIAA. J.*, 19: 1350-1356, 1981.

[110] Weideman, M.H., Loos, A.C., Dexter, H.B., and Hasko, G.H. An infiltration/cure model for manufacture of fabric composites by the resin infusion process. NASA Contractor Report VPI-E-92-05 CCMS-92-05, 1992.

[111] White, S.R., and Hahn, H.T., Process modeling of composite materials: residual stress development during cure. Part II. Experimental validation. *J. Compos. Mater.*, 26: 2423-2453, 1992.

[112] Whitmore, G.A. Prediction limits for a univariate normal observation. *Am. Stat.*, 40: 141-143, 1986.

[113] Williams, J.G. On the calculation of energy release rates for cracked laminates. *Int. J. Fract.*, 36: 101-119, 1988.

[114] Williams, M.L. The stresses around a fault or crack in dissimilar media. *B. Seismol. Soc. Am.*, 49: 199-204, 1959.

[115] Yen, S.-C., Craddock, J.N., and Teh, K.T. Evaluation of a modified Arcan fixture for the in-plane shear test of materials. *Exp. Tech.*, 12: 22-25, 1988.

Appendix A

Lekhnitskii Formalism

In this appendix a brief summary of the Lekhnitskii (1950) formalism is given based on the presentation of Ting (1996). Lekhnitskii (1950) developed the expressions for the stress and displacement fields within an anisotropic elastic material, under the assumption that the three-dimensional stress field depends solely on the two in-plane coordinates, say x_1 and x_2, of the media, meaning

$$\sigma_{ij} = \sigma_{ij}(x_1, x_2). \tag{A-1}$$

Hence, the equilibrium equations may be written in a reduced form as

$$\sigma_{i1,1} + \sigma_{i2,2} = 0, \tag{A-2}$$

where $i = 1, 2, 3$. eq. (A-1) allows description of the stress components by means of two Airy potential functions, ψ and χ, resulting in

$$\begin{gathered} \sigma_{11} = \chi_{,22}, \qquad \sigma_{22} = \chi_{,11}, \qquad \sigma_{12} = -\chi_{,12}, \\ \sigma_{32} = -\psi_{,1}, \qquad \sigma_{31} = \psi_{,2}, \end{gathered} \tag{A-3}$$

so that the stress components remain independent of x_3. The strain components ε_{ij} must also be independent of x_3, resulting in the strain-displacement relations

$$\begin{aligned} &\varepsilon_{11} = u_{1,1}, && \varepsilon_{22} = u_{2,2}, && \varepsilon_{33} = Ax_1 + Bx_2 + C, \\ &2\varepsilon_{23} = u_{3,2} + \omega x_1, && 2\varepsilon_{13} = u_{3,1} - \omega x_2, && 2\varepsilon_{12} = u_{1,2} + u_{1,2}. \end{aligned} \tag{A-4}$$

The displacements u_i, are independent of x_3, ω is an arbitrary constant associated with torsion about the x_3-axis and the arbitrary constants A, B, and C are associated with bending about the line $Ax_1 + Bx_2 + C = 0$. The non-zero compatibility conditions are given by

$$\varepsilon_{13,2} - \varepsilon_{23,1} = -\omega, \qquad \varepsilon_{11,22} + \varepsilon_{22,11} - 2\varepsilon_{12,12} = 0. \tag{A-5}$$

The constants A, B, C and ω must be set to zero so that the total displacements, derived from eq. (A-4), remain independent of x_3.

Following the contracted notation where $11 \rightarrow 1$, $22 \rightarrow 2$, $33 \rightarrow 3$, $23 \rightarrow 4$, $13 \rightarrow 5$, $12 \rightarrow 6$, the stress-strain relations are given by

$$\varepsilon_\alpha = s_{\alpha\beta}\sigma_\beta. \tag{A-6}$$

Here $\alpha, \beta = 1, \ldots, 6$, $s_{\alpha\beta}$ are the elastic compliance components of the material and ε_α and σ_α are the strain and stress components, respectively, in their contracted form. Elimination of σ_3 from eq. (A-6) leads to the stress-strain relations given as

$$\varepsilon_\alpha = s'_{\alpha\beta}\sigma_\beta + \frac{s_{\alpha 3}}{s_{33}}\varepsilon_3, \tag{A-7}$$

where the reduced elastic compliance components are given by

$$s'_{\alpha\beta} = s_{\alpha\beta} - \frac{s_{\alpha 3}s_{3\beta}}{s_{33}}. \tag{A-8}$$

A simple substitution of the elastic compliance components $s_{\alpha\beta}$ in eq. (A-8) reveals the symmetry of the reduced elastic compliance matrix $\mathbf{s}'$ and that

$$s'_{\alpha 3} = s'_{3\alpha} = 0 \qquad (\alpha = 1, \ldots, 6). \tag{A-9}$$

Hence, omission of the components $s'_{\alpha 3}$ and $s'_{3\alpha}$ leads to a 5×5 reduced compliance matrix, $\mathbf{s}'$.

The stress-strain relations in terms of the two Airy potential functions, ψ and χ, is obtained by substitution of the stress components given in eq. (A-3) into eq. (A-7), resulting in

$$\varepsilon_\alpha = s'_{\alpha 1}\chi_{,22} + s'_{\alpha 2}\chi_{,11} - s'_{\alpha 4}\psi_{,1} + s'_{\alpha 5}\psi_{,2} - s'_{\alpha 6}\chi_{,12} + \frac{s_{\alpha 3}}{s_{33}}\varepsilon_3. \tag{A-10}$$

Satisfaction of the compatibility conditions, given in eq. (A-5) (with $\omega = 0$), in contracted notation and after some mathematical manipulations, as describe by Ting (1996, pp. 121-122), leads to the homogeneous differential equation of sixth order

$$(L_2L_4 - L_3L_3)\chi = 0. \tag{A-11}$$

The operators L_j for $j = 2, 3, 4$ are differential operators of order j, which are given in detail by Ting (1996, pp. 122).

Without loss of generality, χ may be defined as

$$\chi(x_1, x_2) = F(z), \tag{A-12}$$

where

$$z = x_1 + px_2. \tag{A-13}$$

Substitution of eq. (A-12) into eq. (A-11) leads to the sextic equation in p, given by

$$l_2(p)l_4(p) - l_3(p)l_3(p) = 0. \tag{A-14}$$

The equations $l_j(p)$ for $j = 2, 3, 4$ represent polynomials in p of degree j and are given by

$$\begin{aligned} l_2(p) &= s'_{55}p^2 - 2s'_{45}p + s'_{44}, \\ l_3(p) &= s'_{15}p^3 - (s'_{14} + s'_{56})p^2 + (s'_{25} + s'_{46})p - s'_{24}, \\ l_4(p) &= s'_{11}p^4 - 2s'_{16}p^3 + (2s'_{12} + s'_{66})p^2 - 2s'_{26}p + s'_{22}. \end{aligned} \tag{A-15}$$

The six roots p of eq. (A-14) are the eigenvalues of the compatability equations and depend on the elastic constants of the material. They consist of three pairs of complex conjugates in the form of

$$p_{\alpha+3} = \overline{p}_\alpha, \qquad \Im(p_\alpha) > 0, \qquad (\alpha = 1, 2, 3), \tag{A-16}$$

where the overbar designates the complex conjugate of the quantity and $\Im$ designates the imaginary part of the quantity in parentheses.

A representation of a general solution for both, the stress function and the displacement, fields is given in Ting (1996, pp. 128-131). The displacements u_i are expressed with the aid of two auxiliary functions which depend upon the eigenvalues p_β ($\beta = 1, 2$) and the reduced compliance components $s'_{\alpha m}$ for $m = 1, 2, 4, 5, 6$. For $\alpha = 1, 2, 4$, these auxiliary functions take the form

$$\begin{aligned} \xi_\alpha(p_\beta) &= p_\beta^2 s'_{\alpha 1} - p_\beta s'_{\alpha 6} + s'_{\alpha 2} + \lambda_\beta(p_\beta s'_{\alpha 5} - s'_{\alpha 4}), \\ \eta_\alpha(p_3) &= \lambda_3(p_3^2 s'_{\alpha 1} - p_3 s'_{\alpha 6} + s'_{\alpha 2}) + (p_3 s'_{\alpha 5} - s'_{\alpha 4}), \end{aligned} \tag{A-17}$$

where

$$\begin{aligned} \lambda_\alpha &= -\frac{l_3(p_\alpha)}{l_2(p_\alpha)} = -\frac{l_4(p_\alpha)}{l_3(p_\alpha)}, \qquad \text{for } \alpha = 1, 2, \\ \lambda_3 &= -\frac{l_2(p_3)}{l_3(p_3)} = -\frac{l_3(p_3)}{l_4(p_3)}, \end{aligned} \tag{A-18}$$

and $l_j(p)$ for $j = 2, 3, 4$ are as defined in eqs. (A-15).

Appendix B

Stroh Formalism

In this appendix, a brief summary of the Stroh (1958) formalism is given based on the presentation of Ting (1996). Stroh (1958) developed the expressions for the stress and displacement fields within an anisotropic elastic material, under the assumption that the three-dimensional displacement field depends solely on the two in-plane coordinates, say x_1 and x_2, of the media, meaning

$$u_i = u_i(x_1, x_2) \qquad \text{for } i = 1, 2, 3. \tag{B-1}$$

The strain components are related to the displacement components by

$$\varepsilon_{ij} = \frac{1}{2}(u_{i,j} + u_{j,i}) \qquad \text{for } i, j = 1, 2, 3. \tag{B-2}$$

Hence, the stress-strain relations may be expressed as

$$\sigma_{ij} = C_{ijmn} u_{m,n} \qquad \text{for } i, j, m, n = 1, 2, 3. \tag{B-3}$$

The elastic stiffness components are denoted by C_{ijmn} and based on eq. (B-3) the equations of equilibrium are found as

$$C_{ijmn} u_{m,nj} = 0. \tag{B-4}$$

Without loss of generality, the displacements may be written as

$$u_i = a_i f(z), \tag{B-5}$$

where z is given in eq. (A-13), $f(z)$ is an arbitrary function of z and a_i are unknown complex constants to be determined. Differentiation of the displacement expressions and substitution into the equations of equilibrium (eq. (B-4)) result in

$$\left\{ \mathbf{Q} + p(\mathbf{R} + \mathbf{R}^T) + p^2 \mathbf{T} \right\} \mathbf{a} = 0. \tag{B-6}$$

As in the Lekhnitskii (1950) formalism, p represents the eigenvalues of the equations of compatibility, and the 3×3 matrices $\mathbf{Q}$, $\mathbf{R}$ and $\mathbf{T}$ depend on the elastic stiffness components by

$$Q_{im} = C_{i1m1} \qquad R_{im} = C_{i1m2} \qquad T_{im} = C_{i2m2}. \tag{B-7}$$

The sextic equation for p is obtained by demanding that eq. (B-6) produce a nontrivial solution for $\mathbf{a}$. Hence,

$$|\mathbf{Q} + p(\mathbf{R} + \mathbf{R}^T) + p^2\mathbf{T}| = 0 \tag{B-8}$$

leading to three pairs of complex conjugate values for p in the form of eq. (A-16).

Since the strain components, ε_{ij}, are independent of x_3, the stress components, σ_{ij}, are also independent of x_3. Therefore, the equilibrium equations may be represented in their reduced form, as shown in eq. (A-2). Eq. (A-2) allows definition of an Airy stress function, φ_i, resulting in

$$\sigma_{i1} = -\varphi_{i,2} \qquad \sigma_{i2} = \varphi_{i,1}. \tag{B-9}$$

The stress expressions may also be represented by

$$\sigma_{i1} = -pb_i f'(z) \qquad \sigma_{i2} = b_i f'(z) \qquad \text{for } i = 1, 2, 3. \tag{B-10}$$

Thus, the stress function φ_i is found as

$$\varphi_i = b_i f(z). \tag{B-11}$$

Based on the stress-strain relations, which contains displacement expressions as shown in eq. (B-3), it may be seen that the unknown complex constants b_i are associated with a_i by

$$\mathbf{b} = (\mathbf{R}^T + p\mathbf{T})\mathbf{a} = -\frac{1}{p}(\mathbf{Q} + p\mathbf{R})\mathbf{a}. \tag{B-12}$$

The general solutions for the displacement field and stress function are obtained by superposing the six solutions of each eigenvalue and eigenvector as

$$\begin{aligned} \mathbf{u} &= \sum_{\alpha=1}^{3} \left\{ a_\alpha f_\alpha(z_\alpha) + \overline{a}_\alpha f_{\alpha+3}(\overline{z}_\alpha) \right\}, \\ \boldsymbol{\phi} &= \sum_{\alpha=1}^{3} \left\{ b_\alpha f_\alpha(z_\alpha) + \overline{b}_\alpha f_{\alpha+3}(\overline{z}_\alpha) \right\}. \end{aligned} \tag{B-13}$$

The complex eigenvectors a_α and b_α are known as Stroh eigenvectors and are associated with their conjugates by

$$a_{\alpha+3} = \overline{a}_\alpha \qquad b_{\alpha+3} = \overline{b}_\alpha \qquad \text{for } \alpha = 1, 2, 3. \tag{B-14}$$

The arbitrary functions $f_\alpha(z_\alpha)$ may posses the following form

$$f_\alpha(z_\alpha) = f(z_\alpha)q_\alpha \qquad f_{\alpha+3}(\overline{z}_\alpha) = f(\overline{z}_\alpha)\tilde{q}_\alpha \qquad \text{for } \alpha = 1,2,3, \tag{B-15}$$

where q_α and $\tilde{q}_\alpha$ are arbitrary complex constants and $z_\alpha = x_1 + p_\alpha x_2$, as noted in eq. (A-13). In matrix notation, the Stroh eigenvectors are defined by $\mathbf{A}$ and $\mathbf{B}$, where $\mathbf{A} = [\boldsymbol{a}_1, \boldsymbol{a}_2, \boldsymbol{a}_3]$ and $\mathbf{B} = [\boldsymbol{b}_1, \boldsymbol{b}_2, \boldsymbol{b}_3]$. In this form it may be seen that $\mathbf{A}$ and $\mathbf{B}$ span the space of the displacement and traction vectors, respectively.

Explicitly the general expressions of the Stroh eigenvectors $\mathbf{A}$ and $\mathbf{B}$ are obtained by comparing the Lekhnitskii (1950) formalism to the Stroh (1958) formalism, resulting in the expressions given in Ting (1996, pp. 170-171) as

$$\mathbf{A} = \begin{bmatrix} k_1\xi_1(p_1) & k_2\xi_1(p_2) & k_3\eta_1(p_3) \\ k_1{p_1}^{-1}\xi_2(p_1) & k_2{p_2}^{-1}\xi_2(p_2) & k_3{p_3}^{-1}\eta_2(p_3) \\ k_1{p_1}^{-1}\xi_4(p_1) & k_2{p_2}^{-1}\xi_4(p_2) & k_3{p_3}^{-1}\eta_4(p_3) \end{bmatrix}, \tag{B-16}$$

$$\mathbf{B} = \begin{bmatrix} -k_1p_1 & -k_2p_2 & -k_3p_3\lambda_3 \\ k_1 & k_2 & k_3\lambda_3 \\ -k_1\lambda_1 & -k_2\lambda_2 & -k_3 \end{bmatrix} \tag{B-17}$$

and

$$\mathbf{B}^{-1} = \frac{1}{\Delta}\begin{bmatrix} -k_1^{-1}(1-\lambda_2\lambda_3) & -k_1^{-1}(p_2-\lambda_2\lambda_3p_3) & -k_1^{-1}\lambda_3(p_2-p_3) \\ k_2^{-1}(1-\lambda_1\lambda_3) & k_2^{-1}(p_1-\lambda_1\lambda_3p_3) & k_2^{-1}\lambda_3(p_1-p_3) \\ k_3^{-1}(\lambda_1-\lambda_2) & k_3^{-1}(\lambda_1p_2-\lambda_2p_1) & -k_3^{-1}(p_1-p_2) \end{bmatrix}, \tag{B-18}$$

where

$$\Delta = (p_1-p_2) + \lambda_3\{(\lambda_1p_2-\lambda_2p_1) - p_3(\lambda_1-\lambda_2)\}. \tag{B-19}$$

The auxiliary functions $\xi_\alpha(p_\beta)$ and $\eta_\alpha(p_3)$, for $\alpha = 1,2,4$ and $\beta = 1,2$, and the ratios λ_α, for $\alpha = 1,2,3$, are defined in eqs. (A-17) and (A-18), respectively. The normalization factors k_j for $j = 1,2,3$ have to satisfy relations given by Ting (1996, p. 171). A simple matrix multiplication reveals their absence from the resultant of $\mathbf{AB}^{-1}$. In addition, they are not needed to obtain the stress and displacement fields.

Appendix C

Determination of mode mixity for the ACP specimen

In this appendix, the asymmetric cut-ply (ACP) specimen, shown schematically in Fig. 1.13, mode mixity determination is extended for general cases, where the same flexural modulus of laminate and sublaminates is not assumed. Also, some expressions from the analytic characterization, which was developed by Charalambous et al. (2015a) for the investigated ACP specimen and an adjusted four-point bend (FPB) test fixture, are briefly described.

Referring to Williams (1988) and Charalambous et al. (2015a), the ACP specimen may be treated as an Euler-Bernoulli beam. Next to the delamination tip, the change of the elastic potential energy ΔU is equal to the difference between the external work performed by the applied moment and the strain energy (see Williams, 1988). Hence, this change caused by an incremental delamination extension Δa may be obtained to be

$$\Delta U = \frac{M^2}{2(EI)_{Tot}} \left[\frac{(EI)_{Tot}}{(EI)_{Low}} - 1 \right] \Delta a, \tag{C-1}$$

where the bending stiffness of the non-delaminated composite laminate and the lower sublaminate are denoted by $(EI)_{Tot}$ and $(EI)_{Low}$, respectively, and the overall bending moment is denoted by M. It should be noted that the second term in Eq. (C-1) represents the external work of the applied bending moment; since no moment is applied on the upper sublaminate, the change in the strain energy is related only to the lower sublaminate (see Fig. 1.16a).

The expression EI refers to the equivalent bending stiffness, which depends upon the flexural modulus and the second moment of area I_{zz} of all plies within the laminate segment being analyzed. A schematic view of the equivalent cross-section of sublaminate i is shown in Fig. 1.17, in which a local coordinate system is located at the equivalent

cross-section centroid; B and h_i represent the width and the height of sublaminate i, respectively. Thus, the expression for the total energy release rate may be written as

$$\mathcal{G} = \lim_{\Delta a \to 0} \frac{1}{B}\frac{\Delta U}{\Delta a} = \frac{M^2}{2B(EI)_{Tot}}\left[\frac{(EI)_{Tot}}{(EI)_{Low}} - 1\right]. \tag{C-2}$$

Referring to Fig. 1.16b, pure mode I is obtained when M_I is applied to both sublaminates in opposite directions; whereas, pure mode II in Fig. 1.16c is obtained when the curvature of both sublaminates is the same. An identical sublaminate curvature in the vicinity of the delamination tip may be written as

$$\frac{\psi M_{II}}{(EI)_{Up}} = \frac{M_{II}}{(EI)_{Low}}, \tag{C-3}$$

so that

$$\psi = \frac{(EI)_{Up}}{(EI)_{Low}}, \tag{C-4}$$

where $(EI)_{Up}$ is the bending stiffness of the upper sublaminate. Since moment equilibrium in Fig. 1.16 must be fulfilled, one obtains

$$\begin{aligned} M_I &= \frac{\psi M}{(1+\psi)}, \\ M_{II} &= \frac{M}{(1+\psi)}. \end{aligned} \tag{C-5}$$

Referring to Williams (1988), the components of the total energy release rate associated with each delamination deformation mode may be written as

$$\begin{aligned} \mathcal{G}_I &= \frac{{M_I}^2}{2B(EI)_{Tot}}\left[\frac{(EI)_{Tot}}{(EI)_{Low}} + \frac{(EI)_{Tot}}{(EI)_{Up}}\right], \\ \mathcal{G}_{II} &= \frac{(1+\psi)^2{M_{II}}^2}{2B(EI)_{Tot}}\left[\frac{(EI)_{Tot}}{(1+\psi)^2(EI)_{Low}} + \frac{\psi^2(EI)_{Tot}}{(1+\psi)^2(EI)_{Up}} - 1\right]. \end{aligned} \tag{C-6}$$

By substituting Eq. (C-5) into Eq. (C-6), it may be obtained that the components of the total energy release rate associated with each delamination deformation mode written as a function of the overall applied bending moment M may be given as

$$\begin{aligned} \mathcal{G}_I &= \frac{\psi^2 M^2}{2B(1+\psi)^2(EI)_{Tot}}\left[\frac{(EI)_{Tot}}{(EI)_{Low}} + \frac{(EI)_{Tot}}{(EI)_{Up}}\right], \\ \mathcal{G}_{II} &= \frac{M^2}{2B(1+\psi)^2(EI)_{Tot}}\left[\frac{(EI)_{Tot}}{(EI)_{Low}} + \frac{\psi^2(EI)_{Tot}}{(EI)_{Up}} - (1+\psi)^2\right]. \end{aligned} \tag{C-7}$$

Thus, the general expression for the ACP specimen mode-mixture may be written as

$$\phi = \frac{\mathcal{G}_{II}}{\mathcal{G}} = \frac{1}{(1+\psi)}\left[\frac{(EI)_{Tot} - (1+\psi)(EI)_{Low}}{(EI)_{Tot} + (EI)_{Low}}\right]. \tag{C-8}$$

In cases where specimen composite strip lay-up consists plies of identical properties (same thickness, material properties and orientation), the ACP specimen mode-mixture may be expressed solely by means of χ, as presented in the work of Charalambous et al. (2015a), where

$$\phi\big|_{identical\ plies\ lay-up} = \frac{\mathcal{G}_{II}}{\mathcal{G}} = \frac{3(1-\chi)^4}{(1-3\chi+3\chi^2)(3-3\chi+\chi^2)}, \tag{C-9}$$

and χ is described in Table 1.3.

The expression for the overall bending moment, which is based upon the kinematic analysis of the ACP specimen end-tab large rotation performed by Charalambous et al. (2015a), is given by

$$M = \frac{P}{2\cos^2\beta}\left[(D+t_T)\sin\beta - d_x - \mu\, t_T\cos\beta\right]. \tag{C-10}$$

The expressions for the applied forces Q and one of the formed moment arms d_e, which were also obtained from the kinematic analysis of the ACP specimen end-tab large rotation performed by Charalambous et al. (2015a), are given respectively by

$$\begin{aligned} Q &= P/(2\cos\beta), \\ d_e &= (D+t_T)\tan\beta - d_x/\cos\beta, \end{aligned} \tag{C-11}$$

where the relationship between the ACP specimen rigid rotation angle β and the testing machine cross-head displacement c, as was found by Charalambous et al. (2015a), may be written as

$$\beta = \begin{cases} 2\arctan\left(\dfrac{d_x - \sqrt{{d_x}^2 - c\left[2(D+t_T)-c\right]}}{2(D+t_T)-c}\right), & c < 2(D+t_T) \\ 2\arctan\left(\dfrac{c}{2d_x}\right), & c = 2(D+t_T) \\ 2\arctan\left(\dfrac{-d_x + \sqrt{{d_x}^2 + c\left[c-2(D+t_T)\right]}}{c-2(D+t_T)}\right), & c > 2(D+t_T) \end{cases}; \tag{C-12}$$

all relevant parameters are described in Table 1.3.

Employing the same approach considered in the work of Charalambous et al. (2015a), the local curvature of the deformed ACP specimen (see Fig. 1.15b) with respect to the curvilinear abscissa may be written as

$$\frac{\mathrm{d}\theta}{\mathrm{d}s} = \frac{M}{(EI)(s)}, \tag{C-13}$$

where the local bending stiffness is given by

$$(EI)(s) = \begin{cases} (EI)_{Low}\ , & 0 \le s \le a \\ (EI)_{Tot}\ , & a < s \le L \end{cases}. \tag{C-14}$$

Integration of Eq. (C-13), while accounting for symmetry conditions at $s = 0$ and assuming delamination is extended prior specimen axial elongation occurs, leads to the following expressions for the two specimen angles, which are shown in Fig. 1.15b

$$\begin{aligned} \theta^* &= a\frac{M}{(EI)_{Low}}, \\ \beta &= \frac{M}{(EI)_{Tot}}\left\{L + a\left[\frac{(EI)_{Tot}}{(EI)_{Low}} - 1\right]\right\}. \end{aligned} \tag{C-15}$$

The delamination length may be extracted from Eq. (C-15)$_2$, resulting in

$$a = \frac{1}{\bar{k}}\left[\beta\frac{(EI)_{Tot}}{M} - L\right], \tag{C-16}$$

where

$$\bar{k} = \frac{(EI)_{Tot}}{(EI)_{Low}} - 1, \tag{C-17}$$

and the overall bending moment M and the rotation angle β may be evaluate from Eqs. (C-10) and (C-12), respectively.

The fatigue delamination growth rate may be obtained by differentiating Eq. (C-16) with respect to the number of loading cycles N, resulting in

$$\frac{da}{dN} = \frac{\partial a}{\partial M}\frac{\partial M}{\partial N} = -\frac{\beta}{\bar{k}}\frac{(EI)_{Tot}}{M^2}\frac{dM(a)}{dN}. \tag{C-18}$$

In Eq. (C-16), the maximum cyclic bending moment $M(a)$ is a variable, whereas other parameters are constant under displacement control fatigue loading conditions.

A stability analysis of delamination propagation was performed in the work of Charalambous et al. (2015a). It was concluded that when a quasi-static test is carried out in displacement control regime, the obtained delamination propagation is always stable. Also, it was shown that a change in angle β is independent of delamination extension (change in delamination length a). Thus, the applied bending moment in Eq. (C-16) may be also written as

$$M = \beta\left[\frac{(EI)_{Tot}}{a\bar{k} + L}\right]. \tag{C-19}$$

It should be noted that the delamination propagation in displacement control regime is always stable, since

$$\frac{dM}{da} = -\bar{k}\beta\frac{(EI)_{Tot}}{\left(a\bar{k} + L\right)^2} \leq 0. \tag{C-20}$$

Appendix D

Tabulated results of benchmark problems

In order to validate the developed methods for stress intensity factor extraction, using DE (Section 3.1) and the three-dimensional M-integral (Section 3.2), three benchmark problems using the known asymptotic solutions with the stress intensity factors in Table 3.1 were solved by performing numerical analyses. The FE model of a disk with an edge delamination was constructed in ADINA (Bathe, 2011), as described in Section 3.3 and as shown in Fig. 3.3. For each benchmark problem, the corresponding stress intensity factors, as detailed in Table 3.1, were substituted into the first term of the asymptotic displacement field (eqs. (2.64) and (2.65)) in order to evaluate the displacement vector at each nodal point on the outer surfaces of the FE model. The delamination faces were kept traction free. Then, the FE model was analyzed to obtain a displacement field throughout the model. For each benchmark problem, the expected results are the same as the applied stress intensity factors (Table 3.1). The DE evaluated stress intensity factors were found to be very accurate, which is typical for benchmark problems.

In this section, the M-integral obtained stress intensity factors are presented in a tabulated form as a function of the normalized coordinate x_3/B (see Fig. 3.1). In calculating the M-integral, the integration is performed within a domain/volume of elements that surrounds the delamination front, as illustrated in Fig. 3.2 where five representative V_k volumes (domains) are shown. The stress intensity factors were calculated by means of the three-dimensional M-integral (described in Section 3.2) for each slice of elements within domains 1 to 4 (one element thick through the model thickness, see Figs. 3.2a to 3.2d) along the delamination front of each FE model. The M-integral results for the first benchmark problem, where the applied stress intensity factors were $K_1 = 1$, $K_2 = 0$ and $K_{III} = 0$, are presented in Tables D.1 through D.3. The results obtained for the second benchmark problem, where the applied stress intensity factors were $K_1 = 0$, $K_2 = 1$ and $K_{III} = 0$, are

presented in Tables D.4 through D.6. In the third benchmark problem, where the applied stress intensity factors were $K_1 = 0$, $K_2 = 0$ and $K_{III} = 1$, the obtained stress intensity factors extracted by means of the M-integral are presented in Tables D.7 through D.9.

Table D.1: Results for K_1 for the first benchmark problem: $K_1 = 1$, $K_2 = 0$, $K_{III} = 0$. The mesh is shown in Fig. 3.3 and the deformed mesh in Fig. 3.4a.

M	domain 1	domain 2	domain 3	domain 4
x_3/B	K_1	K_1	K_1	K_1
0.025	1.02894	1.00354	1.00278	1.00257
0.075	1.00774	1.00179	1.00126	1.00105
0.125	1.01297	1.00184	1.00125	1.00105
0.175	1.01147	1.00173	1.00115	1.00094
0.225	1.01183	1.00172	1.00113	1.00093
0.275	1.01171	1.00169	1.00111	1.00091
0.325	1.01172	1.00169	1.00111	1.00090
0.375	1.01171	1.00168	1.00110	1.00089
0.425	1.01171	1.00168	1.00110	1.00089
0.475	1.01171	1.00168	1.00110	1.00089
0.525	1.01171	1.00168	1.00110	1.00089
0.575	1.01171	1.00168	1.00110	1.00089
0.625	1.01171	1.00168	1.00110	1.00089
0.675	1.01172	1.00169	1.00111	1.00090
0.725	1.01171	1.00169	1.00111	1.00091
0.775	1.01183	1.00172	1.00113	1.00093
0.825	1.01147	1.00173	1.00115	1.00094
0.875	1.01297	1.00184	1.00125	1.00105
0.925	1.00774	1.00179	1.00126	1.00105
0.975	1.02894	1.00354	1.00278	1.00257

Table D.2: Results for K_2 for the first benchmark problem: $K_1 = 1$, $K_2 = 0$, $K_{III} = 0$. The mesh is shown in Fig. 3.3 and the deformed mesh in Fig. 3.4a.

M	domain 1	domain 2	domain 3	domain 4
x_3/B	K_2	K_2	K_2	K_2
0.025	-0.001993	0.000401	-0.000362	-0.000473
0.075	-0.000980	0.000935	0.000122	-0.000005
0.125	-0.001064	0.000919	0.000106	-0.000018
0.175	-0.001022	0.000938	0.000125	0.000001
0.225	-0.001025	0.000939	0.000126	0.000002
0.275	-0.001025	0.000939	0.000126	0.000002
0.325	-0.001025	0.000939	0.000126	0.000002
0.375	-0.001025	0.000939	0.000126	0.000002
0.425	-0.001025	0.000939	0.000126	0.000002
0.475	-0.001025	0.000939	0.000126	0.000002
0.525	-0.001025	0.000939	0.000126	0.000002
0.575	-0.001025	0.000939	0.000126	0.000002
0.625	-0.001025	0.000939	0.000126	0.000002
0.675	-0.001025	0.000939	0.000126	0.000002
0.725	-0.001025	0.000939	0.000126	0.000002
0.775	-0.001025	0.000939	0.000126	0.000002
0.825	-0.001022	0.000938	0.000125	0.000001
0.875	-0.001064	0.000919	0.000106	-0.000018
0.925	-0.000980	0.000935	0.000122	-0.000005
0.975	-0.001993	0.000401	-0.000362	-0.000473

Table D.3: Results for K_{III} for the first benchmark problem: $K_1 = 1$, $K_2 = 0$, $K_{III} = 0$. The mesh is shown in Fig. 3.3 and the deformed mesh in Fig. 3.4a.

M	domain 1	domain 2	domain 3	domain 4
x_3/B	K_{III}	K_{III}	K_{III}	K_{III}
0.025	0.000689	0.001537	0.001498	0.001494
0.075	0.000154	0.000123	0.000122	0.000121
0.125	0.000003	0.000028	0.000026	0.000026
0.175	0.000000	-0.000004	-0.000003	-0.000003
0.225	-0.000002	-0.000000	-0.000001	-0.000001
0.275	-0.000002	-0.000002	-0.000002	-0.000002
0.325	-0.000001	-0.000001	-0.000001	-0.000001
0.375	-0.000000	-0.000001	-0.000001	-0.000001
0.425	-0.000000	-0.000000	-0.000000	-0.000000
0.475	-0.000000	-0.000000	-0.000000	-0.000000
0.525	0.000000	0.000000	0.000000	0.000000
0.575	0.000000	0.000000	0.000000	0.000000
0.625	0.000000	0.000001	0.000001	0.000001
0.675	0.000001	0.000001	0.000001	0.000001
0.725	0.000002	0.000002	0.000002	0.000002
0.775	0.000002	0.000000	0.000001	0.000001
0.825	-0.000000	0.000004	0.000003	0.000003
0.875	-0.000003	-0.000028	-0.000026	-0.000026
0.925	-0.000154	-0.000123	-0.000122	-0.000121
0.975	-0.000689	-0.001537	-0.001498	-0.001494

Table D.4: Results for K_1 for the second benchmark problem: $K_1 = 0$, $K_2 = 1$, $K_{III} = 0$. The mesh is shown in Fig. 3.3 and the deformed mesh in Fig. 3.4b.

M	domain 1	domain 2	domain 3	domain 4
x_3/B	K_1	K_1	K_1	K_1
0.025	0.007307	-0.000698	-0.000138	-0.000086
0.075	0.010703	-0.000569	-0.000017	0.000049
0.125	0.009804	-0.000585	-0.000028	0.000034
0.175	0.010052	-0.000585	-0.000029	0.000034
0.225	0.009980	-0.000587	-0.000031	0.000032
0.275	0.009999	-0.000588	-0.000031	0.000032
0.325	0.009993	-0.000588	-0.000032	0.000031
0.375	0.009994	-0.000588	-0.000032	0.000031
0.425	0.009993	-0.000588	-0.000032	0.000031
0.475	0.009993	-0.000589	-0.000032	0.000031
0.525	0.009993	-0.000589	-0.000032	0.000031
0.575	0.009993	-0.000588	-0.000032	0.000031
0.625	0.009994	-0.000588	-0.000032	0.000031
0.675	0.009993	-0.000588	-0.000032	0.000031
0.725	0.009999	-0.000588	-0.000031	0.000032
0.775	0.009980	-0.000587	-0.000031	0.000032
0.825	0.010052	-0.000585	-0.000029	0.000034
0.875	0.009804	-0.000585	-0.000028	0.000034
0.925	0.010703	-0.000569	-0.000017	0.000049
0.975	0.007307	-0.000698	-0.000138	-0.000086

Table D.5: Results for K_2 for the second benchmark problem: $K_1 = 0$, $K_2 = 1$, $K_{III} = 0$. The mesh is shown in Fig. 3.3 and the deformed mesh in Fig. 3.4b.

M	domain 1	domain 2	domain 3	domain 4
x_3/B	K_2	K_2	K_2	K_2
0.025	0.78967	0.99962	1.00351	1.00521
0.075	0.79012	0.99398	0.99893	1.00076
0.125	0.78906	0.99427	0.99892	1.00072
0.175	0.78908	0.99392	0.99865	1.00046
0.225	0.78900	0.99391	0.99861	1.00042
0.275	0.78897	0.99385	0.99856	1.00036
0.325	0.78895	0.99383	0.99853	1.00034
0.375	0.78893	0.99381	0.99852	1.00032
0.425	0.78892	0.99380	0.99851	1.00031
0.475	0.78892	0.99379	0.99850	1.00031
0.525	0.78892	0.99379	0.99850	1.00031
0.575	0.78892	0.99380	0.99851	1.00031
0.625	0.78893	0.99381	0.99852	1.00032
0.675	0.78895	0.99383	0.99853	1.00034
0.725	0.78897	0.99385	0.99856	1.00036
0.775	0.78900	0.99391	0.99861	1.00042
0.825	0.78908	0.99392	0.99865	1.00046
0.875	0.78906	0.99427	0.99892	1.00072
0.925	0.79012	0.99398	0.99893	1.00076
0.975	0.78967	0.99962	1.00351	1.00521

Table D.6: Results for K_{III} for the second benchmark problem: $K_1 = 0$, $K_2 = 1$, $K_{III} = 0$. The mesh is shown in Fig. 3.3 and the deformed mesh in Fig. 3.4b.

M	domain 1	domain 2	domain 3	domain 4
x_3/B	K_{III}	K_{III}	K_{III}	K_{III}
0.025	-0.005274	-0.008170	-0.008122	-0.008121
0.075	0.000337	0.000920	0.000936	0.000935
0.125	-0.000266	-0.000496	-0.000496	-0.000496
0.175	-0.000042	0.000019	0.000019	0.000019
0.225	-0.000057	-0.000078	-0.000078	-0.000078
0.275	-0.000037	-0.000033	-0.000033	-0.000033
0.325	-0.000028	-0.000030	-0.000030	-0.000030
0.375	-0.000019	-0.000019	-0.000019	-0.000019
0.425	-0.000011	-0.000012	-0.000012	-0.000012
0.475	-0.000004	-0.000004	-0.000004	-0.000004
0.525	0.000004	0.000004	0.000004	0.000004
0.575	0.000011	0.000012	0.000012	0.000012
0.625	0.000019	0.000019	0.000019	0.000019
0.675	0.000028	0.000030	0.000030	0.000030
0.725	0.000037	0.000033	0.000033	0.000033
0.775	0.000057	0.000078	0.000078	0.000078
0.825	0.000042	-0.000019	-0.000019	-0.000019
0.875	0.000266	0.000496	0.000496	0.000496
0.925	-0.000337	-0.000920	-0.000936	-0.000935
0.975	0.005274	0.008170	0.008122	0.008121

Table D.7: Results for K_1 for the third benchmark problem: $K_1 = 0$, $K_2 = 0$, $K_{III} = 1$. The mesh is shown in Fig. 3.3 and the deformed mesh in Fig. 3.4c.

M	domain 1	domain 2	domain 3	domain 4
x_3/B	K_1	K_1	K_1	K_1
0.025	-0.000276	0.000112	0.000085	0.000083
0.075	0.000049	0.000035	0.000040	0.000040
0.125	0.000021	0.000018	0.000016	0.000016
0.175	-0.000003	0.000000	0.000000	0.000000
0.225	0.000005	0.000004	0.000004	0.000004
0.275	0.000005	0.000001	0.000001	0.000001
0.325	0.000001	0.000001	0.000001	0.000001
0.375	0.000000	0.000000	0.000000	0.000000
0.425	0.000000	0.000000	0.000000	0.000000
0.475	0.000000	0.000000	0.000000	0.000000
0.525	-0.000000	-0.000000	-0.000000	-0.000000
0.575	-0.000000	-0.000000	-0.000000	-0.000000
0.625	-0.000000	-0.000000	-0.000000	-0.000000
0.675	-0.000001	-0.000001	-0.000001	-0.000001
0.725	-0.000005	-0.000001	-0.000001	-0.000001
0.775	-0.000005	-0.000004	-0.000004	-0.000004
0.825	0.000003	-0.000000	-0.000000	-0.000000
0.875	-0.000021	-0.000018	-0.000016	-0.000016
0.925	-0.000049	-0.000035	-0.000040	-0.000040
0.975	0.000276	-0.000112	-0.000085	-0.000083

Table D.8: Results for K_2 for the third benchmark problem: $K_1 = 0$, $K_2 = 0$, $K_{III} = 1$. The mesh is shown in Fig. 3.3 and the deformed mesh in Fig. 3.4c.

M	domain 1	domain 2	domain 3	domain 4
x_3/B	K_2	K_2	K_2	K_2
0.025	-0.002600	-0.004050	-0.004067	-0.004076
0.075	0.000465	0.000496	0.000526	0.000533
0.125	-0.000211	-0.000181	-0.000189	-0.000193
0.175	0.000053	0.000028	0.000030	0.000031
0.225	-0.000025	-0.000018	-0.000018	-0.000019
0.275	0.000001	-0.000003	-0.000003	-0.000003
0.325	-0.000005	-0.000004	-0.000004	-0.000005
0.375	-0.000001	-0.000002	-0.000002	-0.000002
0.425	-0.000001	-0.000001	-0.000001	-0.000001
0.475	-0.000000	-0.000000	-0.000000	-0.000000
0.525	0.000000	0.000000	0.000000	0.000000
0.575	0.000001	0.000001	0.000001	0.000001
0.625	0.000001	0.000002	0.000002	0.000002
0.675	0.000005	0.000004	0.000004	0.000005
0.725	-0.000001	0.000003	0.000003	0.000003
0.775	0.000025	0.000018	0.000018	0.000019
0.825	-0.000053	-0.000028	-0.000030	-0.000031
0.875	0.000211	0.000181	0.000189	0.000193
0.925	-0.000465	-0.000496	-0.000526	-0.000533
0.975	0.002600	0.004050	0.004067	0.004076

Table D.9: Results for K_{III} for the third benchmark problem: $K_1 = 0$, $K_2 = 0$, $K_{III} = 1$. The mesh is shown in Fig. 3.3 and the deformed mesh in Fig. 3.4c.

M	domain 1	domain 2	domain 3	domain 4
x_3/B	K_{III}	K_{III}	K_{III}	K_{III}
0.025	0.96960	1.00157	1.00212	1.00225
0.075	0.96217	1.00027	1.00096	1.00111
0.125	0.96276	0.99954	1.00015	1.00031
0.175	0.96242	0.99948	1.00011	1.00027
0.225	0.96240	0.99939	1.00002	1.00018
0.275	0.96236	0.99937	1.00000	1.00015
0.325	0.96234	0.99934	0.99997	1.00013
0.375	0.96233	0.99933	0.99996	1.00012
0.425	0.96232	0.99932	0.99995	1.00011
0.475	0.96232	0.99932	0.99995	1.00010
0.525	0.96232	0.99932	0.99995	1.00010
0.575	0.96232	0.99932	0.99995	1.00011
0.625	0.96233	0.99933	0.99996	1.00012
0.675	0.96234	0.99934	0.99997	1.00013
0.725	0.96236	0.99937	1.00000	1.00015
0.775	0.96240	0.99939	1.00002	1.00018
0.825	0.96242	0.99948	1.00011	1.00027
0.875	0.96276	0.99954	1.00015	1.00031
0.925	0.96217	1.00027	1.00096	1.00111
0.975	0.96960	1.00157	1.00212	1.00225

Appendix E

Tabulated results of convergence study

In this section, the stress intensity factors obtained by means of the M-integral (Section 3.2) and the DE method (Section 3.1) are presented in a tabulated form as a function of the normalized coordinate x_3/B (see Fig. 3.1). The M-integral results for the finest mesh, in which one of the delamination tips is shown in Fig. 4.8c, are presented in Table E.1. The stress intensity factors obtained by the DE method are also presented for validation reasons. It may be seen that the stress intensity factors obtained by the DE method are related to the normalized location of the common edge of adjacent elements along the delamination front, whereas the M-integral results are related to normalized location of the mid-point of the element thickness or slice of elements (one element thick) in which the integration is performed.

Table E.1: Obtained stress intensity factors calculated by means of the M-integral and the DE method for the finest mesh shown in Fig. 4.8c.

M-integral				DE			
x_3/B	K_1	K_2	K_{III}	x_3/B	K_1	K_2	K_{III}
	$\mathrm{Pa}\sqrt{\mathrm{m}}\cdot\mathrm{m}^{-i\varepsilon}\times 10^6$		$\mathrm{Pa}\sqrt{\mathrm{m}}\times 10^6$		$\mathrm{Pa}\sqrt{\mathrm{m}}\cdot\mathrm{m}^{-i\varepsilon}\times 10^6$		$\mathrm{Pa}\sqrt{\mathrm{m}}\times 10^6$
0.025	1.153	2.282	1.184	0.00	1.548	3.047	2.064
0.075	1.001	2.180	0.673	0.05	1.032	2.443	0.934
0.125	0.979	2.191	0.457	0.10	0.988	2.174	0.550
0.175	0.967	2.203	0.334	0.15	0.974	2.194	0.395
0.225	0.956	2.210	0.251	0.20	0.974	2.280	0.317
0.275	0.946	2.215	0.189	0.25	0.965	2.211	0.223
0.325	0.938	2.218	0.138	0.30	0.956	2.207	0.165
0.375	0.932	2.220	0.094	0.35	0.934	2.209	0.116
0.425	0.927	2.221	0.055	0.40	0.929	2.210	0.075
0.475	0.925	2.221	0.018	0.45	0.926	2.211	0.036
0.525	0.925	2.221	-0.018	0.50	0.924	2.211	0.000
0.575	0.927	2.221	-0.055	0.55	0.926	2.211	-0.036
0.625	0.932	2.220	-0.094	0.60	0.929	2.210	-0.075
0.675	0.938	2.218	-0.138	0.65	0.934	2.209	-0.116
0.725	0.946	2.215	-0.189	0.70	0.956	2.207	-0.165
0.775	0.956	2.210	-0.251	0.75	0.965	2.211	-0.223
0.825	0.967	2.203	-0.334	0.80	0.974	2.280	-0.317
0.875	0.979	2.191	-0.457	0.85	0.974	2.194	-0.395
0.925	1.001	2.180	-0.673	0.90	0.988	2.174	-0.550
0.975	1.153	2.282	-1.184	0.95	1.032	2.443	-0.934
				1.00	1.548	3.047	-2.064

Table E.2: Difference between the stress intensity factors calculated for the fifth (reference) and the fourth (checked) domains of integration of the finer mesh shown in Fig. 4.8c.

	difference (%)		
x_3/B	K_1	K_2	K_{III}
0.025	-0.008	-0.028	0.004
0.075	0.005	-0.045	-0.012
0.125	-0.002	-0.036	-0.003
0.175	-0.000	-0.038	-0.006
0.225	-0.001	-0.037	-0.004
0.275	-0.001	-0.037	-0.005
0.325	-0.001	-0.037	-0.005
0.375	-0.001	-0.037	-0.005
0.425	-0.001	-0.037	-0.005
0.475	-0.001	-0.037	-0.005
0.525	-0.001	-0.037	-0.005
0.575	-0.001	-0.037	-0.005
0.625	-0.001	-0.037	-0.005
0.675	-0.001	-0.037	-0.005
0.725	-0.001	-0.037	-0.005
0.775	-0.001	-0.037	-0.004
0.825	-0.000	-0.038	-0.006
0.875	-0.002	-0.036	-0.003
0.925	0.005	-0.045	-0.012
0.975	-0.008	-0.028	0.004

Appendix F

Brazilian disk specimens: additional data

In this section, the calculated data obtained for the BD test specimens is presented. For each BD specimen, the stress intensity factors calculated by means of the M-integral (Section 3.2) are presented in a tabulated form as a function of the normalized coordinate x_3/B (see Fig. 3.1). The M-integral results for the fine mesh, in which one of the delamination tips is shown in Fig. 4.8b, are presented in Tables F.1 to F.15. The normalized in-plane stress intensity factors with $\hat{L} = 100$ μm, as well as the two phase angles $\hat{\psi}$ in eq. (1.12) and ϕ in eq. (1.14) are also presented. Finally, the critical interface energy release rate $\mathcal{G}_{ic}$ in eq. (1.17) is presented. It may be recalled that the M-integral results are related to normalized location of the mid-point of the element thickness or slice of elements (one element thick) in which the integration is performed.

Table F.1: Stress intensity factors calculated along the delamination front by means of the three-dimensional M-integral for the largest domain of the fine mesh, as shown in Fig. 4.8b, used to analyze specimens **sp8.2** and **sp9.1**, separately, as well as their normalized in-plane stress intensity factors with $\hat{L} = 100$ μm, their two phase angles and their critical interface energy release rate.

sp8.2 ; ω=-2.06°								
x_3/B	K_1	K_2	K_{III}	$\hat{K}_1$	$\hat{K}_2$	$\hat{\psi}$	ϕ	$\mathcal{G}_{ic}$
	(MPa$\sqrt{\text{m}} \cdot \text{m}^{-i\varepsilon}$)		(MPa$\sqrt{\text{m}}$)	(MPa$\sqrt{\text{m}}$)		(rad)	(rad)	(N/m)
0.025	1.514	0.838	0.644	1.576	0.715	0.426	0.337	420.3
0.075	1.453	0.779	0.374	1.510	0.661	0.413	0.211	355.1
0.125	1.428	0.788	0.243	1.486	0.672	0.425	0.140	338.8
0.175	1.405	0.796	0.172	1.464	0.682	0.436	0.100	329.1
0.225	1.384	0.802	0.126	1.444	0.689	0.445	0.074	321.5
0.275	1.367	0.805	0.092	1.427	0.694	0.453	0.055	315.4
0.325	1.353	0.807	0.066	1.413	0.697	0.458	0.040	310.6
0.375	1.343	0.808	0.045	1.403	0.699	0.462	0.027	307.1
0.425	1.336	0.809	0.026	1.396	0.700	0.465	0.016	304.9
0.475	1.333	0.809	0.009	1.393	0.701	0.466	0.005	303.8
0.525	1.333	0.809	-0.009	1.393	0.701	0.466	-0.005	303.8
0.575	1.336	0.809	-0.026	1.396	0.700	0.465	-0.016	304.9
0.625	1.343	0.808	-0.045	1.403	0.699	0.462	-0.027	307.1
0.675	1.353	0.807	-0.066	1.413	0.697	0.458	-0.040	310.6
0.725	1.367	0.805	-0.092	1.427	0.694	0.453	-0.055	315.4
0.775	1.384	0.802	-0.126	1.444	0.689	0.445	-0.074	321.5
0.825	1.405	0.796	-0.172	1.464	0.682	0.436	-0.100	329.1
0.875	1.428	0.788	-0.243	1.486	0.672	0.425	-0.140	338.8
0.925	1.453	0.779	-0.374	1.510	0.661	0.413	-0.211	355.1
0.975	1.514	0.838	-0.644	1.576	0.715	0.426	-0.337	420.3

sp9.1 ; ω=-2.23°								
x_3/B	K_1	K_2	K_{III}	$\hat{K}_1$	$\hat{K}_2$	$\hat{\psi}$	ϕ	$\mathcal{G}_{ic}$
	(MPa$\sqrt{\text{m}} \cdot \text{m}^{-i\varepsilon}$)		(MPa$\sqrt{\text{m}}$)	(MPa$\sqrt{\text{m}}$)		(rad)	(rad)	(N/m)
0.025	1.529	0.881	0.680	1.594	0.756	0.443	0.349	440.4
0.075	1.459	0.818	0.396	1.520	0.699	0.431	0.220	367.1
0.125	1.431	0.827	0.260	1.492	0.710	0.444	0.147	348.6
0.175	1.406	0.835	0.185	1.468	0.721	0.456	0.106	337.9
0.225	1.384	0.841	0.136	1.446	0.728	0.467	0.079	329.6
0.275	1.365	0.845	0.101	1.428	0.733	0.474	0.059	323.0
0.325	1.351	0.847	0.073	1.414	0.736	0.480	0.043	318.0
0.375	1.340	0.848	0.049	1.403	0.739	0.485	0.029	314.3
0.425	1.333	0.849	0.029	1.396	0.740	0.487	0.017	312.0
0.475	1.329	0.849	0.009	1.393	0.741	0.489	0.006	310.8
0.525	1.329	0.849	-0.009	1.393	0.741	0.489	-0.006	310.8
0.575	1.333	0.849	-0.029	1.396	0.740	0.487	-0.017	312.0
0.625	1.340	0.848	-0.049	1.403	0.739	0.485	-0.029	314.3
0.675	1.351	0.847	-0.073	1.414	0.736	0.480	-0.043	318.0
0.725	1.365	0.845	-0.101	1.428	0.733	0.474	-0.059	323.0
0.775	1.384	0.841	-0.136	1.446	0.728	0.467	-0.079	329.6
0.825	1.406	0.835	-0.185	1.468	0.721	0.456	-0.106	337.9
0.875	1.431	0.827	-0.260	1.492	0.710	0.444	-0.147	348.6
0.925	1.459	0.818	-0.396	1.520	0.699	0.431	-0.220	367.1
0.975	1.529	0.881	-0.680	1.594	0.756	0.443	-0.349	440.4

Table F.2: Stress intensity factors calculated along the delamination front by means of the three-dimensional M-integral for the largest domain of the fine mesh, as shown in Fig. 4.8b, used to analyze specimens **sp3.1** and **sp1.1**, separately, as well as their normalized in-plane stress intensity factors with $\hat{L} = 100$ μm, their two phase angles and their critical interface energy release rate.

sp3.1 ; ω=-2.23°								
x_3/B	K_1	K_2	K_{III}	$\hat{K}_1$	$\hat{K}_2$	$\hat{\psi}$	ϕ	$\mathcal{G}_{ic}$
	(MPa$\sqrt{\text{m}} \cdot \text{m}^{-i\varepsilon}$)		(MPa$\sqrt{\text{m}}$)	(MPa$\sqrt{\text{m}}$)		(rad)	(rad)	(N/m)
0.025	1.580	1.006	0.719	1.655	0.877	0.487	0.347	495.8
0.075	1.501	0.941	0.411	1.571	0.819	0.480	0.215	410.9
0.125	1.470	0.951	0.265	1.541	0.831	0.495	0.142	390.7
0.175	1.444	0.960	0.186	1.516	0.842	0.507	0.101	379.4
0.225	1.421	0.966	0.136	1.493	0.849	0.517	0.074	370.7
0.275	1.402	0.969	0.099	1.475	0.854	0.525	0.055	363.9
0.325	1.387	0.971	0.071	1.460	0.857	0.531	0.040	358.7
0.375	1.376	0.972	0.048	1.449	0.860	0.535	0.027	354.9
0.425	1.369	0.973	0.028	1.442	0.861	0.538	0.016	352.4
0.475	1.365	0.973	0.009	1.438	0.861	0.540	0.005	351.2
0.525	1.365	0.973	-0.009	1.438	0.861	0.540	-0.005	351.2
0.575	1.369	0.973	-0.028	1.442	0.861	0.538	-0.016	352.4
0.625	1.376	0.972	-0.048	1.449	0.860	0.535	-0.027	354.9
0.675	1.387	0.971	-0.071	1.460	0.857	0.531	-0.040	358.7
0.725	1.402	0.969	-0.099	1.475	0.854	0.525	-0.055	363.9
0.775	1.421	0.966	-0.136	1.493	0.849	0.517	-0.074	370.7
0.825	1.444	0.960	-0.186	1.516	0.842	0.507	-0.101	379.4
0.875	1.470	0.951	-0.265	1.541	0.831	0.495	-0.142	390.7
0.925	1.501	0.941	-0.411	1.571	0.819	0.480	-0.215	410.9
0.975	1.580	1.006	-0.719	1.655	0.877	0.487	-0.347	495.8

sp1.1 ; ω=-2.64°								
x_3/B	K_1	K_2	K_{III}	$\hat{K}_1$	$\hat{K}_2$	$\hat{\psi}$	ϕ	$\mathcal{G}_{ic}$
	(MPa$\sqrt{\text{m}} \cdot \text{m}^{-i\varepsilon}$)		(MPa$\sqrt{\text{m}}$)	(MPa$\sqrt{\text{m}}$)		(rad)	(rad)	(N/m)
0.025	1.567	1.420	0.863	1.675	1.291	0.657	0.368	641.5
0.075	1.463	1.350	0.479	1.565	1.229	0.666	0.223	520.4
0.125	1.429	1.361	0.303	1.533	1.243	0.681	0.144	496.9
0.175	1.403	1.370	0.208	1.507	1.254	0.694	0.100	485.2
0.225	1.379	1.376	0.148	1.484	1.262	0.705	0.072	476.6
0.275	1.360	1.379	0.107	1.465	1.266	0.713	0.052	469.6
0.325	1.344	1.380	0.075	1.450	1.269	0.719	0.037	464.3
0.375	1.333	1.381	0.050	1.438	1.270	0.723	0.025	460.4
0.425	1.325	1.381	0.029	1.431	1.271	0.726	0.014	457.8
0.475	1.322	1.381	0.009	1.427	1.272	0.728	0.005	456.6
0.525	1.322	1.381	-0.009	1.427	1.272	0.728	-0.005	456.6
0.575	1.325	1.381	-0.029	1.431	1.271	0.726	-0.014	457.8
0.625	1.333	1.381	-0.050	1.438	1.270	0.723	-0.025	460.4
0.675	1.344	1.380	-0.075	1.450	1.269	0.719	-0.037	464.3
0.725	1.360	1.379	-0.107	1.465	1.266	0.713	-0.052	469.6
0.775	1.379	1.376	-0.148	1.484	1.262	0.705	-0.072	476.6
0.825	1.403	1.370	-0.208	1.507	1.254	0.694	-0.100	485.2
0.875	1.429	1.361	-0.303	1.533	1.243	0.681	-0.144	496.9
0.925	1.463	1.350	-0.479	1.565	1.229	0.666	-0.223	520.4
0.975	1.567	1.420	-0.863	1.675	1.291	0.657	-0.368	641.5

Table F.3: Stress intensity factors calculated along the delamination front by means of the three-dimensional M-integral for the largest domain of the fine mesh, as shown in Fig. 4.8b, used to analyze specimens **sp14.1** and **sp7.2**, separately, as well as their normalized in-plane stress intensity factors with $\hat{L} = 100$ μm, their two phase angles and their critical interface energy release rate.

sp14.1 ; ω=-2.73°								
x_3/B	K_1	K_2	K_{III}	$\hat{K}_1$	$\hat{K}_2$	$\hat{\psi}$	ϕ	$\mathcal{G}_{ic}$
	(MPa$\sqrt{\text{m}} \cdot \text{m}^{-i\varepsilon}$)		(MPa$\sqrt{\text{m}}$)	(MPa$\sqrt{\text{m}}$)		(rad)	(rad)	(N/m)
0.025	1.521	1.188	0.775	1.611	1.063	0.583	0.362	532.0
0.075	1.436	1.120	0.448	1.521	1.002	0.583	0.228	436.7
0.125	1.409	1.130	0.295	1.495	1.015	0.596	0.153	417.4
0.175	1.387	1.139	0.211	1.473	1.025	0.608	0.110	407.4
0.225	1.367	1.145	0.156	1.454	1.033	0.618	0.082	399.9
0.275	1.350	1.149	0.115	1.437	1.037	0.625	0.061	393.9
0.325	1.337	1.151	0.083	1.424	1.041	0.631	0.045	389.3
0.375	1.327	1.152	0.057	1.414	1.043	0.635	0.030	386.0
0.425	1.320	1.153	0.033	1.408	1.044	0.638	0.018	383.8
0.475	1.317	1.153	0.011	1.404	1.044	0.639	0.006	382.7
0.525	1.317	1.153	-0.011	1.404	1.044	0.639	-0.006	382.7
0.575	1.320	1.153	-0.033	1.408	1.044	0.638	-0.018	383.8
0.625	1.327	1.152	-0.057	1.414	1.043	0.635	-0.030	386.0
0.675	1.337	1.151	-0.083	1.424	1.041	0.631	-0.045	389.3
0.725	1.350	1.149	-0.115	1.437	1.037	0.625	-0.061	393.9
0.775	1.367	1.145	-0.156	1.454	1.033	0.618	-0.082	399.9
0.825	1.387	1.139	-0.211	1.473	1.025	0.608	-0.110	407.4
0.875	1.409	1.130	-0.295	1.495	1.015	0.596	-0.153	417.4
0.925	1.436	1.120	-0.448	1.521	1.002	0.583	-0.228	436.7
0.975	1.521	1.188	-0.775	1.611	1.063	0.583	-0.362	532.0

sp7.2 ; ω=-4.10°								
x_3/B	K_1	K_2	K_{III}	$\hat{K}_1$	$\hat{K}_2$	$\hat{\psi}$	ϕ	$\mathcal{G}_{ic}$
	(MPa$\sqrt{\text{m}} \cdot \text{m}^{-i\varepsilon}$)		(MPa$\sqrt{\text{m}}$)	(MPa$\sqrt{\text{m}}$)		(rad)	(rad)	(N/m)
0.025	1.455	1.630	0.959	1.580	1.509	0.762	0.393	699.0
0.075	1.331	1.549	0.558	1.450	1.438	0.781	0.253	555.5
0.125	1.300	1.559	0.370	1.420	1.451	0.796	0.170	530.1
0.175	1.278	1.570	0.266	1.399	1.463	0.808	0.123	519.8
0.225	1.259	1.577	0.197	1.381	1.472	0.817	0.092	513.0
0.275	1.243	1.581	0.146	1.365	1.477	0.825	0.068	507.7
0.325	1.230	1.583	0.106	1.353	1.480	0.830	0.050	503.6
0.375	1.221	1.585	0.072	1.343	1.483	0.835	0.034	500.6
0.425	1.215	1.586	0.042	1.337	1.484	0.837	0.020	498.6
0.475	1.212	1.586	0.014	1.334	1.485	0.839	0.006	497.7
0.525	1.212	1.586	-0.014	1.334	1.485	0.839	-0.006	497.7
0.575	1.215	1.586	-0.042	1.337	1.484	0.837	-0.020	498.6
0.625	1.221	1.585	-0.072	1.343	1.483	0.835	-0.034	500.6
0.675	1.230	1.583	-0.106	1.353	1.480	0.830	-0.050	503.6
0.725	1.243	1.581	-0.146	1.365	1.477	0.825	-0.068	507.7
0.775	1.259	1.577	-0.197	1.381	1.472	0.817	-0.092	513.0
0.825	1.278	1.570	-0.266	1.399	1.463	0.808	-0.123	519.8
0.875	1.300	1.559	-0.370	1.420	1.451	0.796	-0.170	530.1
0.925	1.331	1.549	-0.558	1.450	1.438	0.781	-0.253	555.5
0.975	1.455	1.630	-0.959	1.580	1.509	0.762	-0.393	699.0

Table F.4: Stress intensity factors calculated along the delamination front by means of the three-dimensional M-integral for the largest domain of the fine mesh, as shown in Fig. 4.8b, used to analyze specimens **sp1.2** and **sp12.1**, separately, as well as their normalized in-plane stress intensity factors with $\hat{L} = 100$ μm, their two phase angles and their critical interface energy release rate.

sp1.2 ; ω=-4.94°								
x_3/B	K_1	K_2	K_{III}	$\hat{K}_1$	$\hat{K}_2$	$\hat{\psi}$	ϕ	$\mathcal{G}_{ic}$
	(MPa$\sqrt{\text{m}} \cdot \text{m}^{-i\varepsilon}$)		(MPa$\sqrt{\text{m}}$)	(MPa$\sqrt{\text{m}}$)		(rad)	(rad)	(N/m)
0.025	1.118	1.637	0.886	1.244	1.542	0.892	0.399	578.0
0.075	1.001	1.567	0.513	1.123	1.482	0.922	0.255	461.1
0.125	0.978	1.577	0.343	1.100	1.494	0.936	0.173	443.2
0.175	0.962	1.586	0.248	1.085	1.505	0.946	0.125	436.8
0.225	0.948	1.592	0.184	1.072	1.512	0.954	0.093	432.7
0.275	0.936	1.595	0.137	1.060	1.516	0.961	0.070	429.5
0.325	0.926	1.597	0.099	1.050	1.519	0.966	0.051	427.1
0.375	0.919	1.599	0.068	1.043	1.520	0.969	0.035	425.3
0.425	0.914	1.599	0.039	1.039	1.521	0.972	0.020	424.1
0.475	0.912	1.600	0.013	1.036	1.522	0.973	0.007	423.5
0.525	0.912	1.600	-0.013	1.036	1.522	0.973	-0.007	423.5
0.575	0.914	1.599	-0.039	1.039	1.521	0.972	-0.020	424.1
0.625	0.919	1.599	-0.068	1.043	1.520	0.969	-0.035	425.3
0.675	0.926	1.597	-0.099	1.050	1.519	0.966	-0.051	427.1
0.725	0.936	1.595	-0.137	1.060	1.516	0.961	-0.070	429.5
0.775	0.948	1.592	-0.184	1.072	1.512	0.954	-0.093	432.7
0.825	0.962	1.586	-0.248	1.085	1.505	0.946	-0.125	436.8
0.875	0.978	1.577	-0.343	1.100	1.494	0.936	-0.173	443.2
0.925	1.001	1.567	-0.513	1.123	1.482	0.922	-0.255	461.1
0.975	1.118	1.637	-0.886	1.244	1.542	0.892	-0.399	578.0

sp12.1 ; ω=-5.27°								
x_3/B	K_1	K_2	K_{III}	$\hat{K}_1$	$\hat{K}_2$	$\hat{\psi}$	ϕ	$\mathcal{G}_{ic}$
	(MPa$\sqrt{\text{m}} \cdot \text{m}^{-i\varepsilon}$)		(MPa$\sqrt{\text{m}}$)	(MPa$\sqrt{\text{m}}$)		(rad)	(rad)	(N/m)
0.025	1.174	2.245	1.133	1.349	2.145	1.009	0.399	944.9
0.075	1.025	2.161	0.653	1.194	2.072	1.048	0.252	762.1
0.125	1.003	2.175	0.436	1.173	2.089	1.059	0.170	738.0
0.175	0.990	2.187	0.315	1.161	2.102	1.066	0.123	731.2
0.225	0.978	2.195	0.234	1.149	2.110	1.072	0.092	727.5
0.275	0.967	2.200	0.174	1.139	2.116	1.077	0.068	724.6
0.325	0.957	2.203	0.126	1.130	2.119	1.081	0.049	722.3
0.375	0.950	2.204	0.085	1.123	2.122	1.084	0.034	720.7
0.425	0.946	2.205	0.049	1.118	2.123	1.086	0.019	719.6
0.475	0.943	2.206	0.016	1.116	2.124	1.087	0.006	719.1
0.525	0.943	2.206	-0.016	1.116	2.124	1.087	-0.006	719.1
0.575	0.946	2.205	-0.049	1.118	2.123	1.086	-0.019	719.6
0.625	0.950	2.204	-0.085	1.123	2.122	1.084	-0.034	720.7
0.675	0.957	2.203	-0.126	1.130	2.119	1.081	-0.049	722.3
0.725	0.967	2.200	-0.174	1.139	2.116	1.077	-0.068	724.6
0.775	0.978	2.195	-0.234	1.149	2.110	1.072	-0.092	727.5
0.825	0.990	2.187	-0.315	1.161	2.102	1.066	-0.123	731.2
0.875	1.003	2.175	-0.436	1.173	2.089	1.059	-0.170	738.0
0.925	1.025	2.161	-0.653	1.194	2.072	1.048	-0.252	762.1
0.975	1.174	2.245	-1.133	1.349	2.145	1.009	-0.399	944.9

Table F.5: Stress intensity factors calculated along the delamination front by means of the three-dimensional M-integral for the largest domain of the fine mesh, as shown in Fig. 4.8b, used to analyze specimens **sp2.1** and **sp11.2**, separately, as well as their normalized in-plane stress intensity factors with $\hat{L} = 100$ μm, their two phase angles and their critical interface energy release rate.

sp2.1 ; ω=-5.86°								
x_3/B	K_1	K_2	K_{III}	$\hat{K}_1$	$\hat{K}_2$	$\hat{\psi}$	ϕ	$\mathcal{G}_{ic}$
	(MPa$\sqrt{\text{m}} \cdot \text{m}^{-i\varepsilon}$)		(MPa$\sqrt{\text{m}}$)	(MPa$\sqrt{\text{m}}$)		(rad)	(rad)	(N/m)
0.025	1.219	2.251	1.180	1.394	2.147	0.995	0.410	973.2
0.075	1.053	2.156	0.691	1.221	2.066	1.037	0.265	772.5
0.125	1.023	2.169	0.470	1.192	2.081	1.050	0.183	742.9
0.175	1.006	2.181	0.345	1.176	2.094	1.059	0.135	733.7
0.225	0.992	2.188	0.260	1.163	2.103	1.066	0.102	728.7
0.275	0.979	2.193	0.196	1.151	2.108	1.071	0.077	725.1
0.325	0.970	2.196	0.143	1.141	2.112	1.075	0.056	722.3
0.375	0.962	2.198	0.098	1.134	2.115	1.079	0.038	720.4
0.425	0.957	2.199	0.057	1.129	2.116	1.081	0.022	719.1
0.475	0.955	2.200	0.019	1.127	2.117	1.082	0.007	718.5
0.525	0.955	2.200	-0.019	1.127	2.117	1.082	-0.007	718.5
0.575	0.957	2.199	-0.057	1.129	2.116	1.081	-0.022	719.1
0.625	0.962	2.198	-0.098	1.134	2.115	1.079	-0.038	720.4
0.675	0.970	2.196	-0.143	1.141	2.112	1.075	-0.056	722.3
0.725	0.979	2.193	-0.196	1.151	2.108	1.071	-0.077	725.1
0.775	0.992	2.188	-0.260	1.163	2.103	1.066	-0.102	728.7
0.825	1.006	2.181	-0.345	1.176	2.094	1.059	-0.135	733.7
0.875	1.023	2.169	-0.470	1.192	2.081	1.050	-0.183	742.9
0.925	1.053	2.156	-0.691	1.221	2.066	1.037	-0.265	772.5
0.975	1.219	2.251	-1.180	1.394	2.147	0.995	-0.410	973.2

sp11.2 ; ω=-5.90°								
x_3/B	K_1	K_2	K_{III}	$\hat{K}_1$	$\hat{K}_2$	$\hat{\psi}$	ϕ	$\mathcal{G}_{ic}$
	(MPa$\sqrt{\text{m}} \cdot \text{m}^{-i\varepsilon}$)		(MPa$\sqrt{\text{m}}$)	(MPa$\sqrt{\text{m}}$)		(rad)	(rad)	(N/m)
0.025	1.156	2.264	1.145	1.333	2.165	1.019	0.402	953.2
0.075	1.002	2.176	0.671	1.172	2.090	1.060	0.258	767.1
0.125	0.979	2.190	0.456	1.150	2.105	1.071	0.178	741.9
0.175	0.967	2.201	0.334	1.139	2.117	1.077	0.130	734.7
0.225	0.956	2.209	0.251	1.129	2.126	1.083	0.098	731.0
0.275	0.946	2.214	0.189	1.119	2.132	1.087	0.074	728.1
0.325	0.938	2.217	0.138	1.111	2.135	1.091	0.054	725.9
0.375	0.932	2.219	0.094	1.105	2.137	1.094	0.037	724.3
0.425	0.927	2.220	0.055	1.101	2.139	1.095	0.021	723.3
0.475	0.925	2.220	0.018	1.099	2.140	1.096	0.007	722.8
0.525	0.925	2.220	-0.018	1.099	2.140	1.096	-0.007	722.8
0.575	0.927	2.220	-0.055	1.101	2.139	1.095	-0.021	723.3
0.625	0.932	2.219	-0.094	1.105	2.137	1.094	-0.037	724.3
0.675	0.938	2.217	-0.138	1.111	2.135	1.091	-0.054	725.9
0.725	0.946	2.214	-0.189	1.119	2.132	1.087	-0.074	728.1
0.775	0.956	2.209	-0.251	1.129	2.126	1.083	-0.098	731.0
0.825	0.967	2.201	-0.334	1.139	2.117	1.077	-0.130	734.7
0.875	0.979	2.190	-0.456	1.150	2.105	1.071	-0.178	741.9
0.925	1.002	2.176	-0.671	1.172	2.090	1.060	-0.258	767.1
0.975	1.156	2.264	-1.145	1.332	2.165	1.019	-0.402	953.1

Table F.6: Stress intensity factors calculated along the delamination front by means of the three-dimensional M-integral for the largest domain of the fine mesh, as shown in Fig. 4.8b, used to analyze specimens **sp12.2** and **sp13.2**, separately, as well as their normalized in-plane stress intensity factors with $\hat{L} = 100$ μm, their two phase angles and their critical interface energy release rate.

sp12.2 ; ω=-9.21°								
x_3/B	K_1	K_2	K_{III}	$\hat{K}_1$	$\hat{K}_2$	$\hat{\psi}$	ϕ	$\mathcal{G}_{ic}$
	(MPa$\sqrt{\text{m}} \cdot \text{m}^{-i\varepsilon}$)		(MPa$\sqrt{\text{m}}$)	(MPa$\sqrt{\text{m}}$)		(rad)	(rad)	(N/m)
0.025	0.562	2.384	1.117	0.750	2.332	1.260	0.407	888.3
0.075	0.400	2.306	0.664	0.582	2.267	1.320	0.262	733.5
0.125	0.386	2.320	0.466	0.569	2.282	1.326	0.185	715.3
0.175	0.385	2.332	0.351	0.569	2.294	1.327	0.139	711.4
0.225	0.384	2.340	0.270	0.569	2.302	1.328	0.107	710.3
0.275	0.383	2.345	0.206	0.568	2.307	1.329	0.081	709.8
0.325	0.381	2.348	0.152	0.567	2.310	1.330	0.060	709.5
0.375	0.380	2.350	0.104	0.565	2.313	1.331	0.041	709.3
0.425	0.378	2.352	0.061	0.564	2.314	1.332	0.024	709.3
0.475	0.378	2.352	0.020	0.564	2.315	1.332	0.008	709.3
0.525	0.378	2.352	-0.020	0.564	2.315	1.332	-0.008	709.3
0.575	0.378	2.352	-0.061	0.564	2.314	1.332	-0.024	709.3
0.625	0.380	2.350	-0.104	0.565	2.313	1.331	-0.041	709.3
0.675	0.381	2.348	-0.152	0.567	2.310	1.330	-0.060	709.5
0.725	0.383	2.345	-0.206	0.568	2.307	1.329	-0.081	709.8
0.775	0.384	2.340	-0.270	0.569	2.302	1.328	-0.107	710.3
0.825	0.385	2.332	-0.351	0.569	2.294	1.327	-0.139	711.4
0.875	0.386	2.320	-0.466	0.569	2.282	1.326	-0.185	715.3
0.925	0.400	2.306	-0.664	0.582	2.267	1.320	-0.262	733.5
0.975	0.562	2.384	-1.117	0.750	2.332	1.260	-0.407	888.3

sp13.2 ; ω=-9.45°								
x_3/B	K_1	K_2	K_{III}	$\hat{K}_1$	$\hat{K}_2$	$\hat{\psi}$	ϕ	$\mathcal{G}_{ic}$
	(MPa$\sqrt{\text{m}} \cdot \text{m}^{-i\varepsilon}$)		(MPa$\sqrt{\text{m}}$)	(MPa$\sqrt{\text{m}}$)		(rad)	(rad)	(N/m)
0.025	0.591	2.562	1.201	0.793	2.507	1.264	0.407	1023.8
0.075	0.411	2.477	0.715	0.607	2.436	1.327	0.263	844.2
0.125	0.394	2.491	0.499	0.591	2.452	1.334	0.185	822.4
0.175	0.393	2.504	0.374	0.591	2.465	1.336	0.138	818.0
0.225	0.391	2.513	0.286	0.590	2.474	1.337	0.106	817.0
0.275	0.389	2.518	0.218	0.588	2.479	1.338	0.080	816.5
0.325	0.387	2.522	0.160	0.586	2.483	1.339	0.059	816.3
0.375	0.385	2.525	0.110	0.585	2.486	1.340	0.041	816.2
0.425	0.383	2.526	0.064	0.583	2.488	1.340	0.024	816.1
0.475	0.383	2.527	0.021	0.583	2.488	1.341	0.008	816.1
0.525	0.383	2.527	-0.021	0.583	2.488	1.341	-0.008	816.1
0.575	0.383	2.526	-0.064	0.583	2.488	1.340	-0.024	816.1
0.625	0.385	2.525	-0.110	0.585	2.486	1.340	-0.041	816.2
0.675	0.387	2.522	-0.160	0.586	2.483	1.339	-0.059	816.3
0.725	0.389	2.518	-0.218	0.588	2.479	1.338	-0.080	816.5
0.775	0.391	2.513	-0.286	0.590	2.474	1.337	-0.106	817.0
0.825	0.393	2.504	-0.374	0.591	2.465	1.336	-0.138	818.0
0.875	0.394	2.491	-0.499	0.591	2.452	1.334	-0.185	822.4
0.925	0.411	2.477	-0.715	0.607	2.436	1.327	-0.263	844.2
0.975	0.591	2.562	-1.201	0.793	2.507	1.264	-0.407	1023.8

Table F.7: Stress intensity factors calculated along the delamination front by means of the three-dimensional M-integral for the largest domain of the fine mesh, as shown in Fig. 4.8b, used to analyze specimens **sp3.2** and **sp8.1**, separately, as well as their normalized in-plane stress intensity factors with $\hat{L} = 100$ μm, their two phase angles and their critical interface energy release rate.

sp3.2 ; ω=-9.67°								
x_3/B	K_1	K_2	K_{III}	$\hat{K}_1$	$\hat{K}_2$	$\hat{\psi}$	ϕ	$\mathcal{G}_{ic}$
	(MPa$\sqrt{\text{m}} \cdot \text{m}^{-i\varepsilon}$)		(MPa$\sqrt{\text{m}}$)	(MPa$\sqrt{\text{m}}$)		(rad)	(rad)	(N/m)
0.025	0.602	2.565	1.208	0.804	2.508	1.261	0.408	1029.2
0.075	0.421	2.479	0.715	0.617	2.437	1.323	0.262	846.6
0.125	0.403	2.493	0.497	0.600	2.453	1.331	0.183	824.3
0.175	0.399	2.506	0.371	0.597	2.466	1.333	0.137	819.7
0.225	0.396	2.515	0.283	0.595	2.475	1.335	0.104	818.5
0.275	0.393	2.520	0.215	0.592	2.481	1.336	0.079	817.9
0.325	0.390	2.524	0.158	0.589	2.485	1.338	0.058	817.6
0.375	0.387	2.526	0.108	0.587	2.488	1.339	0.040	817.4
0.425	0.385	2.528	0.063	0.585	2.489	1.340	0.023	817.3
0.475	0.384	2.529	0.021	0.584	2.490	1.340	0.008	817.3
0.525	0.384	2.529	-0.021	0.584	2.490	1.340	-0.008	817.3
0.575	0.385	2.528	-0.063	0.585	2.489	1.340	-0.023	817.3
0.625	0.387	2.526	-0.108	0.587	2.488	1.339	-0.040	817.4
0.675	0.390	2.524	-0.158	0.589	2.485	1.338	-0.058	817.6
0.725	0.393	2.520	-0.215	0.592	2.481	1.336	-0.079	817.9
0.775	0.396	2.515	-0.283	0.595	2.475	1.335	-0.104	818.5
0.825	0.399	2.506	-0.371	0.597	2.466	1.333	-0.137	819.7
0.875	0.403	2.493	-0.497	0.600	2.453	1.331	-0.183	824.3
0.925	0.421	2.479	-0.715	0.617	2.437	1.323	-0.262	846.6
0.975	0.602	2.565	-1.208	0.804	2.508	1.261	-0.408	1029.2

sp8.1 ; ω=-10.10°								
x_3/B	K_1	K_2	K_{III}	$\hat{K}_1$	$\hat{K}_2$	$\hat{\psi}$	ϕ	$\mathcal{G}_{ic}$
	(MPa$\sqrt{\text{m}} \cdot \text{m}^{-i\varepsilon}$)		(MPa$\sqrt{\text{m}}$)	(MPa$\sqrt{\text{m}}$)		(rad)	(rad)	(N/m)
0.025	0.560	2.716	1.269	0.775	2.663	1.288	0.407	1139.7
0.075	0.368	2.627	0.752	0.576	2.589	1.352	0.261	941.8
0.125	0.349	2.642	0.523	0.559	2.606	1.360	0.183	917.8
0.175	0.346	2.655	0.392	0.556	2.619	1.361	0.137	912.7
0.225	0.344	2.664	0.299	0.555	2.628	1.363	0.105	911.4
0.275	0.341	2.670	0.227	0.552	2.634	1.364	0.079	910.7
0.325	0.338	2.674	0.167	0.549	2.638	1.365	0.058	910.4
0.375	0.335	2.676	0.115	0.547	2.641	1.366	0.040	910.2
0.425	0.334	2.678	0.067	0.546	2.643	1.367	0.023	910.1
0.475	0.333	2.678	0.022	0.545	2.643	1.368	0.008	910.1
0.525	0.333	2.678	-0.022	0.545	2.643	1.368	-0.008	910.1
0.575	0.334	2.678	-0.067	0.546	2.643	1.367	-0.023	910.1
0.625	0.335	2.676	-0.115	0.547	2.641	1.366	-0.040	910.2
0.675	0.338	2.674	-0.167	0.549	2.638	1.365	-0.058	910.4
0.725	0.341	2.670	-0.227	0.552	2.634	1.364	-0.079	910.7
0.775	0.344	2.664	-0.299	0.555	2.628	1.363	-0.105	911.4
0.825	0.346	2.655	-0.392	0.556	2.619	1.361	-0.137	912.7
0.875	0.349	2.642	-0.523	0.559	2.606	1.360	-0.183	917.8
0.925	0.368	2.627	-0.752	0.576	2.589	1.352	-0.261	941.8
0.975	0.560	2.716	-1.269	0.775	2.663	1.288	-0.407	1139.7

Table F.8: Stress intensity factors calculated along the delamination front by means of the three-dimensional M-integral for the largest domain of the fine mesh, as shown in Fig. 4.8b, used to analyze specimens **sp11.1** and **sp4.2**, separately, as well as their normalized in-plane stress intensity factors with $\hat{L} = 100$ μm, their two phase angles and their critical interface energy release rate.

sp11.1 ; ω=-10.11°								
x_3/B	K_1	K_2	K_{III}	$\hat{K}_1$	$\hat{K}_2$	$\hat{\psi}$	ϕ	$\mathcal{G}_{ic}$
	(MPa$\sqrt{\text{m}} \cdot \text{m}^{-i\varepsilon}$)		(MPa$\sqrt{\text{m}}$)	(MPa$\sqrt{\text{m}}$)		(rad)	(rad)	(N/m)
0.025	0.566	2.535	1.198	0.766	2.482	1.271	0.410	1002.4
0.075	0.387	2.448	0.717	0.581	2.409	1.334	0.267	824.4
0.125	0.371	2.461	0.506	0.566	2.423	1.342	0.190	802.2
0.175	0.370	2.473	0.383	0.565	2.435	1.343	0.144	797.2
0.225	0.369	2.481	0.296	0.566	2.444	1.343	0.111	795.7
0.275	0.368	2.486	0.226	0.565	2.449	1.344	0.085	795.0
0.325	0.367	2.490	0.167	0.564	2.453	1.345	0.063	794.6
0.375	0.366	2.493	0.115	0.563	2.456	1.345	0.043	794.4
0.425	0.365	2.494	0.068	0.563	2.457	1.346	0.025	794.3
0.475	0.365	2.495	0.022	0.562	2.458	1.346	0.008	794.3
0.525	0.365	2.495	-0.022	0.562	2.458	1.346	-0.008	794.3
0.575	0.365	2.494	-0.068	0.563	2.457	1.346	-0.025	794.3
0.625	0.366	2.493	-0.115	0.563	2.456	1.345	-0.043	794.4
0.675	0.367	2.490	-0.167	0.564	2.453	1.345	-0.063	794.6
0.725	0.368	2.486	-0.226	0.565	2.449	1.344	-0.085	795.0
0.775	0.369	2.481	-0.296	0.566	2.444	1.343	-0.111	795.7
0.825	0.370	2.473	-0.383	0.565	2.435	1.343	-0.144	797.2
0.875	0.371	2.461	-0.506	0.566	2.423	1.342	-0.190	802.2
0.925	0.387	2.448	-0.717	0.581	2.409	1.334	-0.267	824.4
0.975	0.566	2.535	-1.198	0.766	2.482	1.271	-0.410	1002.4

sp4.2 ; ω=-12.46°								
x_3/B	K_1	K_2	K_{III}	$\hat{K}_1$	$\hat{K}_2$	$\hat{\psi}$	ϕ	$\mathcal{G}_{ic}$
	(MPa$\sqrt{\text{m}} \cdot \text{m}^{-i\varepsilon}$)		(MPa$\sqrt{\text{m}}$)	(MPa$\sqrt{\text{m}}$)		(rad)	(rad)	(N/m)
0.025	0.239	2.781	1.272	0.460	2.753	1.405	0.406	1153.3
0.075	0.032	2.692	0.769	0.246	2.681	1.479	0.263	971.4
0.125	0.015	2.707	0.548	0.230	2.697	1.486	0.189	948.8
0.175	0.018	2.720	0.419	0.234	2.710	1.485	0.144	943.7
0.225	0.022	2.729	0.326	0.239	2.719	1.483	0.112	942.5
0.275	0.026	2.736	0.251	0.243	2.725	1.482	0.086	942.0
0.325	0.028	2.740	0.186	0.246	2.729	1.481	0.064	941.9
0.375	0.030	2.743	0.129	0.248	2.732	1.480	0.044	941.9
0.425	0.030	2.745	0.076	0.249	2.734	1.480	0.026	942.0
0.475	0.031	2.746	0.025	0.249	2.735	1.480	0.009	942.1
0.525	0.031	2.746	-0.025	0.249	2.735	1.480	-0.009	942.1
0.575	0.030	2.745	-0.076	0.249	2.734	1.480	-0.026	942.0
0.625	0.030	2.743	-0.129	0.248	2.732	1.480	-0.044	941.9
0.675	0.028	2.740	-0.186	0.246	2.729	1.481	-0.064	941.9
0.725	0.026	2.736	-0.251	0.243	2.725	1.482	-0.086	942.0
0.775	0.022	2.729	-0.326	0.239	2.719	1.483	-0.112	942.5
0.825	0.018	2.720	-0.419	0.234	2.710	1.485	-0.144	943.7
0.875	0.015	2.707	-0.548	0.230	2.697	1.486	-0.189	948.8
0.925	0.032	2.692	-0.769	0.246	2.681	1.479	-0.263	971.4
0.975	0.239	2.781	-1.272	0.460	2.753	1.405	-0.406	1153.3

Table F.9: Stress intensity factors calculated along the delamination front by means of the three-dimensional M-integral for the largest domain of the fine mesh, as shown in Fig. 4.8b, used to analyze specimens **sp5.1** and **sp2.2**, separately, as well as their normalized in-plane stress intensity factors with $\hat{L} = 100$ μm, their two phase angles and their critical interface energy release rate.

sp5.1 ; ω=-12.94°								
x_3/B	K_1	K_2	K_{III}	$\hat{K}_1$	$\hat{K}_2$	$\hat{\psi}$	ϕ	$\mathcal{G}_{ic}$
	(MPa$\sqrt{\text{m}} \cdot \text{m}^{-i\varepsilon}$)		(MPa$\sqrt{\text{m}}$)	(MPa$\sqrt{\text{m}}$)		(rad)	(rad)	(N/m)
0.025	0.299	2.744	1.256	0.517	2.712	1.382	0.406	1127.5
0.075	0.098	2.659	0.750	0.309	2.643	1.454	0.260	947.0
0.125	0.080	2.674	0.528	0.293	2.660	1.461	0.184	925.4
0.175	0.080	2.688	0.399	0.294	2.673	1.461	0.139	920.8
0.225	0.081	2.697	0.308	0.295	2.682	1.461	0.107	919.8
0.275	0.081	2.703	0.235	0.296	2.688	1.461	0.082	919.5
0.325	0.081	2.707	0.174	0.296	2.692	1.461	0.061	919.4
0.375	0.080	2.709	0.120	0.296	2.694	1.461	0.042	919.5
0.425	0.080	2.711	0.070	0.296	2.696	1.462	0.024	919.6
0.475	0.080	2.712	0.023	0.295	2.697	1.462	0.008	919.6
0.525	0.080	2.712	-0.023	0.295	2.697	1.462	-0.008	919.6
0.575	0.080	2.711	-0.070	0.296	2.696	1.462	-0.024	919.6
0.625	0.080	2.709	-0.120	0.296	2.694	1.461	-0.042	919.5
0.675	0.081	2.707	-0.174	0.296	2.692	1.461	-0.061	919.4
0.725	0.081	2.703	-0.235	0.296	2.688	1.461	-0.082	919.5
0.775	0.081	2.697	-0.308	0.295	2.682	1.461	-0.107	919.8
0.825	0.080	2.688	-0.399	0.294	2.673	1.461	-0.139	920.8
0.875	0.080	2.674	-0.528	0.293	2.660	1.461	-0.184	925.4
0.925	0.098	2.659	-0.750	0.309	2.643	1.454	-0.260	947.0
0.975	0.299	2.744	-1.256	0.517	2.712	1.382	-0.406	1127.5

sp2.2 ; ω=-13.07°								
x_3/B	K_1	K_2	K_{III}	$\hat{K}_1$	$\hat{K}_2$	$\hat{\psi}$	ϕ	$\mathcal{G}_{ic}$
	(MPa$\sqrt{\text{m}} \cdot \text{m}^{-i\varepsilon}$)		(MPa$\sqrt{\text{m}}$)	(MPa$\sqrt{\text{m}}$)		(rad)	(rad)	(N/m)
0.025	0.246	2.751	1.266	0.464	2.723	1.402	0.408	1131.4
0.075	0.043	2.661	0.762	0.254	2.649	1.475	0.264	949.4
0.125	0.025	2.674	0.542	0.238	2.664	1.482	0.189	926.3
0.175	0.027	2.687	0.413	0.241	2.676	1.481	0.144	920.9
0.225	0.031	2.696	0.320	0.245	2.685	1.480	0.112	919.4
0.275	0.033	2.702	0.246	0.248	2.691	1.479	0.086	918.8
0.325	0.035	2.706	0.183	0.250	2.695	1.478	0.064	918.6
0.375	0.036	2.709	0.126	0.251	2.697	1.478	0.044	918.6
0.425	0.036	2.711	0.074	0.252	2.699	1.478	0.026	918.6
0.475	0.037	2.711	0.024	0.252	2.700	1.478	0.009	918.6
0.525	0.037	2.711	-0.024	0.252	2.700	1.478	-0.009	918.6
0.575	0.036	2.711	-0.074	0.252	2.699	1.478	-0.026	918.6
0.625	0.036	2.709	-0.126	0.251	2.697	1.478	-0.044	918.6
0.675	0.035	2.706	-0.183	0.250	2.695	1.478	-0.064	918.6
0.725	0.033	2.702	-0.246	0.248	2.691	1.479	-0.086	918.8
0.775	0.031	2.696	-0.320	0.245	2.685	1.480	-0.112	919.4
0.825	0.027	2.687	-0.413	0.241	2.676	1.481	-0.144	920.9
0.875	0.025	2.674	-0.542	0.238	2.664	1.482	-0.189	926.3
0.925	0.043	2.661	-0.762	0.254	2.649	1.475	-0.264	949.4
0.975	0.246	2.751	-1.266	0.464	2.723	1.402	-0.408	1131.4

Table F.10: Stress intensity factors calculated along the delamination front by means of the three-dimensional M-integral for the largest domain of the fine mesh, as shown in Fig. 4.8b, used to analyze specimens **sp4.1** and **sp6.2**, separately, as well as their normalized in-plane stress intensity factors with $\hat{L} = 100$ μm, their two phase angles and their critical interface energy release rate.

sp4.1 ; ω=-13.20°								
x_3/B	K_1	K_2	K_{III}	$\hat{K}_1$	$\hat{K}_2$	$\hat{\psi}$	ϕ	$\mathcal{G}_{ic}$
	(MPa$\sqrt{\text{m}} \cdot \text{m}^{-i\varepsilon}$)		(MPa$\sqrt{\text{m}}$)	(MPa$\sqrt{\text{m}}$)		(rad)	(rad)	(N/m)
0.025	0.198	2.854	1.315	0.425	2.829	1.422	0.409	1214.6
0.075	-0.018	2.760	0.795	0.202	2.753	1.498	0.266	1022.1
0.125	-0.035	2.774	0.566	0.185	2.768	1.504	0.190	997.4
0.175	-0.032	2.788	0.432	0.190	2.782	1.503	0.145	991.9
0.225	-0.026	2.798	0.336	0.196	2.791	1.501	0.113	990.7
0.275	-0.022	2.805	0.258	0.201	2.798	1.499	0.087	990.3
0.325	-0.019	2.809	0.192	0.205	2.802	1.498	0.064	990.2
0.375	-0.017	2.813	0.133	0.207	2.805	1.497	0.045	990.3
0.425	-0.016	2.815	0.078	0.208	2.807	1.497	0.026	990.4
0.475	-0.015	2.816	0.026	0.209	2.808	1.497	0.009	990.4
0.525	-0.015	2.816	-0.026	0.209	2.808	1.497	-0.009	990.4
0.575	-0.016	2.815	-0.078	0.208	2.807	1.497	-0.026	990.4
0.625	-0.017	2.813	-0.133	0.207	2.805	1.497	-0.045	990.3
0.675	-0.019	2.809	-0.192	0.205	2.802	1.498	-0.064	990.2
0.725	-0.022	2.805	-0.258	0.201	2.798	1.499	-0.087	990.3
0.775	-0.026	2.798	-0.336	0.196	2.791	1.501	-0.113	990.7
0.825	-0.032	2.788	-0.432	0.190	2.782	1.503	-0.145	991.9
0.875	-0.035	2.774	-0.566	0.185	2.768	1.504	-0.190	997.4
0.925	-0.018	2.760	-0.795	0.202	2.753	1.498	-0.266	1022.1
0.975	0.198	2.854	-1.315	0.425	2.829	1.422	-0.409	1214.6

sp6.2 ; ω=-13.42°								
x_3/B	K_1	K_2	K_{III}	$\hat{K}_1$	$\hat{K}_2$	$\hat{\psi}$	ϕ	$\mathcal{G}_{ic}$
	(MPa$\sqrt{\text{m}} \cdot \text{m}^{-i\varepsilon}$)		(MPa$\sqrt{\text{m}}$)	(MPa$\sqrt{\text{m}}$)		(rad)	(rad)	(N/m)
0.025	0.224	2.899	1.332	0.454	2.872	1.414	0.408	1253.7
0.075	0.009	2.806	0.801	0.233	2.796	1.488	0.263	1054.8
0.125	0.000	2.821	0.568	0.216	2.813	1.494	0.188	1029.9
0.175	0.000	2.834	0.432	0.220	2.826	1.493	0.143	1024.4
0.225	0.000	2.844	0.335	0.225	2.835	1.492	0.111	1023.0
0.275	0.001	2.851	0.257	0.228	2.842	1.491	0.085	1022.6
0.325	0.003	2.855	0.191	0.230	2.846	1.490	0.063	1022.5
0.375	0.004	2.858	0.132	0.232	2.849	1.490	0.043	1022.6
0.425	0.005	2.860	0.077	0.233	2.851	1.489	0.025	1022.7
0.475	0.005	2.861	0.025	0.233	2.852	1.489	0.008	1022.8
0.525	0.005	2.861	-0.025	0.233	2.852	1.489	-0.008	1022.8
0.575	0.005	2.860	-0.077	0.233	2.851	1.489	-0.025	1022.7
0.625	0.004	2.858	-0.132	0.232	2.849	1.490	-0.043	1022.6
0.675	0.003	2.855	-0.191	0.230	2.846	1.490	-0.063	1022.5
0.725	0.001	2.851	-0.257	0.228	2.842	1.491	-0.085	1022.6
0.775	0.000	2.844	-0.335	0.225	2.835	1.492	-0.111	1023.0
0.825	0.000	2.834	-0.432	0.220	2.826	1.493	-0.143	1024.4
0.875	0.000	2.821	-0.568	0.216	2.813	1.494	-0.188	1029.9
0.925	0.009	2.806	-0.801	0.233	2.796	1.488	-0.263	1054.8
0.975	0.224	2.899	-1.332	0.454	2.872	1.414	-0.408	1253.7

Table F.11: Stress intensity factors calculated along the delamination front by means of the three-dimensional M-integral for the largest domain of the fine mesh, as shown in Fig. 4.8b, used to analyze specimens **sp10.1** and **sp14.2**, separately, as well as their normalized in-plane stress intensity factors with $\hat{L} = 100$ μm, their two phase angles and their critical interface energy release rate.

sp10.1 ; ω=1.72°								
x_3/B	K_1	K_2	K_{III}	$\hat{K}_1$	$\hat{K}_2$	$\hat{\psi}$	ϕ	$\mathcal{G}_{ic}$
	(MPa$\sqrt{\text{m}} \cdot \text{m}^{-i\varepsilon}$)		(MPa$\sqrt{\text{m}}$)	(MPa$\sqrt{\text{m}}$)		(rad)	(rad)	(N/m)
0.025	1.238	-1.019	-0.174	1.153	-1.114	-0.768	-0.102	324.3
0.075	1.335	-1.011	-0.111	1.250	-1.114	-0.728	-0.063	351.6
0.125	1.338	-1.003	-0.096	1.254	-1.107	-0.723	-0.054	350.4
0.175	1.326	-0.997	-0.084	1.242	-1.099	-0.725	-0.048	344.5
0.225	1.311	-0.993	-0.071	1.228	-1.094	-0.728	-0.041	338.4
0.275	1.298	-0.989	-0.057	1.215	-1.089	-0.731	-0.033	333.2
0.325	1.288	-0.987	-0.044	1.205	-1.086	-0.734	-0.026	329.0
0.375	1.280	-0.985	-0.031	1.197	-1.084	-0.736	-0.018	325.9
0.425	1.274	-0.984	-0.019	1.192	-1.082	-0.737	-0.011	323.9
0.475	1.272	-0.984	-0.006	1.189	-1.082	-0.738	-0.004	322.9
0.525	1.272	-0.984	0.006	1.189	-1.082	-0.738	0.004	322.9
0.575	1.274	-0.984	0.019	1.192	-1.082	-0.737	0.011	323.9
0.625	1.280	-0.985	0.031	1.197	-1.084	-0.736	0.018	325.9
0.675	1.288	-0.987	0.044	1.205	-1.086	-0.734	0.026	329.0
0.725	1.298	-0.989	0.057	1.215	-1.089	-0.731	0.033	333.2
0.775	1.311	-0.993	0.071	1.228	-1.094	-0.728	0.041	338.4
0.825	1.326	-0.997	0.084	1.242	-1.099	-0.725	0.048	344.5
0.875	1.338	-1.003	0.096	1.254	-1.107	-0.723	0.054	350.4
0.925	1.335	-1.011	0.111	1.250	-1.114	-0.728	0.063	351.6
0.975	1.238	-1.019	0.174	1.153	-1.114	-0.768	0.102	324.3

sp14.2 ; ω=2.50°								
x_3/B	K_1	K_2	K_{III}	$\hat{K}_1$	$\hat{K}_2$	$\hat{\psi}$	ϕ	$\mathcal{G}_{ic}$
	(MPa$\sqrt{\text{m}} \cdot \text{m}^{-i\varepsilon}$)		(MPa$\sqrt{\text{m}}$)	(MPa$\sqrt{\text{m}}$)		(rad)	(rad)	(N/m)
0.025	1.225	-0.549	0.036	1.178	-0.645	-0.501	0.025	225.4
0.075	1.285	-0.568	0.031	1.235	-0.668	-0.496	0.021	246.5
0.125	1.285	-0.565	0.016	1.236	-0.666	-0.494	0.011	246.2
0.175	1.274	-0.562	0.008	1.225	-0.661	-0.495	0.006	242.2
0.225	1.261	-0.559	0.004	1.213	-0.657	-0.497	0.003	237.7
0.275	1.249	-0.557	0.002	1.201	-0.655	-0.499	0.002	233.7
0.325	1.240	-0.556	0.001	1.191	-0.652	-0.501	0.001	230.5
0.375	1.232	-0.555	0.001	1.184	-0.651	-0.503	0.001	228.1
0.425	1.227	-0.554	0.000	1.179	-0.650	-0.504	0.000	226.6
0.475	1.225	-0.554	0.000	1.177	-0.649	-0.504	0.000	225.8
0.525	1.225	-0.554	0.000	1.177	-0.649	-0.504	0.000	225.8
0.575	1.227	-0.554	0.000	1.179	-0.650	-0.504	0.000	226.6
0.625	1.232	-0.555	-0.001	1.184	-0.651	-0.503	-0.001	228.1
0.675	1.240	-0.556	-0.001	1.191	-0.652	-0.501	-0.001	230.5
0.725	1.249	-0.557	-0.002	1.201	-0.655	-0.499	-0.002	233.7
0.775	1.261	-0.559	-0.004	1.213	-0.657	-0.497	-0.003	237.7
0.825	1.274	-0.562	-0.008	1.225	-0.661	-0.495	-0.006	242.2
0.875	1.285	-0.565	-0.016	1.236	-0.666	-0.494	-0.011	246.2
0.925	1.285	-0.568	-0.031	1.235	-0.668	-0.496	-0.021	246.5
0.975	1.225	-0.549	-0.036	1.178	-0.645	-0.501	-0.025	225.4

Table F.12: Stress intensity factors calculated along the delamination front by means of the three-dimensional M-integral for the largest domain of the fine mesh, as shown in Fig. 4.8b, used to analyze specimens **sp10.2** and **sp16.1**, separately, as well as their normalized in-plane stress intensity factors with $\hat{L} = 100$ μm, their two phase angles and their critical interface energy release rate.

sp10.2 ; ω=2.69°								
x_3/B	K_1	K_2	K_{III}	$\hat{K}_1$	$\hat{K}_2$	$\hat{\psi}$	ϕ	$\mathcal{G}_{ic}$
	(MPa$\sqrt{\text{m}} \cdot \text{m}^{-i\varepsilon}$)		(MPa$\sqrt{\text{m}}$)	(MPa$\sqrt{\text{m}}$)		(rad)	(rad)	(N/m)
0.025	1.119	-0.945	-0.153	1.040	-1.031	-0.781	-0.098	270.7
0.075	1.207	-0.942	-0.092	1.128	-1.035	-0.742	-0.056	294.0
0.125	1.210	-0.938	-0.077	1.132	-1.031	-0.739	-0.047	293.4
0.175	1.199	-0.933	-0.066	1.121	-1.026	-0.741	-0.041	288.8
0.225	1.186	-0.930	-0.054	1.108	-1.021	-0.745	-0.034	283.9
0.275	1.174	-0.927	-0.044	1.096	-1.018	-0.748	-0.028	279.7
0.325	1.164	-0.926	-0.033	1.086	-1.015	-0.752	-0.021	276.3
0.375	1.156	-0.924	-0.023	1.079	-1.013	-0.754	-0.015	273.9
0.425	1.152	-0.924	-0.014	1.074	-1.012	-0.756	-0.009	272.2
0.475	1.149	-0.923	-0.005	1.072	-1.012	-0.756	-0.003	271.4
0.525	1.149	-0.923	0.005	1.072	-1.012	-0.756	0.003	271.4
0.575	1.152	-0.924	0.014	1.074	-1.012	-0.756	0.009	272.2
0.625	1.156	-0.924	0.023	1.079	-1.013	-0.754	0.015	273.9
0.675	1.164	-0.926	0.033	1.086	-1.015	-0.752	0.021	276.3
0.725	1.174	-0.927	0.044	1.096	-1.018	-0.748	0.028	279.7
0.775	1.186	-0.930	0.054	1.108	-1.021	-0.745	0.034	283.9
0.825	1.199	-0.933	0.066	1.121	-1.026	-0.741	0.041	288.8
0.875	1.210	-0.938	0.077	1.132	-1.031	-0.739	0.047	293.4
0.925	1.207	-0.942	0.092	1.128	-1.035	-0.742	0.056	294.0
0.975	1.119	-0.945	0.153	1.040	-1.031	-0.781	0.098	270.7

sp16.1 ; ω=2.74°								
x_3/B	K_1	K_2	K_{III}	$\hat{K}_1$	$\hat{K}_2$	$\hat{\psi}$	ϕ	$\mathcal{G}_{ic}$
	(MPa$\sqrt{\text{m}} \cdot \text{m}^{-i\varepsilon}$)		(MPa$\sqrt{\text{m}}$)	(MPa$\sqrt{\text{m}}$)		(rad)	(rad)	(N/m)
0.025	1.117	-0.940	-0.143	1.038	-1.026	-0.779	-0.092	268.4
0.075	1.208	-0.939	-0.086	1.130	-1.032	-0.740	-0.053	293.3
0.125	1.213	-0.934	-0.073	1.135	-1.028	-0.736	-0.045	293.5
0.175	1.203	-0.930	-0.063	1.126	-1.022	-0.737	-0.039	289.3
0.225	1.191	-0.926	-0.053	1.113	-1.018	-0.741	-0.033	284.7
0.275	1.179	-0.924	-0.043	1.102	-1.015	-0.744	-0.027	280.6
0.325	1.170	-0.922	-0.033	1.093	-1.012	-0.747	-0.021	277.3
0.375	1.162	-0.921	-0.023	1.085	-1.011	-0.750	-0.015	274.8
0.425	1.158	-0.920	-0.014	1.081	-1.009	-0.751	-0.009	273.2
0.475	1.155	-0.920	-0.005	1.078	-1.009	-0.752	-0.003	272.4
0.525	1.155	-0.920	0.005	1.078	-1.009	-0.752	0.003	272.4
0.575	1.158	-0.920	0.014	1.081	-1.009	-0.751	0.009	273.2
0.625	1.162	-0.921	0.023	1.085	-1.011	-0.750	0.015	274.8
0.675	1.170	-0.922	0.033	1.093	-1.012	-0.747	0.021	277.3
0.725	1.179	-0.924	0.043	1.102	-1.015	-0.744	0.027	280.6
0.775	1.191	-0.926	0.053	1.113	-1.018	-0.741	0.033	284.7
0.825	1.203	-0.930	0.063	1.126	-1.022	-0.737	0.039	289.3
0.875	1.213	-0.934	0.073	1.135	-1.028	-0.736	0.045	293.5
0.925	1.208	-0.939	0.086	1.130	-1.032	-0.740	0.053	293.3
0.975	1.117	-0.940	0.143	1.038	-1.026	-0.779	0.092	268.4

Table F.13: Stress intensity factors calculated along the delamination front by means of the three-dimensional M-integral for the largest domain of the fine mesh, as shown in Fig. 4.8b, used to analyze specimens **sp15.1** and **sp9.2**, separately, as well as their normalized in-plane stress intensity factors with $\hat{L} = 100$ μm, their two phase angles and their critical interface energy release rate.

sp15.1 ; ω=4.03°								
x_3/B	K_1	K_2	K_{III}	$\hat{K}_1$	$\hat{K}_2$	$\hat{\psi}$	ϕ	$\mathcal{G}_{ic}$
	(MPa$\sqrt{\text{m}} \cdot \text{m}^{-i\varepsilon}$)		(MPa$\sqrt{\text{m}}$)	(MPa$\sqrt{\text{m}}$)		(rad)	(rad)	(N/m)
0.025	1.081	-1.611	-0.413	0.950	-1.692	-1.059	-0.198	489.3
0.075	1.243	-1.590	-0.242	1.112	-1.684	-0.987	-0.113	515.2
0.125	1.263	-1.586	-0.181	1.133	-1.682	-0.978	-0.084	517.3
0.175	1.259	-1.583	-0.144	1.129	-1.678	-0.979	-0.067	513.3
0.225	1.249	-1.580	-0.115	1.119	-1.675	-0.982	-0.054	508.2
0.275	1.239	-1.578	-0.089	1.109	-1.671	-0.985	-0.042	503.6
0.325	1.230	-1.576	-0.067	1.100	-1.669	-0.988	-0.032	499.8
0.375	1.223	-1.575	-0.046	1.094	-1.667	-0.990	-0.022	496.9
0.425	1.218	-1.574	-0.027	1.089	-1.666	-0.992	-0.013	495.0
0.475	1.216	-1.574	-0.009	1.087	-1.665	-0.993	-0.004	494.1
0.525	1.216	-1.574	0.009	1.087	-1.665	-0.993	0.004	494.1
0.575	1.218	-1.574	0.027	1.089	-1.666	-0.992	0.013	495.0
0.625	1.223	-1.575	0.046	1.094	-1.667	-0.990	0.022	496.9
0.675	1.230	-1.576	0.067	1.100	-1.669	-0.988	0.032	499.8
0.725	1.239	-1.578	0.089	1.109	-1.671	-0.985	0.042	503.6
0.775	1.249	-1.580	0.115	1.119	-1.675	-0.982	0.054	508.2
0.825	1.259	-1.583	0.144	1.129	-1.678	-0.979	0.067	513.3
0.875	1.263	-1.586	0.181	1.133	-1.682	-0.978	0.084	517.3
0.925	1.243	-1.590	0.242	1.112	-1.684	-0.987	0.113	515.2
0.975	1.081	-1.611	0.413	0.950	-1.692	-1.059	0.198	489.3

sp9.2 ; ω=4.30°								
x_3/B	K_1	K_2	K_{III}	$\hat{K}_1$	$\hat{K}_2$	$\hat{\psi}$	ϕ	$\mathcal{G}_{ic}$
	(MPa$\sqrt{\text{m}} \cdot \text{m}^{-i\varepsilon}$)		(MPa$\sqrt{\text{m}}$)	(MPa$\sqrt{\text{m}}$)		(rad)	(rad)	(N/m)
0.025	1.116	-1.404	-0.315	1.001	-1.488	-0.979	-0.164	412.8
0.075	1.258	-1.395	-0.174	1.143	-1.491	-0.917	-0.087	444.1
0.125	1.276	-1.394	-0.127	1.161	-1.491	-0.909	-0.063	447.7
0.175	1.271	-1.391	-0.099	1.156	-1.488	-0.910	-0.050	444.7
0.225	1.261	-1.389	-0.078	1.146	-1.485	-0.913	-0.039	440.4
0.275	1.251	-1.388	-0.060	1.136	-1.483	-0.917	-0.030	436.4
0.325	1.242	-1.386	-0.044	1.128	-1.481	-0.920	-0.022	433.0
0.375	1.235	-1.385	-0.031	1.121	-1.479	-0.922	-0.016	430.4
0.425	1.230	-1.385	-0.018	1.116	-1.478	-0.924	-0.009	428.7
0.475	1.228	-1.384	-0.006	1.114	-1.478	-0.925	-0.003	427.8
0.525	1.228	-1.384	0.006	1.114	-1.478	-0.925	0.003	427.8
0.575	1.230	-1.385	0.018	1.116	-1.478	-0.924	0.009	428.7
0.625	1.235	-1.385	0.031	1.121	-1.479	-0.922	0.016	430.4
0.675	1.242	-1.386	0.044	1.128	-1.481	-0.920	0.022	433.0
0.725	1.251	-1.388	0.060	1.136	-1.483	-0.917	0.030	436.4
0.775	1.261	-1.389	0.078	1.146	-1.485	-0.913	0.039	440.4
0.825	1.271	-1.391	0.099	1.156	-1.488	-0.910	0.050	444.7
0.875	1.276	-1.394	0.127	1.161	-1.491	-0.909	0.063	447.7
0.925	1.258	-1.395	0.174	1.143	-1.491	-0.917	0.087	444.1
0.975	1.116	-1.404	0.315	1.001	-1.488	-0.979	0.164	412.8

Table F.14: Stress intensity factors calculated along the delamination front by means of the three-dimensional M-integral for the largest domain of the fine mesh, as shown in Fig. 4.8b, used to analyze specimens **sp15.2** and **sp7.1**, separately, as well as their normalized in-plane stress intensity factors with $\hat{L} = 100$ μm, their two phase angles and their critical interface energy release rate.

sp15.2 ; ω=4.67°								
x_3/B	K_1	K_2	K_{III}	$\hat{K}_1$	$\hat{K}_2$	$\hat{\psi}$	ϕ	$\mathcal{G}_{ic}$
	(MPa$\sqrt{\text{m}} \cdot \text{m}^{-i\varepsilon}$)		(MPa$\sqrt{\text{m}}$)	(MPa$\sqrt{\text{m}}$)		(rad)	(rad)	(N/m)
0.025	1.196	-1.911	-0.510	1.040	-2.000	-1.091	-0.210	663.6
0.075	1.369	-1.880	-0.310	1.215	-1.983	-1.021	-0.125	686.0
0.125	1.382	-1.874	-0.236	1.229	-1.978	-1.015	-0.095	683.9
0.175	1.372	-1.870	-0.190	1.218	-1.973	-1.018	-0.077	675.9
0.225	1.357	-1.867	-0.153	1.204	-1.969	-1.022	-0.062	667.9
0.275	1.343	-1.864	-0.120	1.190	-1.965	-1.026	-0.049	661.0
0.325	1.331	-1.862	-0.091	1.179	-1.962	-1.030	-0.037	655.5
0.375	1.322	-1.861	-0.063	1.170	-1.960	-1.033	-0.026	651.5
0.425	1.317	-1.860	-0.037	1.164	-1.959	-1.035	-0.016	648.9
0.475	1.314	-1.860	-0.012	1.162	-1.958	-1.035	-0.005	647.6
0.525	1.314	-1.860	0.012	1.162	-1.958	-1.035	0.005	647.6
0.575	1.317	-1.860	0.037	1.164	-1.959	-1.035	0.016	648.9
0.625	1.322	-1.861	0.063	1.170	-1.960	-1.033	0.026	651.5
0.675	1.331	-1.862	0.091	1.179	-1.962	-1.030	0.037	655.5
0.725	1.343	-1.864	0.120	1.190	-1.965	-1.026	0.049	661.0
0.775	1.357	-1.867	0.153	1.204	-1.969	-1.022	0.062	667.9
0.825	1.372	-1.870	0.190	1.218	-1.973	-1.018	0.077	675.9
0.875	1.382	-1.874	0.236	1.229	-1.978	-1.015	0.095	683.9
0.925	1.369	-1.880	0.310	1.215	-1.983	-1.021	0.125	686.0
0.975	1.196	-1.911	0.510	1.040	-2.000	-1.091	0.210	663.6

sp7.1 ; ω=5.35°								
x_3/B	K_1	K_2	K_{III}	$\hat{K}_1$	$\hat{K}_2$	$\hat{\psi}$	ϕ	$\mathcal{G}_{ic}$
	(MPa$\sqrt{\text{m}} \cdot \text{m}^{-i\varepsilon}$)		(MPa$\sqrt{\text{m}}$)	(MPa$\sqrt{\text{m}}$)		(rad)	(rad)	(N/m)
0.025	0.896	-2.467	-0.799	0.697	-2.530	-1.302	-0.280	931.4
0.075	1.138	-2.409	-0.487	0.943	-2.492	-1.209	-0.171	913.4
0.125	1.176	-2.405	-0.361	0.981	-2.491	-1.196	-0.126	909.9
0.175	1.179	-2.402	-0.283	0.984	-2.488	-1.194	-0.100	903.6
0.225	1.173	-2.400	-0.224	0.979	-2.486	-1.196	-0.079	897.2
0.275	1.165	-2.398	-0.174	0.971	-2.483	-1.198	-0.062	891.5
0.325	1.158	-2.396	-0.131	0.964	-2.481	-1.200	-0.046	886.9
0.375	1.152	-2.395	-0.091	0.958	-2.479	-1.202	-0.032	883.5
0.425	1.148	-2.394	-0.054	0.954	-2.478	-1.203	-0.019	881.2
0.475	1.146	-2.394	-0.018	0.952	-2.478	-1.204	-0.006	880.1
0.525	1.146	-2.394	0.018	0.952	-2.478	-1.204	0.006	880.1
0.575	1.148	-2.394	0.054	0.954	-2.478	-1.203	0.019	881.2
0.625	1.152	-2.395	0.091	0.958	-2.479	-1.202	0.032	883.5
0.675	1.158	-2.396	0.131	0.964	-2.481	-1.200	0.046	886.9
0.725	1.165	-2.398	0.174	0.971	-2.483	-1.198	0.062	891.5
0.775	1.173	-2.400	0.224	0.979	-2.486	-1.196	0.079	897.2
0.825	1.179	-2.402	0.283	0.984	-2.488	-1.194	0.100	903.6
0.875	1.176	-2.405	0.361	0.981	-2.491	-1.196	0.126	909.9
0.925	1.138	-2.409	0.487	0.943	-2.492	-1.209	0.171	913.4
0.975	0.896	-2.467	0.799	0.697	-2.530	-1.302	0.280	931.4

Table F.15: Stress intensity factors calculated along the delamination front by means of the three-dimensional M-integral for the largest domain of the fine mesh, as shown in Fig. 4.8b, used to analyze specimens **sp6.1** and **sp5.2**, separately, as well as their normalized in-plane stress intensity factors with $\hat{L} = 100$ μm, their two phase angles and their critical interface energy release rate.

sp6.1 ; ω=9.89°								
x_3/B	K_1	K_2	K_{III}	$\hat{K}_1$	$\hat{K}_2$	$\hat{\psi}$	ϕ	$\mathcal{G}_{ic}$
	(MPa$\sqrt{\text{m}} \cdot \text{m}^{-i\varepsilon}$)		(MPa$\sqrt{\text{m}}$)	(MPa$\sqrt{\text{m}}$)		(rad)	(rad)	(N/m)
0.025	0.437	-2.635	-0.988	0.226	-2.662	-1.486	-0.336	1000.0
0.075	0.699	-2.561	-0.613	0.493	-2.609	-1.384	-0.214	922.4
0.125	0.749	-2.562	-0.453	0.543	-2.614	-1.366	-0.159	913.2
0.175	0.764	-2.565	-0.356	0.557	-2.618	-1.361	-0.125	908.9
0.225	0.768	-2.567	-0.281	0.561	-2.620	-1.360	-0.099	905.8
0.275	0.769	-2.569	-0.219	0.562	-2.622	-1.360	-0.077	903.4
0.325	0.768	-2.570	-0.164	0.561	-2.623	-1.360	-0.058	901.5
0.375	0.767	-2.570	-0.114	0.560	-2.623	-1.360	-0.040	900.2
0.425	0.766	-2.571	-0.067	0.559	-2.623	-1.361	-0.024	899.3
0.475	0.766	-2.571	-0.022	0.559	-2.623	-1.361	-0.008	898.9
0.525	0.766	-2.571	0.022	0.559	-2.623	-1.361	0.008	898.9
0.575	0.766	-2.571	0.067	0.559	-2.623	-1.361	0.024	899.3
0.625	0.767	-2.570	0.114	0.560	-2.623	-1.360	0.040	900.2
0.675	0.768	-2.570	0.164	0.561	-2.623	-1.360	0.058	901.5
0.725	0.769	-2.569	0.219	0.562	-2.622	-1.360	0.077	903.4
0.775	0.768	-2.567	0.281	0.561	-2.620	-1.360	0.099	905.8
0.825	0.764	-2.565	0.356	0.557	-2.618	-1.361	0.125	908.9
0.875	0.749	-2.562	0.453	0.543	-2.614	-1.366	0.159	913.2
0.925	0.699	-2.561	0.613	0.493	-2.609	-1.384	0.214	922.4
0.975	0.437	-2.635	0.988	0.226	-2.662	-1.486	0.336	1000.0

sp5.2 ; ω=10.43°								
x_3/B	K_1	K_2	K_{III}	$\hat{K}_1$	$\hat{K}_2$	$\hat{\psi}$	ϕ	$\mathcal{G}_{ic}$
	(MPa$\sqrt{\text{m}} \cdot \text{m}^{-i\varepsilon}$)		(MPa$\sqrt{\text{m}}$)	(MPa$\sqrt{\text{m}}$)		(rad)	(rad)	(N/m)
0.025	0.468	-2.842	-1.053	0.240	-2.870	-1.487	-0.332	1159.5
0.075	0.750	-2.765	-0.652	0.528	-2.816	-1.386	-0.211	1072.7
0.125	0.805	-2.767	-0.483	0.582	-2.822	-1.368	-0.157	1063.3
0.175	0.820	-2.770	-0.379	0.597	-2.827	-1.363	-0.123	1058.8
0.225	0.825	-2.773	-0.300	0.602	-2.830	-1.361	-0.098	1055.7
0.275	0.826	-2.775	-0.234	0.603	-2.831	-1.361	-0.076	1053.1
0.325	0.826	-2.776	-0.176	0.603	-2.833	-1.361	-0.057	1051.1
0.375	0.825	-2.776	-0.122	0.602	-2.833	-1.362	-0.040	1049.7
0.425	0.825	-2.777	-0.072	0.601	-2.834	-1.362	-0.024	1048.8
0.475	0.824	-2.777	-0.024	0.601	-2.834	-1.362	-0.008	1048.3
0.525	0.824	-2.777	0.024	0.601	-2.834	-1.362	0.008	1048.3
0.575	0.825	-2.777	0.072	0.601	-2.834	-1.362	0.024	1048.8
0.625	0.825	-2.776	0.122	0.602	-2.833	-1.362	0.040	1049.7
0.675	0.826	-2.776	0.176	0.603	-2.833	-1.361	0.057	1051.1
0.725	0.826	-2.775	0.234	0.603	-2.831	-1.361	0.076	1053.1
0.775	0.825	-2.773	0.300	0.602	-2.830	-1.361	0.098	1055.7
0.825	0.820	-2.770	0.379	0.597	-2.827	-1.363	0.123	1058.8
0.875	0.805	-2.767	0.483	0.582	-2.822	-1.368	0.157	1063.3
0.925	0.750	-2.765	0.652	0.528	-2.816	-1.386	0.211	1072.7
0.975	0.468	-2.842	1.053	0.240	-2.870	-1.487	0.332	1159.1

Appendix G

Beam-type specimens: additional data

In this appendix, the values measured for the upper and lower sub-laminates of the beam-type specimens described in Section 5.1.1 and as illustrated in Fig. 5.3b are presented in Tables G.1 and G.2, respectively. In addition, their scaled values, calculated by means of eqs. $(5.1)_1$ and $(5.1)_2$, are presented in Tables G.3 and G.4, respectively.

Table G.1: Measured values of the upper sub-laminate height h_T of the beam-type specimens.

specimen no.	h_{T1} (mm)	h_{T2} (mm)	h_{T3} (mm)	h_{T4} (mm)	h_{T5} (mm)	$\overline{h}_T$ (mm)	STD (mm)
DCB-7-1.1	2.25	2.22	2.25	2.26	2.22	2.24	0.01
DCB-7-1.2	2.31	2.29	2.26	2.24	-	2.27	0.02
DCB-7-1.3	2.26	2.27	2.23	2.26	2.25	2.25	0.01
MMELS-7-1.5	2.25	2.22	2.23	2.24	2.26	2.24	0.01
MMELS-7-1.7	2.27	2.24	2.29	2.24	2.23	2.25	0.02
MMELS-7-1.9	2.24	2.24	2.23	2.22	2.25	2.24	0.01
C-ELS-7-1.10	2.23	2.25	2.23	2.24	2.22	2.23	0.01
C-ELS-7-1.11	2.25	2.23	2.26	2.22	2.24	2.24	0.01
C-ELS-7-1.12	2.22	2.22	2.25	2.22	2.21	2.22	0.01
C-ELS-7-1.13	2.28	2.30	2.25	2.29	2.26	2.28	0.02
C-ELS-7-1.14	2.24	2.24	2.22	2.22	2.20	2.22	0.01
MMELS-7-1.17	2.26	2.22	2.25	2.21	2.25	2.23	0.02
MMELS-7-1.18	2.19	2.20	2.21	2.18	2.20	2.20	0.01

Table G.2: Measured values of the lower sub-laminate height h_B of the beam-type specimens.

specimen no.	h_{B1} (mm)	h_{B2} (mm)	h_{B3} (mm)	h_{B4} (mm)	h_{B5} (mm)	$\overline{h}_B$ (mm)	STD (mm)
DCB-7-1.1	2.71	2.71	2.71	2.73	2.71	2.71	0.01
DCB-7-1.2	2.74	2.77	2.77	2.77	-	2.76	0.01
DCB-7-1.3	2.71	2.74	2.75	2.74	2.73	2.73	0.01
MMELS-7-1.5	2.70	2.72	2.70	2.71	2.73	2.71	0.01
MMELS-7-1.7	2.74	2.76	2.75	2.69	2.71	2.73	0.03
MMELS-7-1.9	2.65	2.71	2.70	2.69	2.69	2.69	0.02
C-ELS-7-1.10	2.69	2.74	2.69	2.69	2.70	2.70	0.02
C-ELS-7-1.11	2.71	2.72	2.73	2.72	2.72	2.72	0.01
C-ELS-7-1.12	2.70	2.71	2.70	2.72	2.69	2.71	0.01
C-ELS-7-1.13	2.74	2.75	2.76	2.76	2.74	2.75	0.01
C-ELS-7-1.14	2.71	2.75	2.74	2.74	2.71	2.73	0.02
MMELS-7-1.17	2.70	2.74	2.74	2.72	2.71	2.72	0.01
MMELS-7-1.18	2.69	2.71	2.70	2.72	2.70	2.71	0.01

Table G.3: Scaled values for the upper sub-laminate height $h_T^{(sc)}$ of the beam-type specimens, calculated by means of eq. $(5.1)_1$.

specimen no.	$h_{T1}^{(sc)}$ (mm)	$h_{T2}^{(sc)}$ (mm)	$h_{T3}^{(sc)}$ (mm)	$h_{T4}^{(sc)}$ (mm)	$h_{T5}^{(sc)}$ (mm)	$\overline{h}_T^{(sc)}$ (mm)	STD (mm)
DCB-7-1.1	2.26	2.24	2.27	2.27	2.24	2.26	0.01
DCB-7-1.2	2.31	2.30	2.27	2.25	-	2.28	0.02
DCB-7-1.3	2.29	2.29	2.26	2.29	2.28	2.28	0.01
MMELS-7-1.5	2.28	2.25	2.26	2.27	2.29	2.27	0.01
MMELS-7-1.7	2.26	2.24	2.29	2.23	2.22	2.25	0.02
MMELS-7-1.9	2.25	2.25	2.25	2.24	2.27	2.25	0.01
C-ELS-7-1.10	2.24	2.26	2.24	2.25	2.23	2.24	0.01
C-ELS-7-1.11	2.26	2.24	2.27	2.23	2.24	2.25	0.01
C-ELS-7-1.12	2.24	2.24	2.27	2.24	2.23	2.24	0.01
C-ELS-7-1.13	2.26	2.28	2.23	2.27	2.24	2.26	0.02
C-ELS-7-1.14	2.25	2.25	2.23	2.22	2.21	2.23	0.01
MMELS-7-1.17	2.25	2.21	2.24	2.20	2.24	2.23	0.02
MMELS-7-1.18	2.22	2.23	2.24	2.21	2.23	2.23	0.01

Table G.4: Scaled values for the lower sub-laminate height $h_B^{(sc)}$ of the beam-type specimens, calculated by means of eq. $(5.1)_2$.

specimen no.	$h_{B1}^{(sc)}$ (mm)	$h_{B2}^{(sc)}$ (mm)	$h_{B3}^{(sc)}$ (mm)	$h_{B4}^{(sc)}$ (mm)	$h_{B5}^{(sc)}$ (mm)	$\overline{h}_B^{(sc)}$ (mm)	STD (mm)
DCB-7-1.1	2.72	2.73	2.72	2.75	2.73	2.73	0.01
DCB-7-1.2	2.75	2.78	2.79	2.78	-	2.77	0.01
DCB-7-1.3	2.75	2.78	2.78	2.77	2.77	2.77	0.01
MMELS-7-1.5	2.74	2.76	2.74	2.75	2.77	2.75	0.01
MMELS-7-1.7	2.73	2.75	2.74	2.68	2.71	2.72	0.03
MMELS-7-1.9	2.67	2.73	2.72	2.7	2.71	2.71	0.02
C-ELS-7-1.10	2.70	2.75	2.70	2.70	2.71	2.71	0.02
C-ELS-7-1.11	2.71	2.73	2.73	2.73	2.73	2.73	0.01
C-ELS-7-1.12	2.72	2.73	2.73	2.74	2.72	2.73	0.01
C-ELS-7-1.13	2.72	2.73	2.73	2.73	2.71	2.72	0.01
C-ELS-7-1.14	2.73	2.76	2.75	2.75	2.72	2.74	0.02
MMELS-7-1.17	2.70	2.73	2.73	2.71	2.70	2.71	0.01
MMELS-7-1.18	2.73	2.75	2.74	2.76	2.74	2.74	0.01

The delamination propagation data of specimens DCB-7-1.1, DCB-7-1.2 and DCB-7-1.3 is presented in Tables G.5, G.6 and G.7, respectively, for visually detected and evaluated delamination lengths. The values of the power law fitting parameters of eq. (5.4), g and C_0, as well as the coefficient of determination R^2, used in the determination of the relationship between the specimen compliance and delamination length are presented for each DCB specimen in the captions. In each of these tables, the calculated values of $\mathcal{G}_i$ referred to as $\mathcal{G}_{IR}$, which were obtained by means of the FE method, are presented for both experimentally detected and evaluated delamination lengths of the corresponding DCB specimen.

Table G.5: Delamination propagation parameters for specimen DCB-7-1.1: visually detected and calculated by means of eq. (5.4) with $g = 115.66\ (\mathrm{N \cdot mm^2})^{1/3}$, $C_0 = 6.23 \cdot 10^{-3}$ mm/N and $R^2 = 0.998$.

a (mm)	Δa (mm)	C (mm/N)	P (N)	image no.	delamination details	$\mathcal{G}_{IR}$ (N/m)
50.54	0.0	0.085	53.6	546	visually detected	322.3
51.44	0.9	0.092	58.6	1259	visually detected	398.2
55.54	5.0	0.119	69.8	1507	visually detected	652.4
56.14	5.6	0.121	69.8	1512	calculated	632.4
59.24	8.7	0.155	70.5	1738	visually detected	750.4
64.81	14.3	0.182	66.4	1824	calculated	748.7
66.02	15.5	0.192	60.0	1934	calculated	633.6
68.45	17.9	0.214	62.3	2079	calculated	730.3
74.34	23.8	0.282	55.6	2326	visually detected	717.0
78.04	27.5	0.300	52.0	2487	visually detected	688.5
82.54	32.0	0.358	49.7	2702	visually detected	698.9
85.14	34.6	0.409	48.6	2838	visually detected	708.0
88.58	38.0	0.455	47.5	3074	calculated	692.8
89.88	39.4	0.476	44.9	3276	calculated	637.8
96.99	46.5	0.596	44.7	3664	calculated	730.9
97.83	47.3	0.611	41.9	3847	calculated	654.5
103.37	52.8	0.720	40.7	4100	calculated	686.4
104.54	54.0	0.748	40.8	4105	visually detected	743.4
106.63	56.1	0.790	40.0	4481	calculated	703.0

Table G.6: Delamination propagation parameters for specimen DCB-7-1.2: visually detected and calculated by means of eq. (5.4) with $g = 120.95\ (\mathrm{N \cdot mm^2})^{1/3}$, $C_0 = 1.37 \cdot 10^{-2}$ mm/N and $R^2 = 0.998$.

a (mm)	Δa (mm)	C (mm/N)	P (N)	image no.	delamination details	$\mathcal{G}_{IR}$ (N/m)
51.52	0.0	0.086	63.0	651	visually detected	445.1
52.32	0.8	0.097	62.0	1447	visually detected	444.4
59.46	7.9	0.132	67.2	1635	calculated	629.3
61.92	10.4	0.148	67.3	1708	calculated	679.8
63.90	12.4	0.161	67.2	1942	calculated	719.3
66.02	14.5	0.188	65.0	2116	visually detected	753.6
69.46	17.9	0.203	66.8	2160	calculated	833.9
73.19	21.7	0.235	60.8	2299	calculated	762.7
74.32	22.8	0.260	62.0	2608	visually detected	857.4
79.32	27.8	0.293	52.3	2670	visually detected	689.4
84.52	33.0	0.335	48.8	2944	visually detected	678.2
85.94	34.4	0.372	50.9	3023	calculated	724.8
88.78	37.3	0.409	50.5	3207	calculated	758.2
95.91	44.4	0.512	48.2	3481	calculated	801.6
97.52	46.0	0.529	44.6	3802	visually detected	742.8
107.16	55.6	0.709	42.3	4222	calculated	763.8
109.52	58.0	0.766	38.0	4416	visually detected	674.9
111.25	59.7	0.792	38.9	4465	calculated	693.5

Table G.7: Delamination propagation parameters for specimen DCB-7-1.3: visually detected and calculated by means of eq. (5.4) with $g = 118.83\ (\mathrm{N \cdot mm^2})^{1/3}$, $C_0 = 2.62 \cdot 10^{-2}$ mm/N and $R^2 = 0.994$.

a (mm)	Δa (mm)	C (mm/N)	P (N)	image no.	delamination details	$\mathcal{G}_{IR}$ (N/m)
50.73	0.0	0.086	56.7	600	visually detected	361.5
53.38	0.7	0.107	65.9	1906	calculated	466.0
59.73	9.0	0.156	66.5	2120	visually detected	672.9
64.33	13.6	0.179	62.3	2274	visually detected	680.7
67.53	16.8	0.234	58.6	2423	visually detected	658.5
72.62	21.9	0.254	58.6	2571	calculated	704.3
73.03	22.3	0.261	55.3	2708	visually detected	681.8
74.13	23.4	0.269	55.6	2724	calculated	661.2
76.69	26.0	0.295	53.2	2799	calculated	643.8
79.99	29.3	0.331	51.3	2930	calculated	650.1
83.47	32.7	0.373	48.7	3065	calculated	634.6
84.23	33.5	0.380	49.0	3217	visually detected	702.4
85.37	34.6	0.397	50.4	3294	calculated	710.4
86.64	35.9	0.414	50.1	3470	calculated	720.9
95.06	44.3	0.538	43.0	3702	calculated	635.6
98.23	47.5	0.587	43.6	4048	visually detected	745.7
105.76	55.0	0.731	42.5	4487	calculated	762.0

The delamination propagation data of specimens C-ELS-7-1.10 through C-ELS-7-1.14 is presented in Tables G.8 to G.12 for visually detected delamination lengths. The values of the power law fitting parameters of eq. (5.4), g and C_0, as well as the coefficient of determination R^2, used in the determination of the relationship between the specimen compliance and delamination length are presented for each C-ELS specimen in the captions. In each of these tables, the calculated values of $\mathcal{G}_i$ referred to as $\mathcal{G}_{IIR}$, which were obtained by means of the FE method, are presented for experimentally detected delamination lengths of the corresponding C-ELS specimen.

Table G.8: Delamination propagation parameters for specimen C-ELS-7-1.10: visually detected by means of eq. (5.4) with $g = 206.36\ (\mathrm{N} \cdot \mathrm{mm}^2)^{1/3}$, $C_0 = 2.95 \cdot 10^{-2}$ mm/N and $R^2 = 0.993$.

a (mm)	Δa (mm)	C (mm/N)	P (N)	image no.	delamination details	P^{FEA} (N)	$\mathcal{G}_{IIR}$ (N/m)
50.44	0.0	0.0340	239.9	966	visually detected	243.2	1239.4
53.74	3.3	0.0482	260.0	2970	visually detected	259.9	1558.1
54.34	3.9	0.0485	269.8	3198	visually detected	267.7	1686.9
55.94	5.5	0.0502	294.1	3511	visually detected	295.4	2143.6
56.44	6.0	0.0512	300.0	3659	visually detected	305.0	2319.9
59.24	8.8	0.0532	298.7	3796	visually detected	299.8	2434.1
60.44	10.0	0.0544	300.2	3911	visually detected	301.8	2552.4
61.94	11.5	0.0565	289.9	3936	visually detected	294.2	2537.7
63.94	13.5	0.0580	282.1	3939	visually detected	281.9	2473.4
65.94	15.5	0.0629	260.2	3976	visually detected	272.4	2444.0
66.04	15.6	0.0630	261.1	4001	visually detected	273.5	2469.0
68.44	18.0	0.0659	256.4	4126	visually detected	267.8	2524.0
70.64	20.2	0.0686	248.8	4184	visually detected	258.5	2494.0
72.94	22.5	0.0731	241.3	4352	visually detected	255.9	2584.2

Table G.9: Delamination propagation parameters for specimen C-ELS-7-1.11: visually detected by means of eq. (5.4) with $g = 217.32\ (\mathrm{N} \cdot \mathrm{mm}^2)^{1/3}$, $C_0 = 3.13 \cdot 10^{-2}$ mm/N and $R^2 = 0.995$.

a (mm)	Δa (mm)	C (mm/N)	P (N)	image no.	delamination details	P^{FEA} (N)	$\mathcal{G}_{IIR}$ (N/m)
50.12	0.0	0.0317	207.1	782	visually detected	204.2	845.5
52.09	1.96	0.0451	251.0	2687	visually detected	251.4	1347.5
53.93	3.8	0.0465	278.5	3065	visually detected	276.4	1730.8
54.73	4.6	0.0471	302.2	3375	visually detected	300.8	2089.3
55.13	5.0	0.0477	311.5	3531	visually detected	312.9	2282.1
59.43	9.3	0.0515	293.7	3611	visually detected	293.0	2291.8
59.63	9.5	0.0517	294.7	3639	visually detected	294.0	2323.4
63.33	13.2	0.0563	283.3	3832	visually detected	286.3	2453.8
64.13	14.0	0.0575	279.2	3860	visually detected	283.7	2460.4
67.43	17.3	0.0622	259.0	3898	visually detected	266.2	2377.7
69.13	19.0	0.0630	256.8	3915	visually detected	257.3	2326.5
70.13	20.0	0.0639	255.1	3952	visually detected	253.7	2322.7
71.13	21.0	0.0668	244.8	3977	visually detected	249.7	2308.6
71.93	21.8	0.0693	237.2	4007	visually detected	247.1	2308.4

Table G.10: Delamination propagation parameters for specimen C-ELS-7-1.12: visually detected by means of eq. (5.4) with $g = 219.38\ (\mathrm{N} \cdot \mathrm{mm}^2)^{1/3}$, $C_0 = 3.24 \cdot 10^{-2}$ mm/N and $R^2 = 0.993$.

a (mm)	Δa (mm)	C (mm/N)	P (N)	image no.	delamination details	P^{FEA} (N)	$\mathcal{G}_{IIR}$ (N/m)
50.04	0	0.0321	189.2	1791	visually detected	181.1	681.1
53.04	3.0	0.0478	248.4	2838	visually detected	251.2	1417.1
57.04	7.0	0.0492	289.7	3409	visually detected	279.0	1984.9
57.54	7.5	0.0500	300.6	3602	visually detected	292.8	2210.5
57.74	7.7	0.0504	309.0	3733	visually detected	302.9	2371.7
58.44	8.4	0.0505	309.0	3739	visually detected	298.9	2360.9
59.84	9.8	0.0523	302.3	3792	visually detected	294.6	2392.4
61.04	11.0	0.0542	292.5	3810	visually detected	288.6	2381.2
63.34	13.3	0.0558	291.7	3923	visually detected	283.4	2453.2
67.04	17.0	0.0618	273.5	4088	visually detected	272.9	2519.9
68.04	18.0	0.0626	270.1	4094	visually detected	267.5	2488.1
68.34	18.3	0.0634	267.9	4117	visually detected	267.0	2499.1
70.54	20.5	0.0655	261.5	4162	visually detected	257.0	2454.8
71.04	21.0	0.0673	256.9	4205	visually detected	256.9	2484.3
72.84	22.8	0.0684	255.3	4252	visually detected	249.4	2451.0

Table G.11: Delamination propagation parameters for specimen C-ELS-7-1.13: visually detected by means of eq. (5.4) with $g = 214.47\ (\mathrm{N \cdot mm^2})^{1/3}$, $C_0 = 3.26 \cdot 10^{-2}$ mm/N and $R^2 = 0.996$.

a (mm)	Δa (mm)	C (mm/N)	P (N)	image no.	delamination details	P^{FEA} (N)	$\mathcal{G}_{IIR}$ (N/m)
49.66	0.0	0.0315	227.3	838	visually detected	225.7	1009.2
54.72	5.07	0.0491	259.5	3020	visually detected	257.4	1529.2
55.66	6.0	0.0503	279.5	3323	visually detected	278.2	1837.2
56.66	7.0	0.0515	305.6	3730	visually detected	308.1	2302.6
58.86	9.2	0.0527	298.3	3736	visually detected	295.2	2267.9
58.96	9.3	0.0541	293.3	3782	visually detected	298.6	2323.7
60.16	10.5	0.0549	297.1	3887	visually detected	300.0	2429.0
64.66	15.0	0.0591	279.0	3957	visually detected	278.2	2384.8
66.66	17.0	0.0625	269.7	4059	visually detected	273.8	2439.7
70.06	20.4	0.0662	260.2	4169	visually detected	261.5	2438.2
70.66	21.0	0.0690	249.4	4176	visually detected	258.5	2421.1
73.46	23.8	0.0727	236.5	4194	visually detected	244.0	2320.7
73.66	24.0	0.0740	232.0	4195	visually detected	242.9	2311.6
74.66	25.0	0.0751	228.5	4198	visually detected	237.7	2270.6

Table G.12: Delamination propagation parameters for specimen C-ELS-7-1.14: visually detected by means of eq. (5.4) with $g = 218.44\ (\mathrm{N \cdot mm^2})^{1/3}$, $C_0 = 2.98 \cdot 10^{-2}$ mm/N and $R^2 = 0.997$.

a (mm)	Δa (mm)	C (mm/N)	P (N)	image no.	delamination details	P^{FEA} (N)	$\mathcal{G}_{IIR}$ (N/m)
49.47	0.0	0.0295	196.3	1032	visually detected	183.0	670.2
51.06	1.59	0.0419	237.2	3527	visually detected	226.6	1077.4
52.47	3.0	0.0438	263.6	4100	visually detected	257.1	1444.2
53.47	4.0	0.0441	270.1	4228	visually detected	260.1	1526.0
53.97	4.5	0.0444	274.1	4324	visually detected	263.5	1591.1
54.17	4.7	0.0447	276.6	4395	visually detected	266.8	1640.3
55.37	5.9	0.0463	298.6	4935	visually detected	293.3	2050.4
55.47	6.0	0.0468	300.1	5019	visually detected	298.6	2119.0
56.47	7.0	0.0472	300.2	5062	visually detected	294.7	2136.2
57.27	7.8	0.0479	298.0	5110	visually detected	292.9	2162.3
59.87	10.4	0.0505	286.3	5193	visually detected	281.5	2166.5
60.77	11.3	0.0515	280.9	5203	visually detected	276.6	2150.1
63.27	13.8	0.0537	269.6	5221	visually detected	262.5	2086.3
64.47	15.0	0.0557	264.5	5331	visually detected	261.2	2135.7
67.67	18.2	0.0588	260.1	5551	visually detected	253.3	2191.8
67.97	18.5	0.0599	256.4	5582	visually detected	253.4	2205.2
69.87	20.4	0.0629	245.8	5643	visually detected	256.1	2256.3
70.27	20.8	0.0632	244.7	5649	visually detected	243.2	2168.5
71.47	22.0	0.0662	233.8	5670	visually detected	237.2	2125.3

The delamination propagation data of specimens MMELS-7-1.5, MMELS-7-1.7, MMELS-7-1.9, MMELS-7-1.17 and MMELS-7-1.18 is presented in Tables G.13 to G.17 for visually detected and evaluated delamination lengths. The values of the power law fitting parameters of eq. (5.4), g and C_0, as well as the coefficient of determination R^2, used in the determination of the relationship between the specimen compliance and delamination length are presented for each MMELS specimen in the captions. In each of these tables, the calculated values of $\mathcal{G}_i$, referred to as $\mathcal{G}_{iR}$, which were obtained by means of the FE method, are also presented. These values are actually the global fracture resistance, average through the thickness, values for the experimentally obtained failure loads.

Table G.13: Delamination propagation parameters for specimen MMELS-7-1.5: visually detected by means of eq. (5.4) with $g = 146.66\ (\mathrm{N} \cdot \mathrm{mm}^2)^{1/3}$, $C_0 = 4.10 \cdot 10^{-2}$ mm/N and $R^2 = 0.998$.

a (mm)	Δa (mm)	C (mm/N)	P (N)	image no.	delamination details	$\mathcal{G}_{iR}$ (N/m)
50.50	0.0	0.079	78.5	2234	visually detected	353.8
54.05	3.55	0.091	99.5	3105	visually detected	646.6
55.20	4.70	0.096	103.9	3467	visually detected	734.6
59.50	9.00	0.106	98.6	3665	visually detected	762.0
62.50	12.00	0.123	94.0	4020	visually detected	761.7
69.25	18.75	0.147	83.3	4291	visually detected	726.8
71.75	21.25	0.159	86.6	4870	visually detected	841.7
76.15	25.65	0.178	83.7	5263	visually detected	881.4
80.25	29.75	0.202	80.8	5744	visually detected	909.1
83.75	33.25	0.229	76.2	6161	visually detected	878.7
88.50	38.00	0.261	70.3	6489	visually detected	831.3

Table G.14: Delamination propagation parameters for specimen MMELS-7-1.7: visually detected by means of eq. (5.4) with $g = 147.04\ (\mathrm{N \cdot mm^2})^{1/3}$, $C_0 = 4.36 \cdot 10^{-2}$ mm/N and $R^2 = 0.997$.

a (mm)	Δa (mm)	C (mm/N)	P (N)	image no.	delamination details	$\mathcal{G}_{iR}$ (N/m)
51.20	0.0	0.082	79.9	2350	visually detected	385.9
54.95	3.75	0.094	92.3	3000	visually detected	589.8
56.50	5.30	0.099	106.9	3721	visually detected	833.1
62.20	11.00	0.120	93.8	3958	visually detected	771.5
66.20	15.00	0.139	91.5	4470	visually detected	827.3
70.20	19.00	0.157	88.1	4872	visually detected	858.4
75.45	24.25	0.18	82.1	5215	visually detected	856.0
79.04	27.84	0.202	79.2	5654	visually detected	871.5
82.74	31.54	0.230	74.6	6080	visually detected	845.5
84.74	33.54	0.231	76.9	6291	visually detected	940.8
87.74	36.54	0.257	73.4	6697	visually detected	915.9
88.24	37.04	0.258	73.9	6837	visually detected	938.3

Table G.15: Delamination propagation parameters for specimen MMELS-7-1.9: visually detected and calculated by means of eq. (5.4) with $g = 148.96\ (\mathrm{N \cdot mm^2})^{1/3}$, $C_0 = 4.05 \cdot 10^{-2}$ mm/N and $R^2 = 0.999$.

a (mm)	Δa (mm)	C (mm/N)	P (N)	image no.	delamination details	$\mathcal{G}_{iR}$ (N/m)
50.69	0.0	0.083	80.8	1216	visually detected	388.5
54.29	3.60	0.086	99.8	1546	visually detected	675.4
57.79	7.10	0.100	106.8	1871	visually detected	871.4
62.49	11.80	0.115	96.7	1992	visually detected	829.2
64.69	14.00	0.119	97.8	2092	visually detected	905.0
67.59	16.90	0.134	91.5	2200	evaluated	861.5
69.90	19.21	0.144	88.7	2296	evaluated	863.7
71.49	20.80	0.152	88.3	2415	visually detected	894.1
76.16	25.46	0.174	81.5	2553	evaluated	860.8
76.24	25.54	0.175	83.4	2621	evaluated	903.4
79.69	29.00	0.195	77.7	2715	visually detected	853.8
82.69	32.00	0.213	74.6	2850	visually detected	843.4
85.69	35.00	0.231	70.9	2941	visually detected	817.5
86.89	36.20	0.238	71.5	3056	visually detected	854.1
89.69	39.00	0.258	68.4	3178	visually detected	831.2

Table G.16: Delamination propagation parameters for specimen MMELS-7-1.17: visually detected and calculated by means of eq. (5.4) with $g = 146.01\ (\mathrm{N \cdot mm^2})^{1/3}$, $C_0 = 4.48 \cdot 10^{-2}$ mm/N and $R^2 = 0.999$.

a (mm)	Δa (mm)	C (mm/N)	P (N)	image no.	delamination details	$\mathcal{G}_{iR}$ (N/m)
51.20	0.0	0.085	79.1	2439	visually detected	392.5
52.10	0.90	0.089	93.8	2850	visually detected	569.7
52.60	1.40	0.090	112	3508	visually detected	827.2
54.90	3.70	0.097	106.5	3587	visually detected	811.5
60.70	9.50	0.118	101.2	4165	visually detected	887.4
67.95	16.75	0.149	83.0	4288	visually detected	740.3
68.20	17.00	0.147	87.4	4525	visually detected	827.0
71.95	20.75	0.165	80.6	4650	visually detected	780.2
72.05	20.85	0.167	82.3	4802	visually detected	815.0
76.45	25.25	0.189	75.9	5024	visually detected	778.1
76.95	25.75	0.191	78.2	5241	visually detected	836.6
77.60	26.40	0.197	77.5	5351	visually detected	833.4
80.50	29.30	0.212	77.3	5760	evaluated	890.4
84.30	33.10	0.234	75.6	6224	visually detected	930.9
87.73	36.53	0.262	69.3	6358	evaluated	845.2
89.35	38.15	0.273	67.8	6493	visually detected	840.0

Table G.17: Delamination propagation parameters for specimen MMELS-7-1.18: visually detected by means of eq. (5.4) with $g = 144.91\ (\mathrm{N \cdot mm^2})^{1/3}$, $C_0 = 4.16 \cdot 10^{-2}$ mm/N and $R^2 = 0.999$.

a (mm)	Δa (mm)	C (mm/N)	P (N)	image no.	delamination details	$\mathcal{G}_{iR}$ (N/m)
51.22	0.0	0.086	84.2	2615	visually detected	445.6
54.27	3.05	0.093	93.8	2860	visually detected	616.8
59.22	8.00	0.108	96.7	3642	visually detected	773.9
59.57	8.35	0.109	98.4	3732	visually detected	810.7
60.57	9.35	0.115	95.7	3835	visually detected	792.0
63.87	12.65	0.128	91.5	4098	visually detected	802.0
63.97	12.75	0.128	93.1	4176	visually detected	832.9
64.32	13.10	0.128	94.3	4236	visually detected	863.5
69.92	18.70	0.156	80.8	4425	visually detected	743.0
72.32	21.10	0.166	78.7	4600	visually detected	751.9
76.17	24.95	0.191	75.0	4889	visually detected	754.8
76.82	25.60	0.191	78.2	5256	visually detected	833.8
80.57	29.35	0.216	71.1	5439	visually detected	757.2
80.72	29.50	0.216	73.8	5614	visually detected	818.9
84.27	33.05	0.24	67.9	5810	visually detected	752.0
88.07	36.85	0.264	65.1	6128	visually detected	754.3
88.32	37.10	0.267	66.7	6240	visually detected	796.3
88.97	37.75	0.271	67.2	6429	visually detected	818.3

ההתנגדות להתקדמות ההפרדה $\mathcal{G}_{iR}$, לכל אחת מתצורות הדגמים. בנוסף, נקבעים גם ערכי החסינות לשבר $\mathcal{G}_{ic}$ ולהתקדמות הפרדה במצב יציב $\mathcal{G}_{iss}$.

הצגה כמותית של ערכי קצב שחרור האנרגיה הקריטיים $\mathcal{G}_{ic}$ שהתקבלו עבור אתחול שבר בכל דגמי הניסויים השונים, מופיעה כתלות במוד העירוב התוך מישורי. עבור דגמי beam-type מיושם קריטריון כשל אמפירי, כפי שהוצע על ידי Benzeggagh and Kenane (1996). בשתי תצורות הדגמים (BD ו-beam-type), ניכר כי ככל שערך מוד העירוב התוך מישורי $\hat{\psi}$ מתקרב ל-0, ערכו של $\mathcal{G}_{ic}$ קטן. עם זאת, נמצא כי הערך של $\mathcal{G}_{ic}$ עבור $\hat{\psi} = 0$ רגיש לעובי של דגם הניסוי. לפיכך, מסתמן כי עבור דפורמציה בכמעט מוד-I, העובי של האלמנט המבני הנבחן צריך להכתיב עוביו של דגם הניסוי.

תקציר

יתרונותיהם של חומרים מרוכבים, כדוגמת חוזק וקשיחות גבוהים עם משקל נמוך, תנגודת גבוהה לקורוזיה ולהתעייפות, הופכים אותם לאטרקטיביים ומועדפים לשימוש, בפרט בתעשיית התעופה. עם זאת, מבנים מחומרים מרוכבים רגישים להמצאות פגמים כדוגמת הפרדות (דלמינציות), שמהוות אחד מאופני הכשל הטיפוסיים בליווחי חומרים מרוכבים. הפרדה בין שכבות יכולה להווצר במהלך תהליך הייצור או כתוצאה מפגיעה לא מכוונת לאחר הייצור. הבעיה המרכזית במבנים מחומרים מרוכבים הנה הקושי הרב באיתור ומעקב אחר פגמים. המחסור במידע מדוייק ואמין המאפשר הערכת התקדמות הנזק בתוך המבנה, כדוגמת ערכי החסינות לשבר, להתעייפות וסבולת נזק, מסתכם בתכנון יתר ובמשקל עודף של המבנה עקב דרישות הרגולציה למרווחי בטחון גבוהים. כדי להבין טוב יותר התנהגות שבר (אתחול והתקדמות) במוד מעורב I/II, הממוקם בממשק בין שני אריגים מישוריים העשויים מטריצת אפוקסי וסיבי פחמן בכיוונים $0^\circ/90^\circ$ ו- $+45^\circ/-45^\circ$, נעשה מחקר מקיף הכולל פיתוחים אנליטיים, אנליזות נומריות וביצוע ניסויים.

פיתוח אנליטי להרחבת ביטוי האיבר הראשון בטור האסימפטוטי של שדות המאמצים והזזות בקרבת קצה ההפרדה הנחקרת מבוצע תוך שימוש בשיטות Lekhnitskii (1950) ו- Stroh (1958). שדות המאמצים וההזזות התוך-מישוריים מתוארים באמצעות מקדם עוצמת המאמץ המרוכב (קומפלקסי) ; שדות המאמצים וההזזות החוץ-מישוריים מתוארים באמצעות מקדם עוצמת המאמץ הממשי . הביטויים שפותחו מיושמים לאחר מכן בשתי שיטות נפרדות, אקסטרפולציית ההזזות (DE) ואינטגרל-M המשמר, המשמשות לחישוב מקדמי עוצמת המאמץ.

חישוב מקדמי עוצמת המאמץ עבור כל אחד מדגמי הניסוי מבוצע באמצעות אנליזות אלמנטים סופיים ושימוש באינטגרל-M ו/או DE ; מקדמי עוצמת המאמץ המחושבים משמשים בקביעת קצב שחרור האנרגיה הקריטי בממשק (חסינות לשבר) ושתי זוויות הפאזה (עירוב המודים). התוכנה שנכתבה עבור אינטגרל-M ו-DE, כמו גם הביטוי לאיבר הראשון בטור האסימפטוטי של שדות המאמצים והזזות, נבדקים על ידי ביצוע אנליזה נומרית לשלושה מקרי בוחן, ושתי השיטות נמצאות קבילות. התאמה מצויינת של ערכי מקדמי עוצמת המאמץ מתקבלת מביצוע השוואת הערכים המחושבים (אינטגרל-M ו-DE) לאלו המדוייקים (פתרון אנליטי). כמו כן, נבחנים ומאומתים התכנסות הפתרון ואי התלות במסלול האינטגרציה.

ניסויי חסינות לשבר במוד מעורב מבוצעים בדגם דיסקה ברזילאית (BD) בעל ליווח רב כיווני, המכיל הפרדה, בזוויות עומס שונות במטרה להשיג טווח רחב של עירוב מודים. מפותח קריטריון לכשל במתכונת דו ותלת-מימדית, תוך שימוש בתוצאות הניסוייות והנומריות בשבר. כדי לכלול הפיזור הקיים בתוצאות, מבוצעת אנליזה סטטיסטית עם 10% התכנות לכשל בלתי צפוי ברמת סמך של 95%. ניתן להשתמש בקריטריוני כשל אלו, עבור הממשק מושא המחקר, לטובת תכן בטוח יותר.

ניסויי חסינות ל אתחול שבר והתקדמות ההפרדה תחת עומס קוואזי-סטטי מבוצעים בשלושה דגמי beam-type : DCB, C-ELS ו-MMELS. הדפורמציות הנשקלות הנן כמעט מוד-I, כמעט מוד-II ויחס אחד של מוד מעורב, בהתאמה. בהתבסס על התוצאות הניסוייות והנומריות, מיוצרת עקומת

אוניברסיטת תל-אביב

הפקולטה להנדסה ע"ש איבי ואלדר פליישמן

בית הספר לתארים מתקדמים ע"ש זנדמן סליינר

התנהגות בשבר של אריגים מישוריים מרוכבים רב כיווניים במודים מעורבים: דלמינציה בממשק בין אריגים בכיוונים $0^\circ/90^\circ$ ו- $+45^\circ/-45^\circ$

על ידי

אורלי דולב

חיבור לשם קבלת התואר "דוקטור לפילוסופיה"

הוגש לסנאט של אוניברסיטת תל-אביב

עבודה זו נעשתה באוניברסיטת תל-אביב בפקולטה להנדסה בהדרכת

פרופ' לסלי בנקס-סילס

טבת תשפ"א

אוניברסיטת תל-אביב

הפקולטה להנדסה ע"ש איבי ואלדר פליישמן

בית הספר לתארים מתקדמים ע"ש זנדמן סליינר

התנהגות בשבר של אריגים מישוריים מרוכבים רב כיווניים במודים מעורבים: דלמינציה בממשק בין אריגים בכיוונים $0^\circ/90^\circ$ ו- $+45^\circ/-45^\circ$

על ידי

אורלי דולב

חיבור לשם קבלת התואר "דוקטור לפילוסופיה"

הוגש לסנאט של אוניברסיטת תל-אביב

טבת תשפ"א